



저작자표시-비영리-변경금지 2.0 대한민국

이용자는 아래의 조건을 따르는 경우에 한하여 자유롭게

- 이 저작물을 복제, 배포, 전송, 전시, 공연 및 방송할 수 있습니다.

다음과 같은 조건을 따라야 합니다:



저작자표시. 귀하는 원저작자를 표시하여야 합니다.



비영리. 귀하는 이 저작물을 영리 목적으로 이용할 수 없습니다.



변경금지. 귀하는 이 저작물을 개작, 변형 또는 가공할 수 없습니다.

- 귀하는, 이 저작물의 재이용이나 배포의 경우, 이 저작물에 적용된 이용허락조건을 명확하게 나타내어야 합니다.
- 저작권자로부터 별도의 허가를 받으면 이러한 조건들은 적용되지 않습니다.

저작권법에 따른 이용자의 권리는 위의 내용에 의하여 영향을 받지 않습니다.

이것은 [이용허락규약\(Legal Code\)](#)을 이해하기 쉽게 요약한 것입니다.

[Disclaimer](#)

이학박사 학위논문

**Synthetic Methodology and Various
Applications for Versatile Functional Polymers:
Chemo-Sensing, Multi-Color Luminescence,
and Controlled Self-Assembly**

다기능성 고분자의 합성 방법론 및 다양한 응용:
화학종 검출, 다색발광 및 조절된 자가조립

2023 년 2 월

서울대학교 대학원

화학부 유기화학 전공

황 순 혁

**Synthetic Methodology and Various
Applications for Versatile Functional Polymers:
Chemo-Sensing, Multi-Color Luminescence,
and Controlled Self-Assembly**

지도 교수 김 경 택

이 논문을 이학박사 학위논문으로 제출함
2023 년 2 월

서울대학교 대학원
화학부 유기화학 전공
황 순 혁

황순혁의 이학박사 학위논문을 인준함
2023 년 2 월

위 원 장 이 동 환 (인)

부위원장 김 경 택 (인)

위 원 최 태 립 (인)

위 원 권 민 상 (인)

위 원 이 인 환 (인)

Abstract

Synthetic Methodology and Various Applications for Versatile Functional Polymers: Chemo-Sensing, Multi-Color Luminescence, and Controlled Self-Assembly

Soon-Hyeok Hwang
Department of Chemistry
The Graduate School
Seoul National University

The academic researches on functional polymers have been driven to meet the continuous demand for new functional materials that can be used in industrial applications. Polymers can possess specific functions by either certain polymerization methods, modulating functional groups, or external stimuli. In addition to the chemical structure of polymer chains, morphology of nanostructures has great effects on the resulting functions. To facilitate the development of new functional polymers, numerous research efforts have been devoted toward new polymerization methodologies. However, the tedious process for monomer preparation has been one of the primary factors for retarding the creation of functional polymers.

This dissertation describes an example of developing a polymerization methodology to overcome the factor slowing the growth of the functional polymer field. Furthermore, we demonstrate several research directions, including stimuli-responsive polymeric materials, luminescent materials, and semiconducting nanostructures.

Because of the intrinsic feature of [3,3]-sigmatropic rearrangement undergoing simultaneous bond formation and breakage, this versatile reaction has not been utilized in polymerization. **Chapter 2** demonstrates the development of a new tandem diaza-Cope rearrangement polymerization (DCRP) that can synthesize polymers with defect-free C–C bond formation from easy and efficient imine formation. This polymerization produces chiral polymers containing enantiopure salen moieties, which lead to high-performance Zn²⁺-selective turn-on chemosensors with high amplification.

It is desirable to develop a versatile and efficient synthetic method capable of predictably preparing multicolor fluorophores under a single set of synthetic conditions or, more desirably, from a common reagent. In this regard, **Chapter 3** describes direct C–H amidation (DCA) as an efficient synthetic method to prepare a library of multicolor fluorophores, even including a compound capable of emitting white-light via an excited-state intramolecular proton-transfer (ESIPT) process. Furthermore, due to the excellent synthetic efficiency, regardless of the positions of functional groups and their electronic properties, DCA could result in the predictable preparation of targeted fluorescence.

Enormous research efforts for preparing white-light-emitting polymers have focused on multi-fluorophore-based random copolymers to cover the entire visible region effectively. However, the conventional strategy suffers from poor color reproducibility. By taking advantage of modular synthesis demonstrated in **Chapter 3** to incorporate various substituents, **Chapter 4** describes a powerful direct C–H amidation polymerization (DCAP) strategy to afford single-fluorophore-based white-light-emitting homopolymers with excellent color reproducibility via ESIPT process. Furthermore, because this polymer emits white-light even in the solid state (powder and thin film) without the help of another matrix, we could easily fabricate white-light-emitting coated LED by a solution process.

While the precise size and morphological controls of semiconducting nanomaterials from conjugated polymers are crucial for optoelectronic applications, the low solubility of the polymers makes this challenging. Lastly, in **Chapter 5**, we describe a powerful crystallization-driven *in situ* nanoparticlization of conjugated polymers (CD-INCP) strategy to afford length-controlled one-dimensional (1D) semiconducting nanoparticles directly during living Suzuki-Miyaura catalyst-transfer polymerization (SCTP), which could enhance preparation efficiency.

Keywords: Functional polymers, diaza-Cope rearrangement polymerization, turn-on chemosensors, direct C–H amidation polymerization, excited-state intramolecular proton-transfer, luminescent materials, crystallization-driven *in situ* nanoparticlization of conjugated polymers, semiconducting nanoparticles.

Student Number: 2017-23693

Table of Contents

Abstract	1
Table of Contents	3

Chapter 1. Introduction

1.1. Research Background.....	6
1.2. Thesis Research.....	11
1.3. References	12

Chapter 2. Tandem Diaza-Cope Rearrangement Polymerization: Turning Intramolecular Reaction into Powerful Polymerization to Give Enantiopure Materials for Zn²⁺ Sensor

2.1. Abstract.....	16
2.2. Introduction	17
2.3. Results and Discussion.....	18
2.4. Conclusion.....	26
2.5. Experimental Section	27
2.6. Supporting Information	31
2.7. References	47

Chapter 3. Iridium-Catalyzed Direct C–H Amidation Producing Multicolor Fluorescent Molecules Emitting Blue-to-Red and White-Light

3.1. Abstract.....	50
3.2. Introduction	50
3.3. Results and Discussion.....	52
3.4. Conclusion.....	59
3.5. Experimental Section	60
3.6. Supporting Information	70
3.7. References	88

Chapter 4. Powerful Direct C–H Amidation Polymerization Affords Single-Fluorophore-Based White-Light-Emitting Polysulfonamides by Fine-Tuning Hydrogen Bonds

4.1. Abstract.....	91
4.2. Introduction	92
4.3. Results and Discussion.....	93
4.4. Conclusion.....	102
4.5. Experimental Section	103
4.6. Supporting Information	116
4.7. References	144

Chapter 5. Synchronous Preparation of Length-Controllable 1D Nanoparticles via Crystallization-Driven in Situ Nanoparticlization of Conjugated Polymers

5.1. Abstract.....	148
5.2. Introduction	149
5.3. Results and Discussion.....	151
5.4. Conclusion.....	159
5.5. Experimental Section	160
5.6. Supporting Information	164
5.7. References	191

Abstract (Korean)	194
--------------------------------	------------

Chapter 1. Introduction

1.1. Research Background

1.1.1. Functional Polymeric Materials

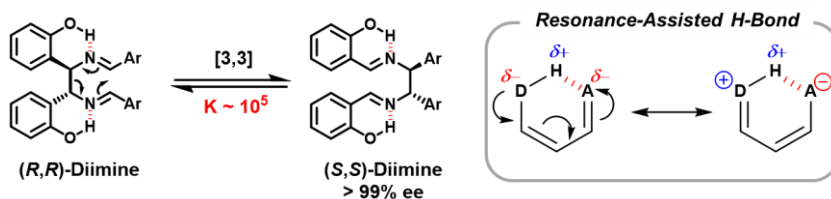
The development of new functional polymers has been actively pursued to meet continuously growing demand for potential applications in many industrial fields, such as luminescence, optoelectronics, stimuli-responsive materials, etc., where conventional polymers (e.g., plastics, artificial fibers, and rubbers) cannot fulfill needs.¹

Much effort has been devoted toward the development of new polymerization methods because it is highly necessary either to introduce monomers' functions into polymer backbone or, more importantly, to create new functions, which can be realized by new chemical bonds formed during a certain polymerization. The resulting polymers can either possess functions intrinsically or be endowed with specific functions by external stimuli. Moreover, not only the chemical structures but also aggregate or self-assembled structures of the polymers are closely related with their functions. For example, precise control on the size of semiconducting nanomaterials has a significant effect on device performance in optoelectronic applications. Thus, it is highly desirable to encompass the polymerization methodology, post-processing, and morphology of polymer nanostructures to afford versatile functions.

1.1.2. Diaza-Cope Rearrangement

Pericyclic reaction, the reorganization of π -bonds in a concerted manner, is one of the most widely used transformations in synthetic organic chemistry. Among the various pericyclic reactions, [3,3]-sigmatropic rearrangement has been employed as the powerful and reliable tool to construct C–C bond stereospecifically.²

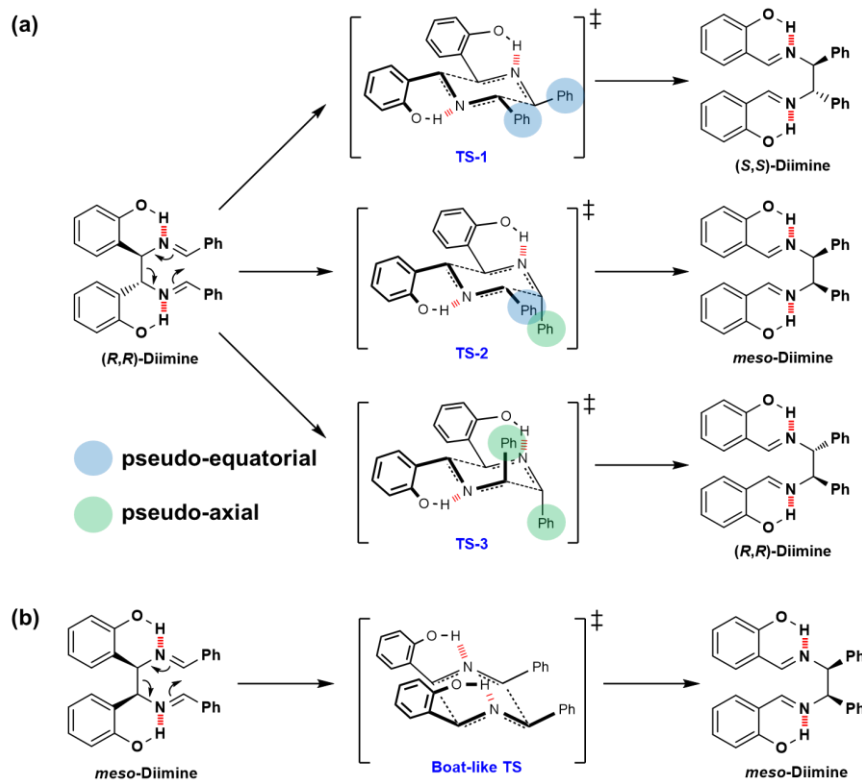
Scheme 1.1. Diaza-Cope Rearrangement (DCR) of Chiral Diimine Driven by Resonance-Assisted Hydrogen Bond (RAHB)



In this context, Chin and co-workers reported highly versatile diaza-Cope rearrangement (DCR) reactions using chiral diamine and benzaldehydes.^{3–11} After efficient imine formation, DCR proceeded rapidly to form a C–C bond with apparent inversion of stereochemistry (Scheme 1.1). Density functional theory (DFT) computation demonstrated that resonance-assisted hydrogen bond (RAHB), which makes hydrogen more acidic and

hydrogen bond acceptor more basic, is the main driving force allowing for stereospecific rearrangement.

Scheme 1.2. (a) Three Possible Chair-Like Transition States (TS) during DCR Process from Chiral Diimine. (b) Boat-Like TS during DCR Process from *meso*-Diimine.



Among three possible chair-like transition states from *(R,R)*-diimine, **TS-1**, which is expected to give the desired *(S,S)*-diimine through a stereoinvertive manner, was found to be thermodynamically most favorable because all phenyl substituents are located in pseudo-equatorial positions, while other transition states (**TS-2** and **TS-3**) contain at least one pseudo-axial phenyl ring to give *meso*- and a stereoretentive *(R,R)*-diimines, respectively (Scheme 1.2a).⁶ Compared to chiral diimines in which two hydrogen bonds are positioned to stabilize the chair-like transition state, the DCR process of *meso*-diimines is much slower and maintains the stereochemistry because two internal hydrogen bonds of *meso*-starting isomer are guaranteed in the boat-like transition state (Scheme 1.2b).⁴

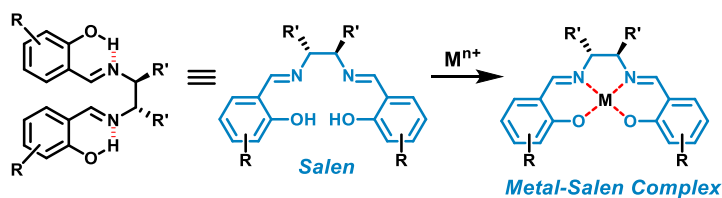


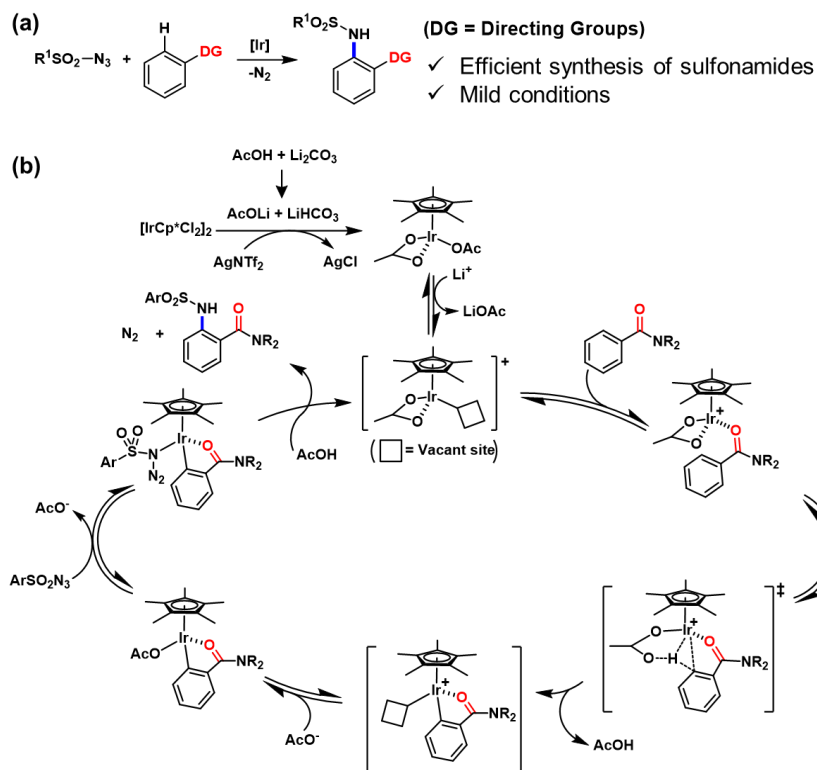
Figure 1.1. Salen structure resulting from DCR of chiral diimine and its metal complex.

Notably, DCR reaction affords chiral salen structures, which have gained enormous attentions due to their high complexation ability with transition metal ions, leading to versatile application potentials in chemo-sensing^{12–14} as well as stereoselective catalysis^{15,16} for a wide range of organic reactions (Figure 1.1).

1.1.3. Direct C–H Amidation

During the last two decades, C–H activation chemistry has gained widespread attention because it provides an atom- and step-economical route for preparing various complex molecules. In the field of C–H activation chemistry, C–C bond formation has been mainly studied so far, but recently, direct C–H amination/amidation strategies resulting in C–N bond formation have also been actively investigated.^{17–23} Among them, Chang’s group developed iridium-catalyzed direct C–H amidation (DCA) reactions between sulfonyl azides and arenes containing carbonyl (or imine) directing groups, thus enabling efficient synthesis of various sulfonamides (Scheme 1.3).^{20,24–28} This reaction is versatile because its high efficiency results in high yields, even under mild conditions, and releases nitrogen gas as a single byproduct.

Scheme 1.3. (a) Direct C–H Amidation (DCA) and (b) Its Proposed Mechanism.



1.1.4. Excited-State Intramolecular Proton-Transfer

Excited-state intramolecular proton-transfer (ESIPT) is one of the versatile luminescence mechanisms.^{29,30} As shown in Figure 1.2a, the ESIPT process requires a preformed intramolecular hydrogen bond between proton donor ($-\text{OH}$ or $-\text{NH}_2$) and proton acceptor ($\text{C}=\text{O}$ or $\text{C}=\text{N}$) groups in close proximity. The ESIPT reaction is a photophysical event consisting of a four-level photocycle and starts from the ground (normal) state (N). Upon photo-excitation to N^* , the electronic redistribution charge occurs, making the proton donor and acceptor more acidic and basic, respectively. As a result, rapid proton transfer occurs to form an electronically excited tautomeric form (T^*), which either emits light or undergoes nonradiative decay to give the ground-state tautomer (T). Finally, thermal reverse proton transfer takes place into the initial N state. The ESIPT process is extremely fast ($k_{\text{ESIPT}} > 10^{12} \text{ s}^{-1}$) and irreversible ($\Delta E_{\text{ESIPT}} \ll 0$). Moreover, it results in a uniquely large Stokes' shifted fluorescence emission ($6,000\text{--}12,000 \text{ cm}^{-1}$) with the total exclusion of self-absorption.

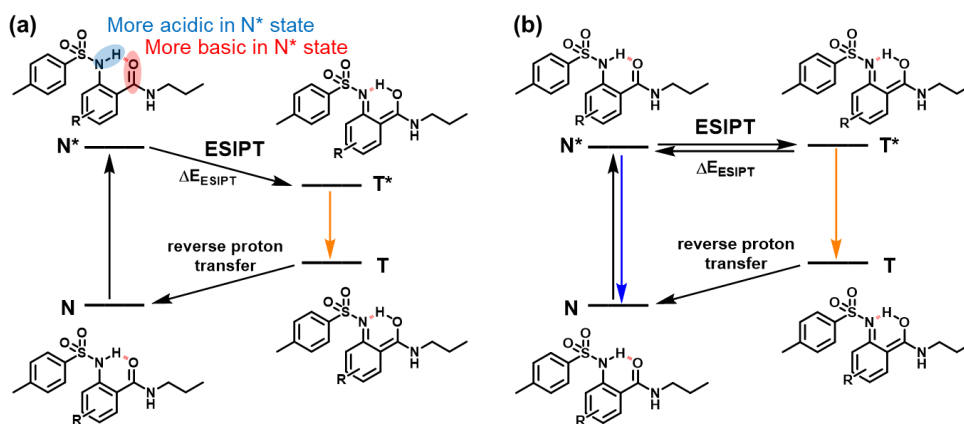


Figure 1.2. Schematic representation of excited-state intramolecular proton-transfer (ESIPT) processes resulting in (a) tautomer emission as a major de-excitation and (b) dual emission from normal (N^*) and tautomer (T^*) excited-states in equilibrium.

However, such a photocycle can be fully reversible by modulating its thermodynamics (Figure 1.2b). As a result, dual emission from both N^* and T^* states can be obtained when a dynamic equilibrium exists between N^* and T^* (i.e., making ΔE_{ESIPT} close to 0).

1.1.5. *In Situ* Nanoparticlization of Conjugated Polymers

Self-assembly (SA) of block copolymers (BCPs) can afford various nanostructures with a broad range of morphologies, and it has expanded the range of potential applications by imparting various functionalities of functional polymers into the nanostructures. Despite these versatilityes, however, the SA typically requires tedious post-polymerization treatment steps, such as adding selective solvents or additives, changing temperature or pH, aging, or dialysis.

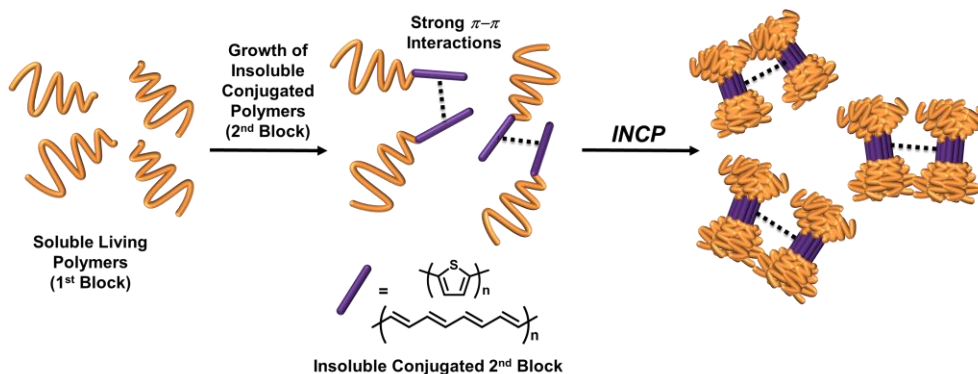


Figure 1.3. Schematic representation of *in situ* nanoparticlization of conjugated polymers (INCP).

To prepare semiconducting nanoparticles more efficiently, a one-pot process called *in situ* nanoparticlization of conjugated polymers (INCP) has been developed using living olefin metathesis polymerization^{31–34} or Kumada catalyst-transfer polymerization (KCTP)^{35–38} of thiophenes to give fully conjugated BCPs (Figure 1.3). After synthesizing soluble first blocks, living polymerization to produce the second block containing conjugated polymers without side chains could enhance π - π interactions among the growing chains, thereby providing a strong driving force for spontaneous self-assembly during the synthesis, even without any post-synthetic treatment. This efficient strategy is potentially meaningful for applications because of its straightforward production of various conjugated nanomaterials.

1.2. Thesis Research

One of the key elements for creating functional polymers is its preparation methods, and the methodologies have been fundamentally based on organic reactions to expand polymer science greatly. Despite numerous and versatile organic reactions, however, one of the primary factors retarding the development of functional polymers is the laborious preparation of monomers, which includes diverse and complex organic chemistry and catalysis. In this context, this dissertation begins by discussing polymerization methodology using synthetically accessible or even commercially available monomers, inspired by efficient and straightforward organic reactions. Then, we describe several research directions involving stimuli-responsive polymers, multi-color luminescent materials, and length-controllable semiconducting 1D nanofibers.

Although [3,3]-sigmatropic rearrangement is a powerful and reliable tool to generate C–C bonds stereospecifically, this versatile method has not been utilized in polymerization because it is an intramolecular reaction, which undergoes simultaneous bond formation and breakage. **Chapter 2** reports the first development of a tandem diaza-Cope rearrangement polymerization (DCRP), utilizing an intramolecular DCR reaction as a polymerization method in a tandem process with imine-formation. Furthermore, this method afforded enantiopure salen-based polymeric materials showing high performance as selective turn-on Zn^{2+} sensors.

To prepare multicolor fluorescent molecules, chemists have generally synthesized fluorophores from various precursors, or frequently, under different reaction conditions. Sometimes one must use even totally different synthetic pathways because of a lack of versatility of synthetic schemes. In this regard, **Chapter 3** demonstrates a powerful strategy, iridium-catalyzed direct C–H amidation (DCA), for synthesizing various fluorescent sulfonamides that emit light over the entire visible spectrum with high synthetic yields irrespective of the positions of functional groups and their electronic properties. By controlling the electronic characters of the resulting sulfonamides, a wide range of blue-to-red emissions was predictably obtained via the ESIPT process. Furthermore, we even succeeded in a white-light generation, highlighting that this DCA is an excellent synthetic method to prepare a library of fluorophores.

Due to the importance of white-light-emitting polymers in various applications, the development of such polymers has been actively pursued. However, due to their intrinsic synthetic and structural features arising from multifluorophore-based random copolymers to effectively cover the entire visible region, this strategy has limitations in securing color reproducibility. By taking advantage of the modular synthesis demonstrated in **Chapter 3** to incorporate various substituents, **Chapter 4** describes the rational design

principle for white-light emission through detailed model studies by understanding structure–photophysical property relationship. Based on the model studies, we extended the design principle to versatile direct C–H amidation polymerization (DCAP), affording well-defined and high-molecular-weight polysulfonamides with single-fluorophore emitting white-light, thereby securing excellent color reproducibility. Furthermore, we achieved consistent fluorescence regardless of such polymers’ molecular weights or phases (solution, powder, thin film, and even coated LED), further demonstrating their excellent color reproducibility, mechanical property, and solution processability.

Self-assembly of conjugated polymers (CPs) is an attractive method for preparing electronically useful semiconducting nanomaterials, and their precise control of size and shape has become a crucial subject. However, this has been challenging due to the high crystallinity and low solubility of the CPs, leading to irregular aggregation. Finally, in **Chapter 5**, we successfully achieved the first living Suzuki-Miyaura catalyst-transfer polymerization (SCTP) of a highly soluble conjugated polymer, poly(3,4-dihexylthiophene) (P34DHT). It led us to prepare a highly solubilizing P34DHT shell, and by combining the slow growth of the insoluble core block, we developed a new self-assembly strategy, so-called crystallization-driven INCP (CD-INCP). As a result, length-controllable semiconducting 1D nanoparticles were prepared in high preparation efficiency without any post-synthetic treatment. We also succeeded in further chain-extension from the pre-synthesized seeds, demonstrating the “living” CD-INCP process.

1.3. References

- (1) Wang, K.; Amin, K.; An, Z.; Cai, Z.; Chen, H.; Chen, H.; Dong, Y.; Feng, X.; Fu, W.; Gu, J.; Han, Y.; Hu, D.; Hu, R.; Huang, D.; Huang, F.; Huang, F.; Huang, Y.; Jin, J.; Jin, X.; Li, Q.; Li, T.; Li, Z.; Li, Z.; Liu, J.; Liu, J.; Liu, S.; Peng, H.; Qin, A.; Qing, X.; Shen, Y.; Shi, J.; Sun, X.; Tong, B.; Wang, B.; Wang, H.; Wang, L.; Wang, S.; Wei, Z.; Xie, T.; Xu, C.; Xu, H.; Xu, Z.-K.; Yang, B.; Yu, Y.; Zeng, X.; Zhan, X.; Zhang, X.; Zhang, Y.; Zhang, Y.; Zhao, C.; Zhao, W.; Zhou, Y.; Zhou, Z.; Zhu, J.; Zhu, X.; Tang, B. Z. *Mater. Chem. Front.* **2020**, *4*, 1803–1915.
- (2) Ilardi, E. A.; Stivala, C. E.; Zakarian, A. *Chem. Soc. Rev.* **2009**, *38*, 3133–3148.
- (3) Chin, J.; Mancin, F.; Thavarajah, N.; Lee, D.; Lough, A.; Chung, D. S. *J. Am. Chem. Soc.* **2003**, *125*, 15276–15277.
- (4) Kim, H.-J.; Kim, H.; Alhakimi, G.; Jeong, E. J.; Thavarajah, N.; Stud-nicki, L.; Koprianiuk, A.; Lough, A. J. Suh, J.; Chin, J. *J. Am. Chem. Soc.* **2005**, *127*, 16370–16371.

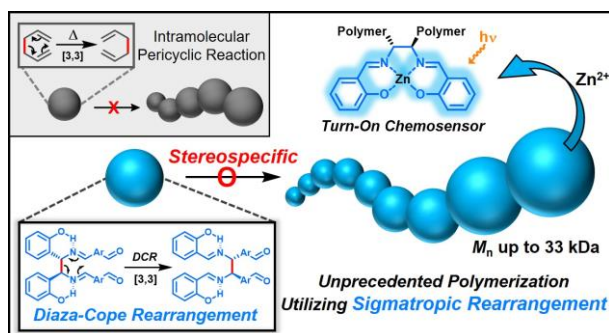
- (5) Kim, H.-J.; Kim, W.; Lough, A. J.; Kim, B. M.; Chin, J. *J. Am. Chem. Soc.* **2005**, *127*, 16776–16777.
- (6) Kim, H.; Nguyen, Y.; Yen, C. P.-H.; Chagal, L.; Lough, A. J.; Kim, B. M. Chin, J. *J. Am. Chem. Soc.* **2008**, *130*, 12184–12191.
- (7) Kim, H.; Nguyen, Y.; Lough, A. J.; Chin, J. *Angew. Chem., Int. Ed.* **2008**, *47*, 8678–8681.
- (8) Lee, D.-N.; Kim, H.; Mui, L.; Myung, S.-W.; Chin, J.; Kim, H.-J. *J. Org. Chem.* **2009**, *74*, 3330–3334.
- (9) Kim, H.; Staikova, M.; Lough, A. J.; Chin, J. *Org. Lett.* **2009**, *11*, 157–160.
- (10) Kwon, S. H.; Lee, S. M.; Byun, S. M.; Chin, J.; Kim, B. M. *Org. Lett.* **2012**, *14*, 3664–3667.
- (11) Kim, M.; Kim, H.; Kim, H. Chin, J. *J. Org. Chem.* **2017**, *82*, 12050–12058.
- (12) Xu, Y.; Meng, J.; Meng, L.; Dong, Y.; Cheng, Y.; Zhu, C. *Chem. Eur. J.* **2010**, *16*, 12898–12903.
- (13) Li, J.; Wu, Y.; Song, F. Wei, G. Cheng, Y. Zhu, C. *J. Mater. Chem.* **2012**, *22*, 478–482.
- (14) Bera, M. K.; Chakraborty, C. Malik, S. *New J. Chem.* **2015**, *39*, 9207–9214.
- (15) Yoon, P. T.; Jacobsen, E. N. *Science* **2003**, *299*, 1691–1693.
- (16) Jacobsen, E. N. *Acc. Chem. Res.* **2000**, *33*, 421–431.
- (17) Armstrong, A.; Collins, J. C. *Angew. Chem., Int. Ed.* **2010**, *49*, 2282–2285.
- (18) Wencel-Delord, J.; Dröge, T.; Liu, F.; Glorius, F. *Chem. Soc. Rev.* **2011**, *40*, 4740–4761.
- (19) Dong, Z.; Dong, G. *J. Am. Chem. Soc.* **2013**, *135*, 18350–18353.
- (20) Park, Y.; Kim, Y.; Chang, S. *Chem. Rev.* **2017**, *117*, 9247–9301.
- (21) Kim, S.; Chakrasali, P.; Suh, H. S.; Mishra, N. K.; Kim, T.; Han, S. H.; Kim, H. S.; Lee, B. M.; Han, S. B.; Kim, I. S. *J. Org. Chem.* **2017**, *82*, 7555–7563.
- (22) Han, S. H.; Suh, H. S.; Jo, H.; Oh, Y.; Mishra, N. K.; Han, S.; Kim, H. S.; Jung, Y. H.; Lee, B. M.; Kim, I. S. *Bioorg. Med. Chem. Lett.* **2017**, *27*, 2129–2134.
- (23) Yoon, K.-Y.; Dong, G. *Angew. Chem., Int. Ed.* **2018**, *57*, 8592–8596.
- (24) Kim, J. Y.; Park, S. H.; Ryu, J.; Cho, S. H.; Kim, S. H.; Chang, S. *J. Am. Chem. Soc.* **2012**, *134*, 9110–9113.
- (25) Lee, D.; Kim, Y.; Chang, S. *J. Org. Chem.* **2013**, *78*, 11102–11109.
- (26) Kim, J.; Chang, S. *Angew. Chem., Int. Ed.* **2014**, *53*, 2203–2207.
- (27) Kang, T.; Kim, Y.; Lee, D.; Wang, Z.; Chang, S. *J. Am. Chem. Soc.* **2014**, *136*, 4141–4144.
- (28) Shin, K.; Chang, S. *J. Org. Chem.* **2014**, *79*, 12197–12204.

- (29) K. J. E.; Park, S. Y. *Adv. Mater.* **2011**, *23*, 3615–3645.
- (30) Chen, C.-L.; Chen, Y.-T.; Demchenko, A. P.; Chou, P.-T. *Nat. Rev. Chem.* **2018**, *2*, 13–143.
- (31) Yoon, K.-Y.; Lee, I.-H.; Kim, K. O.; Jang, J.; Lee, E.; Choi, T.-L. *J. Am. Chem. Soc.* **2012**, *134*, 14291–14294.
- (32) Yoon, K.-Y.; Lee, I.-H.; Choi, T.-L. *RSC Adv.* **2014**, *4*, 49180–49185.
- (33) Yoon, K.-Y.; Shin, S.; Kim, Y.-J.; Kim, I.; Lee, E.; Choi, T.-L. *Macromol. Rapid Commun.* **2015**, *36*, 1069–1074.
- (34) Shin, S.; Yoon, K.-Y.; Choi, T.-L. *Macromolecules* **2015**, *48*, 1390–1397.
- (35) Lee, I.-H.; Amaladass, P.; Yoon, K.-Y.; Shin, S.; Kim, Y.-J.; Kim, I.; Lee, E.; Choi, T.-L. *J. Am. Chem. Soc.* **2013**, *135*, 17695–17698.
- (36) Lee, I.-H.; Amaladass, P.; Choi, T.-L. *Chem. Commun.* **2014**, *50*, 7945–7948.
- (37) Lee, I.-H.; Amaladass, P.; Choi, I.; Bergmann, V. W.; Weber, S. A. L.; Choi, T.-L. *Polym. Chem.* **2016**, *7*, 1422–1428.
- (38) Lee, I.-H.; Choi, T.-L. *Polym. Chem.* **2016**, *7*, 7135–7141.

**Chapter 2. Tandem Diaza-Cope Rearrangement
Polymerization: Turning Intramolecular Reaction
into Powerful Polymerization to Give Enantiopure
Materials for Zn²⁺ Sensor**

2.1. Abstract

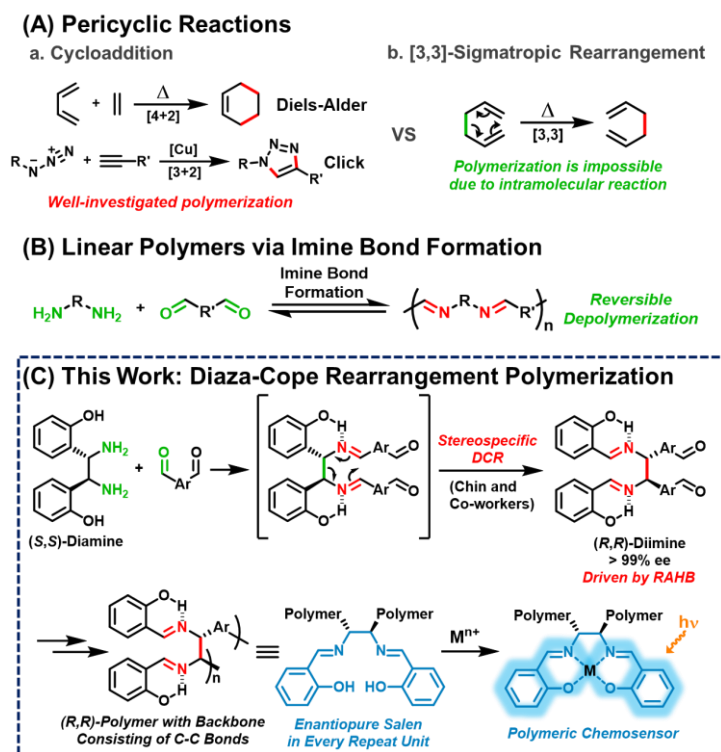
[3,3]-Sigmatropic rearrangement is a powerful reaction to form C–C bonds stereospecifically; however, owing to intrinsic simultaneous bond formation and breakage, this versatile method has not been utilized in polymerization. In this chapter, we demonstrate a new tandem diaza-Cope rearrangement polymerization (DCRP) that can synthesize polymers with defect-free C–C bond formation from easy and efficient imine formation. A mechanistic investigation by *in situ* ^1H NMR experiments suggests that this polymerization proceeds by a rapid DCR process, forming an enantiospecific C–C bond that occurs almost simultaneously with imine formation. This polymerization produces not only highly stable polymers against hydrolysis due to resonance-assisted hydrogen bonds (RAHBs) but also chiral polymers containing enantiopure salen moieties, which lead to high-performance Zn^{2+} -selective turn-on chemosensors with up to 73-fold amplification. We also found that their optical activities and sensing performances are heavily dependent on the reaction temperature, which significantly affects the stereoselectivity of DCR.



2.2. Introduction

Pericyclic reaction, the reorganization of π -bonds in a concerted manner, is one of the most widely used transformations in synthetic organic chemistry. Among the various pericyclic reactions, highly efficient cycloadditions, such as Diels–Alder and Cu-catalyzed azide–alkyne cycloaddition reactions, have been employed as powerful tools to prepare polymers^{1–10} because of their high efficiency and orthogonality (Scheme 2.1A(a)). [3,3]-Sigmatropic rearrangement is another powerful and reliable pericyclic reaction, allowing for the stereoselective construction of C–C bonds.¹¹ However, this rearrangement cannot be applied to polymerization other than the post-modification of side-chains^{12–16} because it is an intramolecular reaction, which intrinsically forms and breaks the bond simultaneously (Scheme 2.1A(b)).

Scheme 2.1. Polymerization via Pericyclic Reactions and Imine Bond Formation.

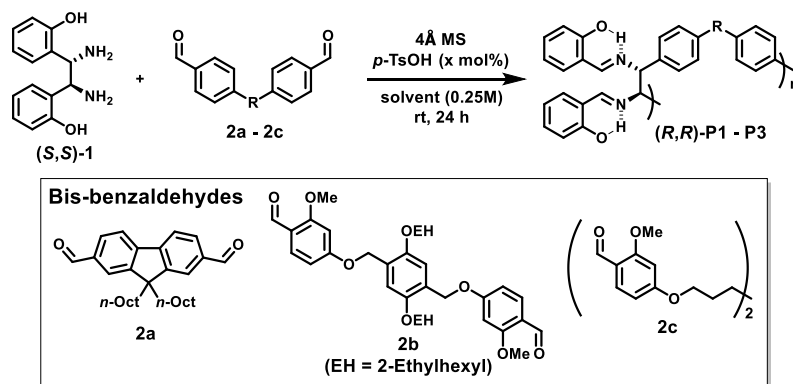


Meanwhile, imine formation between an amine and an aldehyde is an efficient and straightforward reaction and occurs reversibly under equilibrium control. Ironically, extending this method to obtain high molecular-weight linear polymers is still quite challenging due to its inherent reversible imine formation (Scheme 2.1B).^{17–30} Therefore, to solve the depolymerization issue, an appropriate strategy is needed to provide a sufficient driving force.

Then, we paid attention to Chin and co-workers' reports of highly versatile diaza-Cope rearrangement (DCR) reactions using chiral diamine and benzaldehydes (see **Chapter 1.1.2** for details).^{31–39} After efficient imine formation, DCR proceeded rapidly to form C–C bond stereospecifically, driven by a strong resonance-assisted hydrogen bond (RAHB). Inspired by this powerful DCR, we envisioned a new polymerization ironically using the intramolecular [3,3]-sigmatropic rearrangement in a tandem process with efficient imine formation. In this chapter, we demonstrate stereospecific and defect-free tandem diaza-Cope rearrangement polymerization (DCRP) between chiral diamine and bis-benzaldehyde via a rapid DCR process where RAHB provided an enthalpic driving force (Scheme 2.1C). The DCR transforms the polymer backbone from reversible imine bonds to irreversible and strong C–C bonds; thus, this new polymerization provides high-molecular-weight linear polymers that are stable against hydrolysis. Furthermore, these chiral polymers containing salen side-chains can be applied as powerful turn-on chemosensors showing up to 73-fold amplification in fluorescence intensity.

2.3. Results and Discussion

To test the feasibility of DCRP, we screened various conditions using two commercially available diamine (**(S,S)**-**1**) and bis-benzaldehyde **2a** monomers with 10 mol% acid catalyst (*p*-TsOH) (Table 2.1). After testing several solvents at room temperature (rt), we found that the conversion increased (up to 96%) as the solvent polarity increased (entries 1–4). As a result, **(R,R)**-**P1** with the highest number-average molecular weight ($M_n = 14.9$ kDa) was obtained in the most polar DMF (entry 4). Additionally, increasing the catalyst to 20 mol%, **(R,R)**-**P1** with a higher M_n of 22.3 kDa and reasonable D of 1.87 was obtained in 80% yield (entry 5 and Table S2.1). Next, other bis-benzaldehydes (**2b** and **2c**) were examined to expand the monomer scope. Likewise, **(R,R)**-**P2** obtained from **2b** also showed a high M_n of 33.3 kDa under identical conditions (entry 6 and Table S2.2). Due to the solubility issue of **2c** monomer, the polymerization was carried out in chloroform at 40 °C to give **(R,R)**-**P3** with M_n of 16.7 kDa (entry 7 and Table S2.3). Notably, the degree of polymerization (DP) calculated from the MALLS analysis matched the DP calculated from the Carothers equation using the conversion obtained by NMR analysis. Finally, all SEC traces showed a good Gaussian distribution, suggesting minimal cyclization (Figure S2.6).

Table 2.1. Optimization of Tandem Diaza-Cope Rearrangement Polymerization (DCRP).

Entry	Polymer	Bis-aldehyde	Solvent	<i>p</i> -TsOH (mol%)	Conv. ^a	<i>M_n</i> (Đ) ^b	Yield ^c
1	(<i>R,R</i>)-P1	2a	DCM	10	88%	9.6 k (1.49)	97%
2	(<i>R,R</i>)-P1	2a	CHCl ₃	10	88%	9.2 k (1.53)	91%
3	(<i>R,R</i>)-P1	2a	THF	10	93%	14.6 k (1.63)	76%
4	(<i>R,R</i>)-P1	2a	DMF	10	96%	14.9 k (1.40)	64%
5	(<i>R,R</i>)-P1	2a	DMF	20	97%	22.3 k (1.87)	80%
6	(<i>R,R</i>)-P2	2b	DMF	20	97%	33.3 k (1.61)	90%
7 ^d	(<i>R,R</i>)-P3	2c	CHCl ₃	20	96%	16.7 k (1.76)	78%
8 ^e	(<i>S,S</i>)-P1	2a	DMF	20	97%	20.1 k (2.34)	98%
9 ^f	<i>meso</i> -P1	2a	DMF	20	83%	9.4 k (1.60)	71%

^aDetermined by ¹H NMR analysis of the crude reaction mixture. ^bAbsolute molecular weights determined by THF SEC using a multiangle laser light scattering (MALLS) detector. ^cIsolated yields after purification from isopropyl alcohol (IPA). ^dPolymerization proceeded in chloroform at 40 °C to enhance monomer solubility. ^e(*R,R*)-1 was employed instead of (*S,S*)-1. ^fPolymerization proceeded using *meso*-1 instead of (*S,S*)-1 at 50 °C.

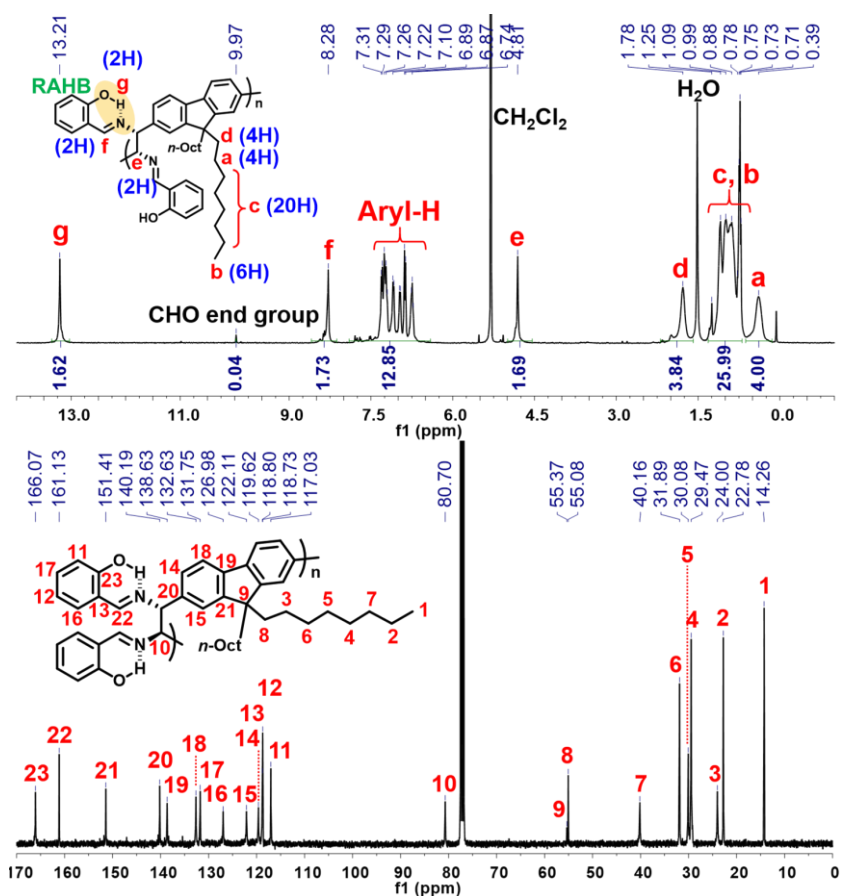


Figure 2.1. ^1H NMR and ^{13}C NMR spectra of $(R,R)\text{-P1}$.

The detailed microstructures of all resulting polymers were easily characterized by ^1H NMR and ^{13}C NMR analysis due to the sharp and well-resolved NMR spectra, facilitating easy assignment of all peaks (Figure 2.1 for $(R,R)\text{-P1}$). Notably, the phenolic O–H proton signals (g peak for $(R,R)\text{-P1}$) of all the resulting polymers commonly appeared at δ 13.2–13.8 ppm as sharp singlets. Considering that the phenolic O–H signals forming normal hydrogen-bonding are generally observed at ca. δ 11 ppm, which was completely absent in Figure 2.1, these new peaks at ca. δ 14 ppm are significantly downfield-shifted due to the unique RAHB.³⁴ This observation confirms that the DCR process successfully occurred during the polymerization without any defect.

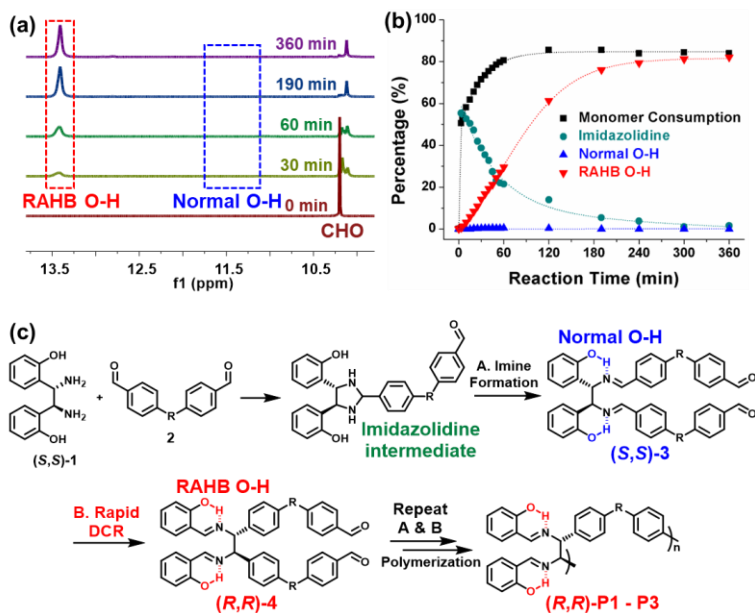


Figure 2.2. (a) Monitoring the polymerization using (S,S) -**1** and **2a** by *in situ* ^1H NMR spectroscopy in $\text{DMF-}d_7$. (b) Plots showing consumption of **2a** (black), formation of imidazolidine intermediate (green), and phenolic O–H groups (blue and red). (c) Detailed polymerization mechanism.

To get a mechanistic insight into tandem DCRP, the polymerization using (S,S) -**1** and **2a** was monitored by *in situ* ^1H NMR experiments under the same conditions as entry 5 in Table 2.1 (Figures 2.2 and S2.1). As reported, an initial imidazolidine intermediate via imine formation was rapidly formed up to 55% (see Figure S2.1 for details).^{38,39} However, (S,S) -**3**, the second intermediate, comprising the normal O–H signal, was hardly observed, whereas only the RAHB O–H signal corresponding to (R,R) -**4** or (R,R) -**P1** gradually increased, implying clean conversion (Figure 2.2a,b). This suggests that a DCR is rapid, occurring almost simultaneously with imine formation (Figure 2.2c). In other words, (R,R) -**P1** was predominantly produced by C–C bond polymerization rather than imine polymerization (if so, the subsequent DCR process would have slowly generated C–C bonds on the pre-formed polymer). On the other hand, in the case of (R,R) -**P2** containing electron-donating groups, the activation energy for DCR increased,³⁴ thereby decelerating the rearrangement. As a result, both normal and RAHB O–H (δ 10.7 ppm and δ 13.7 ppm, respectively) were observed at the beginning of the reaction, but the polymerization progressed to show only the enthalpically favored RAHB O–H (Figure S2.2). In short, because of the defect-free DCR signal regardless of the electronic characters, this tandem DCRP becomes a novel strategy to form more challenging C–C bonds from easier imine formation.

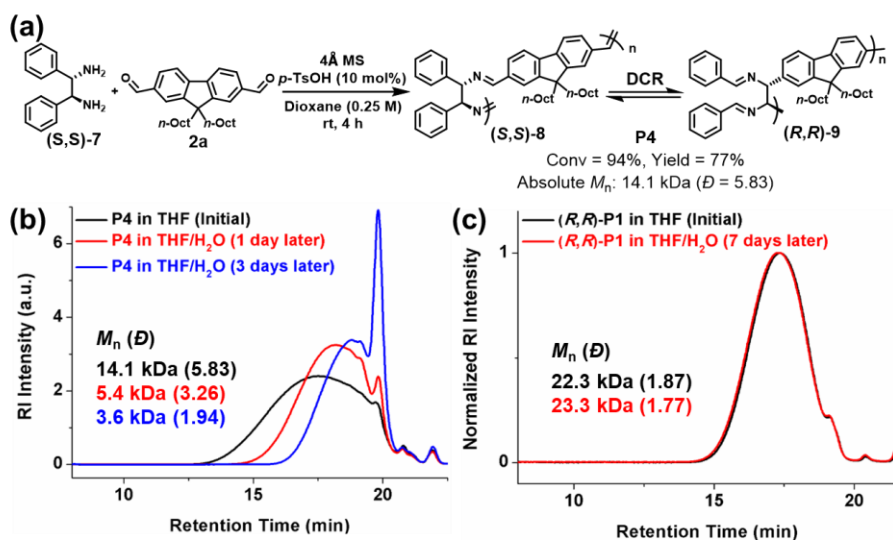


Figure 2.3. Control experiment to compare stability against hydrolysis. (a) Scheme for **P4**. (b) SEC traces of **P4** measured at the initial and measured one/three days after dissolving in THF:H₂O (99:1). (c) SEC traces of **(R,R)-P1** measured at the initial and seven days after dissolving in THF:H₂O (99:1).

DCR polymers contain C–C bonds in the main backbone, while the resulting imine bonds at the side-chains are also stabilized by stronger RAHB. Therefore, we could test their stability against hydrolysis by comparing with analogous polyimine. To conduct a control experiment, we synthesized **P4** by using a diamine monomer ((*S,S*)-**7**) without –OH groups, ensuring that the RAHB that drove the completion of DCR was now absent.³¹ Therefore, **P4** (M_n of 14.1 kDa) contained both the initial imine ((*S,S*)-**8**) and the rearranged C–C bond ((*R,R*)-**9**) in the main chain (Figure 2.3a). As expected, **P4** in the THF solution containing 1% H₂O underwent depolymerization, lowering M_n to 5.4 kDa within a day. After three days, **P4** was further hydrolyzed to 3.6 kDa, which is 1/4 of the initial molecular weight (Figure 2.3b). However, as shown by SEC analysis, the molecular weight of **(R,R)-P1** from the complete DCRP did not change under identical conditions even after seven days (Figure 2.3c). Moreover, **(R,R)-P1** remained stable in CDCl₃ in an NMR tube for three days, but even a small amount of residual acid in CDCl₃ was sufficient to depolymerize **P4** within 11 h, as seen by the reduction in the imine signal (δ 8.3 ppm) and the significant increase in the aldehyde signal (δ 10.0 ppm) (Figure S2.3).

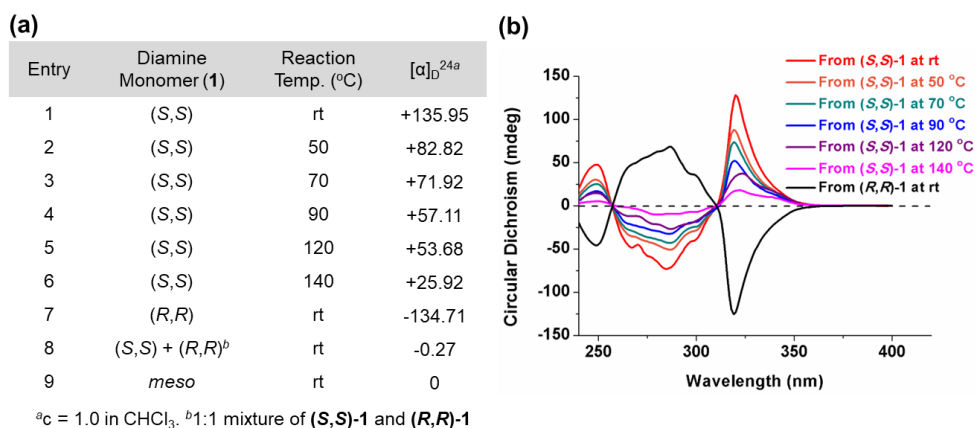


Figure 2.4. (a) Table for optical rotation values showing how temperature affects the stereospecificity of tandem DCRP. (b) Circular dichroism spectra of the resulting polymers (2.5 mg/mL in CHCl₃ at rt, 0.2 mm cell).

The DCR of small molecules undergoes complete stereospecific inversion of stereochemistry at rt because the corresponding transition state (TS) bears all the aryl substituents in pseudo-equatorial positions making this pathway most kinetically preferred (see **Chapter 1.1.2** for details).³⁴ Likewise, to investigate the stereochemistry of the resulting polymers, we prepared **P1** at various temperatures and compared their optical rotations ($[\alpha]_D^{24}$) (Figure 2.4a and Table S2.4). While **P1** synthesized from (S,S)-**1** at rt exhibited the highest $[\alpha]_D^{24}$ of +135.95, the values significantly decreased from +82.82 to +25.92 as the polymerization temperature increased from 50 °C to 140 °C (entries 1–6 in Figure 2.4a). In addition, (S,S)-**P1** obtained from the enantiomer (R,R)-**1** at rt (entry 8 in Table 2.1) showed an expected $[\alpha]_D^{24}$ of similar absolute value but the opposite sign (-134.71) (entry 7 in Figure 2.4a). Lastly, **P1** prepared from the racemic mixture or *meso*-isomer of **1** resulted in $[\alpha]_D^{24}$ close to 0 (entries 8 and 9 in Figure 2.4a). To further support this trend, we measured circular dichroism spectroscopy, which showed a decrease in the amplitudes of the two Cotton effects with an increase in the reaction temperature (Figure 2.4b). Furthermore, (R,R)-**P1** and (S,S)-**P1** synthesized at rt showed Cotton effects of the same amplitude but of the opposite sign. According to the computational studies, the next alternating pathway via the second lowest TS (7.7 kcal/mol higher) would produce a *meso* product, an achiral diastereomer (see **Chapter 1.1.2** for details).³⁴ Therefore, it is suspected that the higher reaction temperature led to more *meso* products in **P1**, thereby lowering $[\alpha]_D^{24}$ and the amplitude of Cotton effects accordingly.

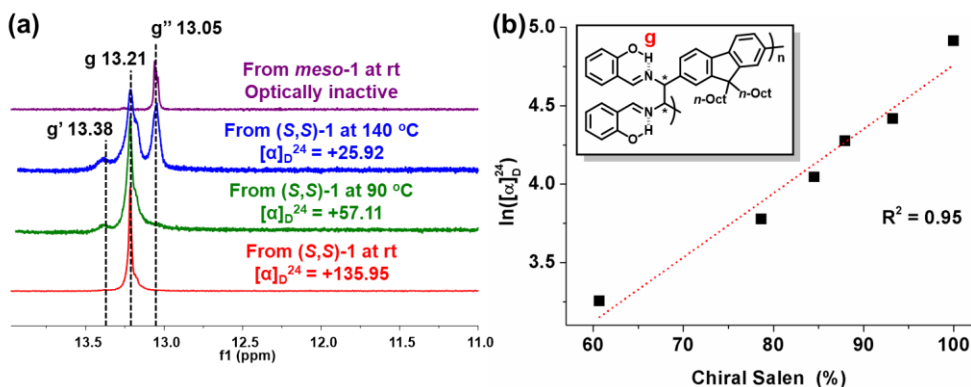


Figure 2.5. (a) ¹H NMR spectra (in CD₂Cl₂) showing RAHB O–H signals of various **P1** (in Table S2.4) synthesized from chiral and *meso* diamines at various reaction temperatures. (b) Plot showing the relationship between ln([α]_D²⁴) and stereospecificity.

To confirm the effect of temperature on *meso*-isomer formation, we thoroughly analyzed the ¹H-NMR spectra of **P1** from (S,S)-**1** and *meso*-**P1** synthesized at various temperatures (Figures 2.5a and S2.4). As the polymerization temperature increased, another peak labeled as g' appeared and gradually increased δ 13.38 ppm (Figures 2.5a and S2.4a–f). Notably, apart from the g and g' peaks, an additional RAHB O–H signal (g'' at δ 13.05 ppm) started to grow for **P1** synthesized at higher temperatures. Fortunately, the last g'' peak was easily identified as *meso* diastereomer as it perfectly matched with the authentic sample of *meso*-**P1** prepared from *meso*-**1** at rt (Figures 2.5a and S2.4g). From these data, we came to a plausible conclusion that the three types of RAHB O–H signals are due to diad tacticities of the salen side-chains in the following cases: (i) g for homo diad (cc) from the chiral-salen-rich units; (ii) g'' for homo diad (mm) from the achiral *meso*-salen-rich units; (iii) g' for hetero diad (cm) from the chiral and *meso* adjacent to each other. Based on this assignment, the content of the chiral salen unit depending on the temperature was estimated from the integration of all RAHB O–H signals (Figure S2.5a). Consistent with the trend observed in [α]_D²⁴, chiral salen content also decreased from 100% to 60.7% as the temperature increased from rt to 140 °C. Moreover, one could plot [α]_D²⁴ to the chiral content, and they showed an exponential relationship (Figure S2.5b). Taking the natural logarithm of [α]_D²⁴ provided a good linear relationship with the chiral content, which should allow for some predictability (Figure 2.5b). In short, increasing the reaction temperature lowered the stereospecificity as well as [α]_D²⁴ due to the formation of the *meso*-isomer.

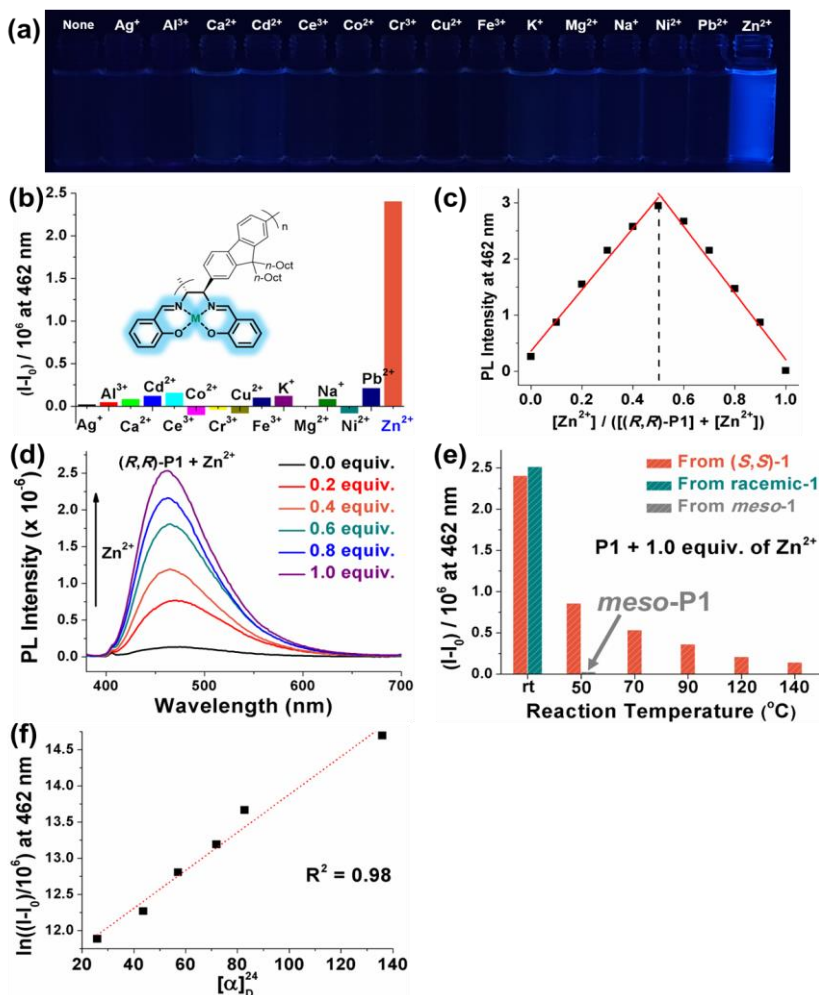


Figure 2.6. (a) ^1H NMR spectra (in CD_2Cl_2) showing RAHB O–H signals of various P1 (in Table S2.4) synthesized from chiral and *meso* diamines at various reaction temperatures. (b) Plot showing the relationship between $\ln([\alpha]_{\text{D}}^{24})$ and stereospecificity.

One useful application of salen moieties is their potential as a metal chemosensor.^{40–42} Since $(\text{R,R})\text{-P1-P3}$ contain salen side-chains, their UV/vis absorption and fluorescence responses to various metal cations in THF/ H_2O (9:1 v/v) were investigated (Figures 2.6 and S2.8–S2.12). Interestingly, all the metal cations showed insignificant fluorescence except for Zn^{2+} , which showed obvious turn-on fluorescence enhancement ($I-I_0$) (Figures 2.6a,b and S2.8). On the other hand, no sensing ability was observed for P4, which only contains diimine side-chains without –OH groups (Figure S2.9). The Job plot using $(\text{R,R})\text{-P1}$ showed the maximum fluorescence intensity at 0.5-mole fraction, indicating 1:1 complexation of Zn^{2+} to the salen group (Figure 2.6c). Increasing the concentration of Zn^{2+} from 0.0 to 1.0 equiv. resulted in a gradual increase in the fluorescence intensities. In

particular, **(R,R)-P3** was an excellent Zn^{2+} sensor showing a high amplification of fluorescence (I/I_0) up to 73-fold and a limit of detection value of $0.577 \mu\text{M}$ (37.7 ppb) (Figures 2.6d, S2.10, and S2.11). Notably, **P1** prepared at various temperatures showed different sensing performances (Figures 2.5e and S2.12). **P1** synthesized at rt using enantiopure **(S,S)-1** or racemic mixture of chiral **1** exhibited the highest I/I_0 of 19-fold, whereas this I/I_0 decreased significantly with the temperature to 4.8-fold (25% compared to that at rt) at $50 \text{ }^\circ\text{C}$, 2.6-fold (14%) at $90 \text{ }^\circ\text{C}$, 1.9-fold (10%) at $120 \text{ }^\circ\text{C}$, and even further down to 1.5-fold (8%) at $140 \text{ }^\circ\text{C}$. The $I-I_0$ and $[\alpha]_{\text{D}}^{24}$ also showed an exponential relationship and applying the natural logarithm to $I-I_0$ provided a good linear relationship with $[\alpha]_{\text{D}}^{24}$, allowing for prediction of the sensor performances (Figures 2.6f and S2.12c). Furthermore, to examine the effect of *meso*-salen unit, we conducted a sensing experiment using **meso-P1** prepared at $50 \text{ }^\circ\text{C}$ to achieve comparable conversion (entry 9 in Table 2.1 and Figure S2.4h). Interestingly, **meso-P1** showed no sensing ability for Zn^{2+} at all, indicating that the stereochemistry of the salen moiety was crucial for Zn^{2+} detection (Figure 2.6e). Therefore, we concluded that the high sensing performances of **(R,R)-P1-P3** synthesized at rt was due to the exclusive formation of the chiral salens, which formed a tetrahedral geometry suitable for selective Zn^{2+} binding.⁴² However, as the reaction temperature increased, the degree of DCR to the undesired *meso*-isomer increased, and their sensing performance decreased due to the resulting square-planar geometry from the *meso* configuration in which selective Zn^{2+} detection is impossible.

2.4. Conclusion

In conclusion of this chapter, we developed a new tandem diaza-Cope rearrangement polymerization (DCRP) to synthesize high-molecular-weight polymers up to 33.3 kDa with excellent stability against hydrolysis. The key factor for the success was the introduction of a defect-free, rapid, and thermodynamically favored DCR process into the polymerization mechanism by forming C–C bonds almost simultaneously with efficient imine formation. Taking advantage of the highly stereospecific DCR, we prepared several highly enantiopure polymers having either *(R,R)*- or *(S,S)*-salen moieties. Lastly, these polymers showed excellent performance as turn-on chemosensors selective for Zn^{2+} detection.

2.5. Experimental Section

Materials

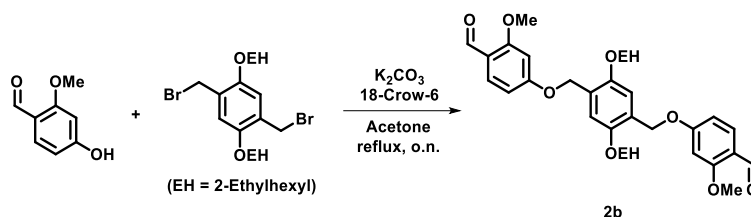
All reagents which are commercially available were used without further purification except for monomers. To avoid unwanted impurities in monomers, recrystallization and flash column chromatography were conducted before using each monomer. Solvents for starting materials synthesis were also commercially obtained. Thin-layer chromatography (TLC) was carried out on MERCK TLC silica gel 60 F₂₅₄ and flash column chromatography was performed using MERCK silica gel 60 (0.040–0.063 mm). For metal sensing experiments, the solutions of the metal ions were prepared from their nitrate salts.

Characterization

¹H NMR and ¹³C NMR spectroscopies were recorded by Varian/Oxford As-500 (125 MHz for ¹³C NMR) and Agilent 400-MR (500 MHz for ¹H NMR and 100 MHz for ¹³C NMR) spectrometers. *High resolution mass spectroscopy (HRMS)* analyses were performed by the ultrahigh resolution ESI Q-TOF mass spectrometer (Bruker, Germany) in the Sogang Centre for Research Facilities. *Size exclusion chromatography (SEC)* analyses were carried out with Waters system (1515 pump and 2707 autosampler) and Shodex GPC LF-804 column eluted with HPLC-grade THF and filtered with a 0.2 μm PTFE filter (Whatman). The flow rate was 1.0 mL/min and temperature of column was maintained at 35 °C. For molecular weight characterization Wyatt DAWN-HELEOS 8+ multi-angle light scatter (MALS) and Wyatt OptiLab T-rEx refractive index (RI) detectors (both maintained at 35 °C) were used. Molecular weights were determined from light scattering using *dn/dc* values calculated from batch mode measurements of polymer solutions at different concentrations. *Optical rotations* were obtained at 589 nm using a JASCO polarimeter. *Circular dichroism (CD) spectra* were taken with an AppliedPhotophysics Inc. circular dichroism detector Chirascan plus in National Instrumentation Center for Environmental Management (NICEM). *UV-vis spectra* were recorded on V-650 spectrometer with Jasco Inc. software. *Fluorescence spectra* were recorded on a Photon Technology International (PTI) QM-400 spectrofluorometer with FelixGX software. *Thermogravimetric analysis (TGA)* and *differential scanning calorimetry (DSC)* were carried out under N₂ gas at a scan rate of 10 °C/min with Q50 model device (TA Instruments).

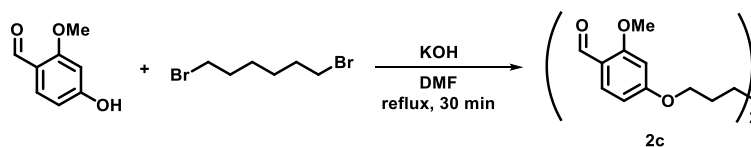
Preparation and Characterization of Monomers

4,4'-(((2,5-bis((2-ethylhexyl)oxy)-1,4-phenylene)bis(methylene))bis(oxy))bis(2-methoxybenzaldehyde) (**2b**)



2b was prepared by the slightly modified procedure from the previous literature.⁴³ To a solution of 4-hydroxy-2-methoxybenzaldehyde (1.94 g, 12.5 mmol) in acetone (16.7 mL) were added K_2CO_3 (2.08 g, 15 mmol), 18-crown-6 (0.27 g, 1.0 mmol). After stirring for 15 min at room temperature, 1,4-bis(bromomethyl)-2,5-bis((2-ethylhexyl)oxy)-benzene (2.6 g, 5.0 mmol)⁴⁴ was added to the reaction mixture. After being refluxed overnight, the mixture was cooled to room temperature, extracted with CH_2Cl_2 three times, dried over $MgSO_4$, and evaporated under reduced pressure to afford crude product, which was purified by column chromatography on silica gel (*n*-hexane/EtOAc = 4/1, R_f = 0.3) to afford **2b** as white solid (2.89 g, 4.36 mmol, 87%); 1H NMR (400 MHz, $CDCl_3$) δ 10.29 (s, 2H), 7.80 (d, J = 8.7 Hz, 2H), 7.01 (s, 2H), 6.64 (dd, J = 8.7, 1.9 Hz, 2H), 6.54 (d, J = 2.0 Hz, 2H), 5.17 (s, 4H), 3.88 (s, 6H), 3.86 (s, 4H), 1.75–1.63 (m, 2H), 1.49–1.22 (m, 16H), 0.96–0.82 (m, 12H). ^{13}C NMR (100 MHz, $CDCl_3$) δ 188.3, 165.5, 163.7, 150.6, 130.8, 125.2, 119.2, 112.7, 106.7, 98.8, 71.4, 65.4, 55.6, 39.6, 30.8, 29.2, 24.1, 23.1, 14.1, 11.3. HRMS (ESI) m/z : $[M + Na]^+$ Calcd for $C_{40}H_{54}O_8Na$ 685.3711; Found 685.3714.

4,4'-(hexane-1,6-diylbis(oxy))bis(2-methoxybenzaldehyde) (**2c**)



2c was prepared by the slightly modified procedure from the previous literature.⁴⁵ To a solution of 4-hydroxy-2-methoxybenzaldehyde (1.55 g, 10 mmol) in DMF (5.0 ml) was added potassium hydroxide (0.59 g, 10 mmol). After stirring for 30 min at room temperature, 1,6-dibromohexane (0.78 ml, 5.0 mmol) was added to the reaction mixture. The mixture was refluxed for 30 min to give **2c** as a white precipitate, then cooled to room temperature and poured onto ice/water. The solid was filtered and washed several times with water to afford crude product, which was further purified by recrystallization ($CHCl_3$ /methanol) to afford **2c** as white solid (1.63 g, 4.22 mmol, 84%); 1H NMR (400

MHz, CDCl₃) δ 10.27 (s, 2H), 7.78 (d, J = 8.7 Hz, 2H), 6.52 (dd, J = 8.7, 1.9 Hz, 2H), 6.43 (d, J = 2.0 Hz, 2H), 4.04 (t, J = 6.4 Hz, 4H), 3.88 (s, 6H), 1.91–1.78 (m, 4H), 1.63–1.49 (m, 4H). ¹³C NMR (100 MHz, CDCl₃) δ 188.4, 165.8, 163.7, 130.9, 119.1, 106.2, 98.5, 68.3, 55.7, 29.2, 25.9. HRMS (ESI) m/z : [M + Na]⁺ Calcd for C₂₂H₂₆O₆Na 409.1622; Found 409.1624.

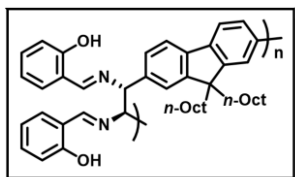
meso-1,2-bis(2-hydroxyphenyl)-ethylenediamine (*meso*-1)

meso-1 was prepared according to the previously reported synthetic method.⁴⁶

General Procedure for the Polymerization and Characterization of Polymers

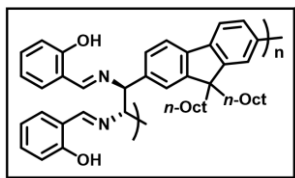
To a 4 mL sized vial with a magnetic bar, 4 Å molecular sieve (0.3 g), diamine (**1**, 0.2 mmol), bis-benzaldehyde (**2**, 0.2 mmol, 1.0 equiv), *p*-toluenesulfonic acid (*p*-TsOH), and experimental solvent (0.8 mL, 0.25 M) were added. The reaction mixture was stirred at experimental temperature during the experimental reaction time, then precipitated in isopropyl alcohol (IPA) at room temperature. The obtained solid was filtered and dried in vacuo.

(*R,R*)-P1 (synthesized from (*S,S*)-1 at rt)



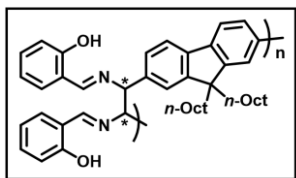
¹H NMR (400 MHz, CD₂Cl₂) δ 13.21 (s, 2H), 8.28 (s, 2H), 7.58–6.41 (m, 14H), 4.81 (s, 2H), 1.78 (br, 4H), 1.31–0.63 (m, 26H), 0.39 (br, 4H). ¹³C NMR (100 MHz, CDCl₃) δ 166.1, 161.1, 151.4, 140.2, 138.6, 132.6, 131.7, 127.0, 122.1, 119.6, 118.8, 118.7, 117.0, 80.7, 55.4, 55.1, 40.2, 31.9, 30.1, 29.5, 24.0, 22.8, 14.3. [α]_D²⁴ +135.95 (c = 1.0 in CHCl₃).

(*S,S*)-P1 (synthesized from (*R,R*)-1 at rt)



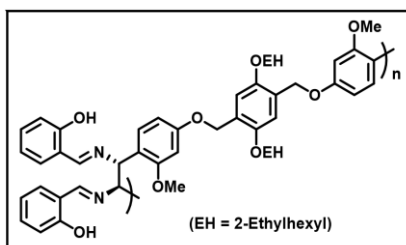
¹H NMR (400 MHz, CD₂Cl₂) δ 13.20 (s, 2H), 8.28 (s, 2H), 7.58–6.41 (m, 14H), 4.80 (s, 2H), 1.78 (br, 4H), 1.31–0.63 (m, 26H), 0.39 (br, 4H). ¹³C NMR (100 MHz, CDCl₃) δ 166.1, 161.1, 151.4, 140.2, 138.6, 132.6, 131.7, 127.0, 122.1, 119.6, 118.8, 118.7, 117.0, 80.7, 55.4, 55.1, 40.2, 31.9, 30.1, 29.5, 24.0, 22.8, 14.3. [α]_D²⁴ -134.71 (c = 1.0 in CHCl₃).

(R,R)-r-(S,S)-P1 (synthesized from racemic mixture of **1** at rt)



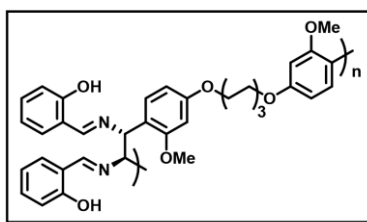
$^1\text{H NMR}$ (400 MHz, CD_2Cl_2) δ 13.21 (s, 2H), 8.27 (s, 2H), 7.58–6.41 (m, 14H), 4.80 (s, 2H), 1.78 (br, 4H), 1.31–0.14 (m, 30H). $^{13}\text{C NMR}$ (100 MHz, CDCl_3) δ 166.1, 161.1, 151.4, 140.2, 138.6, 132.6, 131.7, 127.0, 122.2, 119.6, 118.8, 118.7, 117.0, 80.7, 55.4, 55.0, 40.2, 31.9, 30.1, 29.5, 24.1, 22.8, 14.3. $[\alpha]_{\text{D}}^{24}$ -0.27 (c = 1.0 in CHCl_3).

(R,R)-P2



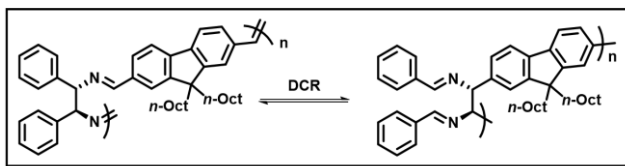
$^1\text{H NMR}$ (400 MHz, CDCl_3) δ 13.78 (s, 2H), 8.21 (s, 2H), 7.24–6.23 (m, 16H), 5.28 (s, 2H), 4.99 (s, 4H), 3.96–3.58 (m, 10H), 1.64 (br, 2H), 1.49–1.16 (m, 16H), 0.84 (t, 12H). $^{13}\text{C NMR}$ (125 MHz, CDCl_3) δ 165.7, 161.5, 159.4, 157.6, 150.5, 132.2, 131.6, 130.0, 125.7, 121.0, 119.0, 118.4, 117.1, 112.5, 105.4, 99.2, 71.4, 71.2, 65.2, 55.5, 39.7, 30.8, 29.2, 24.2, 23.1, 14.2, 11.3. $[\alpha]_{\text{D}}^{24}$ +10.23 (c = 1.0 in CHCl_3).

(R,R)-P3



$^1\text{H NMR}$ (400 MHz, CDCl_3) δ 13.79 (s, 2H), 8.20 (s, 2H), 7.24–6.12 (m, 14H), 5.27 (s, 2H), 4.10–3.52 (m, 10H), 1.72 (br, 4H), 1.45 (br, 4H). $^{13}\text{C NMR}$ (125 MHz, CDCl_3) δ 165.7, 161.6, 159.5, 157.7, 132.2, 131.6, 129.9, 120.8, 119.0, 118.4, 117.1, 105.0, 99.0, 71.1, 68.0, 55.5, 29.4, 26.0. $[\alpha]_{\text{D}}^{24}$ +8.56 (c = 1.0 in CHCl_3).

P4

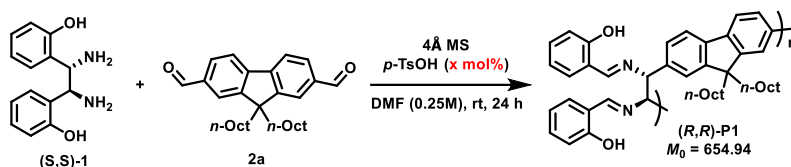


$^1\text{H NMR}$ (400 MHz, CD_2Cl_2) δ 8.29 (s, 2H), 8.00–6.67 (m, 16H), 4.77 (s, 2H), 1.91 (br, 4H), 1.40–0.12 (m, 30H). $^{13}\text{C NMR}$ could not be obtained due to hydrolysis during the measurement. $[\alpha]_{\text{D}}^{24}$ +172.91 (c = 1.0 in CHCl_3).

2.6. Supporting Information

2.6.1. Optimization of Polymerization

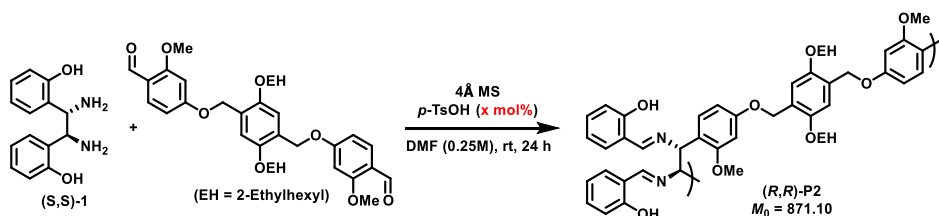
Table S2.1. Optimization of Catalyst Loading for (*R,R*)-P1.



Entry	<i>p</i> -TsOH (mol%)	Conv. ^a	<i>M_n</i> (<i>D</i>) ^b	Yield ^c
1	10	96%	14.9k (1.40)	64%
2	15	96%	16.6 k (1.88)	99%
3	20	97%	22.3 k (1.87)	80%
4	25	95%	14.2 k (1.69)	78%
5	50	95%	15.5 k (1.69)	90%
6	100	96%	16.9k (1.60)	99%

^aDetermined by ¹H NMR analysis of the crude reaction mixture. ^bAbsolute molecular weights determined by THF SEC using a multiangle laser light scattering (MALLS) detector. ^cIsolated yields after purification from IPA.

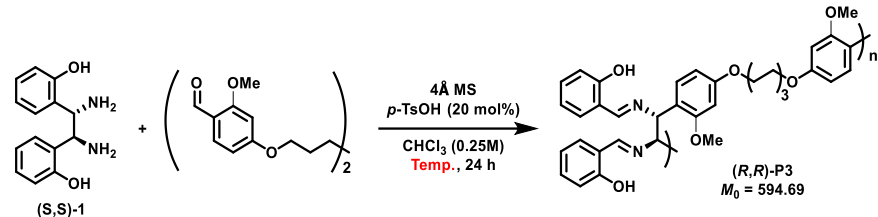
Table S2.2. Optimization of Catalyst Loading for (*R,R*)-P2.



Entry	<i>p</i> -TsOH (mol%)	Conv. ^a	<i>M_n</i> (<i>D</i>) ^b	Yield ^c
1	20	97%	33.3 k (1.61)	90%
2	25	96%	19.9 k (1.74)	85%
3	30	95%	18.5 k (1.94)	98%

^aDetermined by ¹H NMR analysis of the crude reaction mixture. ^bAbsolute molecular weights determined by THF SEC using a multiangle laser light scattering (MALLS) detector. ^cIsolated yields after purification from IPA.

Table S2.3. Optimization of Reaction Temperature for **(R,R)-P3**.



Entry	<i>p</i> -TsOH (mol%)	Conv. ^a	<i>M_n</i> (<i>Đ</i>) ^b	Yield ^c
1	rt	96%	14.6 k (2.45)	79%
2	40	97%	16.7 k (1.76)	78%
3	60	95%	10.0 k (1.66)	77%

^aDetermined by ¹H NMR analysis of the crude reaction mixture. ^bAbsolute molecular weights determined by THF SEC using a multiangle laser light scattering (MALLS) detector. ^cIsolated yields after purification from IPA.

2.6.2. *In situ* ¹H NMR Experiment in DMF-*d*₇

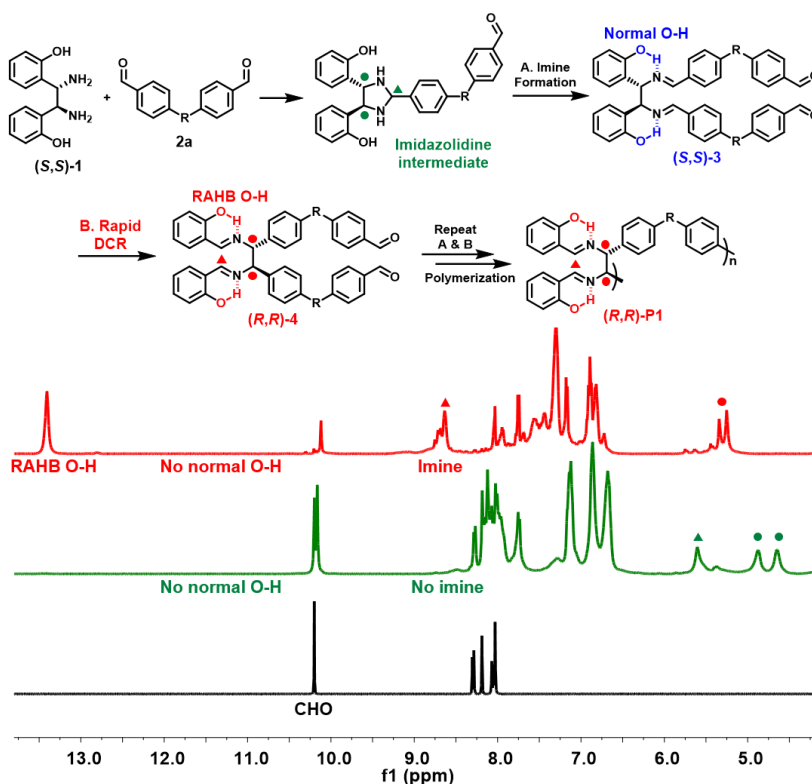


Figure S2.1. *In situ* ¹H NMR monitoring for the formation of imidazole intermediate before DCR in early stage of the polymerization in DMF-*d*₇. Assignment of peaks corresponding imidazolidine intermediate is supported by the previous literature.³⁹

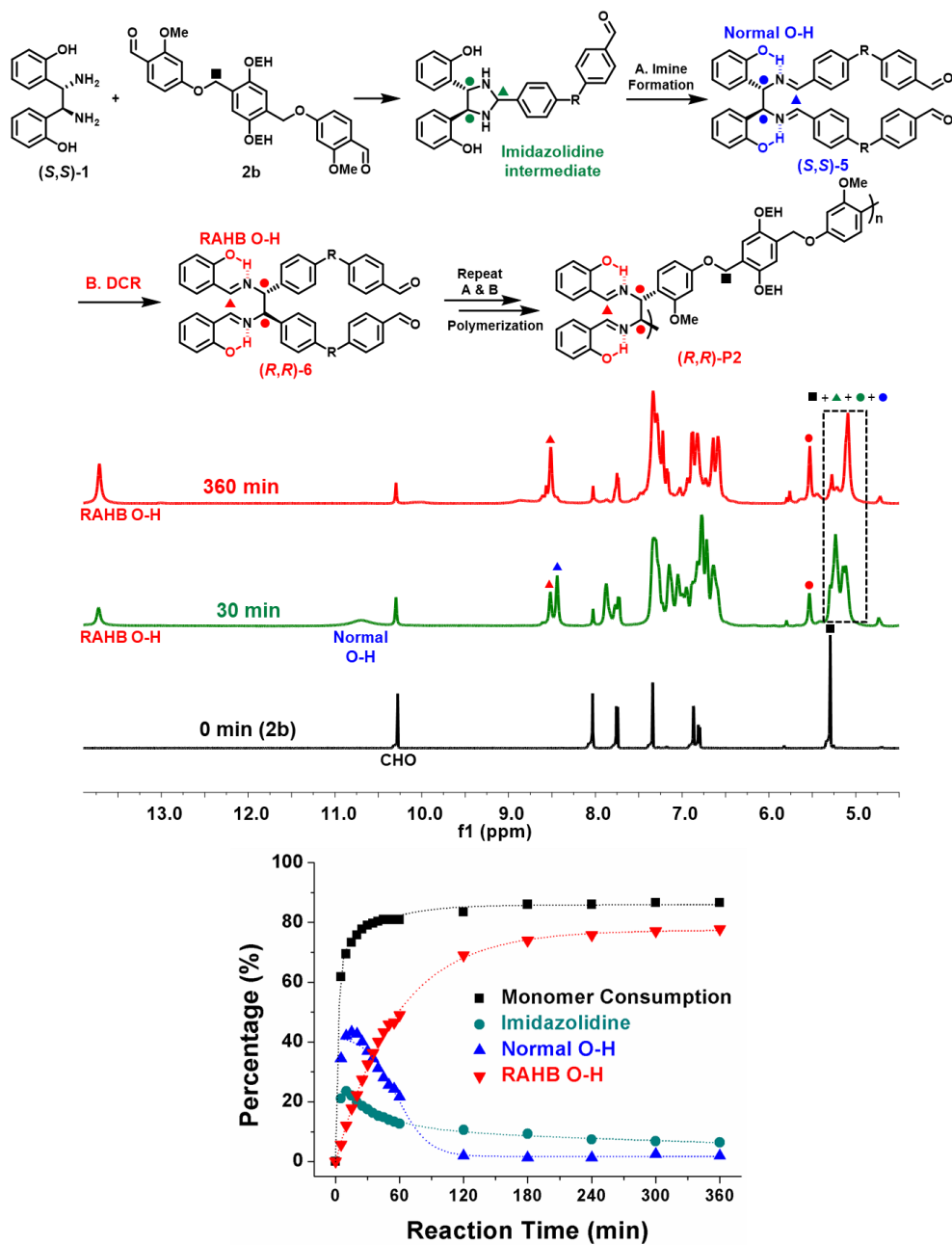


Figure S2.2. Monitoring the polymerization using (S,S) -1 and **2b** by *in situ* ^1H NMR spectroscopy in $\text{DMF-}d_7$.

2.6.3. Control Experiment to Compare Stability against Hydrolysis

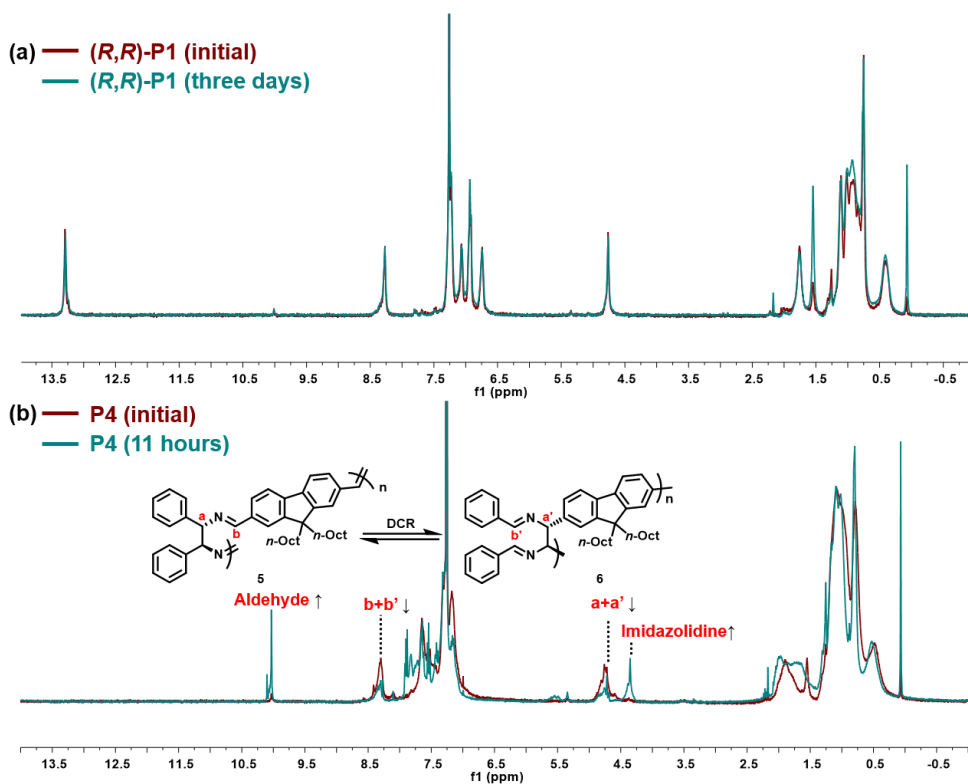
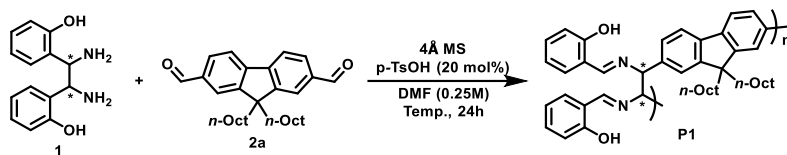


Figure S2.3. (a) ^1H NMR spectra of (R,R) -P1 measured at the initial and three days after dissolving in CDCl_3 . (b) ^1H NMR spectra of P4 measured at the initial and 11 hours after dissolving in CDCl_3 .

2.6.4. Temperature Affecting Stereospecificity of Tandem DCRP

Table S2.4. Various P1 Synthesis by Varying Reaction Temperature and Configuration of **1**.



Entry	Config. of 1	Temp. (°C)	$[\alpha]_D^{24}$ ^a	Conv. ^b	M_n (\bar{M}) ^c	Yield ^d
1	(<i>S,S</i>)	10	+134.47	95%	13.9 k (1.60)	70%
2	(<i>S,S</i>)	rt	+135.95	97%	22.3 k (1.87)	80%
3	(<i>S,S</i>)	50	+82.82	97%	24.0 k (2.85)	99%
4	(<i>S,S</i>)	70	+71.92	98%	30.6 k (4.13)	99%
5	(<i>S,S</i>)	90	+57.11	98%	42.9 k (5.06)	99%
6 ^e	(<i>S,S</i>)	120	+53.68	94%	35.8 k (2.20)	65%
7 ^e	(<i>S,S</i>)	140	+25.92	91%	23.4 k (1.82)	62%
8	(<i>R,R</i>)	rt	-134.71	97%	20.1 k (2.34)	98%
9	Racemic	rt	-0.27	97%	21.1 k (2.77)	98%
10	<i>meso</i>	rt	0	63%	6.9 k (1.17)	65%
11	<i>meso</i>	50	0	83%	9.4 k (1.60)	71%

^a $c = 1.0$ in CHCl_3 . ^bDetermined by ^1H NMR analysis of the crude reaction mixture.

^cAbsolute molecular weights determined by THF SEC using a multiangle laser light scattering (MALLS) detector. ^dIsolated yields after purification from IPA. ^ePolymerization proceeded for 5 h.

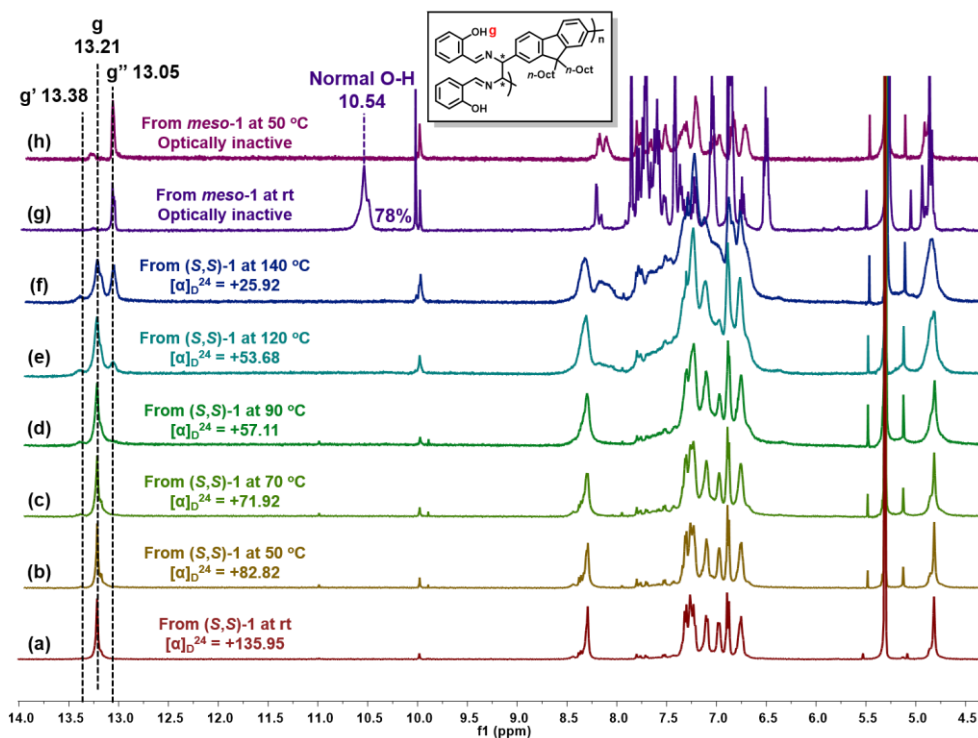


Figure S2.4. ^1H NMR spectra (in CD_2Cl_2) of various **P1** (in Table S2.4) synthesized from chiral and *meso* diamines at various reaction temperatures.

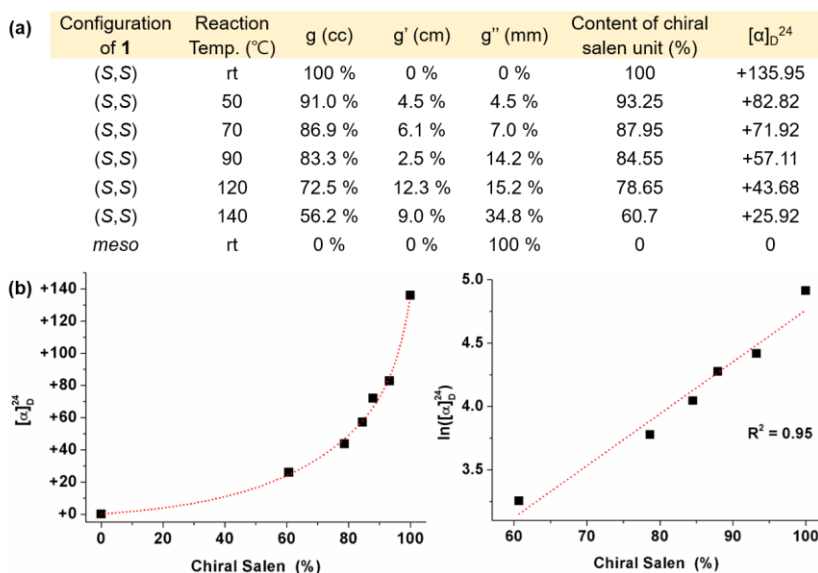


Figure S2.5. (a) Table for integrations of all RAHB O–H signals (g, g', and g'' peaks) and optical rotation values depending on reaction temperature. (b) Plots showing relationship between $[\alpha]_{\text{D}}^{24}$ and content of chiral salen unit determined by ^1H NMR spectra (in CD_2Cl_2). Chiral salen (%) was calculated by $(g + 0.5 \cdot g'') / (g + g' + g'')$.

2.6.5. SEC Traces of Polymers

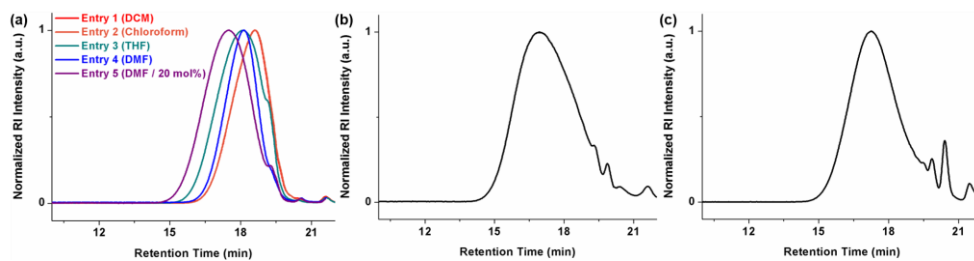


Figure S2.6. SEC traces for polymers in Table 2.1. (a) (R,R) -P1 (entries 1–5). (b) (R,R) -P2 (entry 6). (c) (R,R) -P3 (entry 7).

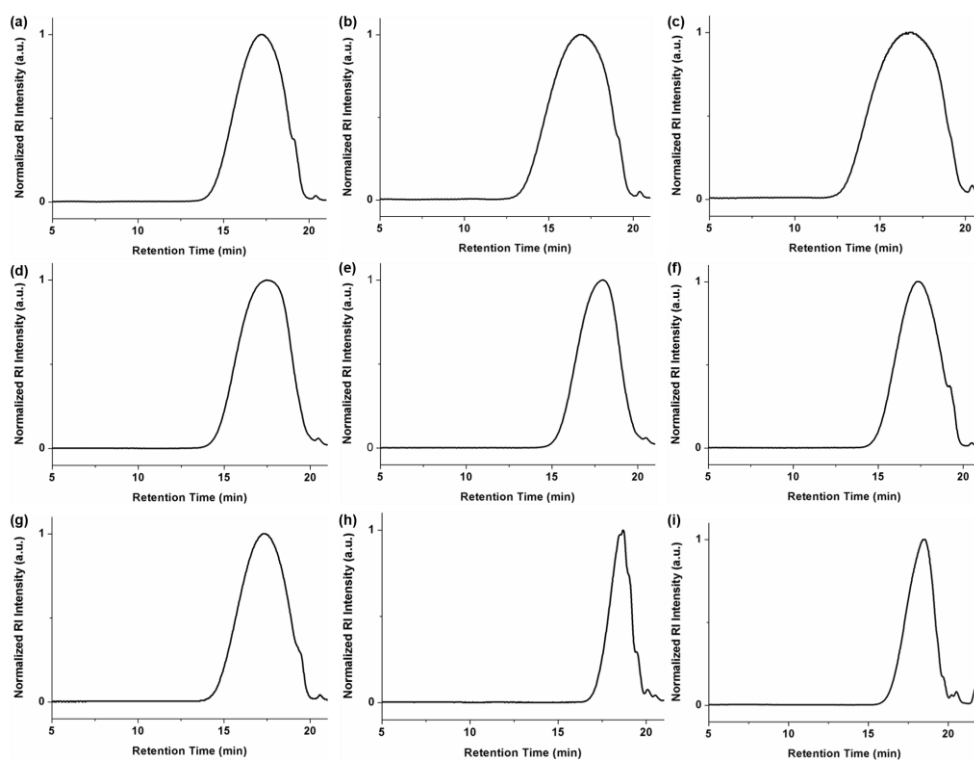


Figure S2.7. SEC traces for other polymers in Table S2.4. (a) P1 synthesized at 50 °C from (S,S) -1 (entry 2). (b) P1 synthesized at 70 °C from (S,S) -1 (entry 3). (c) P1 synthesized at 90 °C from (S,S) -1 (entry 4). (d) P1 synthesized at 120 °C from (S,S) -1 (entry 5). (e) P1 synthesized at 140 °C from (S,S) -1 (entry 6). (f) P1 synthesized at room temperature from (R,R) -1 (entry 7). (g) P1 synthesized at room temperature from 1:1 mixture of (S,S) -1 and (R,R) -1 (entry 8). (h) P1 synthesized at rt from *meso*-1 (entry 9). (i) P1 synthesized at 50 °C from *meso*-1 (entry 10).

2.6.6. Metal Sensing Experiments

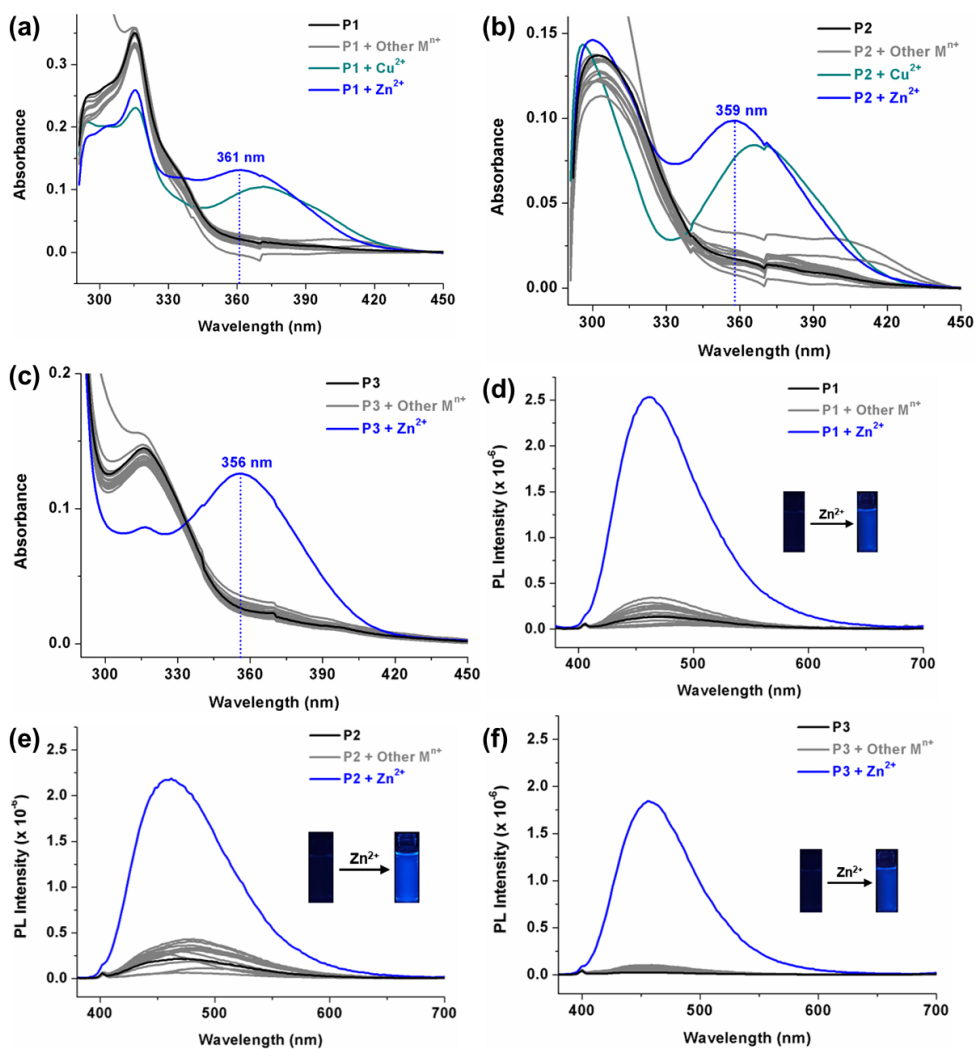


Figure S2.8. Absorption spectra of polymers: (a) (*R,R*)-P1, (b) (*R,R*)-P2, and (c) (*R,R*)-P3. Emission spectra of polymers: (d) (*R,R*)-P1, (e) (*R,R*)-P2, and (f) (*R,R*)-P3 in THF:H₂O = 9:1 (v/v) solution (10 μ M) at 298 K in the absence or presence of 1.0 equiv. of various metal cations.

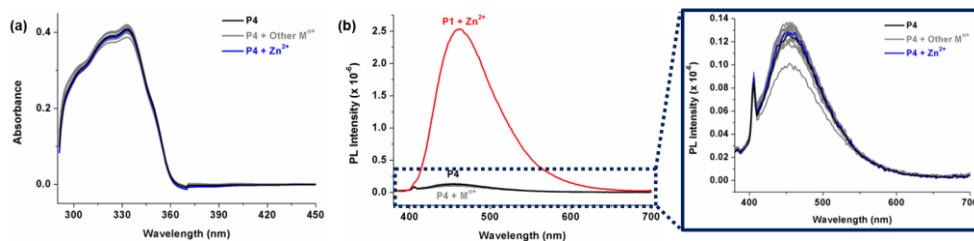


Figure S2.9. Control experiment to compare sensing ability. (a) Absorption and (b) emission spectra of **P4** in THF:H₂O = 9:1 (v/v) solution (10 μM) at 298 K in the absence or presence of 1.0 equiv. of various metal cations.

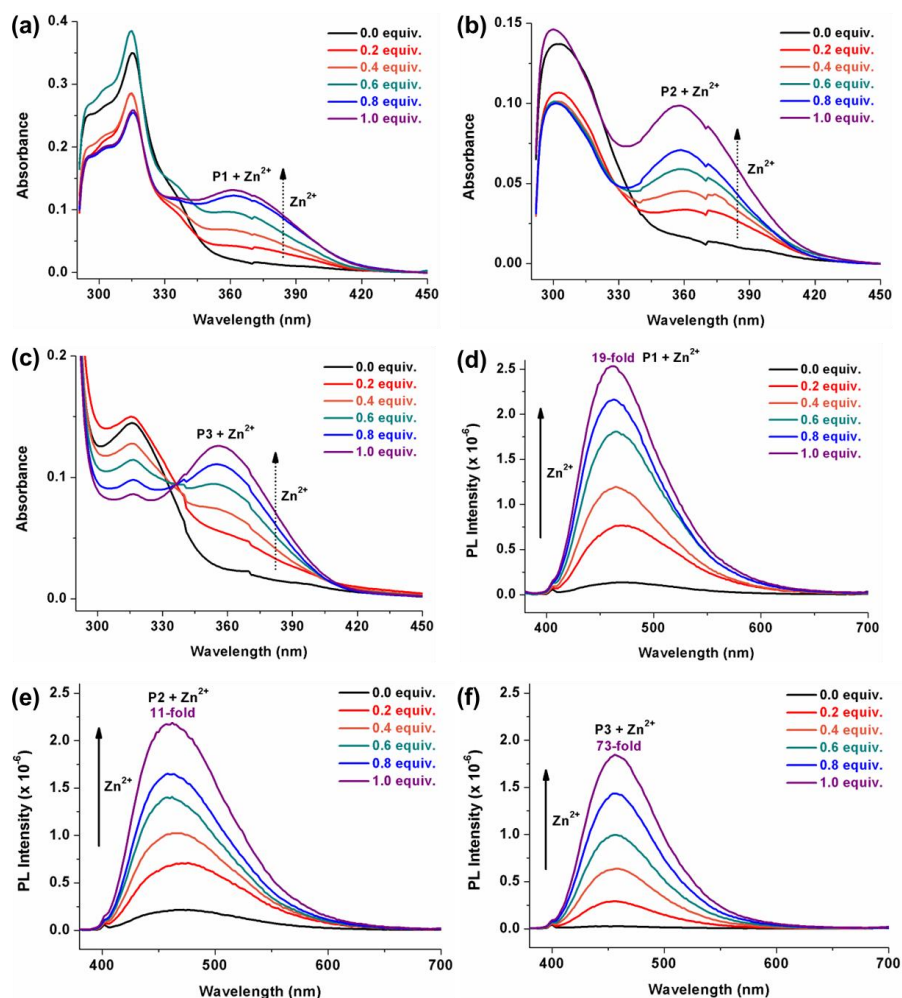


Figure S2.10. Absorption spectra of polymers: (a) *(R,R)*-**P1**, (b) *(R,R)*-**P2**, and (c) *(R,R)*-**P3**. Emission spectra of polymers: (d) *(R,R)*-**P1** ($I/I_0 = 19$), (e) *(R,R)*-**P2** ($I/I_0 = 11$), and (f) *(R,R)*-**P3** ($I/I_0 = 73$) in THF:H₂O = 9:1 (v/v) solution (10 μM) at 298 K with increasing amounts of Zn²⁺ (0.0–1.0 equiv.).

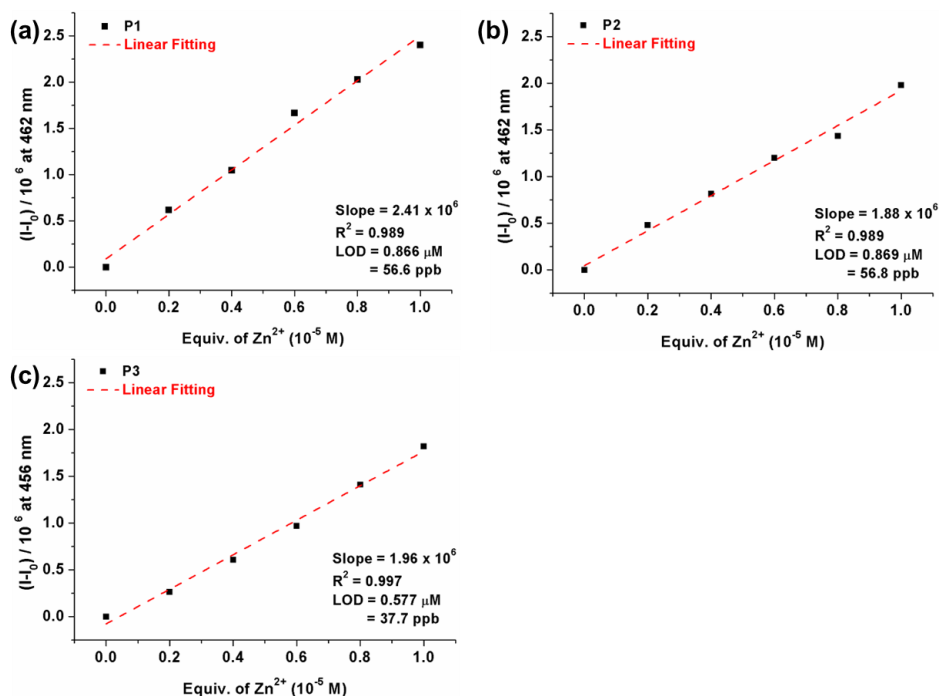


Figure S2.11. The linear relationship between $I-I_0$ and $[Zn^{2+}]$: (a) (*R,R*)-P1, (b) (*R,R*)-P2, and (c) (*R,R*)-P3.

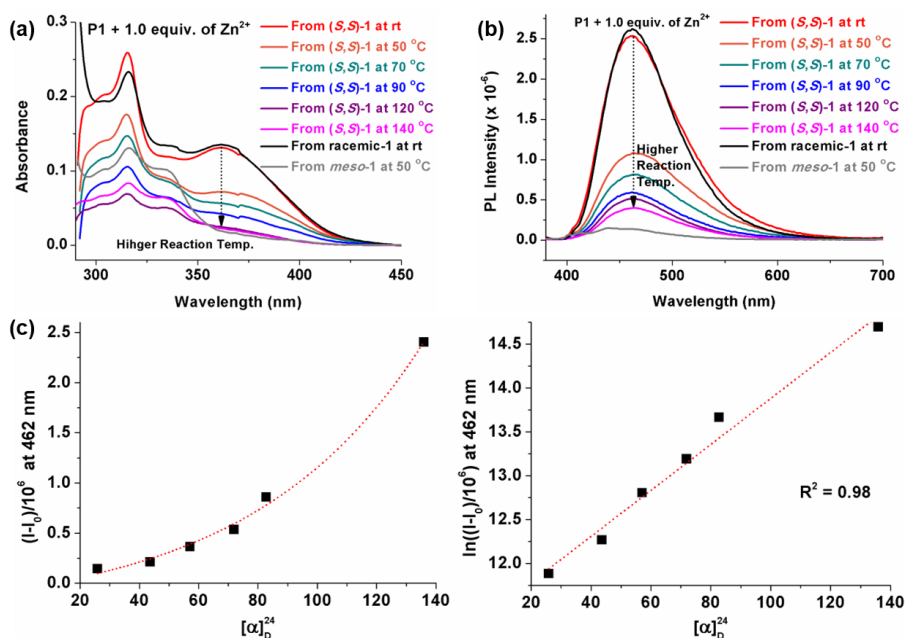


Figure S2.12. (a) Absorption and (b) emission spectra of various P1 in THF:H₂O = 9:1 (v/v) solution (10 μM) at 298 K in the presence of 1.0 equiv. of Zn^{2+} . (c) Plots showing relationship between $I-I_0$ and $[\alpha]_D^{24}$.

2.6.7. TGA and DSC Profiles of Polymers

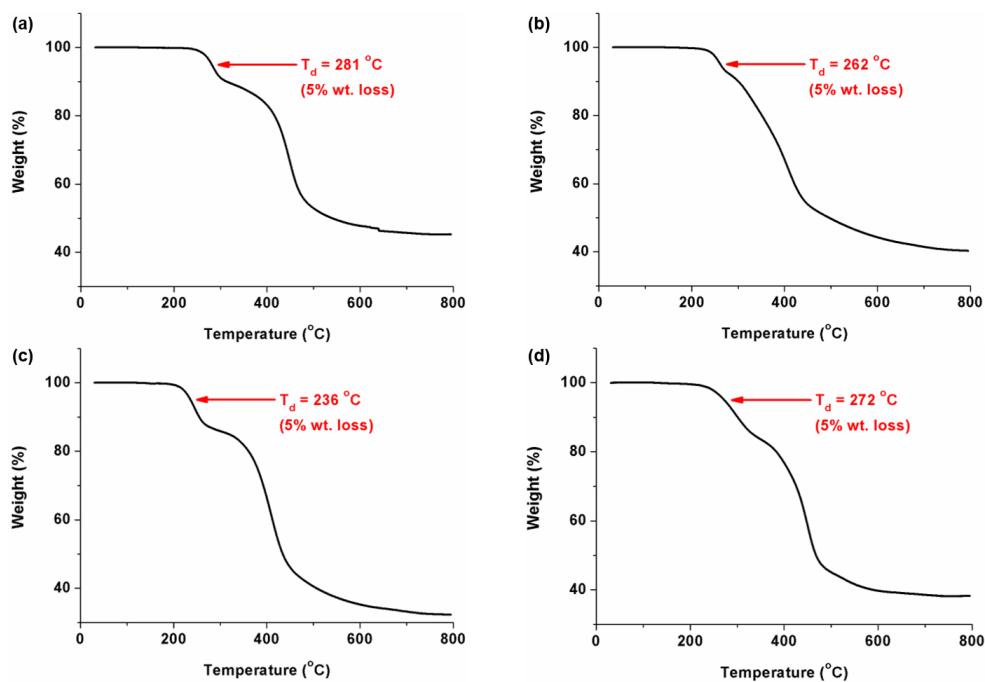


Figure S2.13. TGA profiles of (a) (R,R) -P1, (b) (R,R) -P2, (c) (R,R) -P3, and (d) P4.

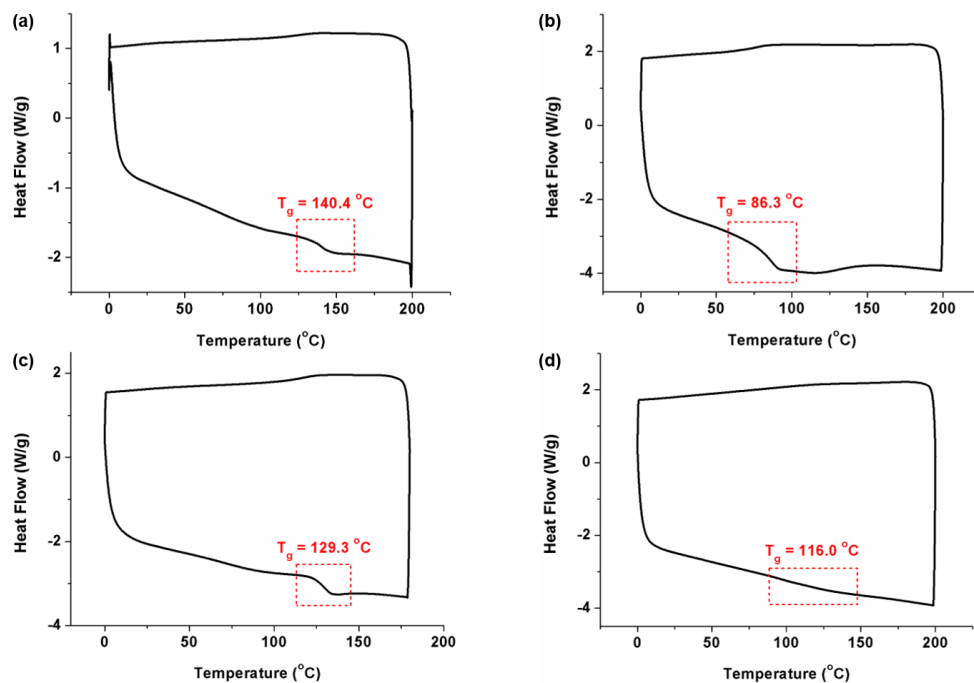
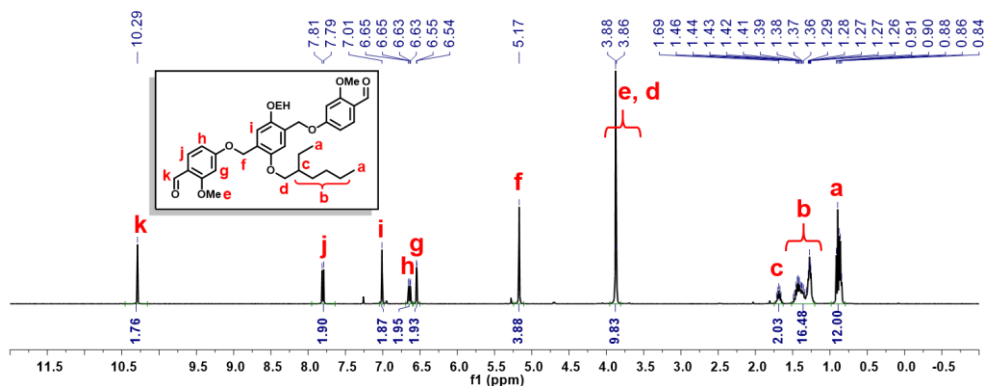


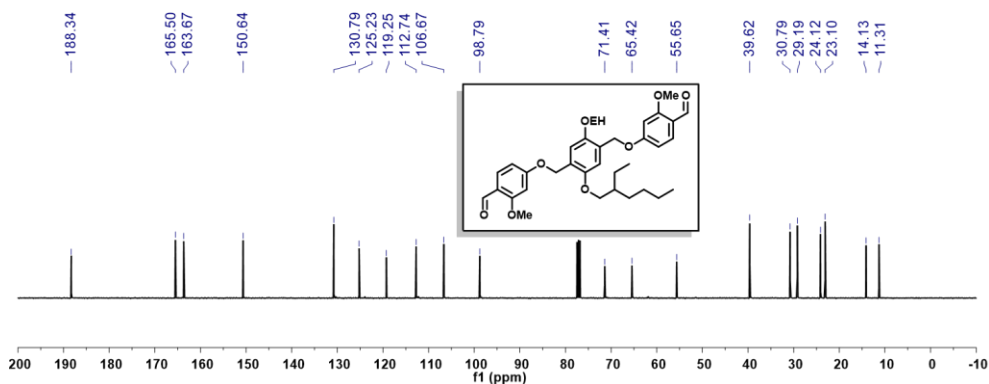
Figure S2.14. DSC profiles of (a) (R,R) -P1, (b) (R,R) -P2, (c) (R,R) -P3, and (d) P4.

2.6.8. ^1H and ^{13}C NMR Spectra of Monomers and Polymers

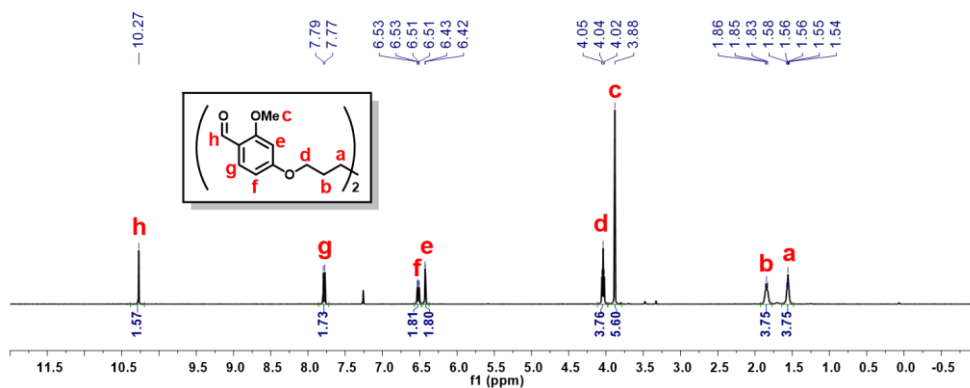
2b ^1H NMR (400 MHz, CDCl_3)



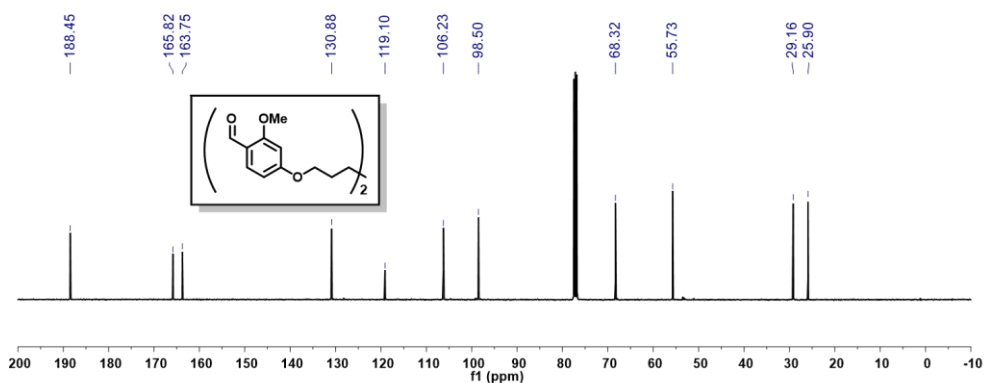
2b ^{13}C NMR (100 MHz, CDCl_3)



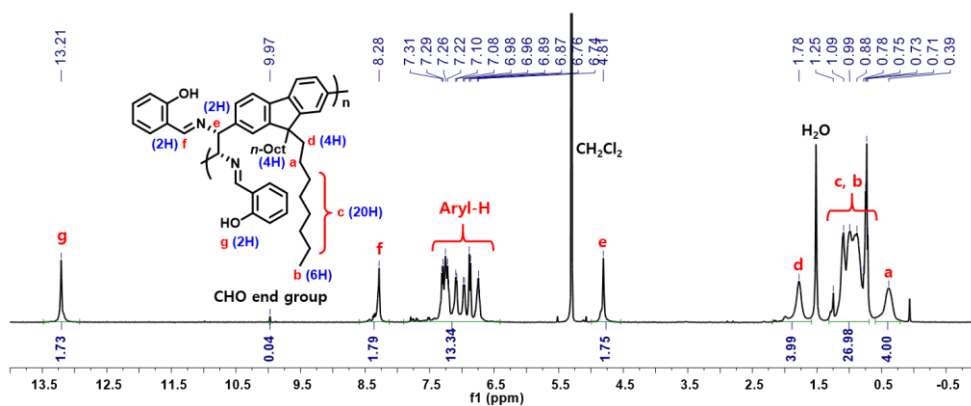
2c ^1H NMR (400 MHz, CDCl_3)



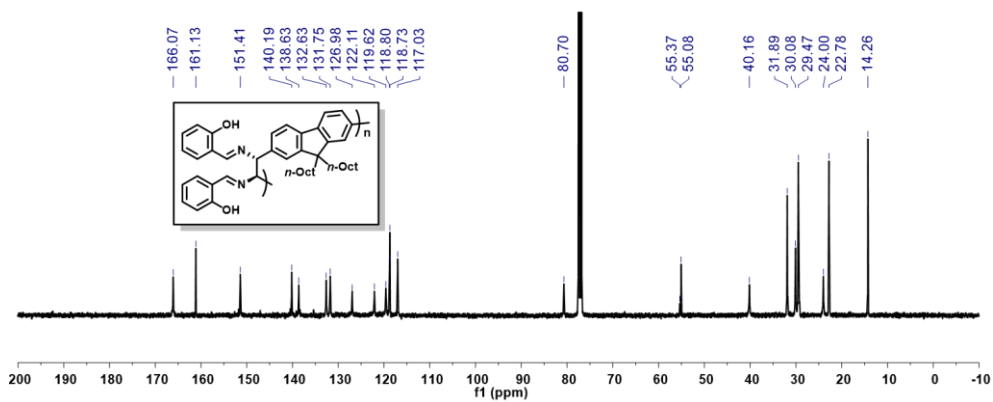
2c ^{13}C NMR (100 MHz, CDCl_3)



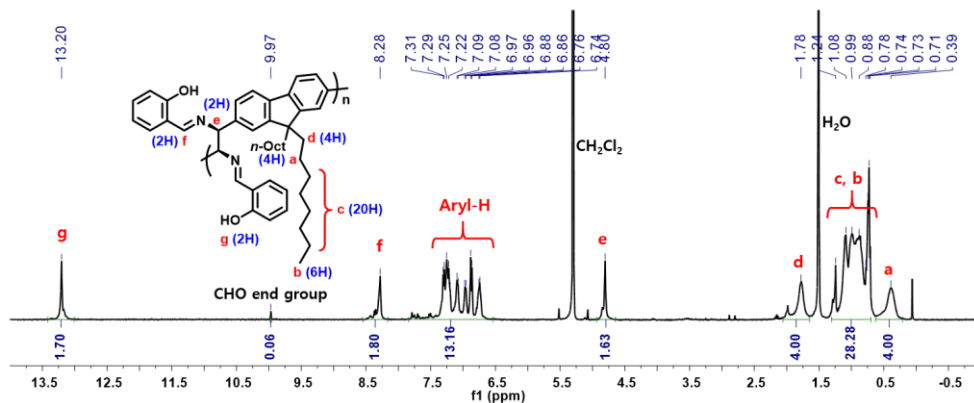
(R,R)-P1 (synthesized from **(S,S)-1** at rt) ^1H NMR (400 MHz, CDCl_3)



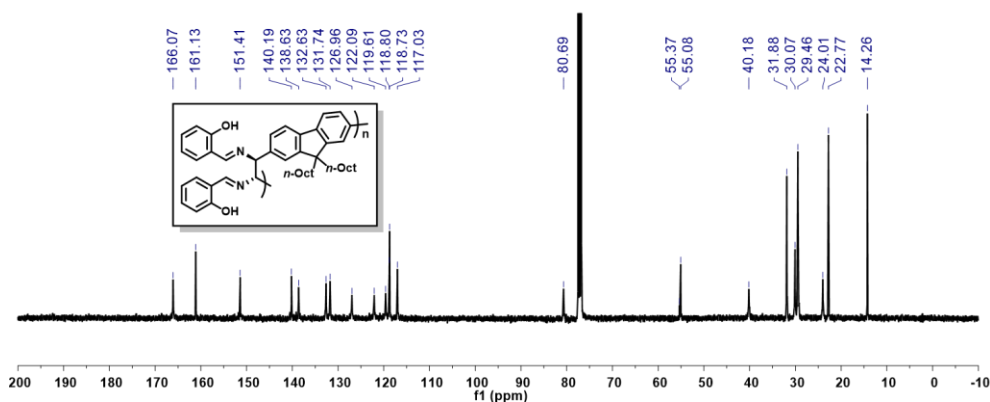
(R,R)-P1 (synthesized from **(S,S)-1** at rt) ^{13}C NMR (100 MHz, CDCl_3)



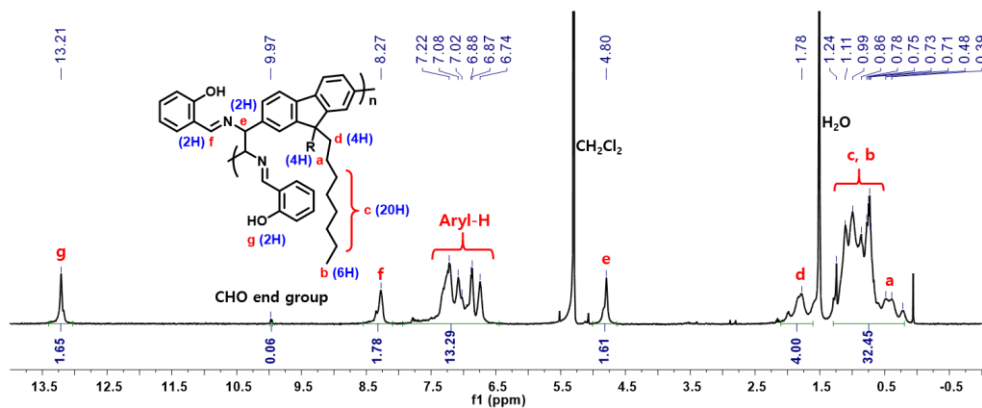
(*S,S*)-**P1** (synthesized from (*R,R*)-**1** at rt) ^1H NMR (400 MHz, CDCl_3)



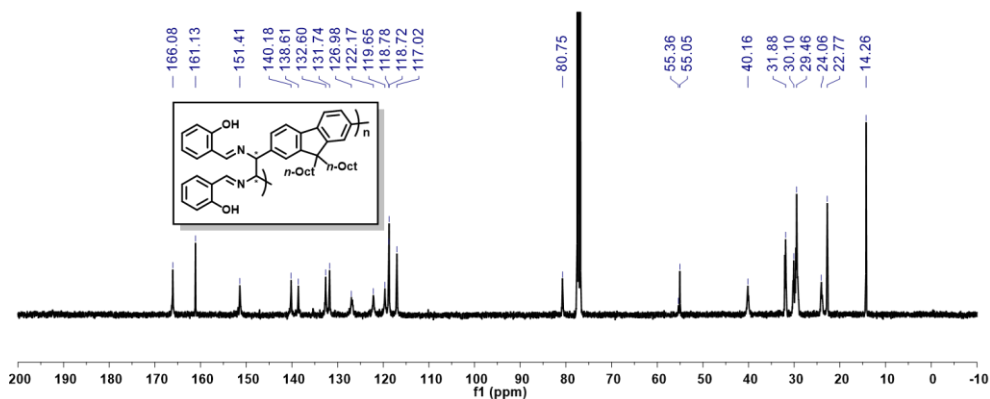
(*S,S*)-**P1** (synthesized from (*R,R*)-**1** at rt) ^{13}C NMR (100 MHz, CDCl_3)



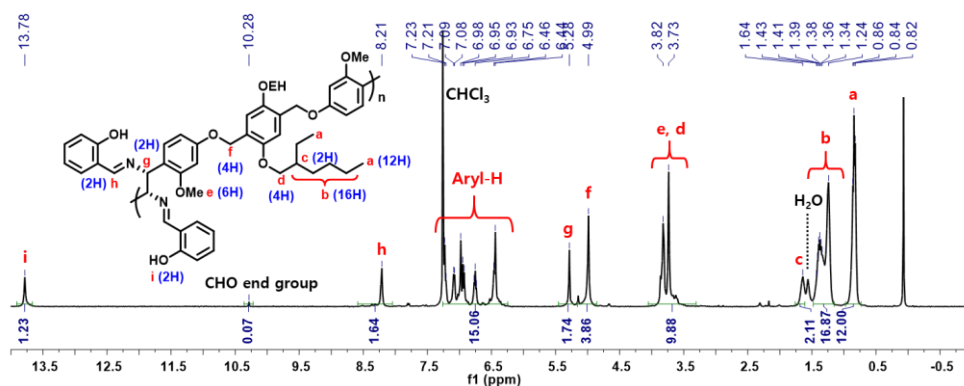
(*R,R*)-*r*-(*S,S*)-**P1** (synthesized from racemic mixture of **1** at rt) ^1H NMR (400 MHz, CDCl_3)



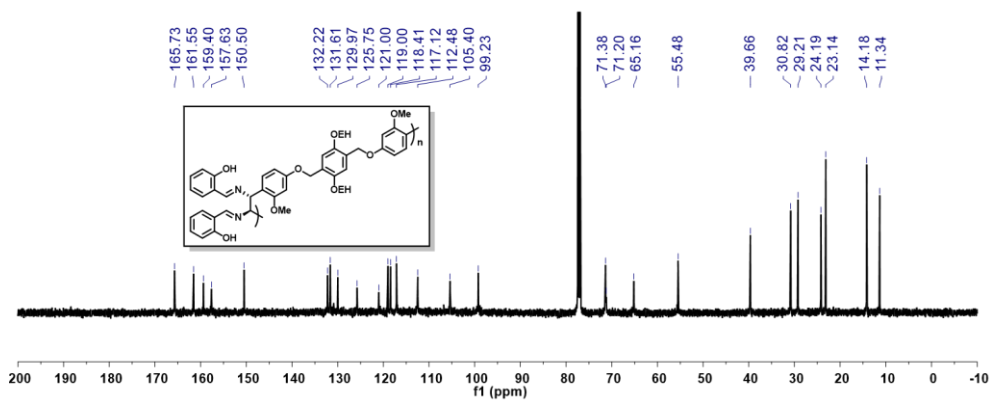
(*R,R*)-*r*-(*S,S*)-P1 (from racemic mixture of **1** at rt) ^{13}C NMR (100 MHz, CDCl_3)



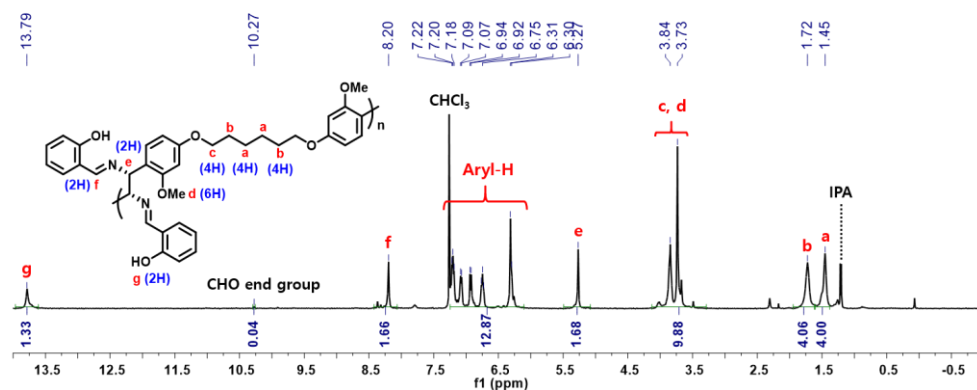
(*R,R*)-P2 ^1H NMR (400 MHz, CDCl_3)



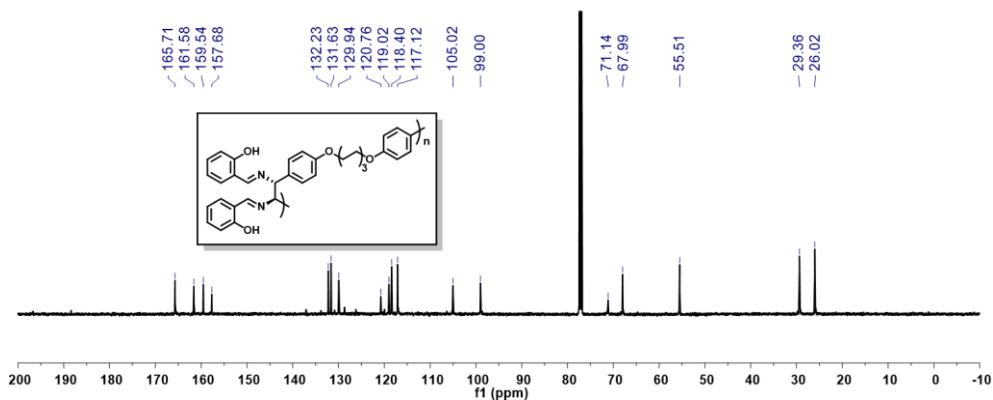
(*R,R*)-P2 ^{13}C NMR (125 MHz, CDCl_3)



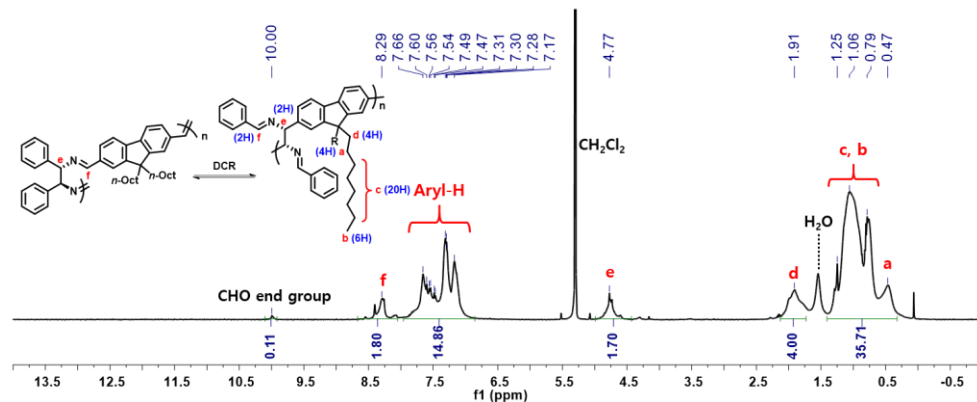
(R,R)-P3 ^1H NMR (400 MHz, CDCl_3)



(R,R)-P3 ^{13}C NMR (125 MHz, CDCl_3)



P4 ^1H NMR (400 MHz, CDCl_3)



2.7. References

*Portions of this chapter have been previously reported, see: Hwang, S.-H.; Choi, T.-L. *Chem. Sci.* **2021**, *12*, 2404–2409.

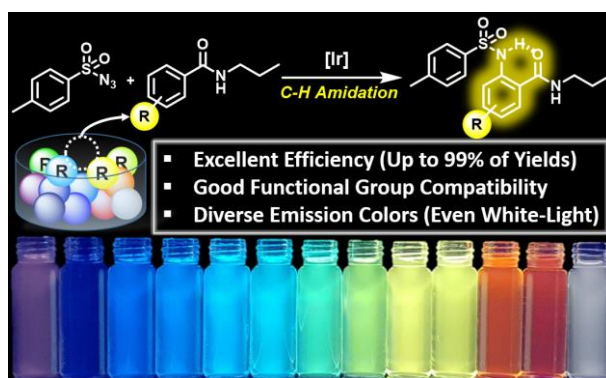
- (1) Goussé, C.; Gandini, A. *Polym. Int.* **1999**, *48*, 723–731.
- (2) Fujimoto, C. H.; Hickner, M. A.; Cornelius, C. J.; Loy, D. A. *Macromolecules* **2005**, *38*, 5010–5016.
- (3) Meldal, M.; *Macromol. Rapid Commun.* **2008**, *29*, 1016–1051.
- (4) Tasdelen, M. A. *Polym. Chem.* **2011**, *2*, 2133–2145.
- (5) Gong, T.; Adzima, B. J.; Baker, N. H.; Bowman, C. N. *Adv. Mater.* **2013**, *25*, 2024–2028.
- (6) Delaittre, G.; Guimard, N. K.; Barner-Kowollik, C. *Acc. Chem. Res.* **2015**, *48*, 1296–1307.
- (7) Cao, X.; Shi, Y.; Gan, W.; Naguib, H.; Wang, X.; Graff, R. W.; Gao, H. *Macromolecules* **2016**, *49*, 5342–5349.
- (8) Zou, L.; Shi, Y.; Cao, X.; Gan, W.; Wang, X.; Graff, R. W.; Hu, D.; Gao, H. *Polym. Chem.* **2016**, *7*, 5512–5517.
- (9) Ye, L.; Wan, L.; Huang, F. *New J. Chem.* **2017**, *41*, 4424–4430.
- (10) Fuchs, P.; Vana, P.; Zhang, K. *J. Polym. Sci.* **2020**, *58*, 1535–1543.
- (11) Ilardi, E. A.; Stivala, C. E.; Zakarian, A. *Chem. Soc. Rev.* **2009**, *38*, 3133–3148.
- (12) Yang, G.; Matsuzono, S.-i.; Hoyama, E.; Tokuhisa, H.; Hiratani, K. *Macromolecules* **2001**, *34*, 6545–6547.
- (13) Wang, W.; Qi, X.; Guan, Y.; Zhang, F.; Zhang, J.; Yan, C.; Zhu, Y. Wan, X. *J. Polym. Sci., Part A Polym. Chem.* **2016**, *54*, 2050–2059.
- (14) Tena, A.; Rangou, S.; Shishatskiy, S.; Filiz, V.; Abetz, V. *Sci. Adv.* **2016**, *2*, e151859.
- (15) Meis, D.; Tena, A.; Neumann, S.; Georgopoulos, P.; Emmler, T.; Shishatskiy, S.; Rangou, S.; Filiz, V.; Abetz, V. *Polym. Chem.* **2018**, *9*, 3987–3999.
- (16) Viuda, M. R. d. l.; Tena, A.; Neumann, S.; Willruth, S.; Filiz, V.; Abetz, V. *Polym. Chem.* **2018**, *9*, 4007–4016.
- (17) Marvel, C. S.; Tarköy, N. *J. Am. Chem. Soc.* **1957**, *79*, 6000–6002.
- (18) Suematsu, K.; Nakamura, K.; Takeda, J. *Polymer J.* **1983**, *15*, 71–79.
- (19) Lee, K.-S.; Won, J. C. *Makromol. Chem.* **1989**, *190*, 1547–1552.
- (20) Park, S.-B.; Kim, H.; Zin, W.-C.; Jung, J. C. *Macromolecules* **1993**, *26*, 1627–1632.
- (21) Yang, C.-J.; Jenekhe, S. A. *Macromolecules* **1995**, *28*, 1180–1196.
- (22) Sun, W.; Gao, X.; Lu, F. *Appl. Poly. Sci.* **1997**, *64*, 2309–2315.
- (23) Thomas, O.; Inganäs, O.; Andersson, M. R. *Macromolecules* **1998**, *31*, 2676–2678.

- (24) Destri, S.; Pasini, M.; Pelizzi, C.; Porzio, W.; Predieri, G.; Vignali, C. *Macromolecules* **1999**, *32*, 353–360.
- (25) Suh, S. C.; Shim, S. C. *Synth. Met.* **2000**, *114*, 91–95.
- (26) Catanescu, O.; Grigoras, M.; Colotin, G.; Dobreanu, A.; Hurduc, N.; Simionescu, C. I. *Eur. Polym. J.* **2001**, *37*, 2213–2216.
- (27) Niu, H.-J.; Huang, Y.-D.; Bai, X.-D.; Li, X. *Mater. Lett.* **2004**, *58*, 2979–2983.
- (28) Grigoras, M.; Catanescu, C. O. *J. Macromol. Sci., Polym. Rev.* **2004**, *44*, 131–173.
- (29) Hindson, J. C.; Ulgut, B.; Friend, R. H.; Greenham, N. C.; Norder, B.; Kotlewski, A.; Dingemans, T. J. *J. Mater. Chem.* **2010**, *20*, 937–944.
- (30) Iwan, A.; Palewicz, M.; Chuchmala, A.; Gorecki, L.; Sikora, A.; Ma-zurek, B.; Pasciak, G. *Synth. Met.* **2012**, *162*, 143–153.
- (31) Chin, J.; Mancin, F.; Thavarajah, N.; Lee, D.; Lough, A.; Chung, D. S. *J. Am. Chem. Soc.* **2003**, *125*, 15276–15277.
- (32) Kim, H.-J.; Kim, H.; Alhakimi, G.; Jeong, E. J.; Thavarajah, N.; Stud-nicki, L.; Koprianiuk, A.; Lough, A. J.; Suh, J.; Chin, J. *J. Am. Chem. Soc.* **2005**, *127*, 16370–16371.
- (33) Kim, H.-J.; Kim, W.; Lough, A. J.; Kim, B. M.; Chin, J. *J. Am. Chem. Soc.* **2005**, *127*, 16776–16777.
- (34) Kim, H.; Nguyen, Y.; Yen, C. P.-H.; Chagal, L.; Lough, A. J.; Kim, B. M.; Chin, J. *J. Am. Chem. Soc.* **2008**, *130*, 12184–12191.
- (35) Kim, H.; Nguyen, Y.; Lough, A. J.; Chin, J. *Angew. Chem., Int. Ed.* **2008**, *47*, 8678–8681.
- (36) Lee, D.-N.; Kim, H.; Mui, L.; Myung, S.-W.; Chin, J.; Kim, H.-J. *J. Org. Chem.* **2009**, *74*, 3330–3334.
- (37) Kim, H.; Staikova, M.; Lough, A. J.; Chin, J. *Org. Lett.* **2009**, *11*, 157–160.
- (38) Kwon, S. H.; Lee, S. M.; Byun, S. M.; Chin, J.; Kim, B. M. *Org. Lett.* **2012**, *14*, 3664–3667.
- (39) Kim, M.; Kim, H.; Kim, H.; Chin, J. *J. Org. Chem.* **2017**, *82*, 12050–12058.
- (40) Xu, Y.; Meng, J.; Meng, L.; Dong, Y.; Cheng, Y.; Zhu, C. *Chem. Eur. J.* **2010**, *16*, 12898–12903.
- (41) Li, J.; Wu, Y.; Song, F.; Wei, G.; Cheng, Y.; Zhu, C. *J. Mater. Chem.* **2012**, *22*, 478–482.
- (42) Bera, M. K.; Chakraborty, C.; Malik, S. *New J. Chem.* **2015**, *39*, 9207–9214.
- (43) Jang, Y.-J.; Hwang, S.-H.; Choi, T.-L. *Macromolecules* **2018**, *51*, 7476–7482.
- (44) Iadevaia, G.; Stross, A. E.; Neumann, A.; Hunter, C. A. *Chem. Sci.* **2016**, *7*, 1760–1767.
- (45) Dickmeis, M.; Cinar, H.; Ritter, H. *Angew. Chem., Int. Ed.* **2012**, *51*, 3957–3959.
- (46) Vögtle, F.; Goldschmitt, E. *Chem. Ber.* **1976**, *109*, 1–40.

**Chapter 3. Iridium-Catalyzed Direct C–H Amidation
Producing Multicolor Fluorescent Molecules Emitting
Blue-to-Red and White-Light**

3.1. Abstract

In this chapter, we demonstrate a powerful strategy, iridium-catalyzed direct C–H amidation (DCA), for synthesizing various fluorescent sulfonamides that emit light over the entire visible spectrum with excellent efficiency (up to 99% yields). By controlling electronic characters of the resulting sulfonamides, a wide range of blue-to-red emissions was predictably obtained via an excited-state intramolecular proton-transfer process. Furthermore, we even succeeded in a white-light generation, highlighting that this DCA is an excellent synthetic method to prepare a library of fluorophores.

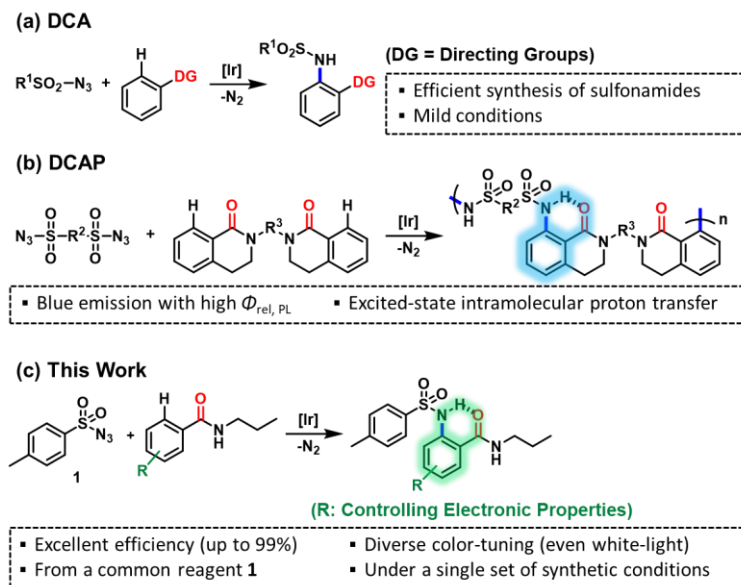


3.2. Introduction

Over the past decades, multicolor fluorescent materials have received extensive attention because of their potential applications in the next-generation lighting sources and displays.^{1–8} To prepare multicolor fluorescent molecules, chemists have generally synthesized fluorophores from various precursors, or frequently, under different reaction conditions. Sometimes one must use even totally different synthetic pathways due to lack of versatility of synthetic scheme. Therefore, it is crucial to develop a versatile and efficient synthetic method capable of predictably preparing multicolor fluorophores under a single set of synthetic conditions, or more desirably, from a common reagent.

Chang's group developed iridium-catalyzed direct C–H amidation (DCA) reactions between sulfonyl azides and arenes containing carbonyl (or imine) directing groups, thus enabling efficient synthesis of various sulfonamides under mild conditions (Scheme 3.1a).^{9–14} Inspired by the highly efficient DCA (see **Chapter 1.1.3** for details), we recently reported direct C–H amidation polymerization (DCAP) of bis-sulfonyl azides and bis-benzamides to produce polysulfonamides by an atom-economical and green method (Scheme 3.1b).^{15,16} Interestingly, unique intramolecular hydrogen-bonds are formed

Scheme 3.1. Iridium-Catalyzed Direct C–H Amidation (Polymerization).

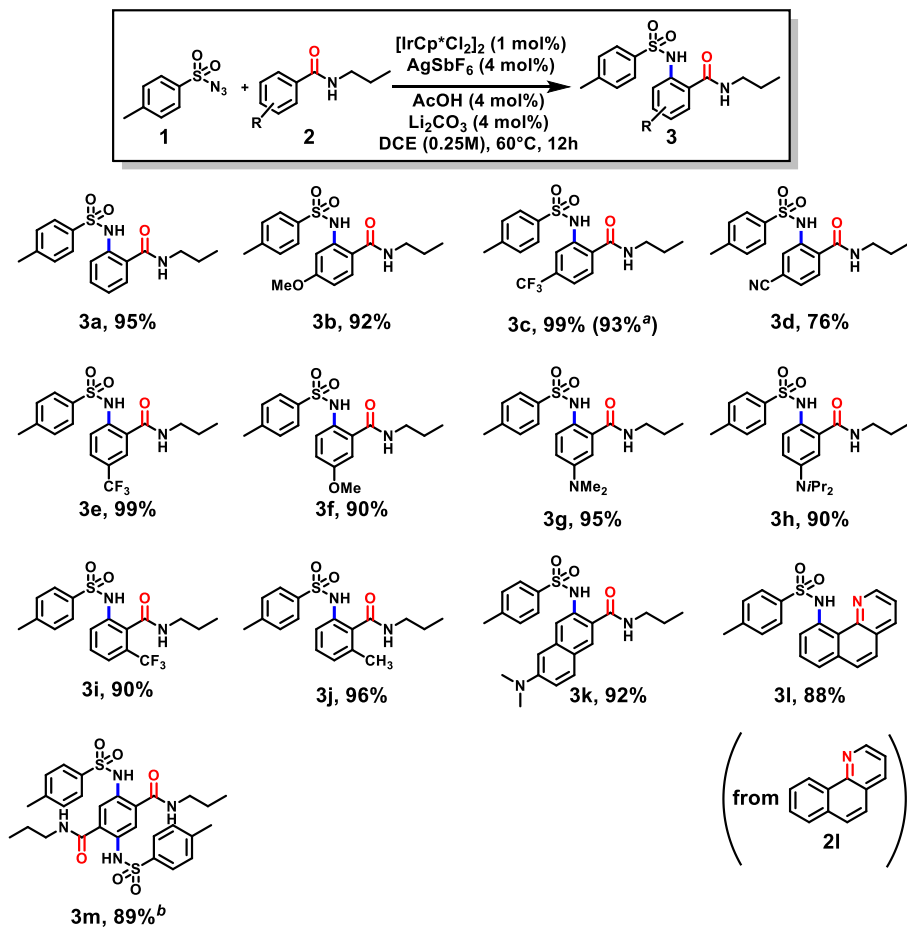


between the proton on the sulfonamide group and adjacent carbonyl group throughout the polymer backbone, causing polysulfonamides to undergo an excited-state intramolecular proton-transfer (ESIPT; see **Chapter 1.1.4** for details) process and emit blue-light with high quantum yields. This process occurs when photoexcited molecule emits light with very large Stokes shift by transfer of protons, leading to keto-enol tautomerization.

Inspired by versatile C–H activation chemistry^{9–14} and numerous examples^{17–29} of fluorescent molecules by the ESIPT process, we envisioned a new strategy to prepare a series of multicolor fluorophores simply by controlling the electronic properties of functional groups. In this chapter, we demonstrate the DCA as an efficient synthetic strategy to give diverse fluorescent molecules in good-to-quantitative yields from a common reagent, tosyl azide (**1**), under a single set of synthetic conditions (Scheme 3.1c). By adjusting the electronic characters of the substituents, it was possible to tune our synthesis to produce a broad range of multicolor fluorescent compounds, emitting light between blue and red, and even emitting white-light.

3.3. Results and Discussion

Scheme 3.2. Scope of Direct C–H Amidation.



Reaction conditions: **1** (0.2 mmol), **2** (0.2 mmol), [IrCp*Cl₂]₂ (2 μmol), AgSbF₆ (8 μmol), AcOH (8 μmol), Li₂CO₃ (8 μmol) in DCE (0.8 mL) at 60 °C for 12 h (isolated yields). ^aThe isolated yield in 1 mmol scale. ^b**1** (0.4 mmol) in DCE (1.6 mL).

To investigate the scope of DCA, we reacted various arenes containing *ortho*-directing groups (**2a–m**) with the common reagent **1** under the optimal conditions determined in our previous studies.^{15,16} High synthetic yields were consistently achieved and were largely unaffected by the position of substituents (*para*-, *meta*-, or *ortho*-) and their electronic variation in benzamides, **2** (Scheme 3.2). First, non-substituted *N*-propylbenzamide (**2a**) was successfully amidated in an excellent yield (95%). Also, amidations of *para*-substituted substrates such as **2b**, containing the electron-donating group (EDG, methoxy), as well as **2c** and **2d** bearing electron-withdrawing groups (trifluoromethyl and nitrile, respectively) proceeded in good-to-quantitative yields (76–99%). Furthermore, **2e** with electron-

withdrawing $-\text{CF}_3$ group at the *meta*-position underwent DCA with reagent **1** in 99% yield, and **2f–2h** with EDGs ($-\text{OMe}$ and amino groups) at *meta*-positions resulted in excellent yields (90–95%). In addition, the reactions of *ortho*-functionalized *N*-propylbenzamides containing $-\text{CF}_3$ group (**2i**) and the methyl group (**2j**) were also obtained in excellent yields (90% and 96%, respectively), regardless of electronic properties. To broaden the substrate scope, we tested DCA of compounds having extended π -systems (**2k** and **2l**) and isolated the desired products in high yields (92% and 88%, respectively). Notably, unlike in the previously reported method,²⁷ which required pre-functionalization of NH_2 at the 10-position of **2l** to synthesize the red-emitting **3l**, this DCA could directly synthesize the same compound in a high yield from commercially available **2l** in a single step similar to other successful DCA using different catalysts.¹⁰ Lastly, the terephthalamide derivative (**2m**) containing two amides selectively underwent the desired bis-amidation in the presence of 2.0 equiv of **1** in a high yield (89%) without additional side reactions that would result in tri- and tetra-amidation products.

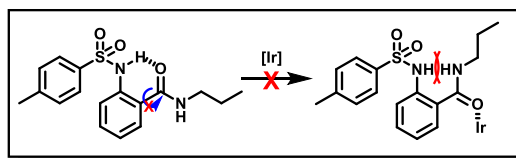


Figure 3.1. Proposed models for suppression of the second amidation.

All reactions proceeded regioselectively at the *ortho*-position to the directing group to exclusively afford the mono-amidation per directing group without bis-amidation, even though benzamide derivatives (**2a–2h**, **2k**, and **2m**) have two chemically equivalent *ortho*-C–H bonds to the directing group. These results suggest that after the first DCA, favorable intramolecular hydrogen bond between the sulfonamide N–H and adjacent carbonyl group would restrict $\text{C}_{\text{aryl}}-\text{C}_{\text{carbonyl}}$ bond rotation, thereby suppressing the second amidation. Moreover, steric repulsions between two N–H of sulfonamide and amide might further hinder the second amidation (Figure 3.1). Furthermore, although compounds **2e–2h**, **2k**, and **2m** (after the first amidation) each possess two non-symmetric *ortho*-C–H bonds, the reactions were again highly regioselective, occurring at the sterically more accessible site.

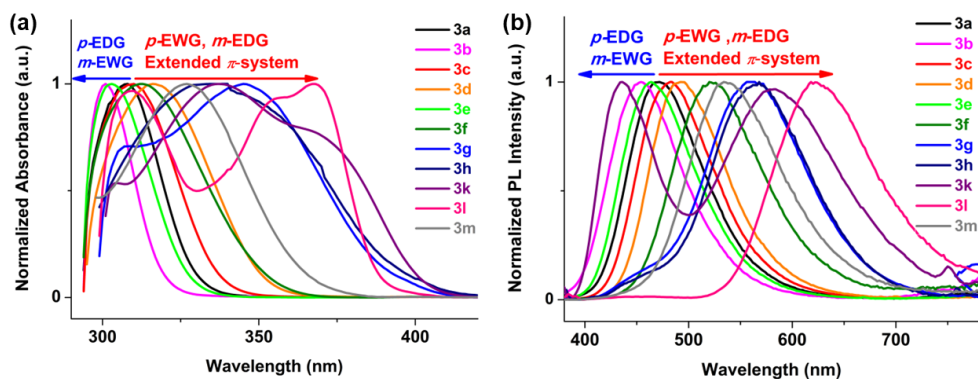


Figure 3.2. (a) Normalized absorption and (b) emission spectra in THF solutions ($10 \mu\text{M}$) at 298 K. The excitation wavelengths were 308, 301, 310, 316, 303, 312, 345, 340, 337, 368, and 327 nm for **3a**, **3b**, **3c**, **3d**, **3e**, **3f**, **3g**, **3h**, **3k**, **3l**, and **3m**, respectively.

Table 3.1. Photophysical Properties of **3a–3m**.

Compound (solvent)	$\lambda_{\text{max, abs}}$ (nm) ^a	$\lambda_{\text{max, em}}$ (nm) ^b	$\phi_{\text{rel, PL}}$ ^c	CIE coordinates (x, y)
3a (THF)	308	472	0.16	0.166, 0.236
3b (THF)	301	454	0.05	0.161, 0.154
3c (THF)	310	484	0.15	0.177, 0.299
3d (THF)	316	492	0.14	0.198, 0.390
3e (THF)	303	464	0.13	0.162, 0.200
3f (THF)	312	520	0.11	0.300, 0.518
3g (THF)	345	562	0.07	0.398, 0.469
3h (THF)	340	568	0.12	0.413, 0.485
3h (MeOH)	340	422, 554	0.04	0.310, 0.348
3i (THF)	294	508	2.4×10^{-3}	0.275, 0.458
3j (THF)	296	480	2.2×10^{-3}	0.204, 0.302
3k (THF)	337	436, 584	1.5×10^{-2}	0.351, 0.321
3l (CHCl ₃)	368	616	2.4×10^{-2}	0.577, 0.413
3l (THF)	368	618	1.4×10^{-2}	0.583, 0.389
3m (THF)	327	534	0.20	0.357, 0.538

^aAbsorption maxima in solutions ($10 \mu\text{M}$) at 298 K. ^bEmission maxima in solutions ($10 \mu\text{M}$) at 298 K. ^cDetermined by using quinine sulfate dihydrate in 0.5 M H₂SO₄ as a fluorescence standard.

After preparing the DCA products (**3a–3m**) with excellent efficiency, we next studied their optical properties in THF solutions (Figure 3.2 and Table 3.1). First, the non-substituted **3a** exhibited blue emission ($\lambda_{\text{max, em}} = 472$ nm) with $\lambda_{\text{max, abs}}$ at 308 nm. When EWGs were attached at the *para*-positions (**3c** and **3d**), red-shifts were observed in both the absorptions ($\lambda_{\text{max, abs}} = 310$ and 316 nm) and the emissions ($\lambda_{\text{max, em}} = 484$ and 492 nm), resulting in bright-blue and cyan fluorescence, respectively. On the other hand, the spectra of compound **3b** bearing an EDG at the *para*-position underwent blue-shifts in both the absorption ($\lambda_{\text{max, abs}} = 301$ nm) and the emission ($\lambda_{\text{max, em}} = 454$ nm) and thus emitted a dark-blue light. In contrast to the trend observed with *para*-substituents, increased electron-withdrawing power at the *meta*-position (**3e**) gave blue-shifted spectra in both absorption ($\lambda_{\text{max, abs}} = 303$ nm) and emission ($\lambda_{\text{max, em}} = 464$ nm) in comparison to the non-substituted **3a**. Similarly, an increase in the electron-donating power (**3f–3h**) led to red-shifts for both the ab absorption ($\lambda_{\text{max, abs}} = 312\text{--}345$ nm) and emission ($\lambda_{\text{max, em}} = 520\text{--}568$ nm), resulting in green-to-yellow emissions. Each corresponding excitation spectrum was almost identical to the absorption spectrum (Figure S3.4). This indicates that the same ground-state species was responsible for the emission excluding any artifact caused by impurity.

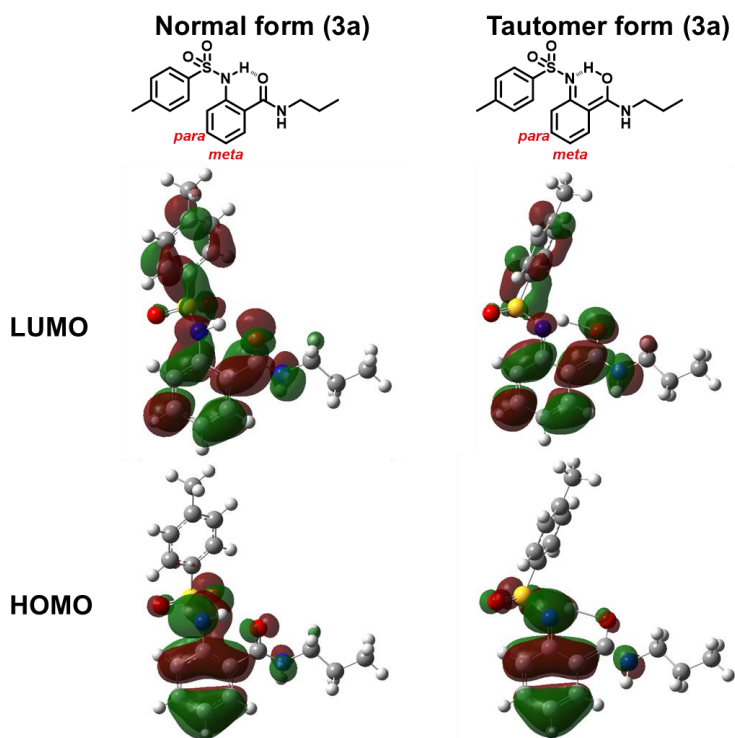


Figure 3.3. Calculated frontier orbitals of normal and tautomer forms of **3a** (by B3LYP/6-31++G(d,p)/IEFPCM).

In cases involving substituents at the *para*-position to the carbonyl group, electronic contributions to lowest unoccupied molecular orbitals (LUMOs) seem to be greater than those to highest occupied molecular orbitals (HOMOs) in both the normal (N) and tautomer (T) forms. This is well-supported by time-dependent density-functional theory (TD-DFT) calculation of **3a**, which show that π -electron densities of the LUMOs at the *para*-position are greater than those of the HOMOs in both the N and T forms (Figure 3.3). Therefore, EWGs would stabilize energy levels of excited-states more than those of ground-states, thereby resulting in red-shifted spectra. In contrast, π -electron densities on the HOMOs at the *meta*-position are more dominant than those on the LUMOs. Thus, EWGs would lower the HOMO levels more than the LUMO levels and increase both energy differences (ΔE_N and ΔE_T), thereby showing blue-shifted spectra. Conversely, the EDGs at *meta*- or *para*-position would show the opposite effect, based on the same logic. This argument was further supported by experimentally measuring HOMO and LUMO levels by cyclic voltammetry and UV-vis spectroscopy, as well as TD-DFT calculation ($S_0 \rightarrow S_1$ transition, see Figure S3.1).

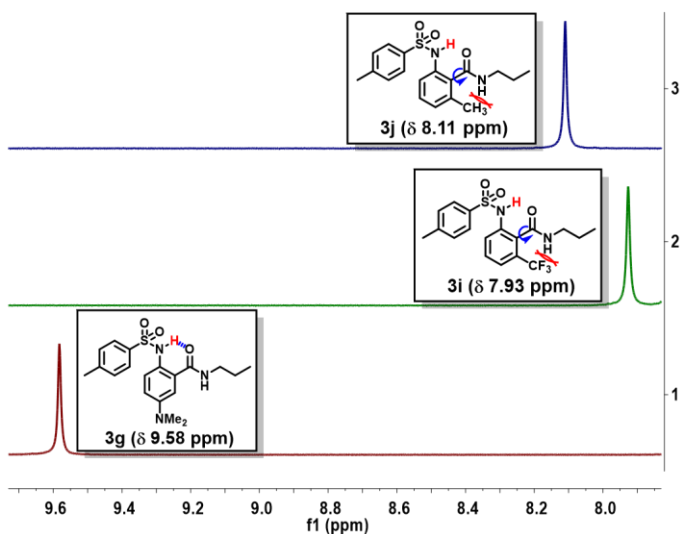


Figure 3.4. ^1H NMR spectra of the N–H protons of **3g**, **3i**, and **3j**.

Interestingly, *ortho*-substituted products (**3i** and **3j**) showed negligible fluorescence regardless of the electronic nature of the substituents (Table 3.1 and Figure S3.3). In CD_2Cl_2 , the chemical shifts of their N–H protons appeared at relatively upfield region (δ 7.93 and δ 8.11 ppm, respectively), whereas those of compounds **3a–3k** appeared at downfield region (δ 9.58–11.49 ppm), because of the formation of strong intramolecular hydrogen bonds (Figure 3.4). Based on these observations, we concluded that steric repulsion between the amide group and the *ortho*-substituents in **3i** and **3j** prevented the formation of intramolecular hydrogen bonding, thereby inhibiting the ESIPT process.

A fluorophore containing the extended π -system, **3k**, showed a more red-shifted absorption spectrum ($\lambda_{\text{max, abs}} = 337$ nm) than that of **3a**. Interestingly, the purplish-pink fluorescence was characterized by dual emission ($\lambda_{\text{max, em}} = 436$ and 584 nm) that likely resulted from thermal equilibrium between the excited-states of the normal (N^*) and the tautomer (T^*) forms (Figure 3.2b and Table 3.1, as well as Figure 3.5c,d). Upon monitoring at the respective photoluminescence (PL) bands, the excitation spectra were identical each other, and also similar to the absorption spectrum, suggesting that dual emission originated from the identical excited species (Figure S3.5a).^{36,37} The absorption and emission spectra of another example of the extended π -system, **3l**, underwent even greater red-shifts ($\lambda_{\text{max, abs}} = 368$ nm and $\lambda_{\text{max, em}} = 618$ nm, corresponding to red-emission). In the case of the bis-amidated **3m** containing two directing groups, the second directing group acts as EWG at *para*-position, and the second sulfonamide group acts as EDG at *meta*-position. Thus, due to the synergistic effect of two substituents, red-shifted emission ($\lambda_{\text{max, em}} = 534$ nm) occurred, resulting in a yellowish-green color.

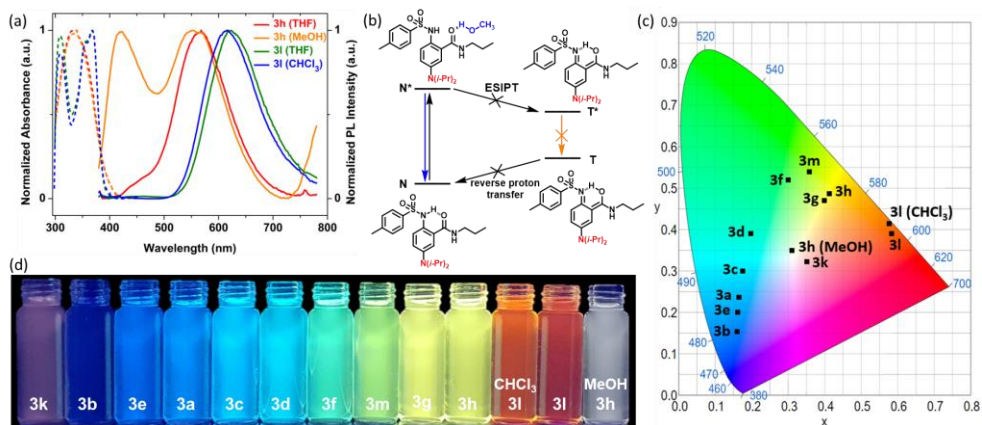


Figure 3.5. (a) Normalized absorption (dashed lines) and emission spectra (solid lines) of **3h** ($\lambda_{\text{ex}} = 340$ nm) and **3l** ($\lambda_{\text{ex}} = 368$ nm) in solutions ($10 \mu\text{M}$) at 298 K. (b) Proposed mechanism for the white-light emission of **3h** in methanol; White-light emission appears in MeOH because ES IPT is partially quenched by intermolecular hydrogen bond with protic solvent. (c) Emission color coordinates of **3a–3h** and **3k–3m** in solutions in the CIE 1931 chromaticity diagram. (d) The photo of **3a–3h** and **3k–3m** in solutions under 365 nm UV irradiation.

During the investigation on the effect of various solvents on the ES IPT process, we observed some notable solvatochromisms (see Table 3.1, as well as Figure 3.5a and 3.5d). For example, in less-polar chloroform, **3l** produced an orange-emission with chromaticity coordinates of (0.58, 0.43) via positive solvatochromism. Interestingly, when compound **3h** was dissolved in methanol (MeOH), white-light emission occurred with chromaticity coordinates of (0.31, 0.35) resulting from simultaneous emissions of the N^* form at 422 nm and the T^* form at 554 nm. This dual emission is rationalized by the partial ES IPT quenching through hydrogen bonding between the protic solvent, MeOH, and the ES IPT molecule (Figure 3.5b).^{32–34} In other words, some molecules of **3h** emitted light at the longer wavelength (554 nm), as a result of the ES IPT process, while other molecules underwent intermolecular hydrogen bonding with MeOH to emit the shorter wavelength light (442 nm). This rationale is supported by a series of experiments involving the comparison of fluorescence in various solvents with varying degree of hydrogen bond donors as well as excitation spectra monitored at the respective PL bands (see Figures S3.5b and S3.6 for details). These results clearly indicate that this DCA is an efficient and modular synthetic method synthesizing numerous ES IPT molecules capable of emitting a broad range of colors in the visible-light spectrum, even including white-light.

3.4. Conclusion

In conclusion of chapter 3, this Ir-catalyzed DCA has proved to be a very efficient method to prepare multicolor fluorophores (up to 99% of yields) regardless of the positions of substituents and their electronic characters under uniform and mild conditions. Since the reaction efficiency is not influenced by the electronic nature of the functional groups, the energy levels of HOMOs and LUMOs can be readily controlled. As a result, we were able to produce a broad range of multicolor fluorescent compounds capable of emitting light between blue and red, even including white-light using only a single synthetic strategy and a common coupling reagent. We are currently studying white-light emission by other polymeric materials.

3.5. Experimental Section

Materials

All reagents which are commercially available were used without further purification. Solvents for starting materials synthesis were also commercially obtained. For the Ir-catalyzed C–H amidation of arenes, all solvents and reagents were degassed via three freeze-pump-thaw cycles before the use. Thin-layer chromatography (TLC) was carried out on MERCK TLC silica gel 60 F₂₅₄ and flash column chromatography was performed using MERCK silica gel 60 (0.040–0.063 mm).

Characterization

¹H NMR and ¹³C NMR spectroscopies were recorded by Varian/Oxford As-500 (500 MHz for ¹H NMR and 125 MHz for ¹³C NMR) and Agilent 400-MR (100 MHz for ¹³C NMR) spectrometers. *High resolution mass spectroscopy (HRMS)* analyses were performed by the ultrahigh resolution ESI Q-TOF mass spectrometer (Bruker, Germany) in the Sogang Centre for Research Facilities. *UV-vis spectra* were recorded on V-650 spectrometer with Jasco Inc. software. *Fluorescence spectra* were recorded on a Photon Technology International (PTI) QM-400 spectrofluorometer with FelixGX software. Solution quantum yields were determined by standard methods, using quinine sulfate dihydrate in 0.5 M H₂SO₄ as fluorescence standard. The sample absorbance was maintained <0.1 to minimize internal absorption. Corrections were made to account for the differences in solvent refractive indexes. *Cyclic voltammetry (CV)* measurement was carried out on a CHI 660 Electrochemical Analyzer (CH Instruments, Inc., Texas, US) at RT using a degassed ACN solution of tetrabutylammonium hexafluorophosphate (Bu₄NPF₆, 0.1 M). The CV was recorded using a glassy carbon working electrode, a reference electrode of Ag/Ag⁺ (0.1 M AgNO₃ in acetonitrile) with a platinum wired counter electrode at a scan rate of 100 mV/s.

Computational Methodology

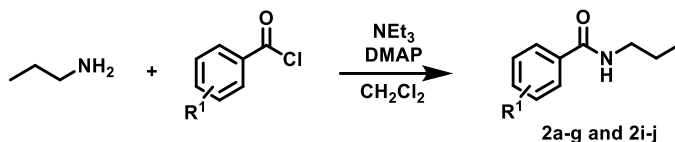
All the theoretical calculations were performed with the Gaussian 09 program.³⁵ The geometries of the singlet ground states of normal and tautomer forms were optimized by the density functional theory (DFT) method with B3LYP hybrid function in combination with integral equation formalism of the polarizable continuum model (IEFPCM) in THF. For the first singlet excited states, we calculated Frank–Condon states with time-dependent density functional theory (TD-DFT) methodology with the B3LYP hybrid function. The 6-31++G(d,p) basis sets were employed for all atoms. Vibrational frequencies were calculated with the optimized geometries at the same level of theory optimizations. All compounds were calculated by observing almost no imaginary frequency.

Procedures for the Preparation of Starting Materials

Preparation of *p*-Toluenesulfonyl azide (1)

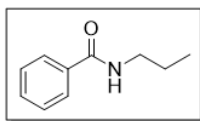
1 was prepared according to the previously reported synthetic method.³⁶

General Procedure for the Preparation of *N*-Propylbenzamides (2a–g and 2i–j)



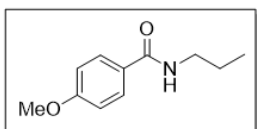
Benzamides (**2a–g**, **2i** and **j**) were prepared by the slightly modified procedure from the previous literature.³⁷ To a solution of corresponding benzoyl chloride (5.0 mmol) and 4-dimethylaminopyridine (0.06 g, 0.5 mmol) in dichloromethane (20 mL) were added dropwise *n*-propylamine (0.49 mL, 6.0 mmol) and triethylamine (1.06 mL, 7.5 mmol) at 0 °C under Ar atmosphere. After stirring for 2 h at room temperature, the reaction mixture was quenched with 1N HCl (10 mL), extracted with CH₂Cl₂ three times, dried over MgSO₄, and evaporated under reduced pressure to afford crude product, which was purified by column chromatography on silica gel (*n*-hexane/EtOAc) to obtain the desired product.

N-propylbenzamide (**2a**)



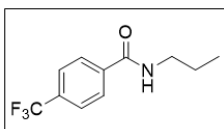
White solid (810 mg, 99%), purified by column chromatography on silica gel (*n*-hexane/EtOAc = 2/1, *R_f* = 0.3); The structure of **2a** was confirmed by comparison of its spectroscopic data with reported data.³⁸

4-Methoxy-*N*-propylbenzamide (**2b**)



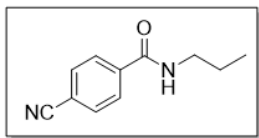
White solid (966 mg, 99%), purified by column chromatography on silica gel (*n*-hexane/EtOAc = 2/1, *R_f* = 0.3); The structure of **2b** was confirmed by comparison of its spectroscopic data with reported data.⁴⁴

N-Propyl-4-(trifluoromethyl)benzamide (**2c**)



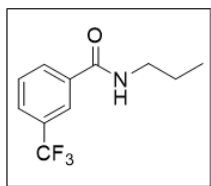
White solid (1146 mg, 99%), purified by column chromatography on silica gel (*n*-hexane/EtOAc = 3/1 *R_f* = 0.3); ¹H NMR (500 MHz, CDCl₃) δ 7.86 (d, *J* = 8.1 Hz, 2H), 7.68 (d, *J* = 8.1 Hz, 2H), 6.27 (s, 1H), 3.43 (dd, *J* = 13.5, 6.7 Hz, 2H), 1.71–1.60 (m, *J* = 14.7, 7.4 Hz, 2H), 0.99 (t, *J* = 7.4 Hz, 3H). ¹³C NMR (125 MHz, CDCl₃) δ 166.7, 138.3, 133.4, 133.1, 132.9, 132.6, 127.5, 127.0, 125.4, 125.4, 125.3, 124.8, 122.7, 120.5, 42.1, 22.8, 11.3. HRMS (ESI) *m/z*: [M + Na]⁺ Calcd for C₁₁H₁₂F₃NONa 254.0763; Found 254.0765.

4-Cyano-*N*-propylbenzamide (2d)



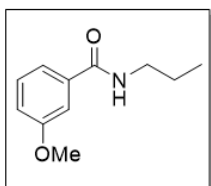
White solid (904 mg, 96%), purified by column chromatography on silica gel (*n*-hexane/EtOAc = 2/1, R_f = 0.2); The structure of **2d** was confirmed by comparison of its spectroscopic data with reported data.³⁸

N-Propyl-3-(trifluoromethyl)benzamide (2e)



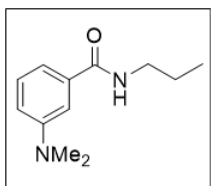
White solid (1145 mg, 99%), purified by column chromatography on silica gel (*n*-hexane/EtOAc = 3/1, R_f = 0.3); **¹H NMR** (500 MHz, CDCl₃) δ 8.01 (s, 1H), 7.95 (d, J = 7.8 Hz, 1H), 7.74 (d, J = 7.8 Hz, 1H), 7.56 (t, J = 7.8 Hz, 1H), 6.30 (s, 1H), 3.43 (dd, J = 13.7, 6.6 Hz, 2H), 1.71–1.60 (m, 2H), 0.99 (t, J = 7.4 Hz, 3H). **¹³C NMR** (125 MHz, CDCl₃) δ 166.5, 135.8, 131.4, 131.1, 130.9, 130.6, 130.3, 129.0, 127.8, 127.8, 127.7, 127.7, 127.1, 124.9, 124.2, 124.1, 122.8, 120.6, 42.1, 22.8, 11.3. **HRMS (ESI)** m/z : [M + Na]⁺ Calcd for C₁₁H₁₂F₃NONa 254.0763; Found 254.0765.

3-Methoxy-*N*-propylbenzamide (2f)



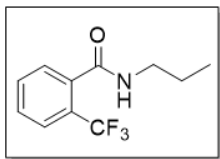
White solid (1055 mg, 99%), purified by column chromatography on silica gel (*n*-hexane/EtOAc = 2/1, R_f = 0.3); **¹H NMR** (500 MHz, CD₂Cl₂) δ 7.36–7.21 (m, 3H), 7.03–6.98 (m, 1H), 6.33 (s, 1H), 3.80 (s, 3H), 3.34 (dd, J = 13.6, 6.5 Hz, 2H), 1.64–1.54 (m, 2H), 0.94 (t, J = 7.4 Hz, 3H). **¹³C NMR** (125 MHz, CDCl₃) δ 167.5, 159.7, 136.3, 129.3, 118.8, 117.2, 112.4, 55.2, 55.2, 41.8, 22.8, 11.3. **HRMS (ESI)** m/z : [M + Na]⁺ Calcd for C₁₁H₁₅NO₂Na 216.0995; Found 216.0995.

3-(Dimethylamino)-*N*-propylbenzamide (2g)



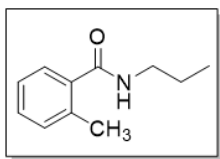
White solid (784 mg, 76%), purified by column chromatography on silica gel (*n*-hexane/EtOAc = 1/1, R_f = 0.4); **¹H NMR** (500 MHz, CD₂Cl₂) δ 7.22 (t, J = 7.9 Hz, 1H), 7.14 (d, J = 0.8 Hz, 1H), 6.99 (d, J = 7.5 Hz, 1H), 6.80 (dd, J = 8.3, 2.4 Hz, 1H), 6.54 (s, 1H), 3.33 (dd, J = 13.5, 6.7 Hz, 2H), 2.94 (s, 6H), 1.64–1.54 (m, 2H), 0.94 (t, J = 7.4 Hz, 3H). **¹³C NMR** (125 MHz, CDCl₃) δ 168.3, 150.6, 135.7, 128.9, 114.9, 114.1, 111.3, 41.7, 40.3, 22.8, 11.3. **HRMS (ESI)** m/z : [M + Na]⁺ Calcd for C₁₂H₁₈N₂ONa 229.1311; Found 229.1313.

***N*-Propyl-2-(trifluoromethyl)benzamide (2i)**



White solid (1133 mg, 98%), purified by column chromatography on silica gel (*n*-hexane/EtOAc = 2/1, R_f = 0.25); $^1\text{H NMR}$ (500 MHz, CDCl_3) δ 7.66 (d, J = 7.8 Hz, 1H), 7.57–7.45 (m, 3H), 5.96 (s, 1H), 3.36 (dd, J = 13.6, 6.6 Hz, 2H), 1.64–1.54 (m, 2H), 0.95 (t, J = 7.4 Hz, 3H). $^{13}\text{C NMR}$ (125 MHz, cdcl_3) δ 167.9, 136.3, 131.9, 129.5, 128.5, 127.5, 127.2, 127.0, 126.9, 126.7, 126.3, 126.2, 126.2, 126.1, 124.8, 122.6, 120.4, 41.8, 22.5, 11.2. **HRMS (ESI)** m/z : $[\text{M} + \text{Na}]^+$ Calcd for $\text{C}_{11}\text{H}_{12}\text{F}_3\text{NONa}$ 254.0763; Found 254.0764.

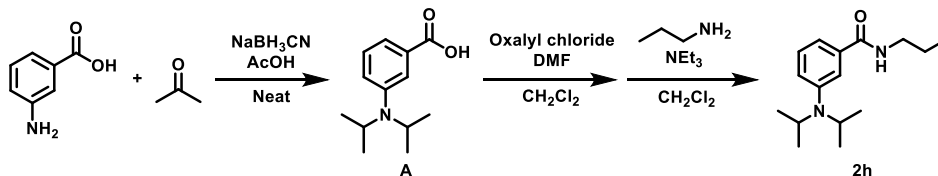
2-Methyl-*N*-propylbenzamide (2j)



White solid (877 mg, 99%), purified by column chromatography on silica gel (*n*-hexane/EtOAc = 2/1, R_f = 0.3); $^1\text{H NMR}$ (500 MHz, CDCl_3) δ 7.37–7.27 (m, 2H), 7.24–7.15 (m, 2H), 5.78 (s, 1H), 3.40 (dd, J = 13.4, 6.7 Hz, 2H), 2.44 (s, 3H), 1.67–1.57 (m, 2H), 0.99 (t, J = 7.4 Hz, 3H). $^{13}\text{C NMR}$ (125 MHz, cdcl_3) δ 170.1, 136.8, 135.7, 130.7, 129.4, 126.6, 125.5, 41.4, 22.8, 19.6, 11.3. **HRMS (ESI)** m/z : $[\text{M} + \text{Na}]^+$ Calcd for $\text{C}_{11}\text{H}_{15}\text{NONa}$ 200.1046; Found 200.1044.

Additional *N*-Propylbenzamide derivatives (2h, 2k and 2m)

***N*-propyl-3-(diisopropylamino)benzamide (2h)**

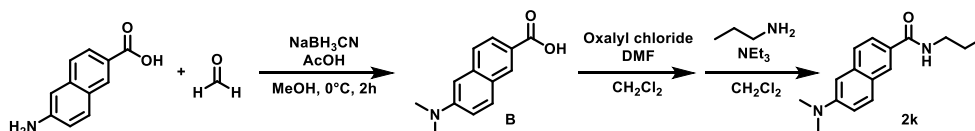


To a solution of 3-aminobenzoic acid (1.40 g, 10 mmol) in glacial acetic acid (53 mL) were added acetone (7.4 mL, 100 mmol) and sodium cyanoborohydride (3.11 g, 47 mmol) at 0 °C. After stirring at 0 °C until the bubbling disappeared, the resulting solution was stirred at room temperature overnight. The suspension was filtered and the glacial acetic acid of filtrate was removed under reduced pressure. The crude mixture of **A** was used for the next step without further purification.

2h was prepared by the slightly modified procedure from the previous literature.³⁹ To a solution of the crude mixture of **A** in CH_2Cl_2 (20 mL) was added oxalyl chloride (0.98 mL, 11 mmol) and catalytic amount of DMF (1–2 drops) under Ar atmosphere. Stirring was continued till the solid disappeared at room temperature. The volatile was removed under reduced pressure. Then CH_2Cl_2 (20 mL) was added followed by addition of 4-

dimethylaminopyridine (0.12 g, 1 mmol), *n*-propylamine (0.99 mL, 12 mmol) and triethylamine (2.11 mL, 15 mmol) at 0 °C under Ar atmosphere. After being stirred at room temperature for 2 h, the reaction mixture was quenched with 1N HCl (10 mL), extracted with CH₂Cl₂ three times, dried over MgSO₄, and evaporated under reduced pressure to afford crude product, which was further purified by flash column chromatography on silica gel (*n*-hexane/EtOAc = 3/1, R_f=0.3) to afford **2h** as white solid (1.99 g, 7.58 mmol, Overall yield: 76%); ¹H NMR (500 MHz, CDCl₃) δ 7.34 (s, 1H), 7.19 (t, *J* = 7.9 Hz, 1H), 7.00–6.94 (m, 2H), 6.11 (s, 1H), 3.88–3.78 (m, 2H), 3.40 (dd, *J* = 13.4, 6.7 Hz, 2H), 1.67–1.58 (m, 2H), 1.24 (d, *J* = 6.8 Hz, 12H), 0.98 (t, *J* = 7.4 Hz, 3H). ¹³C NMR (125 MHz, CDCl₃) δ 168.3, 148.4, 135.3, 128.3, 120.9, 117.0, 115.1, 47.5, 41.7, 22.9, 21.3, 11.4. HRMS (ESI) *m/z*: [M + H]⁺ Calcd for C₁₆H₂₇N₂O 263.2118; Found 263.2120.

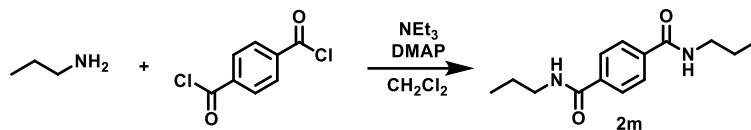
6-(Dimethylamino)-*N*-propyl-2-naphthamide (**2k**)



B was prepared according to the previously reported synthetic method.⁴⁰ White solid (1.89 g, 8.8 mmol, 88%); The structure of **B** was confirmed by comparison of its spectroscopic data with reported data.⁴¹

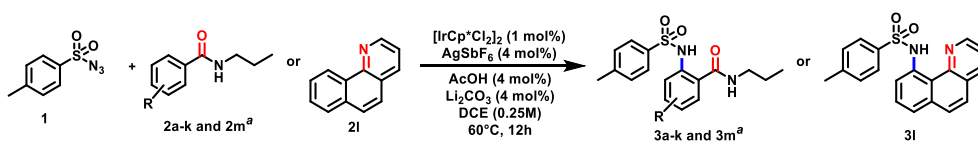
2k was prepared by the slightly modified procedure from the previous literature.³⁹ To a solution of **B** (1.89 g, 8.8 mmol) in CH₂Cl₂ (18 mL) was added oxalyl chloride (0.86 mL, 9.7 mmol) and catalytic amount of DMF (1–2 drops) under Ar atmosphere. Stirring was continued till the solid disappeared at room temperature. The volatile was removed under reduced pressure. Then CH₂Cl₂ (18 mL) was added followed by addition of 4-dimethylaminopyridine (0.11 g, 0.88 mmol), *n*-propylamine (0.87 mL, 10.6 mmol) and triethylamine (1.86 mL, 13.2 mmol) at 0 °C under Ar atmosphere. After being stirred at room temperature for 2 h, the reaction mixture was quenched with 1N HCl (9 mL), extracted with CH₂Cl₂ three times, dried over MgSO₄, and evaporated under reduced pressure to afford crude product, which was further purified by flash column chromatography on silica gel (*n*-hexane/EtOAc = 2/1, R_f = 0.2) to afford **2k** as white solid (1.76 g, 6.86 mmol, 78%); ¹H NMR (500 MHz, CDCl₃) δ 8.16 (s, 1H), 7.74 (dd, *J* = 8.6, 1.6 Hz, 1H), 7.68 (d, *J* = 9.1 Hz, 1H), 7.60 (d, *J* = 8.6 Hz, 1H), 7.10 (dd, *J* = 9.1, 2.3 Hz, 1H), 6.84 (d, *J* = 1.8 Hz, 1H), 6.59 (s, 1H), 3.42 (dd, *J* = 13.6, 6.6 Hz, 2H), 3.03 (s, 6H), 1.69–1.59 (m, 2H), 0.97 (t, *J* = 7.4 Hz, 3H). ¹³C NMR (125 MHz, CDCl₃) δ 167.9, 149.6, 136.6, 129.9, 127.9, 127.2, 126.2, 125.6, 124.1, 116.5, 105.5, 41.8, 40.5, 23.1, 11.5. HRMS (ESI) *m/z*: [M + H]⁺ Calcd for C₁₆H₂₁N₂O 257.1648; Found 257.1649.

N,N'-dipropylterephthalamide (**2m**)



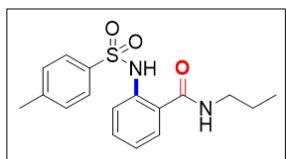
2m was prepared by the slightly modified procedure from the previous literature.³⁷ To a solution of terephthaloyl chloride (1.02 g, 5.0 mmol) and 4-dimethylaminopyridine (0.12 g, 1.0 mmol) in dichloromethane (20 mL) were added dropwise *n*-propylamine (0.98 mL, 12.0 mmol) and triethylamine (2.12 mL, 15.0 mmol) at 0 °C under Ar atmosphere. After stirring for 2 h at room temperature, the reaction mixture was quenched with 1N HCl (10 mL), extracted with CH₂Cl₂ three times, dried over MgSO₄, and evaporated under reduced pressure to afford crude product, which was further purified by recrystallization (methanol/CH₂Cl₂) to afford **2m** as white solid (0.63 g, 2.55 mmol, 51%); The structure of **2b** was confirmed by comparison of its spectroscopic data with reported data.⁴²

General Procedure for the Ir-Catalyzed C–H Amidation of Arenes



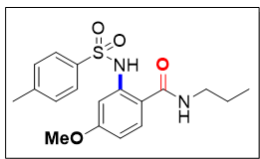
A 4 mL sized screw-cap vial with septum and a magnetic bar were dried in oven for 1 h. *p*-Toluenesulfonyl azide (**1**, 39.44 mg, 0.2 mmol), arene (**2**, 0.2 mmol, 1.0 equiv), [IrCp*Cl₂]₂ (1.59 mg, 2 μmol, 1 mol%), AgSbF₆ (2.80 mg, 8 μmol, 4 mol%), Li₂CO₃ (0.59 mg, 8 μmol, 4 mol%), AcOH (8 μmol, 4 mol%), degassed anhydrous 1,2-dichloroethane (0.8 mL, 0.25 M) were added under argon atmosphere. The reaction mixture was stirred at 60 °C using pie-block for 12 h, filtered through a pad of celite, and then washed with CH₂Cl₂. The solvents were evaporated under reduced pressure and the residue was purified by flash column chromatography on silica gel (*n*-hexane/EtOAc) to afford the desired product (**3**).

2-((4-methylphenyl)sulfonamido)-*N*-propylbenzamide (**3a**)



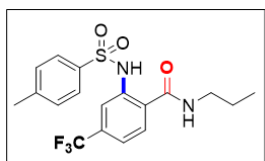
White solid (63.16 mg, 95%), purified by column chromatography on silica gel (*n*-hexane/EtOAc = 3/1, R_f = 0.2); The structure of **3a** was confirmed by comparison of its spectroscopic data with reported data.¹¹

4-Methoxy-2-((4-methylphenyl)sulfonamido)-*N*-propylbenzamide (3b)



White solid (66.69 mg, 92%), purified by column chromatography on silica gel (*n*-hexane/EtOAc = 2/1, R_f = 0.35); $^1\text{H NMR}$ (500 MHz, CD_2Cl_2) δ 11.49 (s, 1H), 7.65 (d, J = 8.2 Hz, 2H), 7.30 (d, J = 8.7 Hz, 1H), 7.20 (d, J = 8.1 Hz, 2H), 7.15 (d, J = 2.4 Hz, 1H), 6.52 (dd, J = 8.8, 2.5 Hz, 1H), 6.13 (s, 1H), 3.77 (s, 3H), 3.26 (dd, J = 13.4, 6.8 Hz, 2H), 2.33 (s, 3H), 1.58–1.49 (m, 2H), 0.91 (t, J = 7.4 Hz, 3H). $^{13}\text{C NMR}$ (125 MHz, CDCl_3) δ 168.4, 162.6, 143.7, 141.1, 136.6, 129.6, 128.5, 127.1, 113.3, 109.3, 105.4, 55.4, 41.6, 22.7, 21.4, 11.4. **HRMS (ESI)** m/z : $[\text{M} + \text{Na}]^+$ Calcd for $\text{C}_{18}\text{H}_{22}\text{N}_2\text{O}_4\text{SNa}$ 385.1192; Found 385.1194.

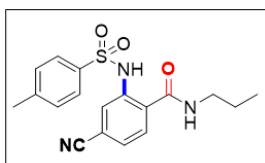
2-((4-Methylphenyl)sulfonamido)-*N*-propyl-4-(trifluoromethyl)benzamide (3c)



White solid (79.28 mg, 99%), purified by column chromatography on silica gel (*n*-hexane/EtOAc = 3/1, R_f = 0.2); $^1\text{H NMR}$ (500 MHz, CD_2Cl_2) δ 10.98 (s, 1H), 7.91 (s, 1H), 7.62 (d, J = 8.3 Hz, 2H), 7.52 (d, J = 8.2 Hz, 1H), 7.27 (d, J = 8.1 Hz, 1H), 7.21 (d, J = 8.1 Hz, 2H), 6.38 (s, 1H), 3.28 (dd, J = 13.6, 6.6 Hz, 2H), 2.33 (s, 3H), 1.59–1.50 (m, 2H), 0.92 (t, J = 7.4 Hz, 3H). $^{13}\text{C NMR}$ (125 MHz, CDCl_3) δ 167.4, 144.3, 139.5, 136.2, 134.5, 134.2, 134.0, 133.7, 129.8, 127.7, 127.3, 126.5, 124.3, 124.1, 122.1, 120.0, 119.9, 119.9, 119.9, 117.6, 42.0, 22.6, 21.6, 11.4. **HRMS (ESI)** m/z : $[\text{M} + \text{Na}]^+$ Calcd for $\text{C}_{18}\text{H}_{19}\text{F}_3\text{N}_2\text{O}_3\text{SNa}$ 423.0961; Found 423.0961.

Scale-up (1 mmol) C–H Amidation of *N*-Propyl-4-(trifluoromethyl)benzamide (2c): A 20 mL sized screw-cap vial with septum and a magnetic bar were dried in oven for 1 h. *p*-Toluenesulfonyl azide (**1**, 197.21 mg, 1 mmol), **2c** (231.21 mg, 1 mmol, 1.0 equiv), $[\text{IrCp}^*\text{Cl}_2]_2$ (7.97 mg, 10 μmol , 1 mol%), AgSbF_6 (13.88 mg, 40 μmol , 4 mol%), Li_2CO_3 (2.96 mg, 40 μmol , 4 mol%), AcOH (40 μmol , 4 mol%), degassed anhydrous 1,2-dichloroethane (4 mL, 0.25 M) were added under argon atmosphere. The reaction mixture was stirred at 60 °C using pie-block for 12 h, filtered through a pad of celite, and then washed with CH_2Cl_2 . The solvents were evaporated under reduced pressure and the residue was purified by flash column chromatography on silica gel (*n*-hexane/EtOAc) to afford the desired product (**3c**) as white solid (0.37 g, 0.93 mmol, 93%).

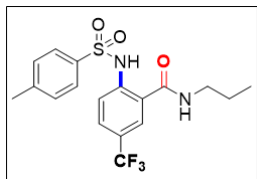
4-Cyano-2-((4-methylphenyl)sulfonamido)-*N*-propylbenzamide (3d)



White solid (54.33 mg, 76%), purified by column chromatography on silica gel (*n*-hexane/EtOAc = 2/1, R_f = 0.15); $^1\text{H NMR}$ (500 MHz, CD_2Cl_2) δ 10.85 (s, 1H), 7.94 (s, 1H), 7.65 (d, J = 8.2 Hz, 2H), 7.44 (d, J = 8.1 Hz, 1H), 7.32 (d,

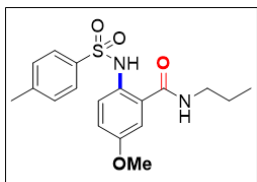
$J = 8.1$ Hz, 1H), 7.24 (d, $J = 8.1$ Hz, 2H), 6.16 (s, 1H), 3.28 (dd, $J = 13.5, 6.7$ Hz, 2H), 2.35 (s, 3H), 1.59–1.50 (m, 2H), 0.92 (t, $J = 7.4$ Hz, 3H). ^{13}C NMR (125 MHz, CDCl_3) δ 167.0, 144.5, 139.7, 130.0, 127.7, 127.3, 126.4, 124.7, 123.6, 117.5, 116.0, 42.1, 22.6, 21.7, 11.5. **HRMS (ESI)** m/z : $[\text{M} + \text{Na}]^+$ Calcd for $\text{C}_{18}\text{H}_{19}\text{N}_3\text{O}_3\text{SNa}$ 380.1039; Found 380.1041.

2-((4-Methylphenyl)sulfonamido)-*N*-propyl-5-(trifluoromethyl)benzamide (3e)



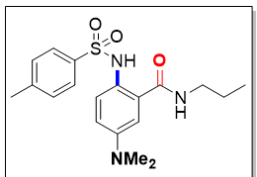
White solid (79.28 mg, 99%), purified by column chromatography on silica gel (*n*-hexane/EtOAc = 4/1, $R_f = 0.3$); ^1H NMR (500 MHz, CD_2Cl_2) δ 11.19 (s, 1H), 7.76 (d, $J = 9.2$ Hz, 1H), 7.69 (d, $J = 7.7$ Hz, 2H), 7.64–7.58 (m, 2H), 7.24 (d, $J = 7.9$ Hz, 2H), 6.23 (s, 1H), 3.32 (dd, $J = 13.3, 6.3$ Hz, 2H), 2.35 (s, 3H), 1.63–1.53 (m, 2H), 0.94 (t, $J = 7.4$ Hz, 3H). ^{13}C NMR (125 MHz, CDCl_3) δ 167.5, 144.3, 142.2, 136.5, 129.9, 129.3, 129.3, 129.2, 129.2, 127.3, 126.9, 125.3, 125.1, 124.8, 124.7, 124.5, 124.2, 124.2, 124.1, 124.1, 122.6, 121.6, 120.7, 120.0, 42.0, 22.7, 21.6, 11.5. **HRMS (ESI)** m/z : $[\text{M} + \text{Na}]^+$ Calcd for $\text{C}_{18}\text{H}_{19}\text{F}_3\text{N}_2\text{O}_3\text{SNa}$ 423.0961; Found 423.0963.

5-Methoxy-2-((4-methylphenyl)sulfonamido)-*N*-propylbenzamide (3f)



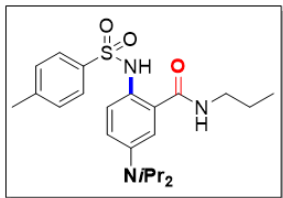
White solid (65.24 mg, 90%), purified by column chromatography on silica gel (*n*-hexane/EtOAc = 2/1, $R_f = 0.25$); ^1H NMR (500 MHz, CD_2Cl_2) δ 9.97 (s, 1H), 7.59 (d, $J = 9.0$ Hz, 1H), 7.49 (d, $J = 8.2$ Hz, 2H), 7.16 (d, $J = 8.0$ Hz, 2H), 6.97 (dd, $J = 9.0, 2.8$ Hz, 1H), 6.79 (d, $J = 2.8$ Hz, 1H), 5.84 (s, 1H), 3.75 (s, 3H), 3.15 (dd, $J = 13.5, 6.7$ Hz, 2H), 2.32 (s, 3H), 1.51–1.42 (m, 2H), 0.89 (t, $J = 7.4$ Hz, 3H). ^{13}C NMR (100 MHz, CDCl_3) δ 167.9, 156.4, 13.4, 136.3, 130.8, 129.4, 127.3, 125.4, 125.4, 117.1, 112.5, 55.7, 55.7, 41.8, 22.6, 21.6, 11.5. **HRMS (ESI)** m/z : $[\text{M} + \text{Na}]^+$ Calcd for $\text{C}_{18}\text{H}_{22}\text{N}_2\text{O}_4\text{SNa}$ 385.1192; Found 385.1194.

5-(Dimethylamino)-2-((4-methylphenyl)sulfonamido)-*N*-propylbenzamide (3g)



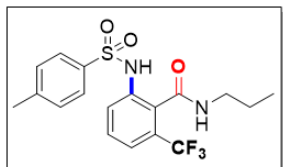
White solid (71.34 mg, 95%), purified by column chromatography on silica gel (*n*-hexane/EtOAc = 1/1, $R_f = 0.3$); ^1H NMR (500 MHz, CD_2Cl_2) δ 9.58 (s, 1H), 7.48 (d, $J = 9.5$ Hz, 2H), 7.45 (s, 1H), 7.15 (d, $J = 8.0$ Hz, 2H), 6.78 (dd, $J = 9.0, 2.9$ Hz, 1H), 6.50 (d, $J = 2.8$ Hz, 1H), 5.80 (s, 1H), 3.11 (dd, $J = 13.7, 6.6$ Hz, 2H), 2.89 (s, 6H), 2.33 (s, 3H), 1.50–1.40 (m, 2H), 0.89 (t, $J = 7.4$ Hz, 3H). ^{13}C NMR (100 MHz, CDCl_3) δ 168.7, 147.9, 143.2, 136.4, 129.3, 127.3, 126.5, 126.2, 126.1, 115.8, 109.6, 41.7, 40.6, 22.6, 21.5, 11.5. **HRMS (ESI)** m/z : $[\text{M} + \text{H}]^+$ Calcd for $\text{C}_{19}\text{H}_{26}\text{N}_3\text{O}_3\text{S}$ 376.1689; Found 376.1689.

5-(Diisopropylamino)-2-((4-methylphenyl)sulfonamido)-*N*-propylbenzamide (3h)



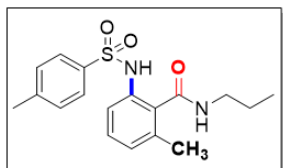
White solid (77.69 mg, 90%), purified by column chromatography on silica gel (*n*-hexane/EtOAc = 2/1, R_f = 0.35); $^1\text{H NMR}$ (500 MHz, CD_2Cl_2) δ 9.76 (s, 1H), 7.50 (d, J = 8.0 Hz, 2H), 7.43 (d, J = 9.0 Hz, 1H), 7.16 (d, J = 8.0 Hz, 2H), 6.96 (d, J = 9.0 Hz, 1H), 6.70 (s, 1H), 5.74 (s, 1H), 3.73–3.62 (m, 2H), 3.13 (dd, J = 13.4, 6.6 Hz, 2H), 2.33 (s, 3H), 1.51–1.42 (m, 2H), 1.13 (d, J = 6.7 Hz, 12H), 0.89 (t, J = 7.4 Hz, 3H). $^{13}\text{C NMR}$ (100 MHz, CDCl_3) δ 168.7, 145.1, 143.2, 136.7, 129.3, 128.9, 127.4, 125.2, 124.6, 123.8, 117.8, 48.0, 41.7, 22.7, 21.6, 21.4, 11.5. **HRMS (ESI)** m/z : $[\text{M} + \text{H}]^+$ Calcd for $\text{C}_{23}\text{H}_{34}\text{N}_3\text{O}_3\text{S}$ 432.2315; Found 432.2317.

2-((4-Methylphenyl)sulfonamido)-*N*-propyl-6-(trifluoromethyl)benzamide (3i)



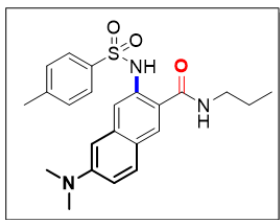
White solid (72.08 mg, 90%), purified by column chromatography on silica gel (*n*-hexane/EtOAc = 3/1, R_f = 0.25); $^1\text{H NMR}$ (500 MHz, CD_2Cl_2) δ 7.93 (s, 1H), 7.81 (d, J = 7.9 Hz, 1H), 7.59 (d, J = 8.3 Hz, 2H), 7.51–7.42 (m, 2H), 7.25 (d, J = 8.3 Hz, 2H), 5.48 (s, 1H), 3.13 (dd, J = 13.7, 6.6 Hz, 2H), 2.37 (s, 3H), 1.50–1.41 (m, 2H), 0.90 (t, J = 7.4 Hz, 3H). $^{13}\text{C NMR}$ (100 MHz, CDCl_3) δ 165.4, 144.2, 136.7, 136.1, 130.5, 129.8, 128.2, 127.9, 127.5, 127.5, 127.5, 127.4, 127.4, 127.4, 127.3, 126.6, 124.7, 122.8, 122.8, 122.7, 122.7, 122.0, 119.3, 42.3, 22.2, 21.6, 11.4. **HRMS (ESI)** m/z : $[\text{M} + \text{Na}]^+$ Calcd for $\text{C}_{18}\text{H}_{19}\text{F}_3\text{N}_2\text{O}_3\text{SNa}$ 423.0961; Found 423.0962.

2-Methyl-6-((4-methylphenyl)sulfonamido)-*N*-propylbenzamide (3j)



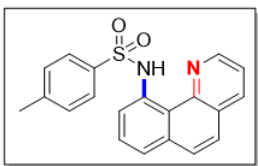
White solid (66.52 mg, 96%), purified by column chromatography on silica gel (*n*-hexane/EtOAc = 1/1, R_f = 0.3); $^1\text{H NMR}$ (500 MHz, CD_2Cl_2) δ 8.11 (s, 1H), 7.58 (d, J = 8.3 Hz, 2H), 7.36 (d, J = 8.2 Hz, 1H), 7.24–7.18 (m, 3H), 6.97 (d, J = 7.7 Hz, 1H), 5.38 (s, 1H), 3.16 (dd, J = 13.7, 6.6 Hz, 2H), 2.36 (s, 3H), 2.28 (s, 3H), 1.53–1.44 (m, 2H), 0.92 (t, J = 7.4 Hz, 3H). $^{13}\text{C NMR}$ (100 MHz, CDCl_3) δ 167.9, 143.7, 136.8, 135.3, 134.5, 129.9, 129.7, 129.6, 127.7, 127.1, 120.8, 41.7, 22.5, 21.5, 20.3, 11.6. **HRMS (ESI)** m/z : $[\text{M} + \text{Na}]^+$ Calcd for $\text{C}_{18}\text{H}_{22}\text{N}_2\text{O}_3\text{SNa}$ 369.1243; Found 369.1246.

6-(Dimethylamino)-3-((4-methylphenyl)sulfonamido)-*N*-propyl-2-naphthamide (3k)



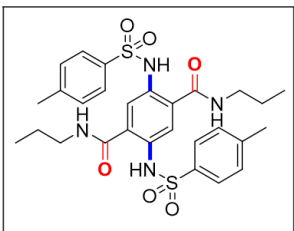
Light yellow solid (78.31 mg, 92%), purified by column chromatography on silica gel (*n*-hexane/EtOAc = 2/1, R_f = 0.25); $^1\text{H NMR}$ (500 MHz, CD_2Cl_2) δ 10.76 (s, 1H), 7.76 (s, 1H), 7.68 (s, 1H), 7.62 (d, J = 8.3 Hz, 2H), 7.57 (d, J = 9.0 Hz, 1H), 7.15 (d, J = 8.0 Hz, 2H), 7.06 (dd, J = 9.1, 2.5 Hz, 1H), 6.79 (d, J = 2.2 Hz, 1H), 6.10 (s, 1H), 3.28 (dd, J = 13.3, 6.8 Hz, 2H), 3.05 (s, 6H), 2.29 (s, 3H), 1.61–1.52 (m, 2H), 0.95 (t, J = 7.4 Hz, 3H). $^{13}\text{C NMR}$ (125 MHz, CDCl_3) δ 169.0, 150.3, 143.2, 137.1, 137.0, 135.0, 129.4, 129.3, 127.4, 127.3, 122.1, 118.5, 117.3, 115.9, 105.1, 41.9, 40.5, 22.9, 21.6, 11.6. **HRMS (ESI)** m/z : $[\text{M} + \text{Na}]^+$ Calcd for $\text{C}_{23}\text{H}_{27}\text{N}_3\text{O}_3\text{SNa}$ 448.1665; Found 448.1664.

N-(Benzo[*h*]quinolin-10-yl)-4-methylbenzenesulfonamide (3l)



Light yellow solid (61.32 mg, 88%), purified by column chromatography on silica gel (*n*-hexane/EtOAc = 3/1, R_f = 0.25); The structure of **3l** was confirmed by comparison of its spectroscopic data with reported data.¹⁰

2,5-Bis((4-methylphenyl)sulfonamido)-*N*¹,*N*⁴-dipropylterephthalamide (3m)



Following the general procedure, *p*-Toluenesulfonyl azide (**1**, 78.88 mg, 0.4 mmol), **2m** (49.66 mg, 0.2 mmol), $[\text{IrCp}^*\text{Cl}_2]_2$ (1.59 mg, 2 μmol), AgSbF_6 (2.80 mg, 8 μmol), Li_2CO_3 (0.59 mg, 8 μmol), AcOH (8 μmol), degassed anhydrous 1,2-dichloroethane (1.6 mL, 0.125 M) were used.

White solid (104.44 mg, 89%), purified by column chromatography on silica gel (*n*-hexane/EtOAc = 2/1, R_f = 0.25); $^1\text{H NMR}$ (500 MHz, CD_2Cl_2) δ 10.34 (s, 2H), 7.65 (s, 2H), 7.47 (d, J = 8.0 Hz, 4H), 7.17 (d, J = 7.9 Hz, 4H), 6.05 (s, 2H), 3.19 (dd, J = 13.5, 6.6 Hz, 4H), 2.34 (s, 6H), 1.53–1.43 (m, 2H), 0.91 (t, J = 7.4 Hz, 6H). $^{13}\text{C NMR}$ (125 MHz, $\text{THF-}d_8$) δ 167.9, 144.2, 137.8, 135.6, 130.2, 128.1, 128.0, 123.5, 42.4, 23.3, 21.3, 11.8. **HRMS (ESI)** m/z : $[\text{M} + \text{Na}]^+$ Calcd for $\text{C}_{28}\text{H}_{34}\text{N}_4\text{O}_6\text{S}_2\text{Na}$ 609.1812; Found 609.1813.

3.6. Supporting Information

3.6.1. Experimental and Calculated Energy Levels of 3a–g

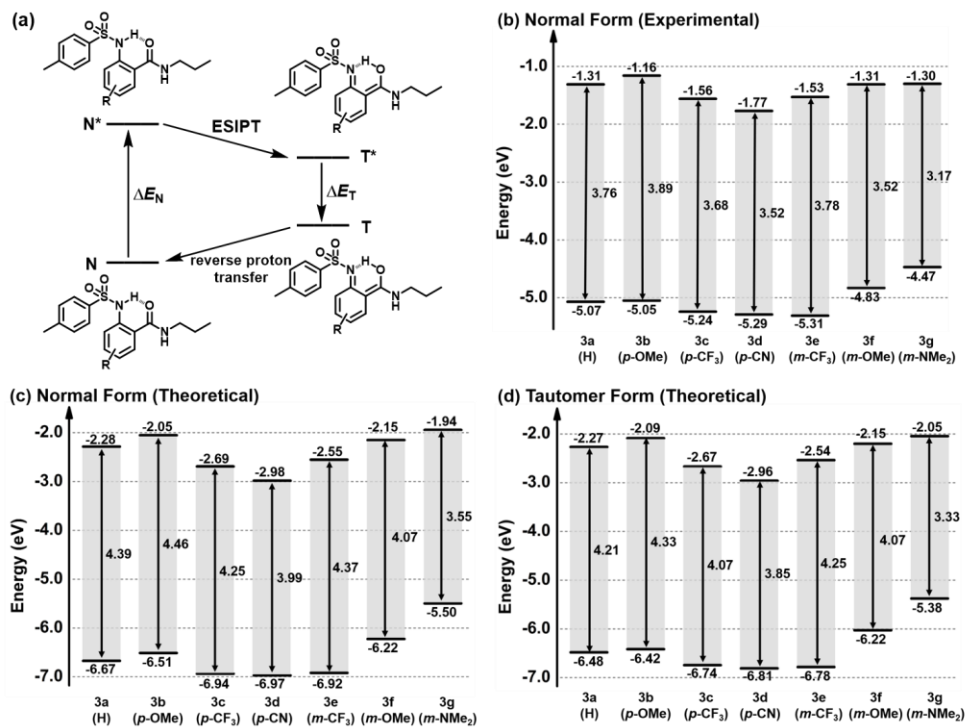
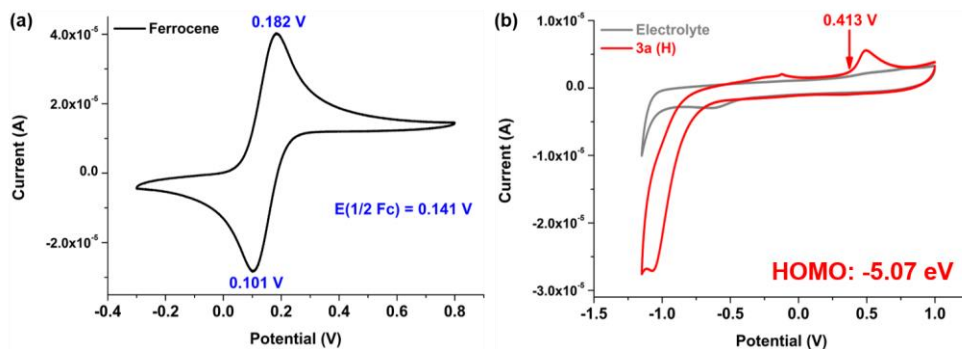


Figure S3.1. (a) Schematic representation of the ESIPT photocycle. (b) Experimental HOMO and LUMO energy levels of normal forms of **3a–3g** obtained by cyclic voltammetry for HOMOs (Figure S3.2) and UV-vis spectroscopy for band gaps. (c) Calculated energy levels ($S_0 \rightarrow S_1$ transition) of **3a–3g** in normal and (d) tautomer forms (TD-DFT/B3LYP/6-31++G(d,p)/IEFPCM).

3.6.2. Cyclic Voltammograms of 3a–g



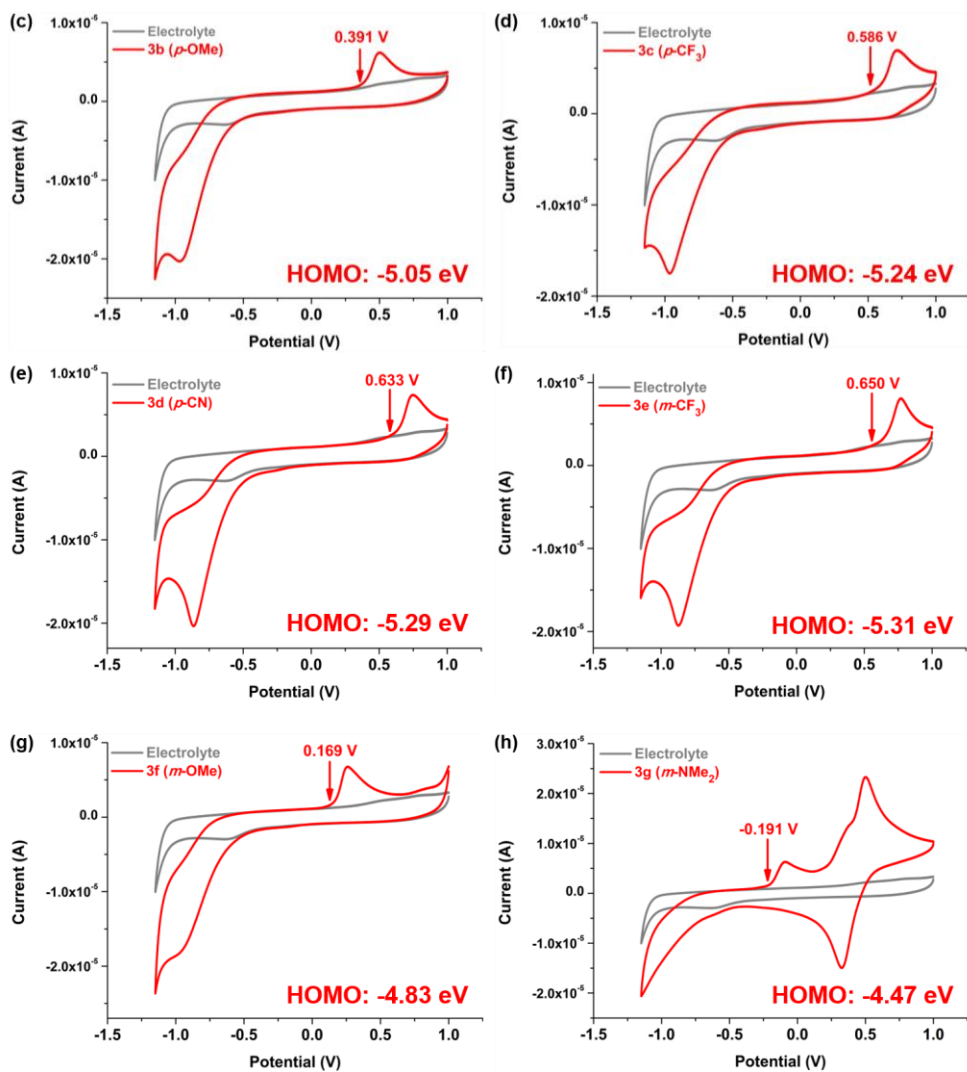


Figure S3.2. (a) $E_{1/2}$ (Ferrocene) = 0.141 V was obtained from a result of ferrocene/ferrocenium. The HOMO energy levels of **3a–g** were (b) -5.07 V, (c) -5.05 V, (d) -5.24 V, (e) -5.29 V, (f) -5.31 V, (g) -4.83 V, and (h) -4.47 V, respectively.

3.6.3. Absorption and Emission Spectra of 3i and 3j

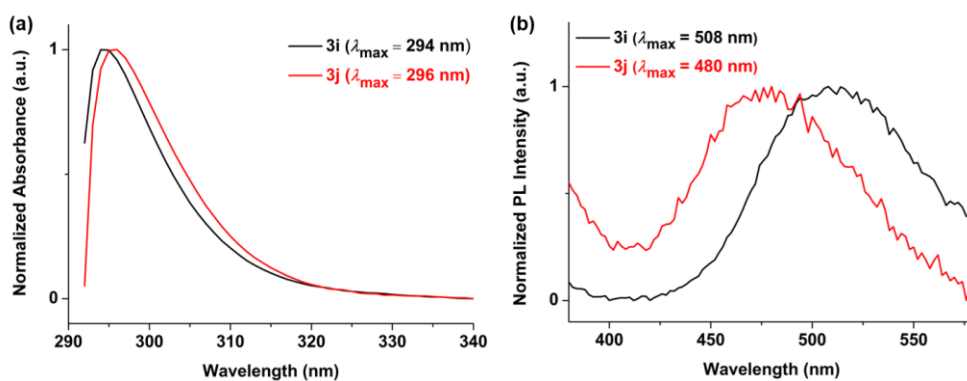
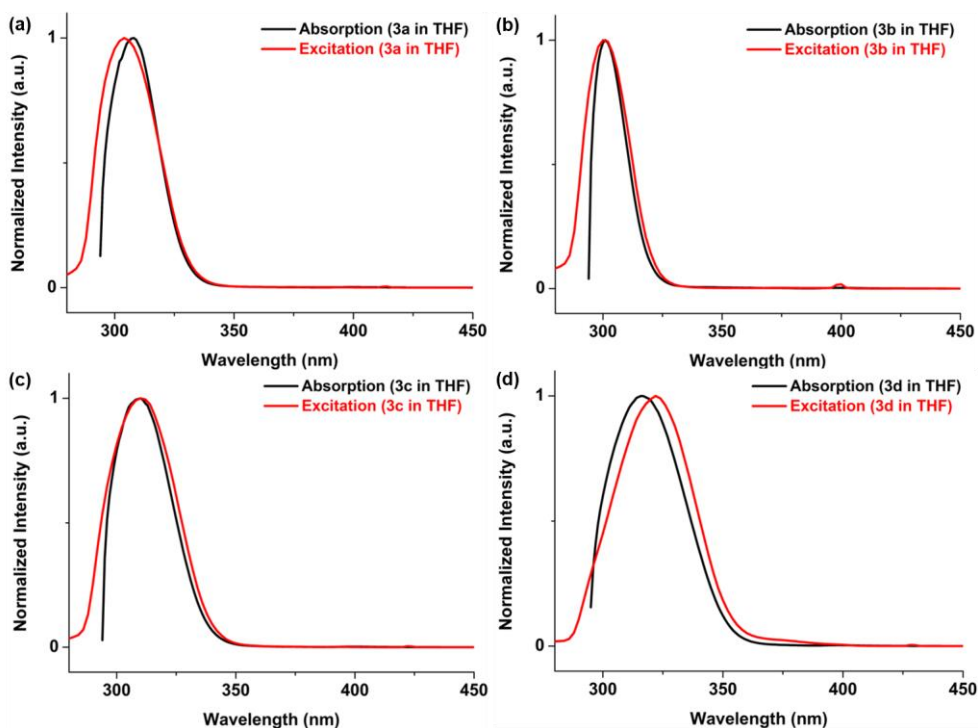


Figure S3.3. (a) Normalized absorption spectra of **3i** and **3j**. (b) Normalized emission spectra of **3i** ($\lambda_{\text{ex}} = 294$ nm) and **3j** ($\lambda_{\text{ex}} = 296$ nm) in THF ($10 \mu\text{M}$) at 298 K.

3.6.4. Excitation Spectra of 3a–h and 3k–m

Excitation Spectra of Amidated Products Showing Single Emission



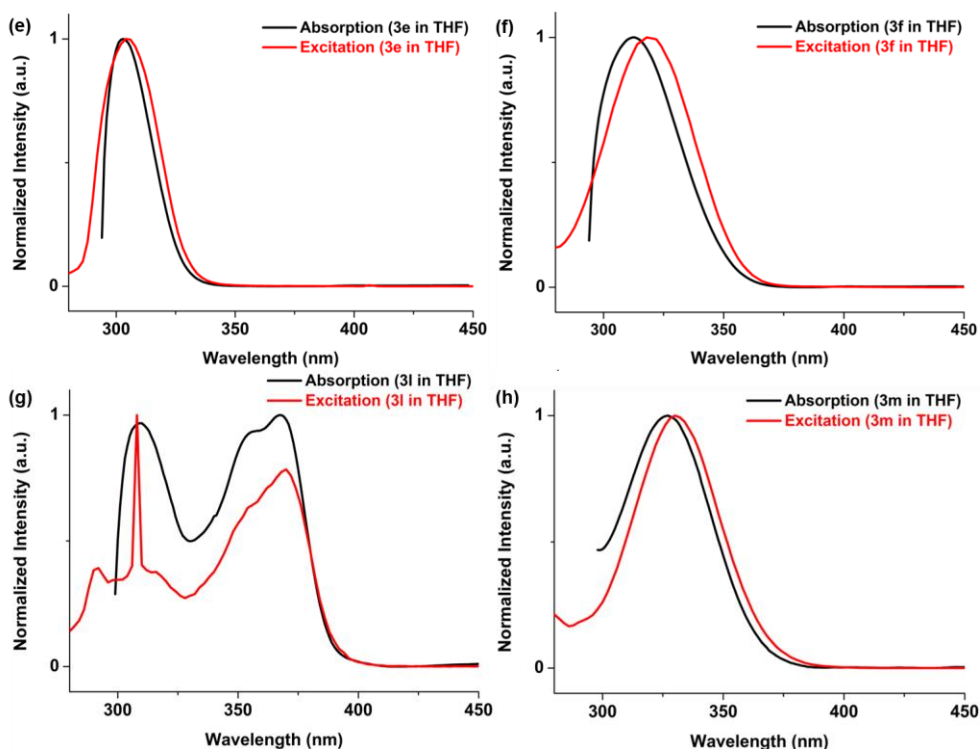


Figure S3.4. The absorption (black line) and excitation (red line that monitored at tautomer peak) spectra of (a) **3a**, (b) **3b**, (c) **3c**, (d) **3d**, (e) **3e**, (f) **3f**, (g) **3l**, and (h) **3m**.

Excitation Spectra of Amidated Products Showing Dual Emission

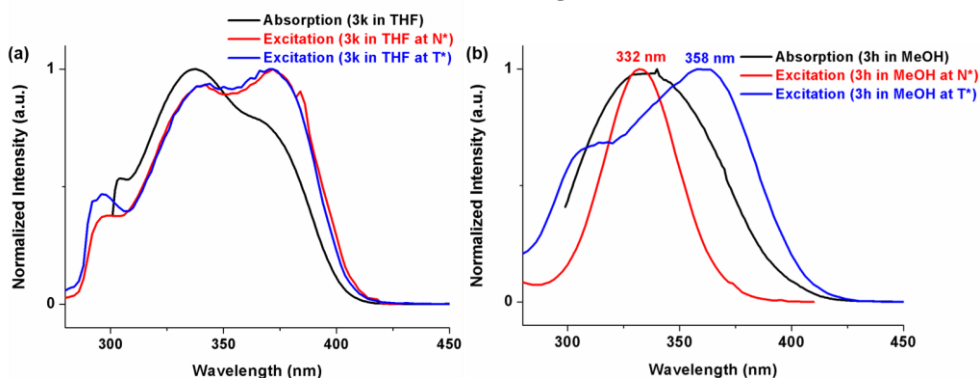


Figure S3.5. The absorption (black line) and excitation (red and blue line that monitored at normal and tautomer peak, respectively) spectra of (a) **3k** in THF and (b) **3h** in MeOH. The excitation spectra of **3h** in MeOH obtained at normal and tautomer peaks were significantly different from its corresponding absorption spectrum. In addition, the excitation spectrum of **3h** in MeOH obtained at the tautomer peak is red shifted by 26 nm, compared to that obtained at the normal peak. The results suggest that each PL band of **3h** in MeOH originated from different initially excited species.

3.6.5. Mechanistic Studies for the White-Light Emission of **3h** in Methanol

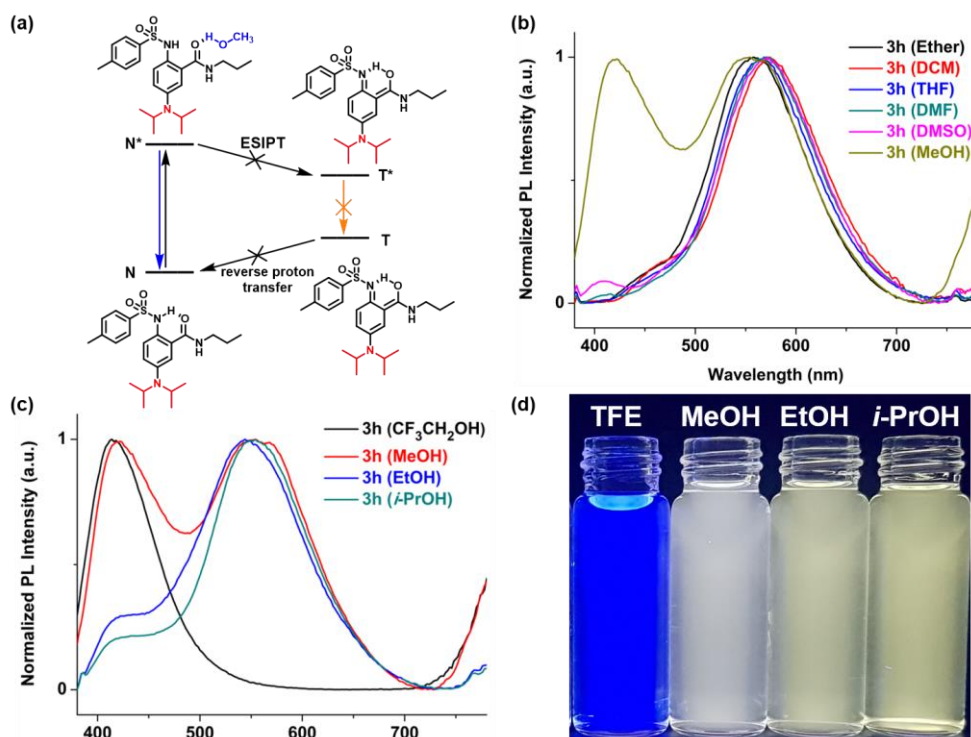
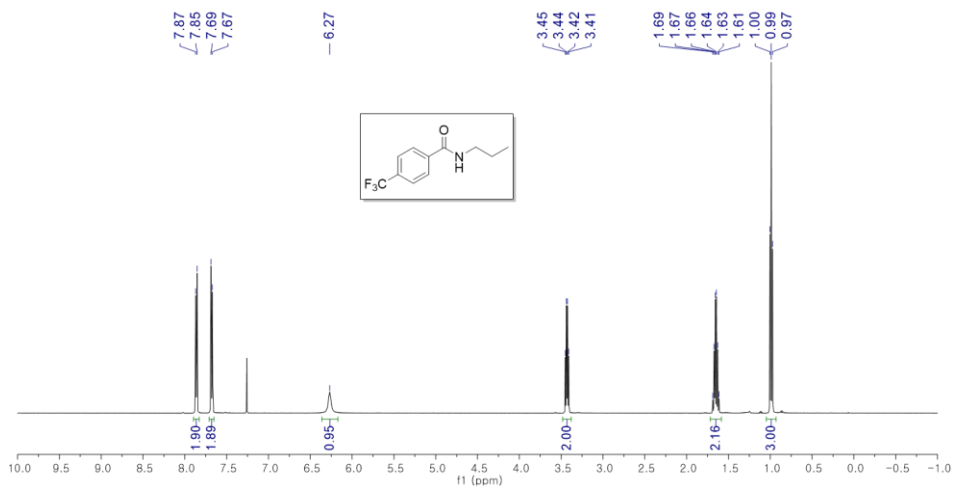


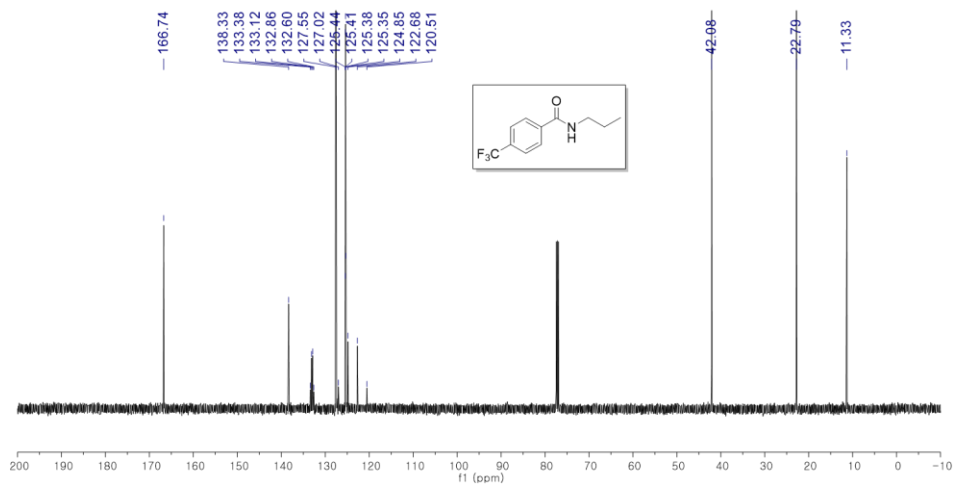
Figure S3.6. (a) Proposed mechanism for the white-light emission of **3h** in methanol; White-light emission appears in MeOH because ESIPT is partially quenched by intermolecular hydrogen bond with the protic solvent, supported by following observations. (b) Normalized emission spectra of **3h** in various solvents (10 μM) at 298 K ($\lambda_{\text{ex}} = 340$ nm); There is almost no normal emission from N^* in other aprotic solvents, whereas clear normal emission appears only in methanol (MeOH). (c) Normalized emission spectra of **3h** in different alcohols (10 μM) at 298 K ($\lambda_{\text{ex}} = 340$ nm); The relative intensity of the normal emission decreased (the relative intensity of the ESIPT emission increased) in the order of 2,2,2-trifluoroethanol (TFE), MeOH, ethanol (EtOH) and isopropanol (*i*-PrOH) (d) The photo of **3h** in different alcohols under 365 nm UV irradiation; In the order of TFE, MeOH, EtOH and *i*-PrOH, the color became gradually closer from blue to yellow. Considering that the ability to hydrogen bonding donor, which is determined by Kamlet-Taft parameters increases in the order of *i*-PrOH, EtOH, MeOH and TFE,⁴³ the reason for the above observation can be explained by the assumption that the stronger hydrogen bonding donor solvent results in more effective intermolecular hydrogen bond, so the relative intensity of normal emission increases.

3.6.6. ^1H and ^{13}C NMR Spectra of Benzamides and Amidated Products

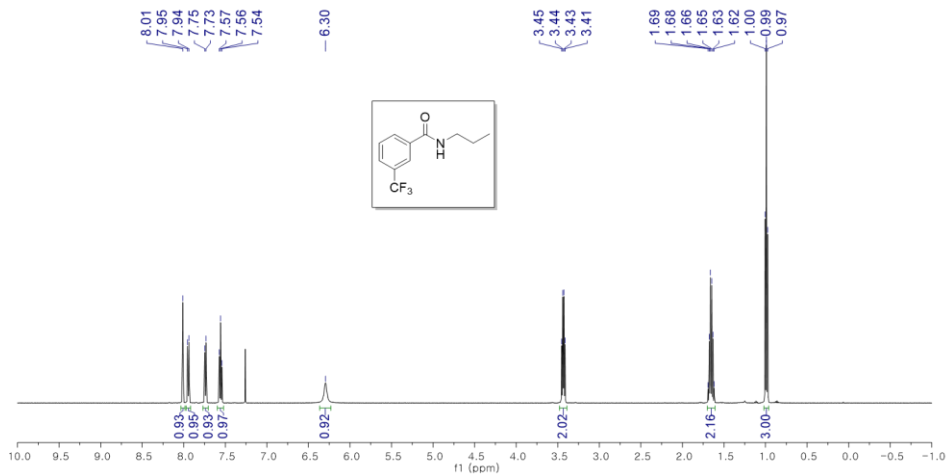
2c ^1H NMR (500 MHz, CDCl_3)



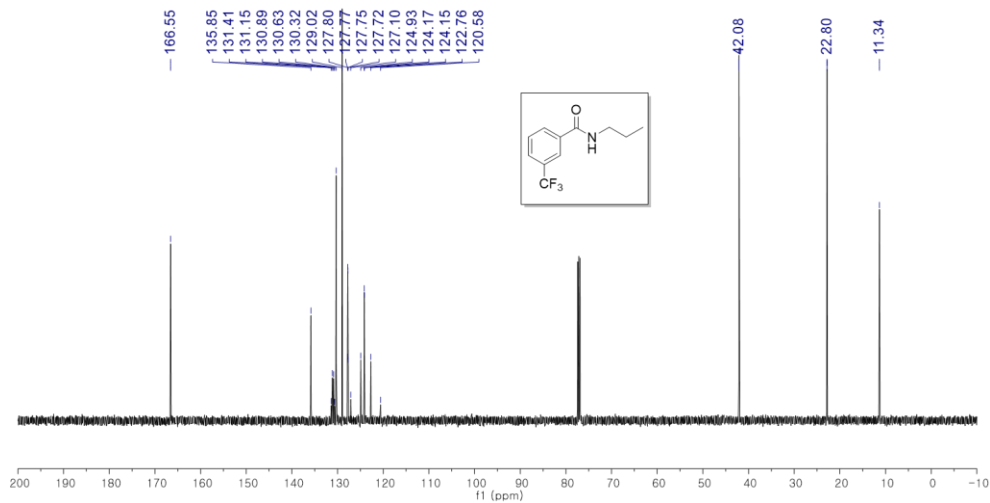
2c ^{13}C NMR (125 MHz, CDCl_3)



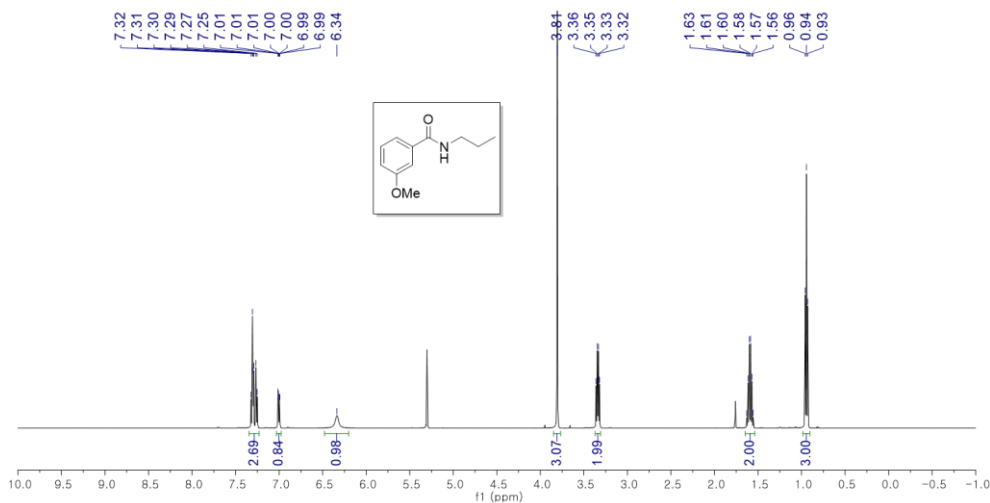
2e ^1H NMR (500 MHz, CDCl_3)



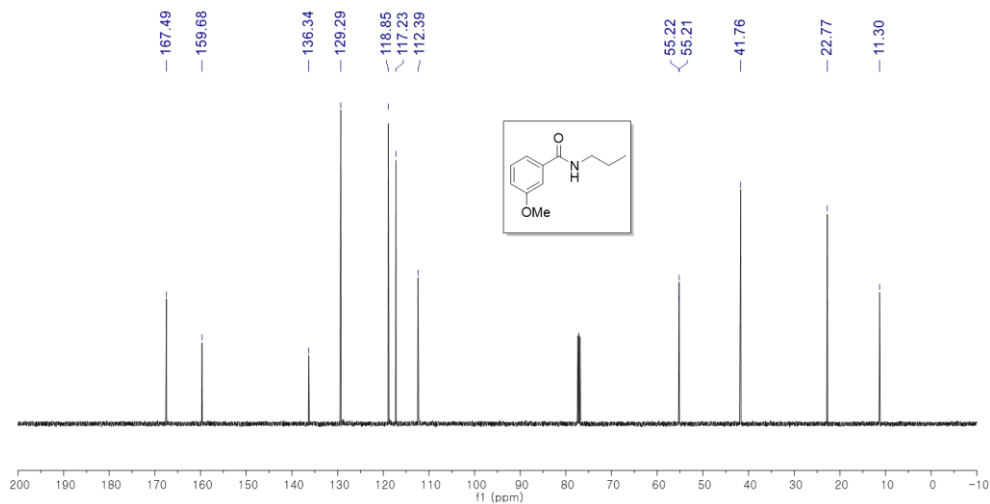
2e ^{13}C NMR (125 MHz, CDCl_3)



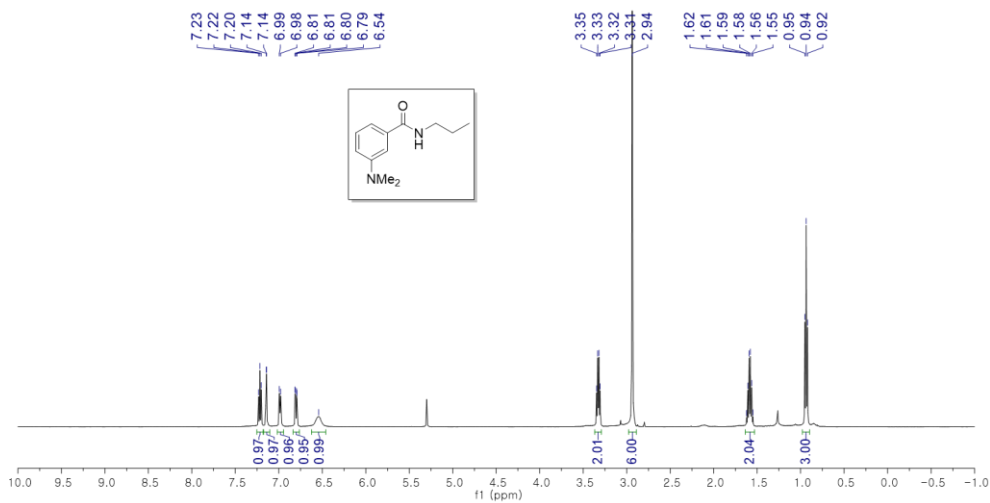
2f ^1H NMR (500 MHz, CD_2Cl_2)



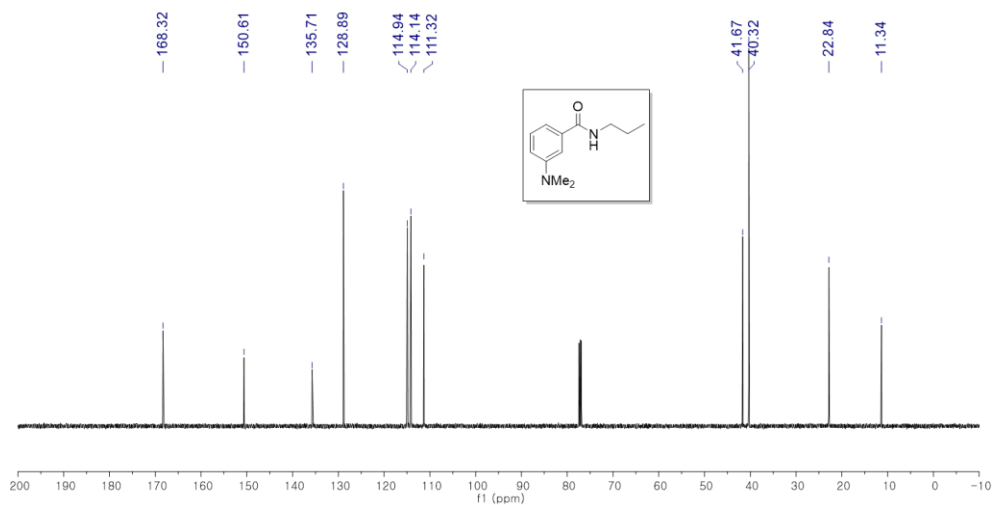
2f ^{13}C NMR (125 MHz, CDCl_3)



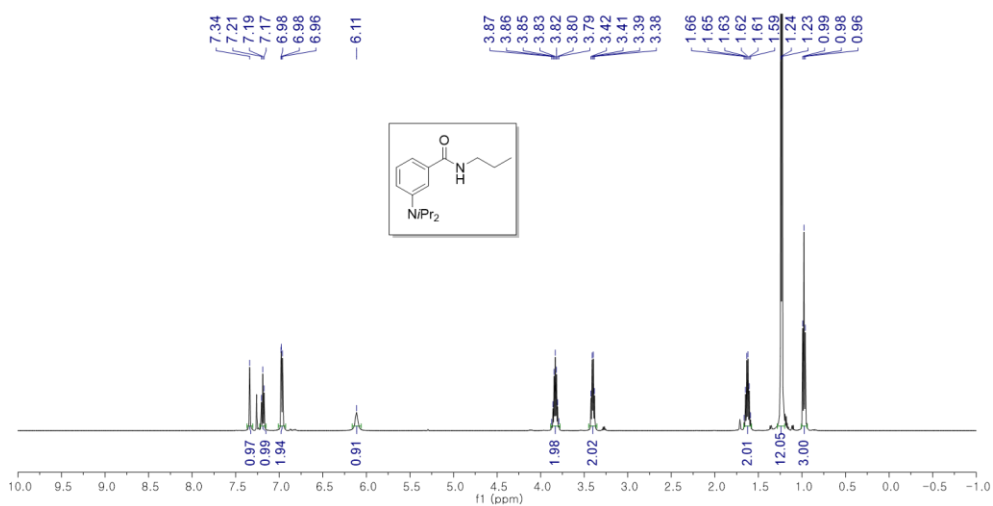
2g ^1H NMR (500 MHz, CD_2Cl_2)



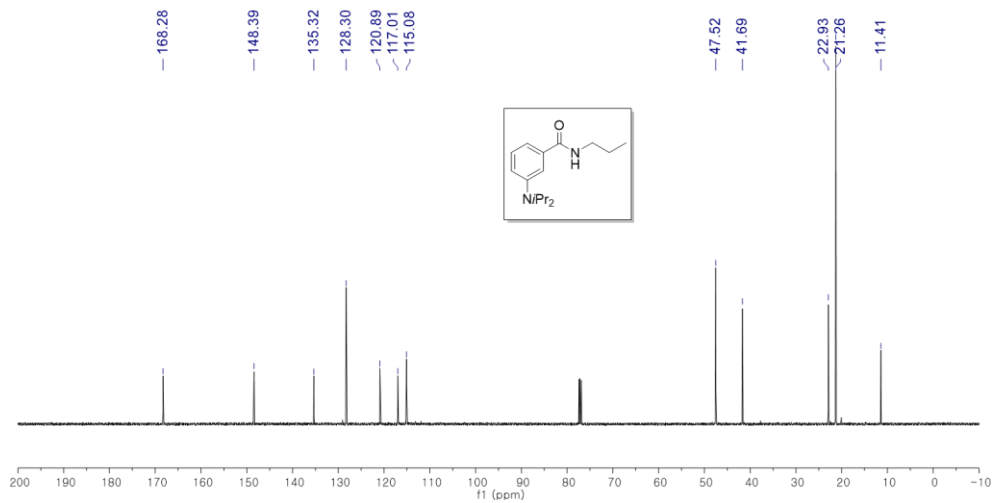
2g ^{13}C NMR (125 MHz, CDCl_3)



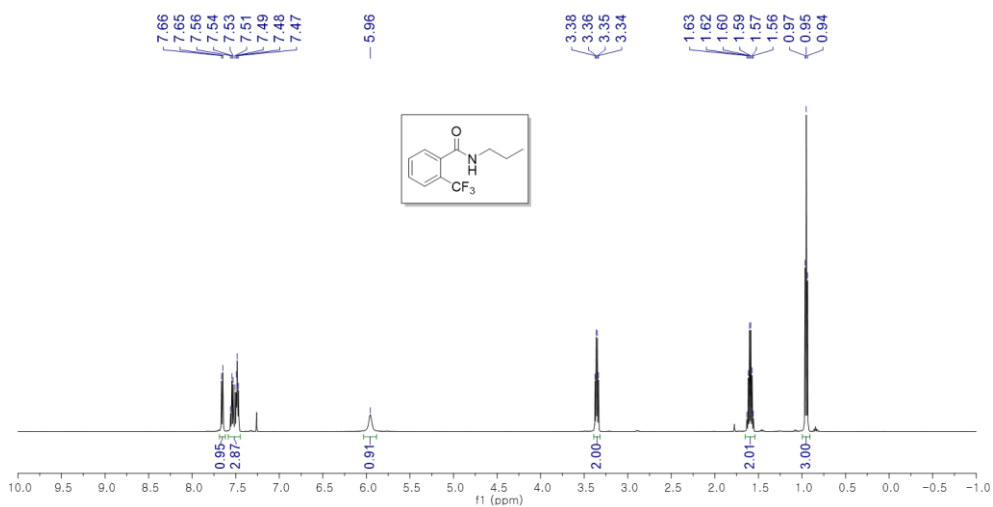
2h ^1H NMR (500 MHz, CDCl_3)



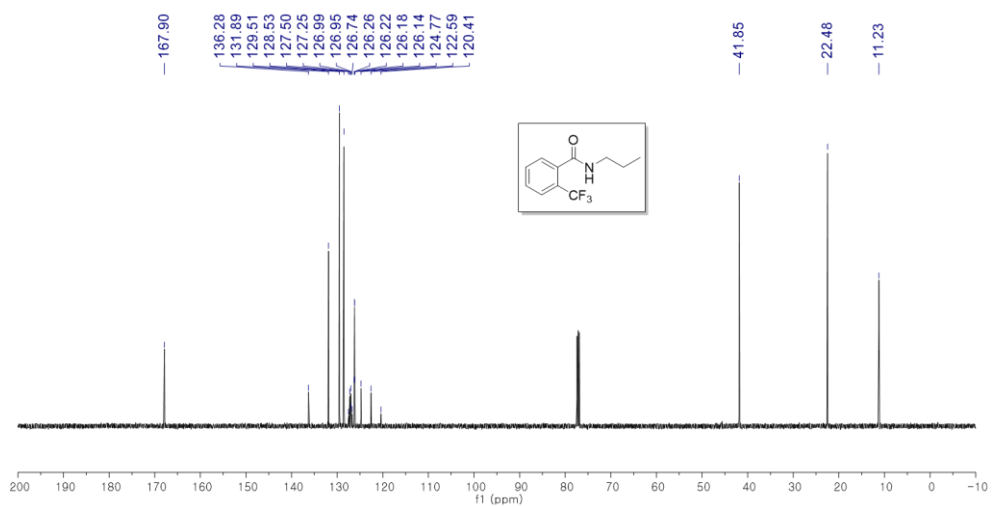
2h ^{13}C NMR (125 MHz, CDCl_3)



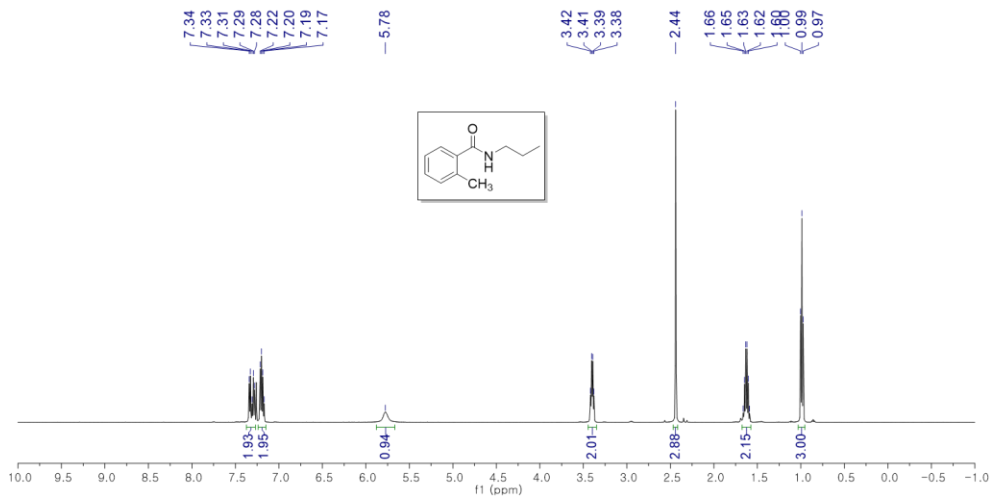
2i ^1H NMR (500 MHz, CDCl_3)



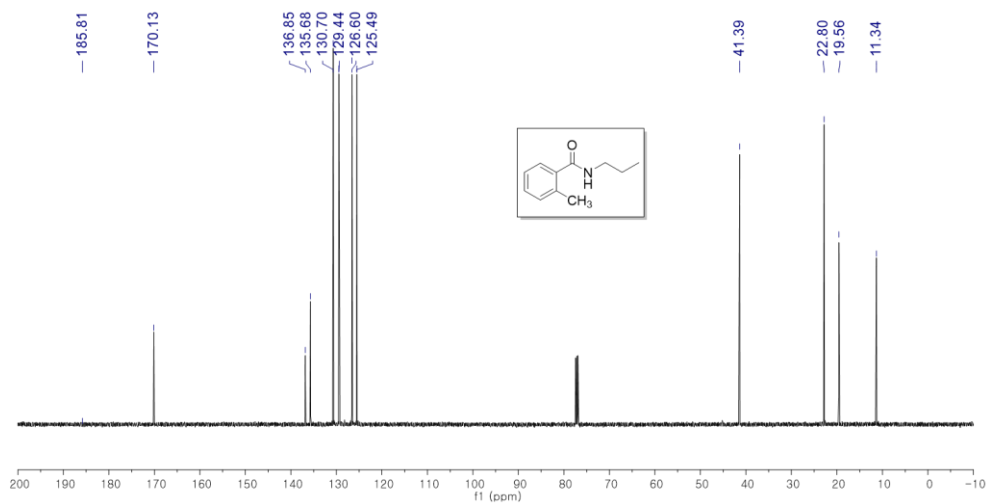
2i ^{13}C NMR (125 MHz, CDCl_3)



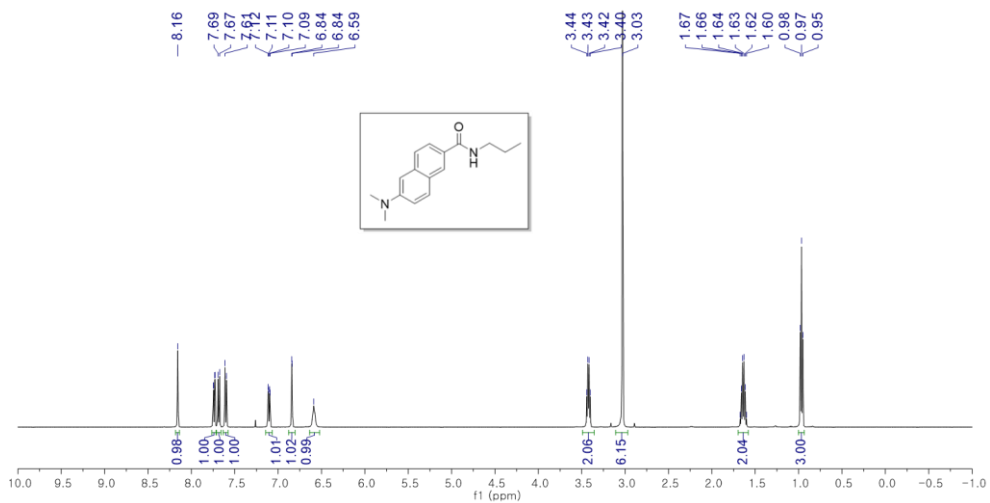
2j ^1H NMR (500 MHz, CDCl_3)



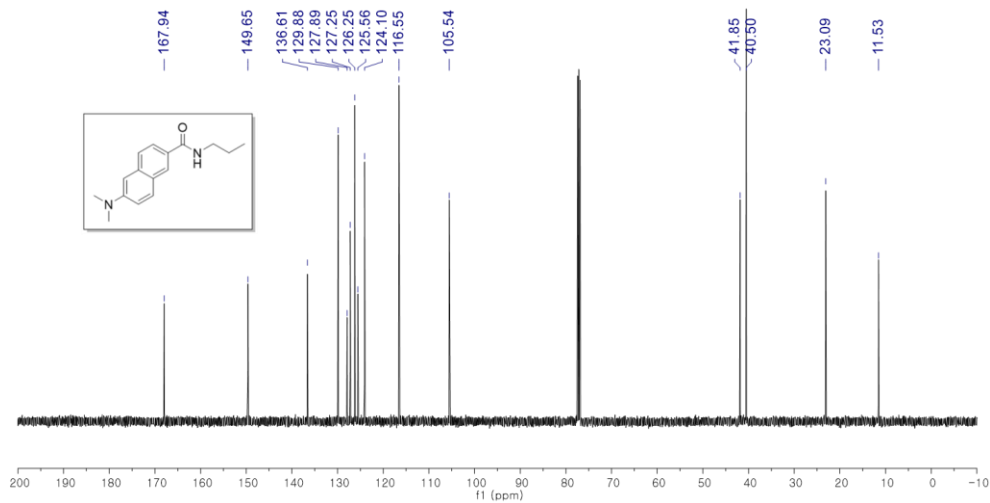
2j ^{13}C NMR (125 MHz, CDCl_3)



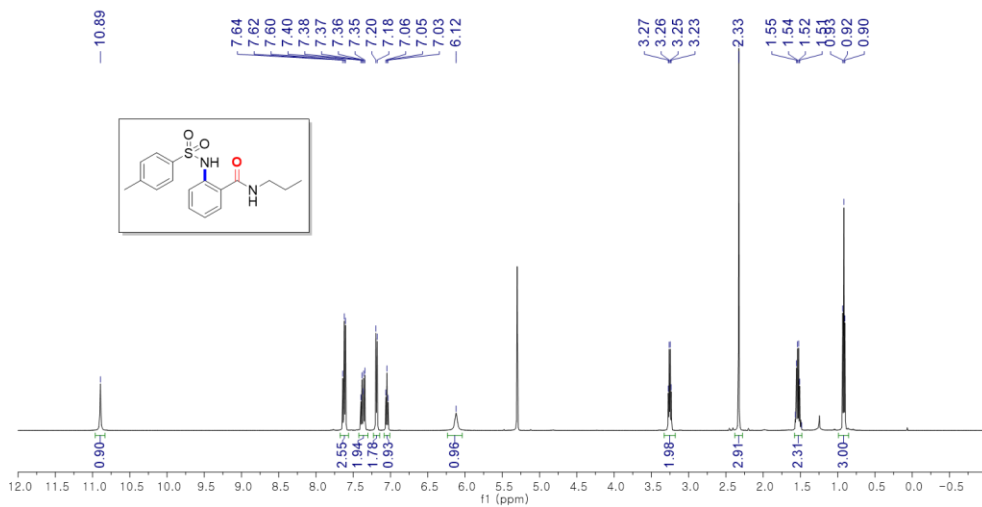
2k ^1H NMR (500 MHz, CDCl_3)



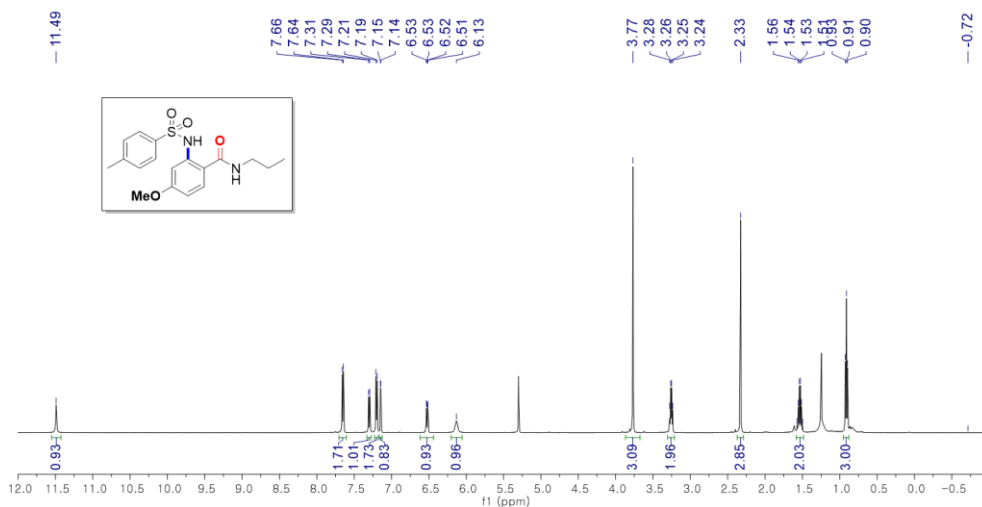
2k ^{13}C NMR (125 MHz, CDCl_3)



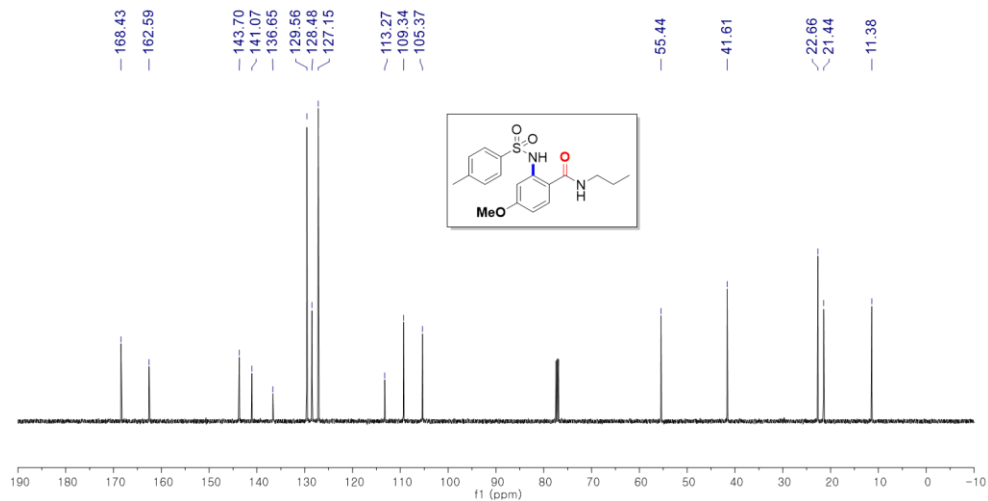
3a ^1H NMR (500 MHz, CD_2Cl_2)



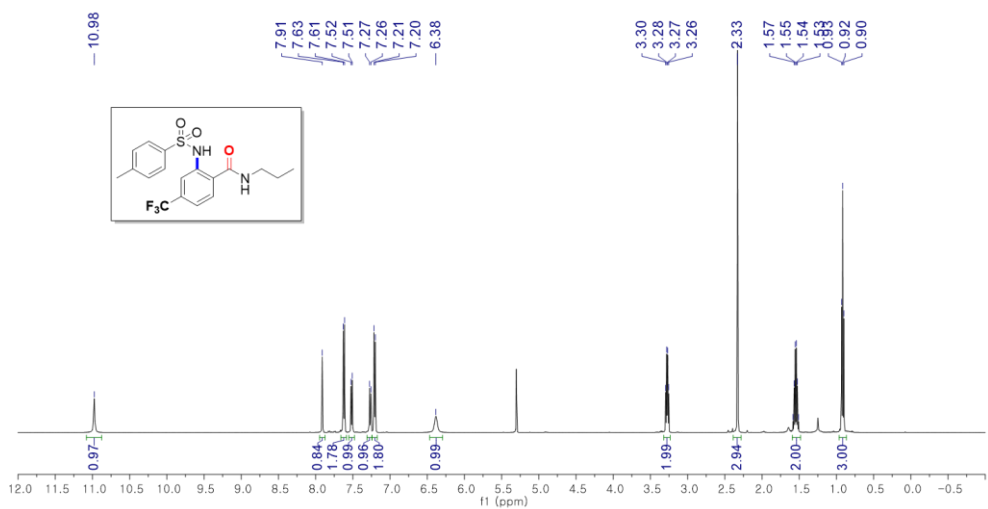
3b ^1H NMR (500 MHz, CD_2Cl_2)



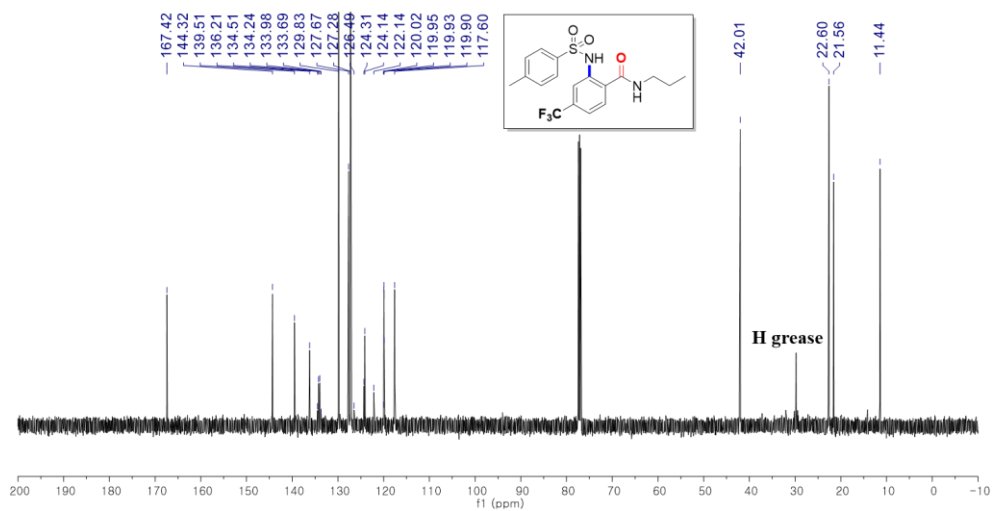
3b ^{13}C NMR (125 MHz, CDCl_3)



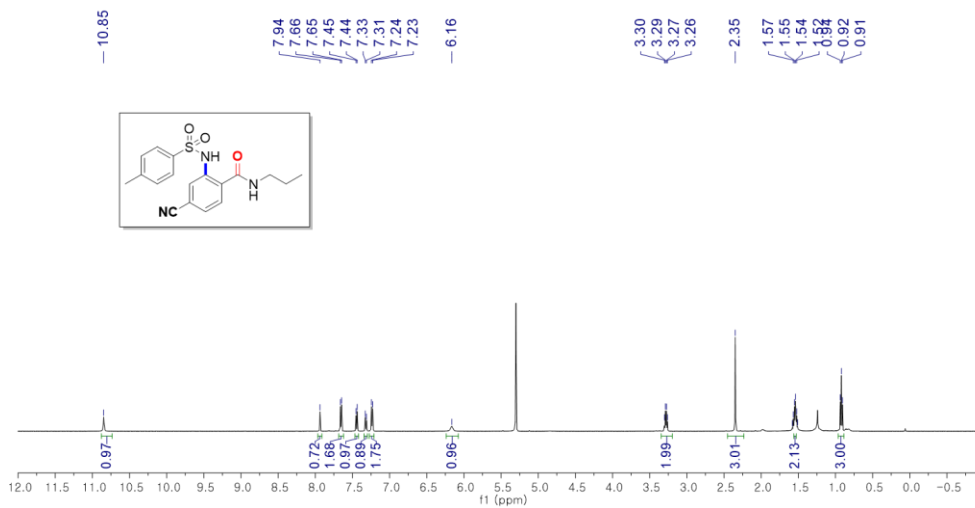
3c ^1H NMR (500 MHz, CD_2Cl_2)



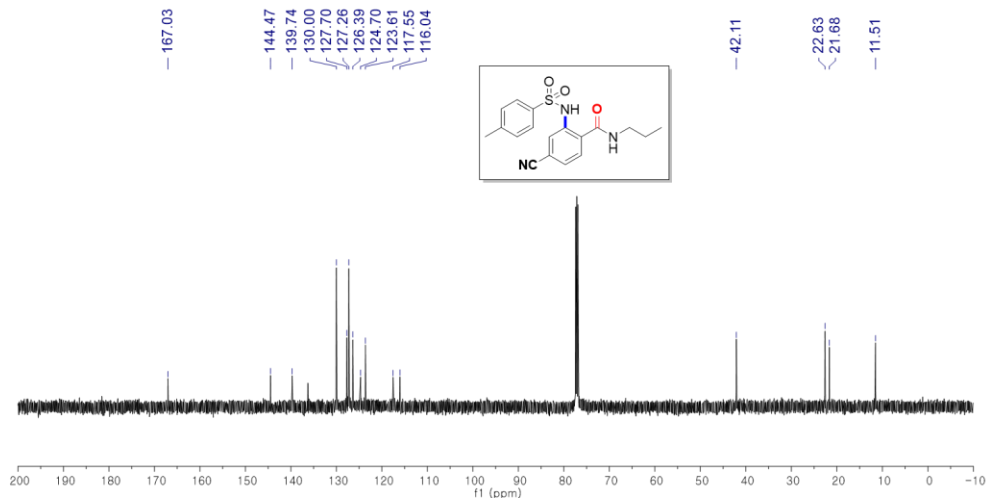
3c ^{13}C NMR (125 MHz, CDCl_3)



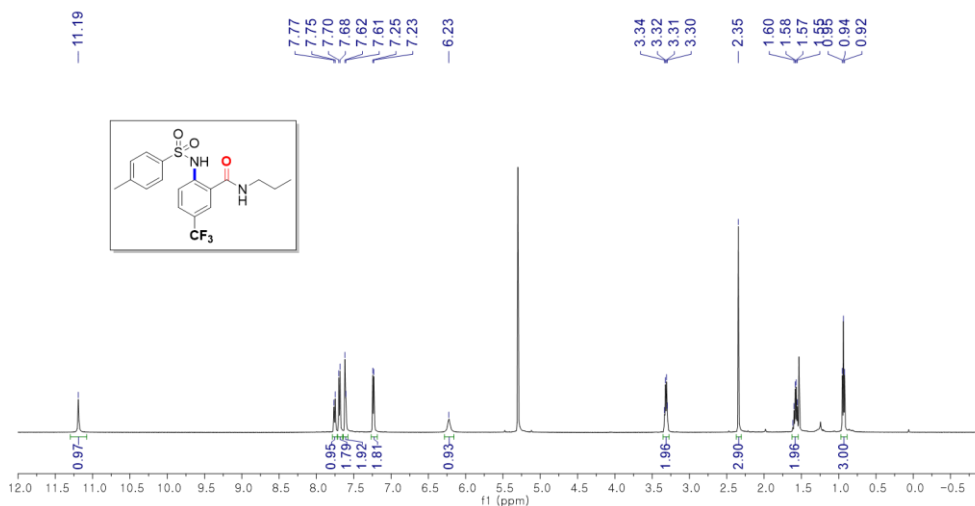
3d ^1H NMR (500 MHz, CD_2Cl_2)



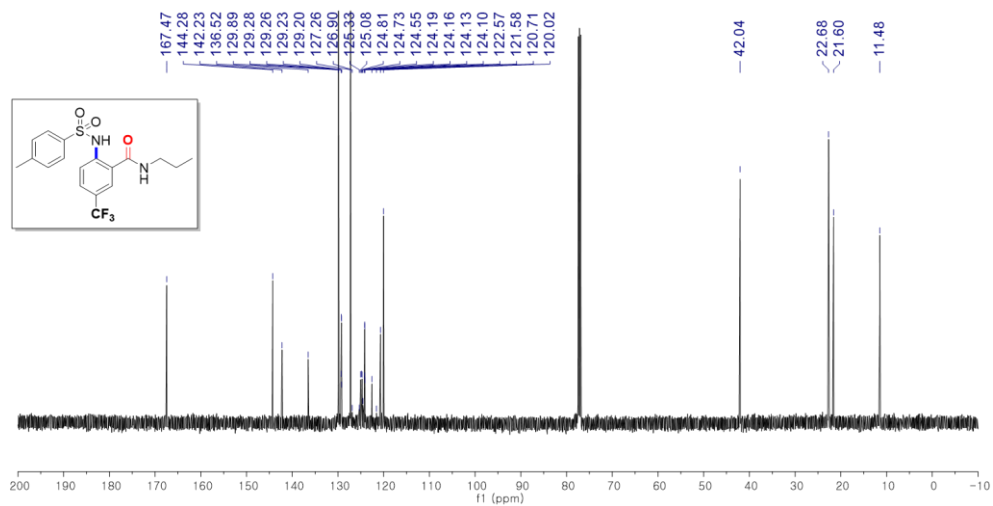
3d ^{13}C NMR (125 MHz, CDCl_3)



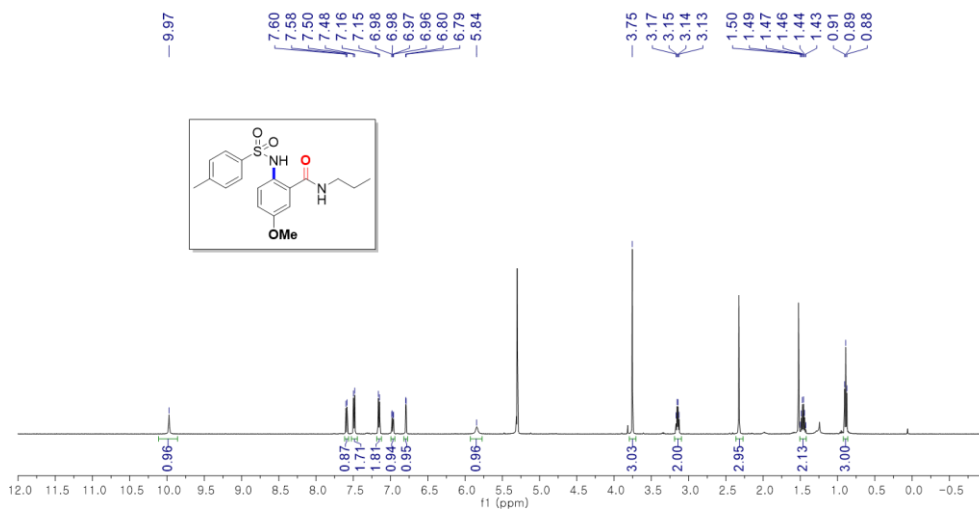
3e ^1H NMR (500 MHz, CD_2Cl_2)



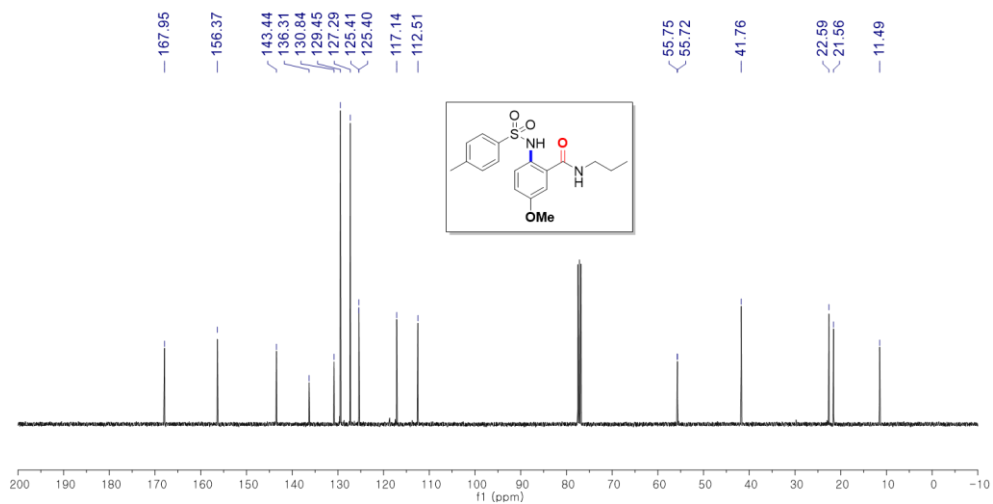
3e ^{13}C NMR (125 MHz, CDCl_3)



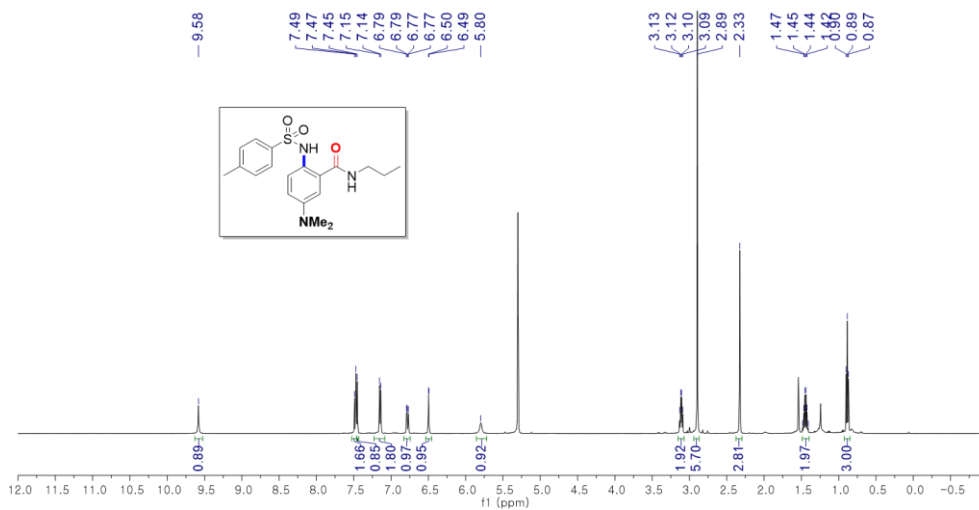
3f ^1H NMR (500 MHz, CD_2Cl_2)



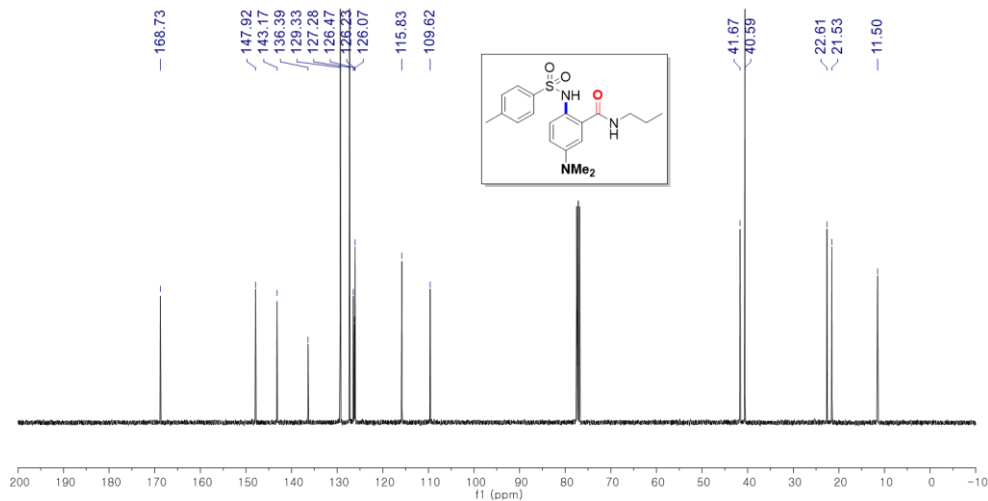
3f ^{13}C NMR (100 MHz, CDCl_3)



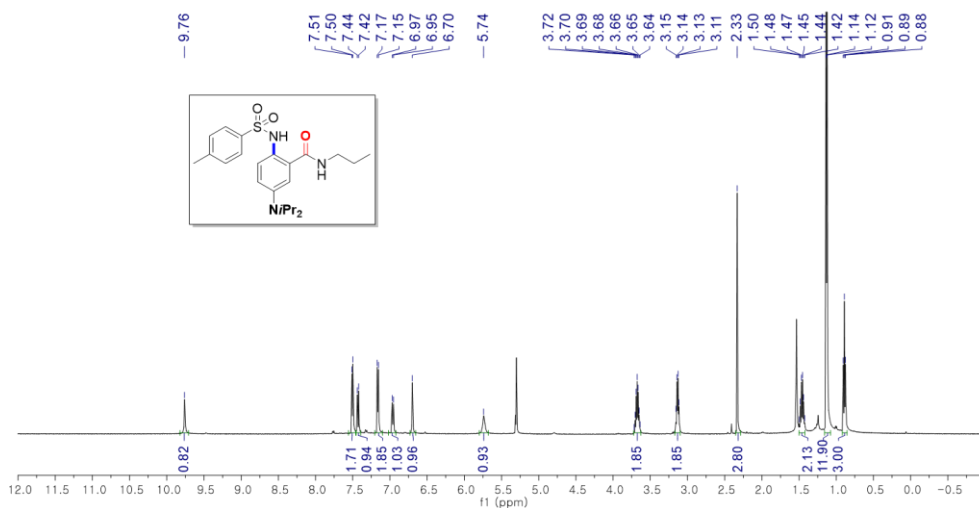
3g ^1H NMR (500 MHz, CD_2Cl_2)



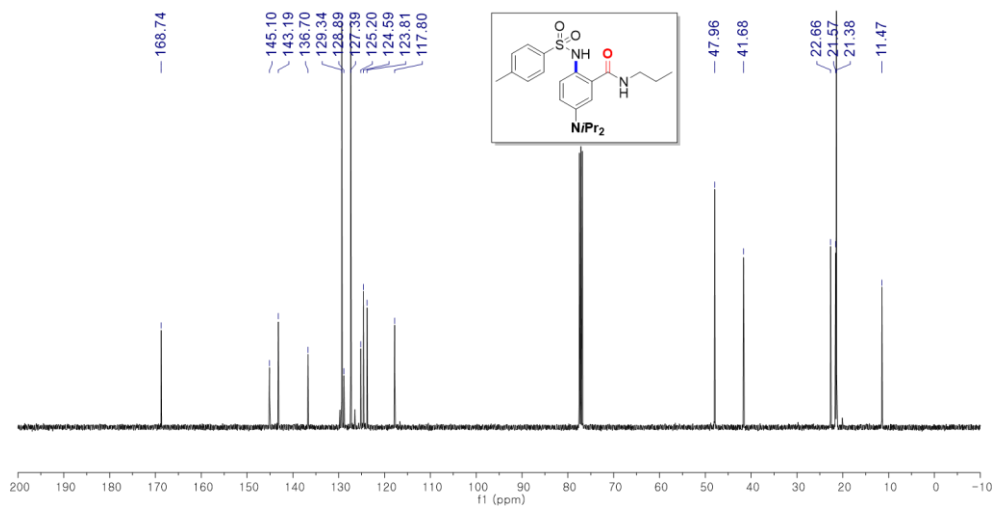
3g ^{13}C NMR (100 MHz, CDCl_3)



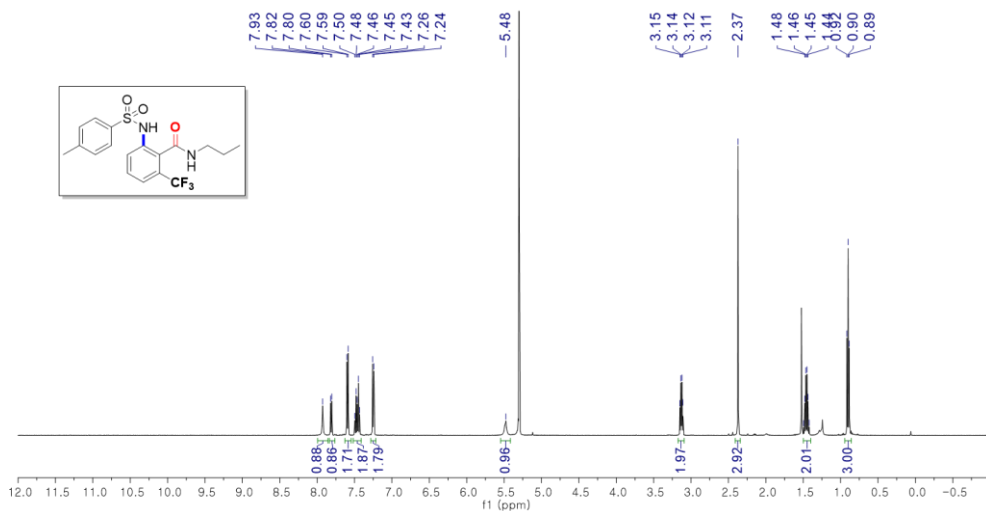
3h ^1H NMR (500 MHz, CD_2Cl_2)



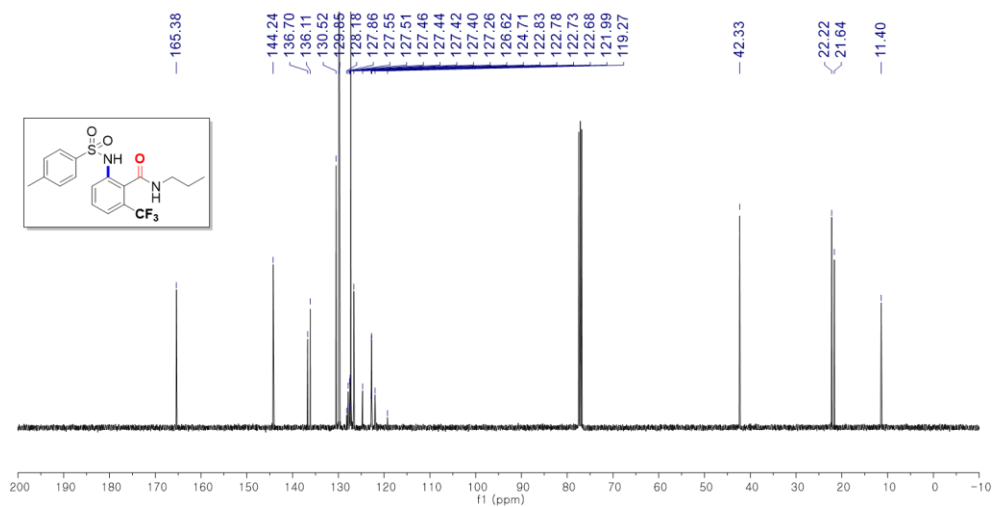
3h ^{13}C NMR (100 MHz, CDCl_3)



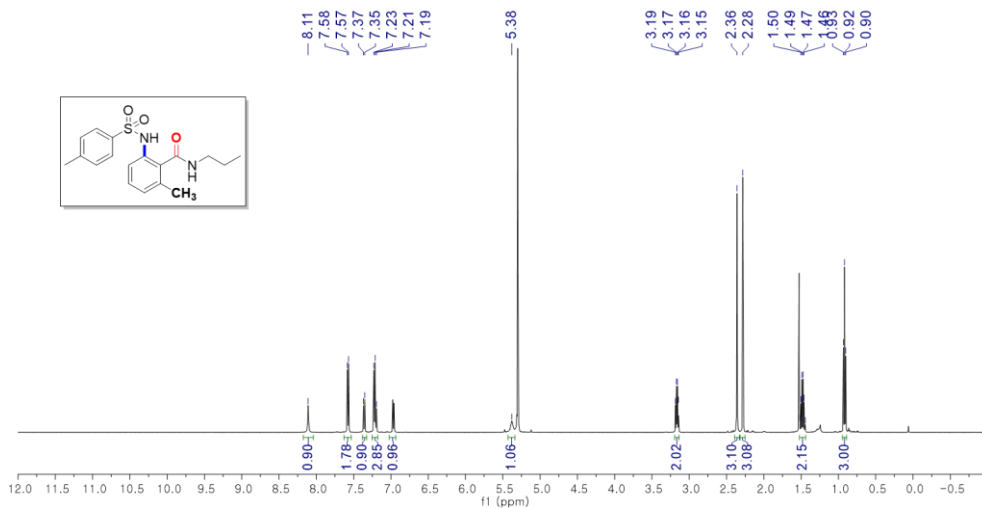
3i ^1H NMR (500 MHz, CD_2Cl_2)



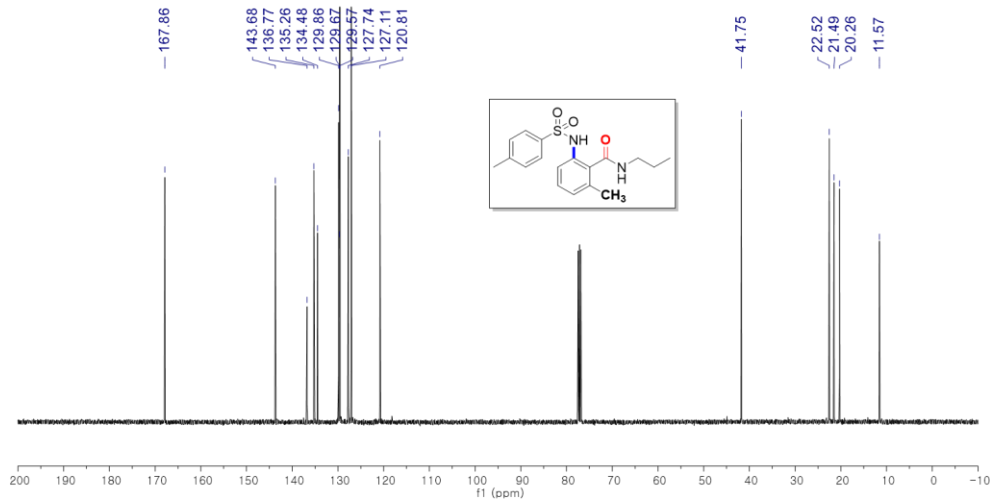
3i ^{13}C NMR (100 MHz, CDCl_3)



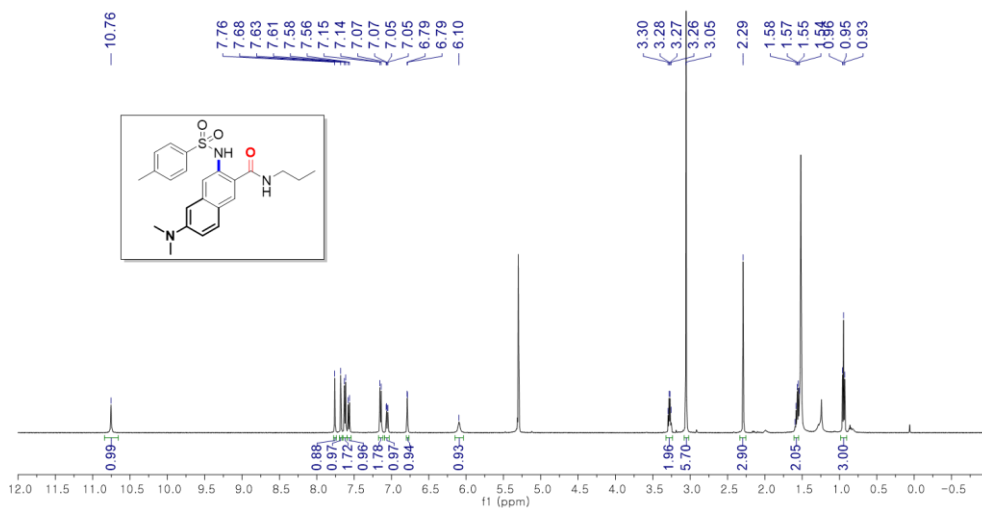
3j ^1H NMR (500 MHz, CD_2Cl_2)



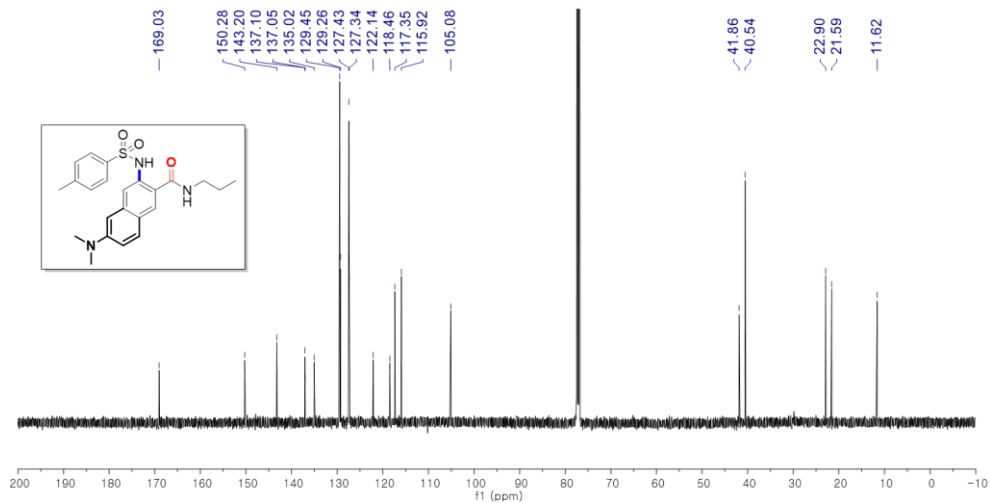
3j ^{13}C NMR (100 MHz, CDCl_3)



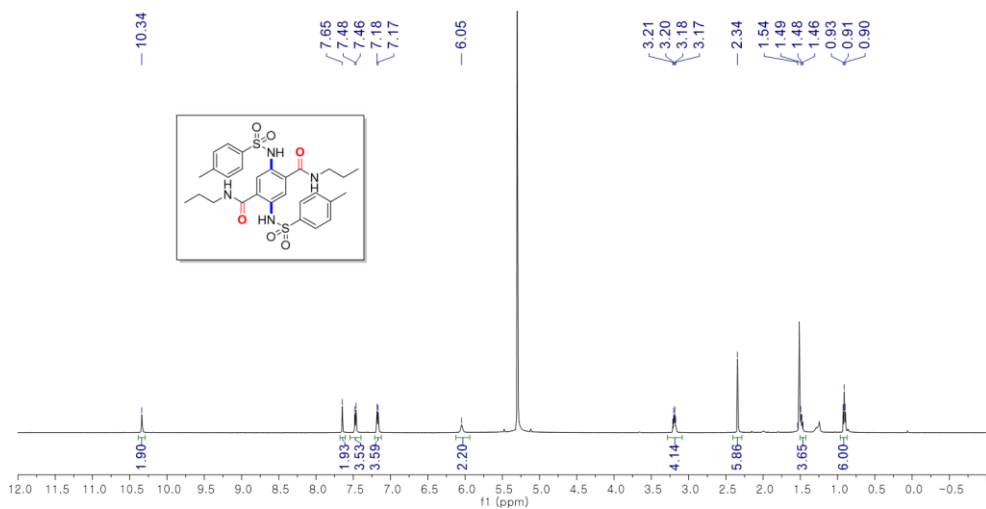
3k ^1H NMR (500 MHz, CD_2Cl_2)



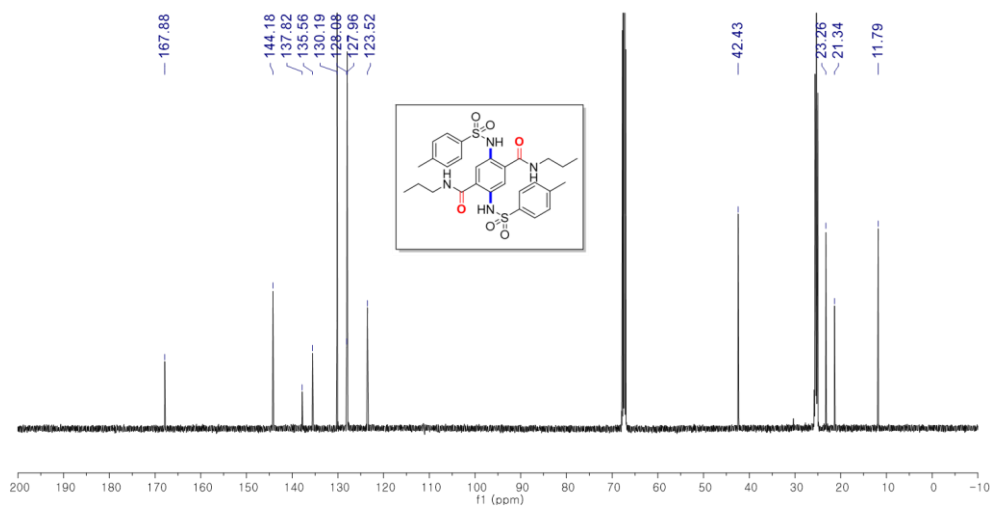
3k ^{13}C NMR (125 MHz, CDCl_3)



3m ^1H NMR (500 MHz, CD_2Cl_2)



3m ^{13}C NMR (125 MHz, $\text{THF-}d_8$)



3.7. References

*Portions of this chapter have been previously reported, see: Hwang, S.-H.; Choi, T.-L. *Org. Lett.* **2020**, *22*, 2935–2940.

- (1) Tang, C. W.; VanSlyke, S. A. *Appl. Phys. Lett.* **1987**, *51*, 913–915.
- (2) Müller, C. D.; Falcou, A.; Reckefuss, N.; Rojahn, M.; Wiederhirn, V.; Rudati, P.; Frohne, H.; Nuyken, O.; Becker, H.; Meerholz, K. *Nature* **2003**, *421*, 829–833.
- (3) Zhao, Y. S.; Fu, H.; Hu, F.; Peng, A. D.; Yao, J. *Adv. Mater.* **2007**, *19*, 3554–3558.
- (4) Wu, H. B.; Ying, L.; Yang, W.; Cao, Y. *Chem. Soc. Rev.* **2009**, *38*, 3391–3400.
- (5) Kamtekar, K. T.; Monkman, A. P.; Bryce, M. R. *Adv. Mater.* **2010**, *22*, 572–582.
- (6) Xiao, L.; Chen, Z.; Qu, B.; Luo, J.; Kong, S.; Gong, Q.; Kido, J. *Adv. Mater.* **2011**, *23*, 926–952.
- (7) Farinola, G. M.; Ragni, R. *Chem. Soc. Rev.* **2011**, *40*, 3467–3482.
- (8) Kwon, J. E.; Park, S.; Park, S. Y. *J. Am. Chem. Soc.* **2013**, *135*, 11239–11246.
- (9) Park, Y.; Kim, Y.; Chang, S. *Chem. Rev.* **2017**, *117*, 9247–9301.
- (10) Kim, J. Y.; Park, S. H.; Ryu, J.; Cho, S. H.; Kim, S. H.; Chang, S. *J. Am. Chem. Soc.* **2012**, *134*, 9110–9113.
- (11) Lee, D.; Kim, Y.; Chang, S. *J. Org. Chem.* **2013**, *78*, 11102–11109.
- (12) Kim, J.; Chang, S. *Angew. Chem., Int. Ed.* **2014**, *53*, 2203–2207.
- (13) Kang, T.; Kim, Y.; Lee, D.; Wang, Z.; Chang, S. *J. Am. Chem. Soc.* **2014**, *136*, 4141–4144.
- (14) Shin, K.; Chang, S. *J. Org. Chem.* **2014**, *79*, 12197–12204.
- (15) Jang, Y.-J.; Hwang, S.-H.; T.-L. Choi, *Angew. Chem., Int. Ed.* **2017**, *56*, 14474–14478.
- (16) Jang, Y.-J.; Hwang, S.-H.; Noh, J.; T.-L. Choi, *Macromolecules* **2018**, *51*, 7476–7482.
- (17) Chou, P. T.; Martinez, M. L.; Clements, J. H. *J. Phys. Chem.* **1993**, *97*, 2618–2622.
- (18) Swinney, T. C.; Kelley, D. F. *J. Chem. Phys.* **1993**, *99*, 211–221.
- (19) Klymchenko, A. S.; Pivovarenko, V. G.; Ozturk, T.; Demchenko, A. P. *New J. Chem.* **2003**, *27*, 1336–1343.
- (20) Chou, P.-T.; Huang, C.-H.; Pu, S.-C.; Cheng, Y.-M.; Liu, Y.-H.; Wang, Y.; Chen, C.-T. *J. Phys. Chem. A* **2004**, *108*, 6452–6454.
- (21) Chen, K.-Y.; Hsieh, C.-C.; Cheng, Y.-M.; Lai, C.-H.; Chou, P.-T. *Chem. Commun.* **2006**, *42*, 4395–4397.
- (22) Hsieh, C.-C.; Jiang, C.-M.; Chou, C.-M. *Acc. Chem. Res.* **2010**, *43*, 1364–1374.
- (23) Kwon, J. E.; Park, S. Y. *Adv. Mater.* **2011**, *23*, 3615–3642.
- (24) Park, S.; Kwon, J. E.; Park, S. Y. *Phys. Chem. Chem. Phys.* **2012**, *14*, 8878–8884.
- (25) Demchenko, A. P.; Tang, K.-C.; Chou, P.-T. *Chem. Soc. Rev.* **2013**, *42*, 1379–1408.

- (26) Furukawa, S.; Shono, H.; Mutai, T.; Araki, K. *ACS Appl. Mater. Interfaces* **2014**, *6*, 16065–16070.
- (27) Tseng, H.-W.; Lin, T.-C.; Chen, C.-L.; Lin, T.-C.; Chen, Y.-A.; Liu, J.-Q.; Hung, C.-H.; Chao, C.-M.; Liu, K.-M.; Chou, P.-T. *Chem. Commun.* **2015**, *51*, 16099–16102.
- (28) Padalkar, V. S.; Seki, S. *Chem. Soc. Rev.* **2016**, *45*, 169–202.
- (29) Stasyuk, A. J.; Chen, Y.-T.; Chen, C.-L.; Wu, P.-J.; Chou, P.-T. *Phys. Chem. Chem. Phys.* **2016**, *18*, 24428–24436.
- (30) Park, S.; Kwon, J. E.; Kim, S. H.; Seo, J.; Chung, K.; Park, S.-Y.; Jang, D.-J.; Medina, B. M.; Gierschner, J.; Park, S. Y. *J. Am. Chem. Soc.* **2009**, *131*, 14043–14049.
- (31) Zhang, Z.; Chen, Y.-A.; Hung, W.-Y.; Tang, W.-F.; Hsu, Y.-H.; Chen, C.-L.; Meng, F.-Y.; Chou, P.-T. *Chem. Mater.* **2016**, *28*, 8815–8824.
- (32) Sengupta, P. K.; Kasha, M. *Phys. Lett.* **1979**, *68*, 382–385.
- (33) Pant, D. D.; Josh, H. C.; Bisht, P. B.; Tripathi, H. B. *Chem. Phys.* **1994**, *185*, 137–144.
- (34) Bisht, P. B.; Tripathi, H. B.; Pant, D. D. *J. Photochem. Photobiol. A* **1995**, *90*, 103–108.
- (35) Frisch, M. J.; Trucks, G. W.; Schlegel, H. B.; Scuseria, G. E.; Robb, M. A.; Cheeseman, J. R.; Scalmani, G.; Barone, V.; Mennucci, B.; Petersson, G. A. Gaussian 09, revision A.02; Gaussian, Inc.: Wallingford, CT, 2009.
- (36) Waser, J.; Gaspar, B.; Nambu, H.; Carreira, E. M. *J. Am. Chem. Soc.* **2006**, *128*, 11693–11712.
- (37) Ryu, J.; Shin, K.; Park, S. H.; Kim, J. Y.; Chang, S. *Angew. Chem., Int. Ed.* **2012**, *51*, 9904–9908.
- (38) Peng, H.; Ma, J.; Luo, W.; Zhang, G.; Yin, B. *Green Chem.* **2019**, *21*, 2252–2256.
- (39) Yao, B.; Wang, Q.; Zhu, J. *Angew. Chem., Int. Ed.* **2013**, *52*, 12992–12996.
- (40) Ling, K.-Q.; Sayre, L. M. *J. Org. Chem.* **2009**, *74*, 339–350.
- (41) Amaro, M.; Brezovký, J.; Kováčová, S.; Maier, L.; Chaloupková, R.; Sýkora, J.; Paruch, K.; Damborský, J.; Hof, M. *J. Phys. Chem. B* **2013**, *117*, 7898–7906.
- (42) Tarannum, N.; Chauhan, M.; Soni, R. K.; Teotia, M. *New J. Chem.* **2019**, *43*, 7972–7983.
- (43) Kamlet, M. J.; Abboud, J.-L. M.; Abraham, M. H.; Taft, R. W. *J. Org. Chem.* **1983**, *48*, 2877–2887.

**Chapter 4. Powerful Direct C–H Amidation
Polymerization Affords Single-Fluorophore-Based
White-Light-Emitting Polysulfonamides by Fine-
Tuning Hydrogen Bonds**

4.1. Abstract

The development of white-light-emitting polymers has been actively pursued because of the importance of such polymers in various applications, such as lighting sources and displays. To generate white-light, numerous research efforts have focused on synthesizing multi-fluorophore-based random copolymers to effectively cover the entire visible region. However, due to their intrinsic synthetic and structural features, this strategy has limitations in securing color reproducibility and stability. In this chapter, we demonstrate the development of single-fluorophore-based white-light-emitting homopolymers with excellent color reproducibility. A powerful direct C–H amidation polymerization (DCAP) strategy enabled the synthesis of defect-free polysulfonamides that emit white-light via excited-state intramolecular proton-transfer (ESIPT). To gain structural insights for designing such polymers, we conducted detailed model studies by varying the electronic nature of substituents that allow facile tuning of the emission colors. Further analysis revealed precise control of the thermodynamics of the ESIPT process by fine-tuning the strength of the intramolecular hydrogen bond. By applying this design principle to polymerization, we successfully produced a series of well-defined polysulfonamides with single-fluorophore emitting white-light. The resulting polymers emitted consistent fluorescence, regardless of their molecular weights or phases (i.e., solution, powder, or thin film), guaranteeing excellent color reproducibility. With these advantages in hand, we also demonstrated practical use of our DCAP system by fabricating a white-light-emitting coated LED.



4.2. Introduction

White polymer organic light-emitting diodes (WPLEDs) have recently gained tremendous research interest because they can further simplify the fabrication process of full-color displays through combination with color filters.^{1–11}

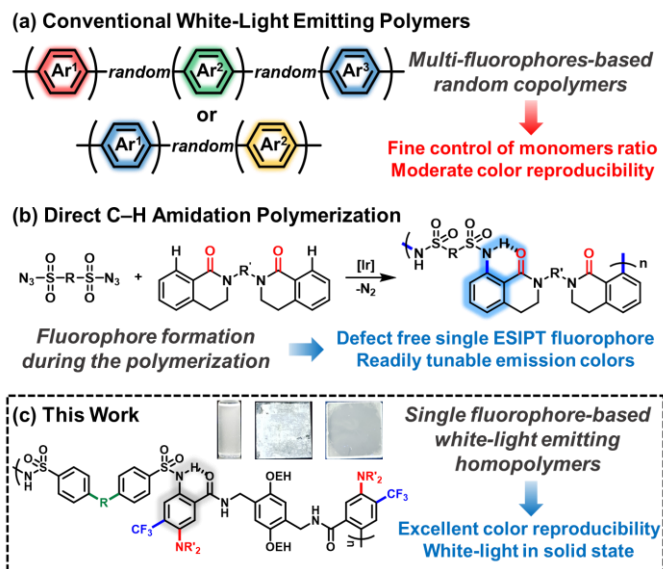


Figure 4.1. (a) Multi-fluorophore-based random copolymers emitting white-light. Single ESIPT fluorophore-based polysulfonamides emitting (b) tunable colors, and (c) white-light via defect-free DCAP.

Most white-light-emitting polymers are prepared as random copolymers, in which multi-component fluorophores emitting three primary colors (red, green, and blue) or at least two complementary colors (blue and yellow) are incorporated into a polymer backbone or side chains to cover the entire visible region ($\lambda = 380$ nm to 780 nm) (Figure 4.1a).^{1–12} However, this multi-fluorophore-based strategy requires a delicate balance of monomer ratios to achieve proper relative emission intensities of multiple fluorophores. Moreover, it is also faced with challenges of color reproducibility and stability that originate from differences in the lifetime of individual fluorescent units. Therefore, it is highly desirable to explore a synthetic method for preparing a new class of single-fluorophore-based white-light-emitting homopolymers that afford high color reproducibility regardless of the synthetic or processing conditions, thereby further improving the device fabrication process.

As described in **Chapter 3**,¹³ we recently reported direct C–H amidation polymerization (DCAP) to produce defect-free polysulfonamides through an atom-economical green method, resulting in blue-light emission with high quantum yields (QYs)

arising from ESIPT process (Figure 4.1b).^{14,15} The DCAP can thus be applicable as a new approach for preparing ESIPT-based fluorescent polymers.^{16–28}

In this chapter, we disclose a design principle to simultaneously achieve dual emission (i.e., blue- and yellow-lights) from a single-fluorophore by systematically modulating intramolecular HBs to control the free energy difference ($\Delta G_{N^* \rightarrow T^*}$) between the excited normal (N^*) and tautomer (T^*) forms that underpin a reversible ESIPT process. On the basis of this strategy, we demonstrate the synthesis of single-fluorophore-based white-light-emitting homopolymers by a powerful DCAP which forms a defect-free single-fluorophore that consistently emits white-light regardless of the molecular weights or phases, thereby ensuring excellent color reproducibility (Figure 4.1c). Because this polymer emits white-light even in the solid state (powder and thin film) without the help of another matrix, we could easily fabricate white-light-emitting coated LED by a solution process.

4.3. Results and Discussion

To gain structural insights into white-light-emitting polymers, we began small molecule-based model studies by adjusting the electronics of substituents to fine-tune the emission properties. From previous research (**Chapter 3**),²⁹ it was noted that the reference molecule (**REF** in Scheme 4.1, **3g** in **Chapter 3**) emitted yellow-light (tautomer emission at $\lambda_{\max,em} = 562$ nm) simultaneously with minor blue-emission (normal emission at $\lambda_{\max,em} = 452$ nm) with a relative emission intensity (I_N/I_T) of 0.18 in benzene solution (Figures 4.2a and S4.1). This is probably because $-NMe_2$, a strong electron-donating group (EDG), weakened the acidity of the HB donor (sulfonamide N–H), thereby making the ESIPT process slightly reversible. Meanwhile, it is known that white-light emission is possible when I_N/I_T for the dual blue and yellow emission is slightly greater than 1.^{30–42} Since the thermodynamics of the ESIPT process that determines the I_N/I_T value can be controlled by modulating the strength of the intramolecular HB,^{36,37,43,44} we envisioned that white-light emission could be realized by further weakening the HB to induce excited-state tautomerization under equilibrium (i.e., making $\Delta G_{N^* \rightarrow T^*}$ close to 0), thereby increasing I_N/I_T (Figure 4.2b,c). We thus prepared a series of model compounds by DCA reactions of sulfonyl azides (**1**) and benzamides (**2**), in which the electronic properties of substituents are varied to modulate the HB strength (Scheme 4.1).

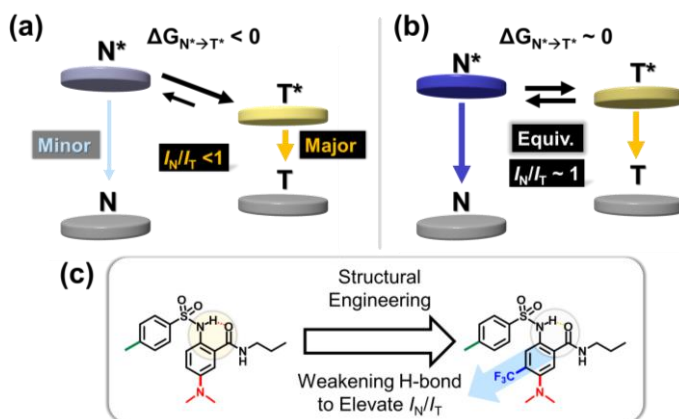
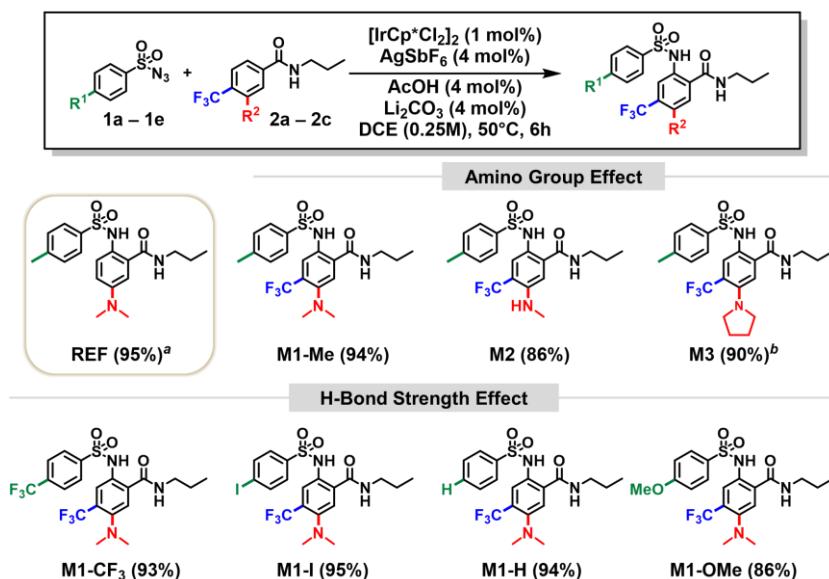


Figure 4.2. Schematic representation of the ESIP processes resulting in (a) tautomer emission as a major de-excitation, and (b) white-light by dual emission from normal (N*) and tautomer (T*) excited-states in equilibrium. (c) Strategy to achieve white-light emission by controlling thermodynamics of ESIP process.

Scheme 4.1. Scope of Direct C–H Amidation* for Model Studies.



*Reaction conditions: **1** (0.2 mmol), **2** (0.2 mmol), [IrCp*Cl₂]₂ (2 μmol), AgSbF₆ (8 μmol), AcOH (8 μmol), Li₂CO₃ (8 μmol) in DCE (0.8 mL) at *T* = 50 °C for 6 h (isolated yields).

^aSynthesized previously (**3g** in chapter 3).¹³ ^b2 mol% of [IrCp*Cl₂]₂.

First, DCA between tosyl azide (**1a**, R¹ = Me) and benzamide (**2a**) produced **M1-Me**, in high yield (94%), containing an additional *para*-CF₃ group to lower the basicity of the HB acceptor (carbonyl group). Next, to understand the effect of the electron-donating power of the *meta*-amino group (R²) on the fluorescence, we synthesized **M2** and **M3**

through DCAs of **1a** with **2b** and **2c**, containing *meta*-NHMe and *meta*-pyrrolidyl, respectively, in high yields (86% and 90%). Lastly, regarding the scope of sulfonyl azides, we varied the R¹-substituent at the *para*-position of the sulfonamide to determine how the electronics affects the ESIPT process. Accordingly, representative sulfonyl azides (**1b–1e**) were subjected to DCA reactions with benzamide (**2a**) to afford **M1-CF₃**, **M1-I**, **M1-H**, and **M1-OMe** in consistently high yields (86–95%). Here, the electronic controller group is varied systematically from the electron-withdrawing –CF₃ to the electron-donating –OMe. Overall, the excellent efficiency of this DCA reaction, regardless of the electronic variation of the substrates, suggested that analogous polymerization would be possible.

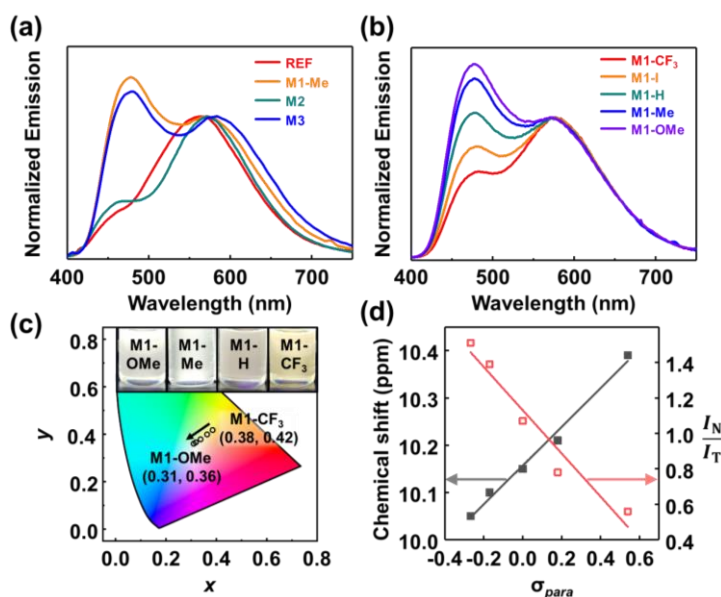


Figure 4.3. Substituent effect on photophysical and chemical properties of model compounds in benzene (sample concentration = 10 μ M) at $T = 298$ K. (a) Normalized emission spectra of **REF**, **M1-Me**, **M2**, and **M3**. (b) Normalized emission spectra and (c) the corresponding CIE coordinates of M1 series molecules: **M1-CF₃** (0.38, 0.42); **M1-I** (0.36, 0.40); **M1-H** (0.34, 0.38); **M1-Me** (0.32, 0.36); **M1-OMe** (0.31, 0.36). (d) Plots showing correlation between *para*-Hammett constants (σ_{para}) and chemical shifts of sulfonamide N–H protons in CDCl₃ (in black), or relative emission intensities (I_N/I_T) in benzene (in red).

With these compounds in hand, we investigated their structure–property relationships, especially the photophysics (Figure 4.3). As anticipated, the –CF₃ group in **M1-Me** led to red-shifts of both the N* and T* emissions ($\lambda_{max,em} = 472$ nm and 580 nm, respectively) and, more significantly, increased the I_N/I_T values from 0.18 to 1.39 for **REF** and **M1-Me**, respectively. Gratifyingly, **M1-Me** in benzene afforded white-light emission

with CIE coordinates of (0.32, 0.36), which is very close to the ideal white-light with the value of (0.33, 0.33) (Figures 4.3a and S4.2a,d).

We note that the I_N/I_T parameters are heavily dependent upon the electron-donating ability of the *meta*-amino substituent. The weaker electron-donating methyl amino group in **M2** favored excited-state tautomerization, thereby producing yellow-light emission with $I_N/I_T = 0.37$ ($\lambda_{\max,em} = 460$ nm and 574 nm for N* and T* emissions, respectively). In stark contrast, the strong electron-donating pyrrolidyl group in **M3** significantly reduced the excited-state tautomerization, leading to I_N/I_T of 1.26, which is similar to that of **M1-Me** ($\lambda_{\max,em} = 474$ nm and 592 nm for N* and T* emissions, respectively) (Figures 4.3a and S4.2b,c). As a result, **M3** also exhibited white-light emission with CIE coordinates of (0.34, 0.37) (Figure S4.2d). Furthermore, **M1-Me** and **M3** displayed white-light emissions in other non-polar solvents as well, such as toluene and xylenes. In particular, **M3** showed near-ideal white-light in xylenes with CIE coordinates of (0.33, 0.35) (Figures S4.3 and S4.4).

As the next step, we investigated the photophysical properties of the **M1** series molecules, in which the acidity of the sulfonamide N–H proton could be systematically controlled by varying the electronic nature of the R¹-substituent. With increasing electron-donation, the I_N/I_T value of the dual emission ($\lambda_{\max,em} = 472$ nm and 580–582 nm for N* and T* emissions, respectively) gradually increased: 0.56, 0.78, 1.07, 1.39, and 1.51 for **M1-CF₃**, **M1-I**, **M1-H**, **M1-Me**, and **M1-OMe**, respectively (Figures 4.3b and S4.5). Accordingly, **M1-OMe** also emitted white-light with CIE coordinates of (0.31, 0.36), similar to **M1-Me** (Figure 4.3c). Notably, for the **M1** series, both the chemical shifts of the sulfonamide N–H protons in the ¹H NMR spectra (in CDCl₃) and the I_N/I_T parameters showed good linear relationships with the *para*-Hammett constants (σ_{para}) (Figure 4.3d). In other words, the HB strength in both the ground- and excited-states can be effectively controlled by modulating the electronic properties of the *para*-substituent of the sulfonamide fragment.

To better understand the effect of HB on the emission process, we measured time-resolved photoluminescence (TRPL) and excitation (Figures S4.6 and S4.7). Regardless of the I_N/I_T values, all **M1** series molecules displayed superimposable fluorescence decay curves and excitation spectra. These observations implicate that the N* and T* excited-states quickly equilibrate before emission occurs. With little dependence on the *kinetics* of such partitioning, the key I_N/I_T parameter can be controlled in a straightforward manner by the *thermodynamic* consideration of HB strength alone.

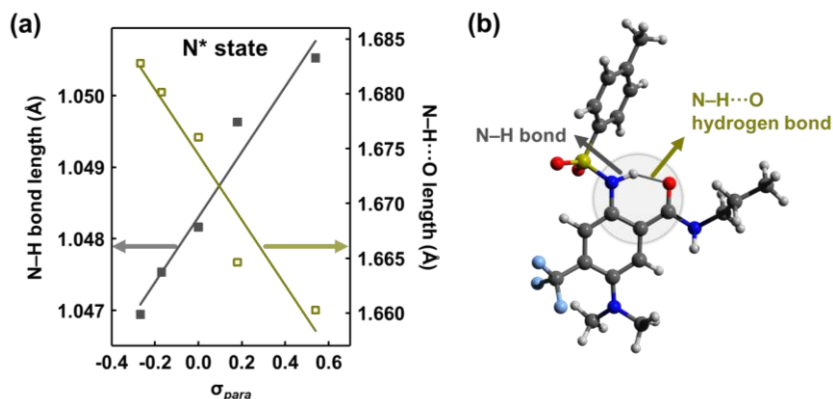


Figure 4.4. Substituent effect on HB strength of **M1** series molecules. (a) Plots showing correlation between *para*-Hammett constants (σ_{para}) and calculated N–H bond length or HB length (between hydrogen and HB acceptor) in the first excited-state of the normal form (N^*). (b) Energy-minimized structure of M1-Me in the N^* state (TD-DFT, M06/6-31++G(d,p) level of theory).

Table 4.1. Parameters Related to Excited-State Tautomer Equilibrium.

Compound	I_N/I_T	$\Delta G_{N^* \rightarrow T^*}$ (eV) ^a	$\Delta G_{N^* \rightarrow T^*}$ (eV) ^b	Dipole moment (N*/T*, Debye) ^b
M1-CF ₃	0.56	-0.022	-0.093	10.532/15.247
M1-I	0.78	-0.013	-0.085	9.323/14.495
M1-H	1.07	-0.005	-0.037	8.636/14.007
M1-Me	1.39	0.001	-0.009	8.322/13.785
M1-OMe	1.51	0.003	0.056	7.775/13.325

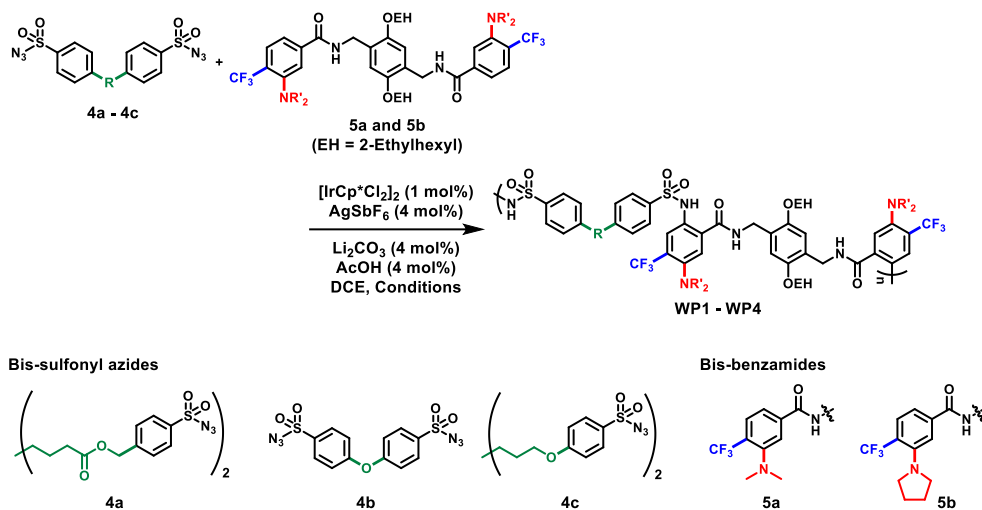
^aSemi-experimental values estimated according to literature methods.^{39,41} ^bTheoretical values determined by DFT/TD-DFT calculations.

A detailed understanding of the relationship among the HB strength, $\Delta G_{N^* \rightarrow T^*}$, and I_N/I_T was aided by density functional theory (DFT) and time-dependent DFT (TD-DFT) calculations. We found that the -CF₃ substituent effectively increases the HB length (N–H...O) in the N^* state (Figure S4.8; 1.662 Å and 1.680 Å for **REF** and **M1-Me**, respectively) and shifts the excited-state equilibrium toward N^* (Figure S4.9; $\Delta G_{N^* \rightarrow T^*}$ = -0.12 eV and -0.01 eV for **REF** and **M1-Me**, respectively). We subsequently investigated the correlation between σ_{para} and the parameters related to HB in the excited-state geometries of the **M1** series molecules. Consistent with the trend of the HB strength in the

ground-state confirmed by ^1H NMR spectroscopy (Figure 4.3d), the calculated N–H (or O–H) bond lengths and N–H \cdots O (or O–H \cdots N) HB lengths (between hydrogen and HB acceptor) in the excited-states N* and T* show excellent linear correlations with the σ_{para} values (Figures 4.4 and S4.10). These results corroborate the notion that the acidity of the sulfonamide N–H group dictates the HB strength in the excited-states as well as in the ground-states. Moreover, we found that the HB strength also impacts the thermodynamic equilibrium between N* and T* (Figure S4.11). With decreasing HB strength, the calculated $\Delta G_{\text{N}^* \rightarrow \text{T}^*}$ values increased gradually from -0.093 eV to $+0.056$ eV, rendering the ESIPT process thermodynamically less favorable. In accordance with this trend, the semi-experimental $\Delta G_{\text{N}^* \rightarrow \text{T}^*}$ values derived from fluorescence and TRPL spectral data also increased gradually from -0.022 eV to $+0.003$ eV (Table 4.1). In other words, both theory and experiments established that the white-light emission can be fine-tuned by controlling the HB strength to modulate the thermodynamics of the ESIPT process.

While investigating the effects of solvent on the ESIPT process, we observed that the $I_{\text{N}}/I_{\text{T}}$ value for **M1-Me** gradually decreased as the solvent polarity increased. For example, in cyclohexane, a non-polar solvent similar to benzene, **M1-Me** showed white-light emission with CIE coordinates of (0.31, 0.34) and $I_{\text{N}}/I_{\text{T}}$ of 1.32. However, in polar solvents, such as chloroform and THF, the T* emissions became dominant ($I_{\text{N}}/I_{\text{T}} = 0.87$ and 0.39 for chloroform and THF, respectively), to produce yellow fluorescence (Figures S4.12a–e). Consistent with the trend for $I_{\text{N}}/I_{\text{T}}$, the semi-experimental and theoretical $\Delta G_{\text{N}^* \rightarrow \text{T}^*}$ values both indicated that ESIPT became more favorable with increasing solvent polarity: from -0.0006 eV to -0.03 eV for semi-experimental estimation; from -0.009 eV to -0.03 eV for DFT/TD-DFT computation (Figure S4.12f). Such solvatochromic behavior can be rationalized by a larger dipole moment of the T* state relative to the corresponding N* state (Table 4.1), which results in its preferential stabilization in polar environment to facilitate the ESIPT process.³⁶

Table 4.2. White-Light-Emitting Polysulfonamides Prepared by Direct C–H Amidation Polymerization.



Entry	Polymer	Benz- amide	Sulfonyl azide	Temp.	Conc.	Time	Conv. ^a	M_n (\bar{M}) ^b	Yield ^c
1	WP1	3a	4a	50 °C	0.5 M	16 h	>99%	46.9 k (1.49)	99%
2	WP2	3b	4a	50 °C	1.5 M	13 h	98%	12.6 k (1.57)	94%
3	WP3	3c	4a	60 °C	0.25 M	5 h	>99%	30.2 k (1.76)	81%
4	WP4	3b	4b	50 °C	0.5 M	3 h	94%	24.3 k (2.70)	92%

^aDetermined by ¹H NMR analysis of the crude reaction mixture. ^bAbsolute molecular weights determined by THF SEC using a multiangle laser light scattering (MALLS) detector. ^cIsolated yields after purification from methanol.

On the basis of the structure–photophysical property relationship established by the small molecule model systems, we designed bis-sulfonyl azides (**3a–3c**) with an EDG linker (R) and two bis-benzamides (**4a** and **4b**) containing *para*-CF₃, *meta*-dialkylamino groups, and solubilizing 2-ethylhexyl (EH) side chains (Table 4.2). First, we attempted DCAP with 1 mol% of [IrCp*Cl₂]₂ using bis-sulfonyl azide (**3a**) bearing methylene linker and bis-benzamide (**4a**) with the –NMe₂ group at 0.25 M, and obtained polysulfonamide (**WP1**) with a number-average molecular-weight (M_n) of 5.9 kDa (Table S4.1, entry 1). Gratifyingly, doubling the concentration significantly increased the M_n and yield to 46.9 kDa and 99%, respectively (entry 1 in Table 4.2; see Table S4.1 for details). The DCAP of **4a** with other bis-sulfonyl azides (**3b** and **3c**) containing ether groups furnished **WP2** and **WP3**, respectively. Likewise, by optimization of the conditions, **WP2** and **WP3** with M_n of

12.6 kDa and 30.2 kDa, respectively, were obtained with excellent conversions (entries 2 and 3, respectively; see Table S4.1 for details). Lastly, **3b** and bis-benzamide (**4b**) containing pyrrolidyl group produced **WP4** with a M_n of 24.3 kDa (entry 4; see Table S4.1 for details). In all cases, minimal cyclization occurred, where the size exclusion chromatography (SEC) traces showed good Gaussian distributions (Figure S4.15).

The resulting polysulfonamides showed sharp and well-resolved chemical shifts, so that the detailed microstructures could be easily determined by ^1H and ^{13}C NMR spectroscopy (Figure 4.5 for **WP1**). Notably, the sulfonamide proton signals (p peak for **WP1**) of all the resulting polymers appeared at 9.69–10.60 ppm region as sharp singlets in the ^1H NMR spectra. These highly downfield-shifted N–H peaks, compared to 7 ppm for the typical proton in sulfonamide,⁴⁵ support selective formation of intramolecular HBs along the polymer backbone via DCAP, producing defect-free ESIPT fluorophores.

With these polysulfonamides, we investigated their fluorescence properties. All the polymers emitted white-light as a result of dual emissions ($I_N/I_T > 1$), as expected (Figures 4.6a,c, S4.16, and S4.17). Specifically, the CIE coordinates of **WP1** and **WP2** are (0.33, 0.38) in benzene, which are similar to those of the model compounds. Notably, the emission of **WP4** with the CIE coordinates of (0.33, 0.36) is closest to ideal white-light (Figure 4.6b). While **WP3** showed low solubility in non-polar solvents, it emitted white-light with CIE coordinates of (0.33, 0.38) even in moderately polar solvents such as chlorobenzene, chloroform, and 1,2-dichloroethane (DCE), in which other polymers emitted yellow-lights (Figure 4.6d). This quite unusual solvent polarity-independent photophysics of **WP3** might be rationalized by the strong electron-donating alkoxy linkers in **WP3** that sufficiently stabilize the N^* state to reduce ESIPT even in polar solvents. Alternatively, a decrease in the local dipole moment, as observed in the **M1** series models (Table 4.1), would make **WP3** less sensitive to the surrounding environment. Accordingly, all polysulfonamides produced white-light emissions in non-polar or polar solvents with up to 3-fold enhancement in QY (13%) compared with the partial ESIPT quenching strategy that we reported in **Chapter 3**¹³ (Figures S4.16d and S4.17f). As in the model studies (Figures S4.6 and S4.7), the fluorescence decay curves and the excitation spectra were essentially identical for each emission band of the white-light-emitting polymers (Figures S4.18 and S4.19a–d), which implies that the excited-state equilibrium is fully established prior to the de-excitation. Furthermore, regardless of their molecular weights (ranging from 8.2 kDa to 30.2 kDa), the fluorescence spectra and the emission quantum yields of **WP3** were maintained consistently (Figure S4.20). These properties account for the good color reproducibility achieved by our DCAP strategy.

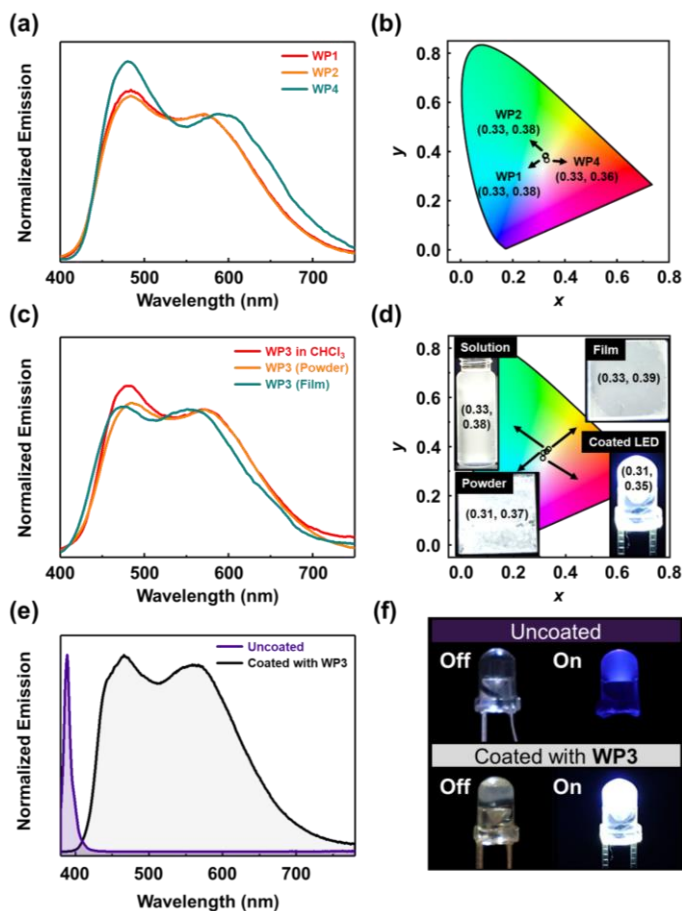


Figure 4.6. (a) Normalized emission spectra, and (b) the corresponding CIE coordinates of **WP1**, **WP2**, and **WP4** in benzene (sample concentration = 10 μM) at $T = 298\text{ K}$. (c) Normalized emission spectra, and (d) the corresponding CIE coordinates of **WP3** in CHCl_3 solution, solid states (powder and thin film), and coated LED. (e) Normalized emission spectra of uncoated LED (in purple) and LED coated with **WP3** (in gray). (f) Photographic images of uncoated LED before and after power on (top): LED coated with **WP3** before and after power on (bottom).

To fabricate a white-light-emitting film using ESIPT fluorophores, an external polymer matrix is typically needed to provide both mechanical property and polarity similar to the solvent in which the materials emit white-light.^{31,36,39} Interestingly, **WP3** itself emitted white-light even in the solid state, either as powder or thin film samples (prepared by spin-coating of a chloroform solution) with CIE coordinates of (0.31, 0.37) and (0.33, 0.39), respectively, and QYs of 16% (Figures 4.6d and S4.17f). We also found that the N^* and T^* excited states of **WP3** were in equilibrium regardless of the polymer phase (Figure S4.19d,e).

The excellent color reproducibility even in the film state without an external matrix is ideal for applying **WP3** as a white-light-emitting bulb. As a proof-of-concept, a polymer-coated LED bulb was easily fabricated by dipping a purple LED bulb into a THF solution of **WP3** several times. The emission wavelength of the bare LED was chosen as 389 nm, similar to the excitation maximum of **WP3** in the solid state (Figure S4.19e; $\lambda_{\text{max,ex}} = 380$ nm). Remarkably, the emission from the bare LED was completely converted to the emission of **WP3** without leaking, to effectively produce dual emission with $I_{\text{N}}/I_{\text{T}} = 1.07$; $\lambda_{\text{max,em}} = 440$ and 569 nm for the N* and T* emissions, respectively (Figures 4.6e and S4.21). As a result, this coated LED successfully generated white-light with CIE coordinates of (0.31, 0.35) (Figure 4.6d,f).

The thermal properties of the polymers were investigated by thermogravimetric analysis (TGA) and differential scanning calorimetry (DSC) (Figures S4.22 and S4.23). **WP1–WP4** showed high decomposition temperatures (T_{d}) of 322–339 °C, indicating excellent thermal stability. All the polymers were amorphous without any melting transition, as judged by DSC analysis; the glass transition temperatures (T_{g}) ranged from 82 to 130 °C depending on the rigidity of the polymer backbones.

4.4. Conclusion

In this chapter, we invented a new class of single-fluorophore-based white-light-emitting homopolymers with excellent color reproducibility by using a powerful DCAP strategy to install defect-free ESIPT fluorophores along the polymer backbone. By taking advantage of the modular synthesis to introduce various substituents, we conducted detailed model studies to precisely control the excited-state energetics of tautomer equilibrium ($\Delta G_{\text{N}^* \rightarrow \text{T}^*}$) by systematically modulating intramolecular HB. After identification of the key design principle to realize white-emission, this approach was extended to DCAP to synthesize high-molecular-weight white-light-emitting homopolymers (up to 47 kDa). The resulting polymers are versatile, reproducibly generating white-light irrespective of their phases (i.e., solution and solid) and molecular weights. The excellent mechanical property and solution processability of the polymers allowed us to demonstrate the practicality of our DCAP strategy by fabricating a coated LED that emits white-light with CIE coordinates of (0.31, 0.35). Overall, this work presents a novel strategy for the synthesis of white-light-emitting polymers by successfully utilizing the design principles learned from model studies to control the bulk properties.

4.5. Experimental Section

Materials

All reagents which are commercially available were used without further purification. Solvents for starting materials synthesis were also commercially obtained. For the Ir-catalyzed C–H amidation of arenes, all solvents and reagents were degassed via three freeze-pump-thaw cycles before the use. Thin-layer chromatography (TLC) was carried out on MERCK TLC silica gel 60 F₂₅₄ and flash column chromatography was performed using MERCK silica gel 60 (0.040–0.063 mm).

Characterization

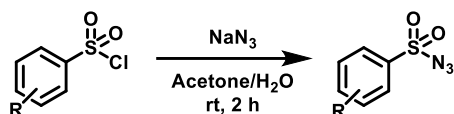
¹H NMR and ¹³C NMR spectroscopies were recorded by Varian/Oxford As-500 (125 MHz for ¹³C NMR) and Agilent 400-MR (5400 MHz for ¹H NMR and 100 MHz for ¹³C NMR) spectrometers. **High resolution mass spectroscopy (HRMS)** analyses were performed by the ultrahigh resolution ESI Q-TOF mass spectrometer (Bruker, Germany) in the Sogang Centre for Research Facilities. **UV-vis spectra** were recorded on V-650 spectrometer with Jasco Inc. software. **Fluorescence spectra** were recorded on a Photon Technology International (PTI) QM-400 spectrofluorometer with FelixGX software. Solution quantum yields were determined by standard methods, using quinine sulfate dihydrate in 0.5 M H₂SO₄ as fluorescence standard. The sample absorbance was maintained <0.1 to minimize internal absorption. Corrections were made to account for the differences in solvent refractive indexes. **Fluorescence decay curves** were recorded on an Edinburgh Instruments FS5 spectrofluorometer equipped with time-correlated single photon counting (TCSPC) module and picosecond pulsed LED (300 nm, EPLED-295). **Size exclusion chromatography (SEC)** analyses were carried out with Waters system (1515 pump and 2707 autosampler) and Shodex GPC LF-804 column eluted with HPLC-grade THF and filtered with a 0.2 μm PTFE filter (Whatman). The flow rate was 1.0 mL/min and temperature of column was maintained at 35 °C. For molecular weight characterization Wyatt DAWN-HELEOS 8+ multi-angle light scatter (MALS) and Wyatt OptiLab T-rEx refractive index (RI) detectors (both maintained at 35 °C) were used. Molecular weights were determined from light scattering using *dn/dc* values calculated from batch mode measurements of polymer solutions at different concentrations. **Thermogravimetric analysis (TGA)** and **differential scanning calorimetry (DSC)** were carried out under N₂ gas at a scan rate of 10 °C/min with Q50 model device (TA Instruments).

Computational Details

Density functional theory (DFT) and time-dependent DFT (TD-DFT) calculations⁴⁶ were carried out using Gaussian 16 suite program.⁴⁷ All geometry optimization and vibrational frequency calculations were carried out with DFT (for N form) or TD-DFT (for N* and T* form) calculation¹ using Minnesota functional, M06,⁴⁸ and 6-31++G(d,p) basis set.⁴⁹ The optimized geometries were verified by frequency calculations: no imaginary frequencies for the minima. Excitation and emission energies for normal and tautomer form were estimated by TD-DFT calculation. Throughout all the theoretical calculation, solvation was considered using self-consistent reaction field (SCRFF) calculation with integral equation formalism of the polarizable continuum model (PCM) of benzene ($\epsilon = 2.27$).⁵⁰

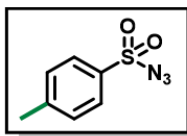
Procedures for the Preparation of Starting Materials

General Procedure for the Preparation of Sulfonyl Azides (**1a–1e**)



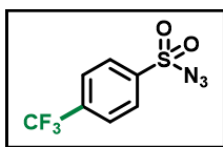
Sulfonyl azides (**1a–1e**) were prepared by the slightly modified procedure from the previous literature.⁵¹ To a stirred solution of sulfonyl chloride (10 mmol, 1.0 eq) in acetone (5 mL), a solution of sodium azide (15 mmol, 1.5 eq) in water (5 mL) was added dropwise at 0°C. The reaction was allowed to warm up to room temperature and stirred for 2 h. The acetone was removed under reduced pressure and the reaction mixture was extracted with EtOAc three times. The combined organic layer was dried over MgSO₄ and concentrated under reduced pressure to afford crude product, which was purified by flash column chromatography on silica gel (*n*-hexane/EtOAc) to obtain the desired product.

Toluenesulfonyl azide (**1a**)



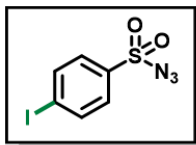
Colorless liquid (1.87 g, 95%), purified by flash column chromatography on silica gel (*n*-hexane/EtOAc = 10/1, $R_f = 0.4$); The structure of **1a** was confirmed by comparison of its spectroscopic data with reported data.⁵²

4-(Trifluoromethyl)benzenesulfonyl azide (**1b**)



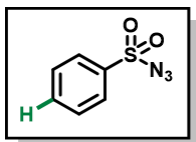
White solid (2.42 g, 96%), purified by flash column chromatography on silica gel (*n*-hexane/EtOAc = 25/1, $R_f = 0.3$); The structure of **1b** was confirmed by comparison of its spectroscopic data with reported data.⁵³

4-Iodobenzenesulfonyl azide (**1c**)



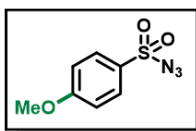
White solid (3.06 g, 99%), purified by flash column chromatography on silica gel (*n*-hexane/EtOAc = 50/1, R_f = 0.2); The structure of **1c** was confirmed by comparison of its spectroscopic data with reported data.⁵⁴

Benzenesulfonyl azide (**1d**)



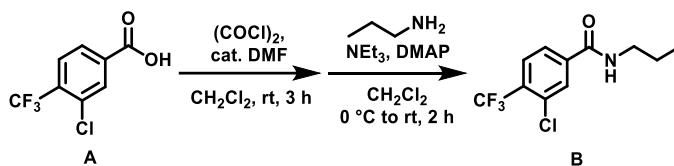
Colorless liquid (1.81 g, 99%), purified by flash column chromatography on silica gel (*n*-hexane/EtOAc = 15/1, R_f = 0.3); The structure of **1d** was confirmed by comparison of its spectroscopic data with reported data.⁵²

4-Methoxybenzenesulfonyl azide (**1e**)



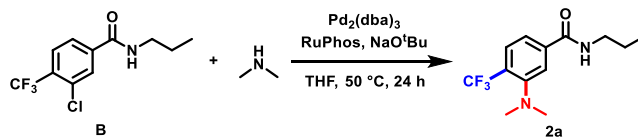
White solid (2.10 g, 99%), purified by flash column chromatography on silica gel (*n*-hexane/EtOAc = 10/1, R_f = 0.2); The structure of **1e** was confirmed by comparison of its spectroscopic data with reported data.⁵²

Preparation of Benzamides (**2a–2c**)



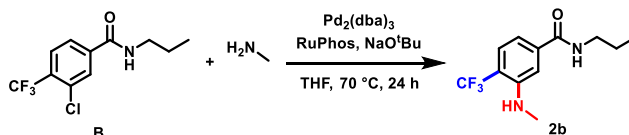
B was prepared by the slightly modified procedure from the previous literature.¹³ To a solution of **A** (6.96 g, 30 mmol) in CH_2Cl_2 (100 mL) was added $(\text{COCl})_2$ (2.94 mL, 33 mmol) and catalytic amount of DMF (4–5 drops). After stirring for 3 h at room temperature, the volatile was removed under reduced pressure. Then CH_2Cl_2 (100 mL) was added followed by addition of 4-dimethylaminopyridine (DMAP, 0.37 g, 3 mmol), *n*-propylamine (2.94 mL, 36 mmol), and triethylamine (6.36 mL, 45 mmol) at 0 °C under Ar atmosphere. After being stirred at room temperature for 2 h, the reaction was quenched with aqueous NaCl solution. The organic fraction was extracted with CH_2Cl_2 three times, dried over MgSO_4 , and concentrated under reduced pressure to afford crude product. The crude mixture was purified by flash column chromatography on silica gel (*n*-hexane/EtOAc = 3/1, R_f = 0.3) to obtain the desired product as a white solid (7.86 g, 29.8 mmol, 99%); ¹H NMR (500 MHz, CDCl_3) δ 7.85 (s, 1H), 7.70 (d, J = 8.0 Hz, 1H), 7.66 (d, J = 8.0 Hz, 1H), 7.00 (s, 1H), 3.37 (dd, J = 13.2, 6.7 Hz, 2H), 1.70–1.54 (m, 2H), 0.94 (t, J = 7.4, 3H). ¹³C NMR (125 MHz, CDCl_3) δ 165.4, 139.5, 132.9, 132.8, 131.0, 130.8, 130.5, 130.3, 130.2, 127.9, 127.8, 127.8, 125.8, 125.3, 123.6, 121.4, 119.2, 42.2, 22.8, 11.5. HRMS (ESI) m/z : $[\text{M} + \text{Na}]^+$ Calcd for $\text{C}_{11}\text{H}_{11}\text{ClF}_3\text{NNaO}$ 288.0373; Found 288.0381.

3-(Dimethylamino)-*N*-propyl-4-(trifluoromethyl)benzamide (2a)



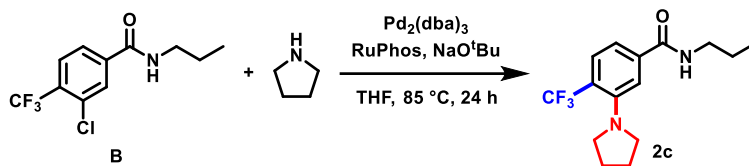
2a was prepared by the slightly modified procedure from the previous literature.⁵⁵ To a flame dried Schlenk tube was added **B** (1.33 g, 5.0 mmol), Pd₂(dba)₃ (0.10 g, 0.10 mmol), RuPhos (0.19 g, 0.40 mmol), and NaO^tBu (0.59 g, 6.0 mmol). Then, dimethylamine (10 mL, 20 mmol, 2M in THF) was added under Ar atmosphere. After stirring for 24 h at 50 °C, the reaction was quenched with aqueous NH₄Cl solution at 0 °C. The organic fraction was extracted with CH₂Cl₂ three times, dried over MgSO₄, and concentrated under reduced pressure to afford crude product. The crude mixture was purified by flash column chromatography on silica gel (*n*-hexane/EtOAc = 3/1, R_f = 0.2) to afford the desired product as a white solid (1.27 g, 4.65 mmol, 92%); ¹H NMR (400 MHz, CDCl₃) δ 7.74 (s, 1H), 7.59 (d, *J* = 8.2 Hz, 1H), 7.38 (d, *J* = 8.2 Hz, 1H), 6.46 (s, 1H), 3.39 (dd, *J* = 13.7, 6.5 Hz, 2H), 2.74 (s, 6H), 1.69–1.54 (m, 2H), 0.96 (t, *J* = 7.4 Hz, 3H). ¹³C NMR (100 MHz, CDCl₃) δ 166.7, 154.1, 154.1, 139.1, 139.1, 128.1, 128.0, 127.9, 127.9, 127.7, 127.4, 127.1, 125.3, 122.6, 121.7, 120.7, 119.8, 45.5, 42.0, 23.0, 11.5. HRMS (ESI) *m/z*: [M + Na]⁺ Calcd for C₁₃H₁₇F₃N₂NaO 297.1185; Found 297.1186.

3-(Methylamino)-*N*-propyl-4-(trifluoromethyl)benzamide (2b)



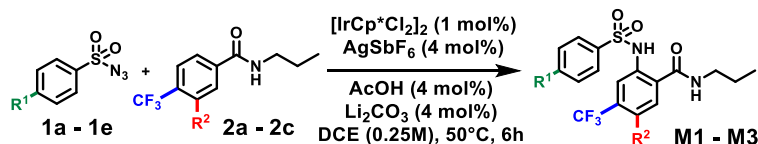
To a flame dried Schlenk tube were added **B** (1.33 g, 5.0 mmol), Pd₂(dba)₃ (0.14 g, 0.15 mmol), RuPhos (0.29 g, 0.60 mmol), and NaO^tBu (0.59 g, 6.0 mmol). Then, methylamine (10 mL, 20 mmol, 2M in THF) was added under Ar atmosphere. After stirring for 24 h at 70 °C, the reaction was quenched with aqueous NH₄Cl solution at 0 °C. The organic fraction was extracted with CH₂Cl₂ three times, dried over MgSO₄, and concentrated under reduced pressure to afford crude product. The crude mixture was purified by flash column chromatography on silica gel (*n*-hexane/EtOAc = 2/1, R_f = 0.2) to afford the desired product as a white solid (1.12 g, 4.32 mmol, 86%); ¹H NMR (400 MHz, CDCl₃) δ 7.40 (d, *J* = 8.0 Hz, 1H), 7.14 (s, 1H), 6.94 (d, *J* = 7.9 Hz, 1H), 6.50 (s, 1H), 4.52 (s, 1H), 3.38 (dd, *J* = 13.2, 6.6 Hz, 2H), 2.89 (d, *J* = 4.7 Hz, 3H), 1.68–1.54 (m, 2H), 0.95 (t, *J* = 7.3 Hz, 3H). ¹³C NMR (100 MHz, CDCl₃) δ 167.4, 146.9, 146.9, 139.6, 128.9, 127.0, 126.9, 126.8, 126.8, 126.2, 123.5, 120.8, 115.8, 115.5, 115.2, 114.9, 113.1, 110.4, 41.9, 30.4, 22.9, 11.5. HRMS (ESI) *m/z*: [M + Na]⁺ Calcd for C₁₂H₁₅F₃N₂NaO 283.1029; Found 283.1031.

N-Propyl-3-(pyrrolidin-1-yl)-4-(trifluoromethyl)benzamide (**2c**)



To a flame dried Schlenk tube were added **B** (1.33 g, 5.0 mmol), Pd₂(dba)₃ (0.047 g, 0.05 mmol), RuPhos (0.095 g, 0.20 mmol), and NaO^tBu (0.59 g, 6.0 mmol). Then, pyrrolidine (0.84 mL, 10 mmol) and THF (10 mL) were added under Ar atmosphere. After stirring for 24 h at 85 °C, the reaction mixture was quenched with aqueous NH₄Cl solution at 0 °C, extracted with CH₂Cl₂ three times, dried over MgSO₄, and concentrated under reduced pressure to afford crude product. The crude mixture was purified by flash column chromatography on silica gel (*n*-hexane/EtOAc = 3/1, R_f = 0.2) to afford the desired product as a white solid (1.27 g, 4.65 mmol, 92%); ¹H NMR (400 MHz, CD₂Cl₂) δ 7.54 (d, *J* = 8.2 Hz, 1H), 7.36 (s, 1H), 7.06 (d, *J* = 8.2 Hz, 1H), 6.63 (s, 1H), 3.42–3.25 (m, 6H), 1.90 (q, *J* = 6.2 Hz, 4H), 1.68–1.51 (m, 2H), 0.93 (t, *J* = 7.4 Hz, 3H). ¹³C NMR (100 MHz, CD₂Cl₂) δ 167.2, 148.6, 139.1, 129.2, 129.0, 129.0, 128.9, 128.8, 126.5, 123.8, 121.1, 118.9, 118.6, 118.3, 118.0, 116.6, 115.0, 51.9, 51.9, 51.9, 51.8, 42.2, 26.1, 23.2, 11.6. HRMS (ESI) *m/z*: [M + Na]⁺ Calcd for C₁₅H₁₉F₃N₂NaO 323.1342; Found 323.1343.

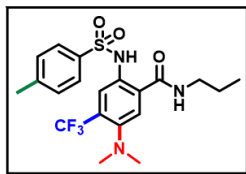
General Procedure for the Preparation of Model Compounds (**M1–M3**)



A 4 mL-sized screw-cap vial with septum and a magnetic stir bar were dried in oven for 30 min. To the vessel were loaded sulfonyl azide (**1**, 0.2 mmol), benzamide (**2**, 0.2 mmol, 1.0 equiv), [IrCp*Cl₂]₂ (1.59 mg, 2 μmol, 1 mol%), AgSbF₆ (2.80 mg, 8 μmol, 4 mol%), Li₂CO₃ (0.59 mg, 8 μmol, 4 mol%), AcOH (8 μmol, 4 mol%), and degassed anhydrous 1,2-dichloroethane (0.8 mL, 0.25 M) under argon atmosphere. The reaction mixture was stirred at 50 °C using pie-block for 6 h and then filtered through a pad of celite with CH₂Cl₂. The volatile was evaporated under reduced pressure and the residue was purified by flash column chromatography on silica gel (*n*-hexane/EtOAc) to afford the desired product (**M1–M3**).

5-(Dimethylamino)-2-((4-methylphenyl)sulfonamido)-*N*-propyl-4

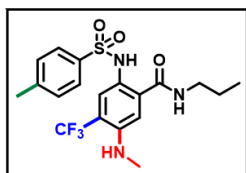
(trifluoromethyl)benzamide (M1-Me)



2 mol% of $[\text{IrCp}^*\text{Cl}_2]_2$ was added. White solid (83.3 mg, 94%), purified by flash column chromatography on silica gel (*n*-hexane/EtOAc = 2/1, R_f = 0.16); $^1\text{H NMR}$ (500 MHz, CDCl_3) δ 10.10 (s, 1H), 7.88 (s, 1H), 7.70 (d, J = 8.3 Hz, 2H), 7.23 (d, J = 8.1 Hz, 2H), 7.18 (s, 1H), 5.95 (s, 1H), 3.30 (dd, J = 13.9, 6.4 Hz, 2H), 2.69 (s, 6H), 2.38 (s, 3H), 1.63–1.56 (m, 2H), 0.96 (t, J = 7.4 Hz, 3H). $^{13}\text{C NMR}$ (100 MHz, CDCl_3) δ 167.3, 149.2, 149.2, 144.1, 136.4, 133.6, 129.8, 129.5, 129.2, 128.9, 128.6, 127.4, 127.3, 126.4, 124.6, 121.8, 121.2, 121.2, 121.1, 121.1, 121.0, 119.1, 45.7, 42.0, 22.7, 21.6, 11.5. **HRMS (ESI)** m/z : $[\text{M} + \text{Na}]^+$ Calcd for $\text{C}_{20}\text{H}_{24}\text{F}_3\text{N}_3\text{NaO}_3\text{S}$ 466.1383; Found 466.1384.

5-(Methylamino)-2-((4-methylphenyl)sulfonamido)-*N*-propyl-4

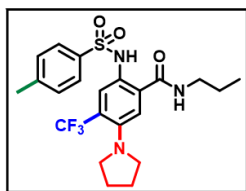
(trifluoromethyl)benzamide (M2)



White solid (73.8 mg, 86%), purified by flash column chromatography on silica gel (*n*-hexane/EtOAc = 2/1, R_f = 0.1); $^1\text{H NMR}$ (400 MHz, CDCl_3) δ 9.29 (s, 1H), 7.66 (s, 1H), 7.49 (d, J = 8.1 Hz, 2H), 7.15 (d, J = 8.1 Hz, 2H), 6.54 (s, 1H), 6.13 (s, 1H), 4.45 (d, J = 3.7 Hz, 1H), 3.14 (dd, J = 13.8, 6.6 Hz, 2H), 2.84 (d, J = 4.9 Hz, 3H), 2.34 (s, 3H), 1.53–1.39 (m, 2H), 0.90 (t, J = 7.4 Hz, 3H). $^{13}\text{C NMR}$ (100 MHz, CDCl_3) δ 167.5, 144.0, 144.0, 143.7, 136.1, 130.7, 129.6, 128.2, 127.4, 125.5, 125.4, 124.3, 124.2, 124.2, 124.1, 122.8, 120.0, 116.4, 116.1, 115.8, 115.5, 109.0, 41.9, 30.5, 22.6, 21.6, 11.5. **HRMS (ESI)** m/z : $[\text{M} + \text{Na}]^+$ Calcd for $\text{C}_{19}\text{H}_{22}\text{F}_3\text{N}_3\text{NaO}_3\text{S}$ 452.1226; Found 452.1228.

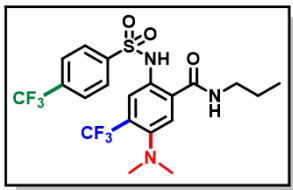
2-((4-Methylphenyl)sulfonamido)-*N*-propyl-5-(pyrrolidin-1-yl)-4

(trifluoromethyl)benzamide (M3)



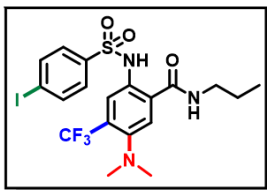
White solid (84.2 mg, 90%), purified by flash column chromatography on silica gel (*n*-hexane/EtOAc = 2/1, R_f = 0.2); $^1\text{H NMR}$ (400 MHz, CDCl_3) δ 9.23 (s, 1H), 7.78 (s, 1H), 7.60 (d, J = 8.2 Hz, 2H), 7.19 (d, J = 8.2 Hz, 2H), 6.81 (s, 1H), 5.93 (s, 1H), 3.29 (t, J = 6.1 Hz, 4H), 3.21 (dd, J = 14.0, 6.3 Hz, 2H), 2.37 (s, 3H), 1.98–1.90 (m, 4H), 1.55–1.45 (m, 2H), 0.93 (t, J = 7.4 Hz, 3H). $^{13}\text{C NMR}$ (100 MHz, CDCl_3) δ 167.6, 144.9, 143.6, 136.5, 129.6, 129.3, 128.0, 127.6, 126.9, 125.3, 124.9, 124.9, 124.8, 124.7, 122.6, 120.0, 119.8, 119.7, 115.2, 51.7, 51.7, 41.9, 25.8, 22.7, 21.7, 11.6. **HRMS (ESI)** m/z : $[\text{M} + \text{Na}]^+$ Calcd for $\text{C}_{22}\text{H}_{26}\text{F}_3\text{N}_3\text{NaO}_3\text{S}$ 492.1539; Found 492.1541.

5-(Dimethylamino)-*N*-propyl-4-(trifluoromethyl)-2-((4-(trifluoromethyl)phenyl)sulfonamido)benzamide (M1-CF₃)



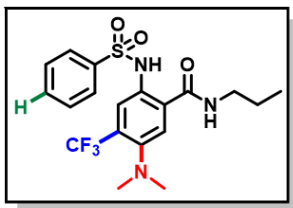
White solid (92.4 mg, 93%), purified by flash column chromatography on silica gel (*n*-hexane/EtOAc = 2/1, R_f = 0.25); $^1\text{H NMR}$ (500 MHz, CDCl_3) δ 10.39 (s, 1H), 7.94 (s, 1H), 7.93 (d, J = 8.2 Hz, 2H), 7.70 (d, J = 8.3 Hz, 2H), 7.15 (s, 1H), 5.93 (s, 1H), 3.27 (dd, J = 14.3, 6.2 Hz, 2H), 2.72 (s, 6H), 1.61–1.51 (m, 2H), 0.94 (t, J = 7.4 Hz, 3H). $^{13}\text{C NMR}$ (125 MHz, CDCl_3) δ 167.1, 149.4, 143.1, 135.1, 134.9, 134.6, 134.3, 133.0, 129.4, 129.1, 128.9, 128.7, 127.9, 126.5, 126.4, 126.3, 126.3, 126.2, 124.3, 124.2, 122.2, 122.0, 120.6, 120.00, 119.8, 110.1, 45.6, 42.0, 22.7, 11.5. **HRMS (ESI)** m/z : $[\text{M} + \text{Na}]^+$ Calcd for $\text{C}_{20}\text{H}_{21}\text{F}_6\text{N}_3\text{NaO}_3\text{S}$ 520.1100; Found 520.1101.

5-(Dimethylamino)-2-((4-iodophenyl)sulfonamido)-*N*-propyl-4-(trifluoromethyl)benzamide (M1-I)



White solid (105.4 mg, 95%), purified by flash column chromatography on silica gel (*n*-hexane/EtOAc = 2/1, R_f = 0.18); $^1\text{H NMR}$ (500 MHz, CDCl_3) δ 10.21 (s, 1H), 7.92 (s, 1H), 7.78 (d, J = 8.5 Hz, 2H), 7.49 (d, J = 8.5 Hz, 2H), 7.16 (s, 1H), 5.92 (s, 1H), 3.29 (dd, J = 14.3, 6.2 Hz, 2H), 2.72 (s, 6H), 1.63–1.57 (m, 2H), 0.97 (t, J = 7.4 Hz, 3H). $^{13}\text{C NMR}$ (100 MHz, CDCl_3) δ 167.2, 149.6, 149.6, 139.1, 138.4, 133.0, 129.4, 129.1, 128.8, 128.7, 128.5, 127.3, 126.5, 124.5, 122.0, 122.0, 121.9, 121.9, 121.8, 120.7, 119.1, 100.7, 45.6, 45.6, 42.0, 22.8, 11.6. **HRMS (ESI)** m/z : $[\text{M} + \text{Na}]^+$ Calcd for $\text{C}_{19}\text{H}_{21}\text{F}_3\text{IN}_3\text{NaO}_3\text{S}$ 578.0193; Found 578.0194.

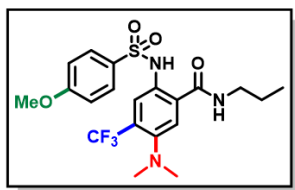
5-(Dimethylamino)-2-(phenylsulfonamido)-*N*-propyl-4-(trifluoromethyl)benzamide (M1-H)



White solid (79.8 mg, 94%), purified by flash column chromatography on silica gel (*n*-hexane/EtOAc = 2/1, R_f = 0.16); $^1\text{H NMR}$ (500 MHz, CDCl_3) δ 10.15 (s, 1H), 7.89 (s, 1H), 7.81 (d, J = 7.6 Hz, 2H), 7.53 (t, J = 7.4 Hz, 1H), 7.44 (t, J = 7.7 Hz, 2H), 7.16 (s, 1H), 5.93 (s, 1H), 3.29 (dd, J = 14.2, 6.2 Hz, 2H), 2.69 (s, 6H), 1.63–1.56 (m, 2H), 0.96 (t, J = 7.4 Hz, 3H). $^{13}\text{C NMR}$ (100 MHz, CDCl_3) δ 167.3, 149.4, 139.2, 133.4, 133.2, 129.4, 129.3, 129.2, 129.1, 128.8, 128.5, 127.3, 126.5, 126.4, 124.6, 121.8, 121.5, 121.4, 121.4, 121.3, 121.0, 119.1, 45.6, 42.0, 22.7, 11.5. **HRMS (ESI)** m/z : $[\text{M} + \text{Na}]^+$ Calcd for $\text{C}_{19}\text{H}_{22}\text{F}_3\text{N}_3\text{NaO}_3\text{S}$ 452.1226; Found

452.1228.

5-(Dimethylamino)-2-((4-methoxyphenyl)sulfonylamido)-*N*-propyl-4-(trifluoromethyl)benzamide (M1-OMe)



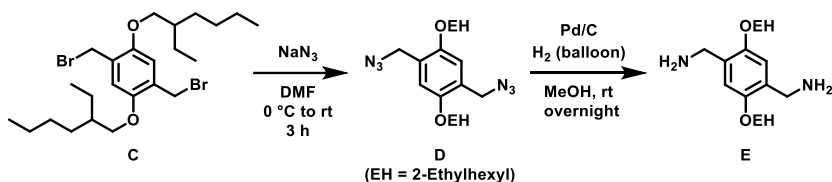
White solid (79.0 mg, 86%), purified by flash column chromatography on silica gel (*n*-hexane/EtOAc = 2/1, R_f = 0.16); $^1\text{H NMR}$ (500 MHz, CDCl_3) δ 10.05 (s, 1H), 7.88 (s, 1H), 7.75 (d, J = 8.9 Hz, 2H), 7.18 (s, 1H), 6.90 (d, J = 8.9 Hz, 2H), 5.94 (s, 1H), 3.83 (s, 3H), 3.32 (dd, J = 13.7, 6.6 Hz, 2H), 2.69 (s, 6H), 1.64–1.55 (m, 2H), 0.97 (t, J = 7.4 Hz, 3H). $^{13}\text{C NMR}$ (100 MHz, CDCl_3) δ 167.3, 163.3, 149.2, 133.7, 130.8, 129.5, 129.4, 129.1, 128.8, 128.6, 128.5, 127.3, 126.3, 124.6, 121.9, 121.2, 121.2, 121.1, 119.1, 114.3, 55.7, 45.7, 42.0, 22.7, 11.4. **HRMS (ESI)** m/z : $[\text{M} + \text{Na}]^+$ Calcd for $\text{C}_{20}\text{H}_{24}\text{F}_3\text{N}_3\text{NaO}_4\text{S}$ 482.1332; Found 482.1332.

Procedures for the Preparation of Monomers

Preparation of Bis-sulfonyl Azides (3a–3c)

3a–3c were prepared according to the previously reported synthetic method.¹⁴

Preparation of Bis-benzamides (4a and 4b)

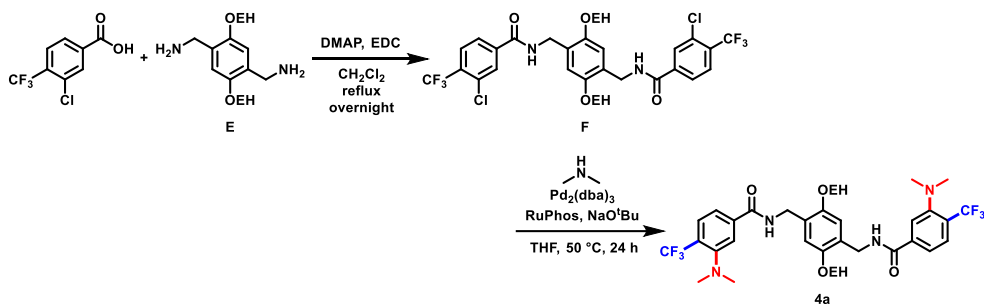


C was prepared according to the previously reported synthetic method.⁵⁶ To a solution of **C** (8.33 g, 16 mmol) in DMF (53 mL) was added NaN_3 (4.20 g, 64 mmol) at 0 °C slowly. After stirring for 3 h at room temperature, the reaction was quenched by aqueous NaCl solution. The mixture was extracted with ether three times, dried over MgSO_4 , and concentrated under reduced pressure to afford crude product. The crude mixture was purified by flash column chromatography on silica gel (*n*-hexane/EtOAc = 60/1, R_f = 0.25) to obtain the desired product (**D**) as a colorless liquid (8.27 g, 18.6 mmol, 86%); $^1\text{H NMR}$ (500 MHz, CDCl_3) δ 6.87 (s, 2H), 4.40 (s, 4H), 3.92–3.84 (m, 4H), 1.82–1.72 (m, 2H), 1.61–1.30 (m, 16H), 1.00–0.90 (m, 12H). $^{13}\text{C NMR}$ (125 MHz, CDCl_3) δ 150.8, 124.6, 113.3, 71.2, 49.9, 39.6, 30.7, 29.2, 24.1, 23.1, 14.2, 11.2. **HRMS (ESI)** m/z : $[\text{M} + \text{Na}]^+$ Calcd for $\text{C}_{24}\text{H}_{40}\text{N}_6\text{NaO}_2$ 467.6132; Found 467.3105.

To a solution of **D** (6.12 g, 13.8 mmol) in MeOH (69 mL) was added Pd/C (2.20 g, 2.07 mmol) and then, H_2 gas (balloon) was added by bubbling in solution. After stirring for

overnight at room temperature, the reaction mixture was filtered through a pad of celite with methanol. The mixture was concentrated under reduced pressure to afford crude product. The crude mixture was purified by flash column chromatography on silica gel (EtOAc = 100 to MeOH = 100) to obtain the desired product (**E**) as a light yellowish solid (4.12 g, 10.5 mmol, yield of 76%); ¹H NMR (500 MHz, CD₃OD) δ 7.10 (s, 2H), 4.05 (s, 4H), 4.01–3.93 (m, 4H), 1.87–1.74 (m, 2H), 1.63–1.24 (m, 16H), 1.05–0.81 (m, 12H). ¹³C NMR (125 MHz, CD₃OD) δ 152.2, 126.1, 114.7, 72.5, 49.0, 40.8, 40.3, 31.7, 30.2, 25.0, 24.1, 14.5, 11.5. HRMS (ESI) m/z: [M + H]⁺ Calcd for C₂₄H₄₅N₂O₂ 393.6353; Found 393.3475.

***N,N'*-((2,5-Bis((2-ethylhexyl)oxy)-1,4-phenylene)bis(methylene))bis(3-(dimethylamino)-4-(trifluoromethyl)benzamide) (**4a**)**

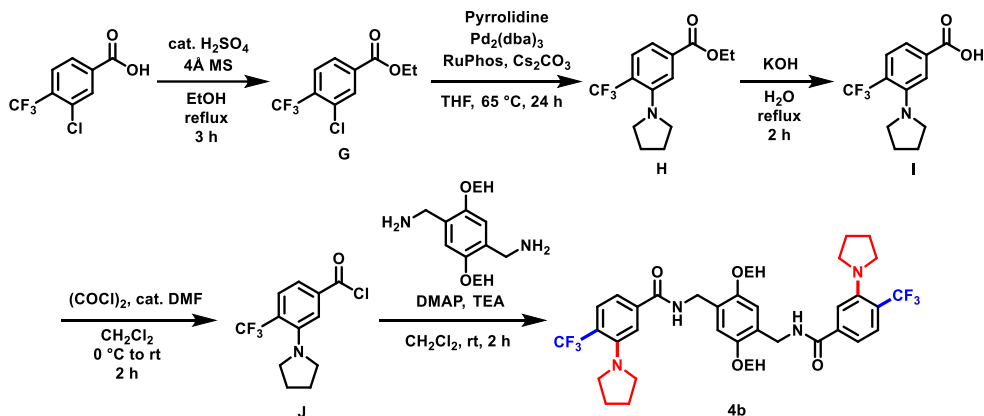


To a solution of 3-chloro-4-(trifluoromethyl)benzoic acid (5.79 g, 25 mmol) and **E** (3.93 g, 10 mmol) in CH₂Cl₂ (67 mL) were added 4-dimethylaminopyridine (0.062 g, 0.5 mmol) and 1-ethyl-3-(3-dimethylaminopropyl)carbodiimide·HCl (6.46g, 33 mmol). After being reflux overnight, the reaction mixture was quenched by aqueous NaCl solution and washed with EtOAc three times. The volatile was evaporated under reduced pressure to afford crude product. The crude mixture was suspended in methanol and filtered. The solid was washed with methanol and dried in vacuo to obtain the desired product (**F**) as a white solid (11.3 g, 14 mmol, 56%); ¹H NMR (400 MHz, CDCl₃) δ 7.84 (s, 2H), 7.73 (d, *J* = 8.2 Hz, 2H), 7.68 (d, *J* = 8.2 Hz, 2H), 6.94 (s, 2H), 6.80 (t, *J* = 5.6 Hz, 2H), 4.61 (d, *J* = 5.6 Hz, 4H), 3.97–3.85 (m, 4H), 1.80–1.66 (m, 2H), 1.56–1.20 (m, 16H), 0.93 (t, *J* = 7.5 Hz, 6H), 0.86 (t, *J* = 7.0 Hz, 6H). ¹³C NMR (100 MHz, CDCl₃) δ 164.6, 151.3, 139.3, 133.1, 133.1, 131.4, 131.1, 130.8, 130.5, 130.1, 128.1, 128.0, 128.0, 127.9, 126.6, 125.9, 125.2, 123.9, 121.2, 118.4, 114.0, 71.0, 41.0, 39.8, 31.0, 29.3, 24.4, 23.1, 14.1, 11.3. HRMS (ESI) m/z: [M + H]⁺ Calcd for C₄₀H₄₉Cl₂F₆N₂O₄ 805.2968; Found 805.2974.

To a flame dried Schlenk tube were added **F** (2.42 g, 3 mmol), Pd₂(dba)₃ (0.14 g, 0.17 mmol), RuPhos (0.29 g, 0.6 mmol), and NaO^tBu (0.74 g, 7.5 mmol). Then, dimethylamine (15 mL, 30 mmol, 2M in THF) was added under Ar atmosphere. After stirring for 24 h at

50 °C, the reaction was quenched by aqueous NH₄Cl solution at 0 °C. The organic fraction was extracted with CH₂Cl₂ three times. The solvents were evaporated under reduced pressure and the residue was purified by flash column chromatography on silica gel (*n*-hexane/EtOAc = 8/1 to 5/1) to afford the desired product (**4a**) as a white solid (1.31 g, 1.59 mmol, 53%); ¹H NMR (500 MHz, CDCl₃) δ 7.77 (s, 2H), 7.61 (d, *J* = 8.2 Hz, 2H), 7.34 (d, *J* = 8.2 Hz, 2H), 6.95 (s, 2H), 6.74 (t, *J* = 5.7 Hz, 2H), 4.61 (d, *J* = 5.8 Hz, 4H), 3.95–3.86 (m, 4H), 2.77 (s, 12H), 1.77–1.68 (m, 2H), 1.53–1.20 (m, 16H), 0.92 (t, *J* = 7.5 Hz, 6H), 0.86 (t, *J* = 7.1 Hz, 6H). ¹³C NMR (125 MHz, CDCl₃) δ 166.1, 153.9, 151.3, 139.0, 128.1, 128.0, 128.0, 127.8, 127.5, 127.3, 127.2, 126.2, 125.0, 122.8, 121.9, 120.7, 120.6, 114.0, 71.0, 45.6, 40.8, 39.8, 31.0, 29.3, 24.4, 23.1, 14.2, 11.4. HRMS (ESI) *m/z*: [M + H]⁺ Calcd for C₄₄H₆₁F₆N₄O₄ 823.4592; Found 823.4595.

***N,N'*-((2,5-Bis((2-ethylhexyl)oxy)-1,4-phenylene)bis(methylene))bis(3-(pyrrolidin-1-yl)-4-(trifluoromethyl)benzamide) (4b)**



To a solution of 3-chloro-4-(trifluoromethyl)benzoic acid (5.80 g, 25 mmol) in EtOH (10 mL), H₂SO₄ (28 mL, 0.5 mmol) and 4 Å molecular sieves were added. After being reflux for 3 h, the reaction was quenched with aqueous NaHCO₃ solution at 0 °C. The organic fraction was extracted with ether three times, dried over MgSO₄, and concentrated under reduced pressure to afford crude product. The crude mixture was purified by column chromatography on silica gel (*n*-hexane/EtOAc = 20/1, R_f = 0.2) to obtain the desired product (**G**) as a colorless liquid (5.5 g, 21.8 mmol, 87%); ¹H NMR (400 MHz, CDCl₃) δ 8.16 (s, 1H), 8.01 (d, *J* = 8.2 Hz, 1H), 7.77 (d, *J* = 8.2 Hz, 1H), 4.42 (q, *J* = 7.1 Hz, 2H), 1.42 (t, *J* = 7.1 Hz, 3H). ¹³C NMR (100 MHz, CDCl₃) δ 164.4, 135.1, 132.9, 132.9, 132.8, 132.8, 132.6, 132.5, 132.5, 132.2, 131.9, 131.6, 127.9, 127.8, 127.8, 127.7, 126.6, 123.9, 121.2, 118.5, 62.1, 14.4. HRMS (ESI) *m/z*: [M + Na]⁺ Calcd for C₁₀H₈ClF₃NaO 275.0057; Found 275.0060.

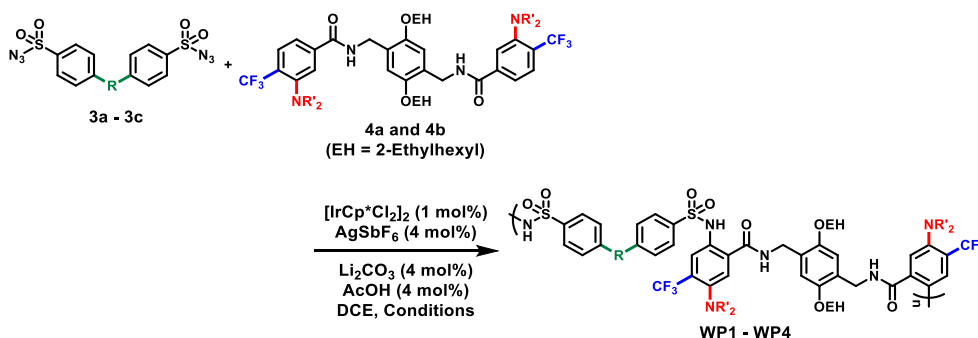
To a flame dried Schlenk tube, were added Pd₂(dba)₃ (0.38 g, 0.4 mmol), RuPhos (0.76 g, 1.6 mmol), and Cs₂CO₃ (13.2 g, 40 mmol). Then, the solution of **G** (5.05 g, 20 mmol) in THF (40 mL) and pyrrolidine (3.3 mL, 40 mmol) were added under Ar atmosphere. After stirring for 24 h at 65 °C, the reaction mixture was quenched by H₂O and washed with EtOAc three times. The solvents were evaporated under reduced pressure and the residue was purified by flash column chromatography on silica gel (*n*-hexane/EtOAc = 50/1, R_f = 0.25) to afford the desired product (**H**) as a colorless liquid (4.13 g, 14.4 mmol, yield of 72%); ¹H NMR (400 MHz, CDCl₃) δ 7.63 (s, 1H), 7.59 (d, *J* = 8.3 Hz, 1H), 7.43 (d, *J* = 8.3 Hz, 1H), 4.38 (q, *J* = 7.1 Hz, 2H), 3.39 (t, *J* = 6.1 Hz, 4H), 2.02–1.91 (m, 4H), 1.40 (t, *J* = 7.1 Hz, 3H). ¹³C NMR (100 MHz, CDCl₃) δ 166.3, 148.0, 133.9, 128.7, 128.7, 128.6, 128.5, 126.0, 123.3, 120.7, 120.6, 120.4, 120.1, 119.7, 118.5, 118.0, 61.4, 51.7, 51.7, 25.8, 14.4. HRMS (ESI) *m/z*: [M + Na]⁺ Calcd for C₁₄H₁₆F₃NNaO₂ 310.1025; Found 310.1028.

To 45% aqueous KOH solution (48 mL) was added **H** (4.12 g, 14 mmol). After being reflux for 2 h, the reaction mixture was cooled to room temperature, and poured onto H₂O (480 mL). The reaction mixture was acidified with HCl until pH 4–5 is reached. The solid was filtered and washed several times with H₂O and *n*-hexane to obtain the desired product (**I**) as a white solid (2.9 g, 11 mmol, 80%); ¹H NMR (500 MHz, CDCl₃) δ 7.68 (s, 1H), 7.66 (d, *J* = 8.3 Hz, 1H), 7.50 (d, *J* = 8.3 Hz, 1H), 3.47–3.36 (m, 4H), 2.05–1.94 (m, 4H). ¹³C NMR (125 MHz, CDCl₃) δ 171.9, 148.0, 132.6, 129.0, 128.9, 128.9, 128.8, 127.8, 125.7, 123.5, 121.3, 121.0, 120.8, 120.5, 120.3, 118.9, 118.3, 51.6, 51.6, 25.9. HRMS (ESI) *m/z*: [M + H]⁺ Calcd for C₁₂H₁₃F₃NO₂ 260.0893; Found 260.0896.

To a solution of **I** (1.04 g, 4 mmol) in CH₂Cl₂ (13 mL) were added (COCl)₂ (0.39 mL, 4.4 mmol) and catalytic amount of DMF (3–4 drops). After stirring for 3 h at room temperature, the volatile was removed under reduced pressure to obtain the acyl chloride (**J**). Then CH₂Cl₂ (13 mL) was added followed by addition of 4-dimethylaminopyridine (0.049 g, 0.4 mmol), **E** (0.71 g, 1.8 mmol) and triethylamine (0.84 mL, 6 mmol) at 0 °C under Ar atmosphere. After being stirred at room temperature for 2 h, the reaction mixture was quenched with aqueous NaCl solution, extracted with CH₂Cl₂ three times, dried over MgSO₄, and concentrated under reduced pressure to afford crude product. The crude mixture was purified by flash column chromatography on silica gel (*n*-hexane/EtOAc = 6/1 to 4/1) to obtain the desired product (**4b**) as a white solid (0.68 g, 0.77 mmol, 42%); ¹H NMR (400 MHz, CDCl₃) δ 7.55 (d, *J* = 8.3 Hz, 2H), 7.40 (s, 2H), 6.95 (d, *J* = 8.3 Hz, 2H), 6.93 (s, 2H), 6.72 (t, *J* = 5.8 Hz, 2H), 4.60 (d, *J* = 5.8 Hz, 4H), 3.95–3.84 (m, 4H), 3.38 (t, *J* = 6.1 Hz, 8H), 2.01–1.89 (m, 8H), 1.78–1.66 (m, 2H), 1.54–1.20 (m, 16H), 0.92 (t, *J* = 7.5 Hz, 6H), 0.86 (t, *J* = 7.0 Hz, 6H). ¹³C NMR (100 MHz, CDCl₃) δ 166.8, 151.3, 148.2,

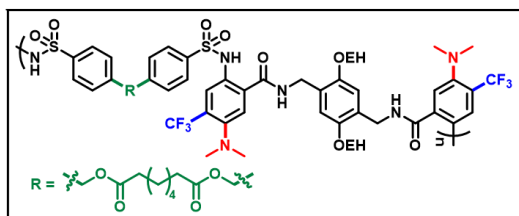
138.3, 129.0, 128.8, 126.2, 126.1, 123.3, 120.6, 119.0, 118.7, 118.4, 118.1, 116.6, 116.3, 114.2, 114.2, 113.9, 113.8, 71.0, 51.5, 51.5, 40.8, 40.7, 40.6, 39.8, 31.0, 29.3, 25.9, 24.3, 23.1, 14.2, 14.1, 11.4, 11.3. **HRMS (ESI)** m/z : $[M + H]^+$ Calcd for $C_{48}H_{65}F_6N_4O_4$ 875.4905; Found 875.4908.

General Procedure for the Polymerization and Characterization of Polymers



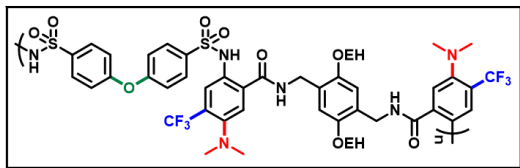
A 4 ml-sized screw-cap vial with septum and a magnetic stir bar were dried in oven for 30 min. Bis-sulfonylazide (**3**, 0.1 mmol), bis-benzamide (**4**, 0.1 mmol), $[IrCp^*Cl_2]_2$, $AgSbF_6$, Li_2CO_3 , $AcOH$, and degassed 1,2-dichloroethane were added under argon atmosphere. The reaction mixture was vigorously stirred at experimental temperature. After experimental reaction time, the reaction mixture was quenched with water and extracted with chloroform, and concentrated under reduced pressure. The crude residue was precipitated in methanol at room temperature. Obtained solid was filtered and dried in vacuo.

WP1



1H NMR (400 MHz, CD_2Cl_2) δ 10.53 (s, 2H), 7.80 (s, 2H), 7.71 (d, $J = 8.0$ Hz, 4H), 7.26 (d, $J = 8.0$ Hz, 4H), 7.23 (s, 2H), 6.95 (s, 2H), 6.84 (s, 2H), 5.00 (s, 4H), 4.52 (d, $J = 5.6$ Hz, 4H), 3.90 (s, 4H), 2.60 (s, 12H), 2.29 (t, $J = 7.5$ Hz, 4H), 1.76–1.65 (m, 2H), 1.61–1.52 (m, 4H), 1.48–1.33 (m, 8H), 1.32–1.14 (m, 12H), 0.86 (t, $J = 7.4$ Hz, 6H), 0.80 (t, $J = 6.7$ Hz, 6H). **^{13}C NMR** (100 MHz, CD_2Cl_2) δ 173.5, 167.3, 151.5, 149.4, 142.2, 139.2, 134.2, 129.8, 129.5, 129.2, 128.9, 128.4, 127.8, 127.7, 126.1, 124.9, 122.2, 121.5, 120.6, 119.5, 113.9, 77.9, 71.7, 65.1, 45.8, 40.6, 40.0, 34.3, 31.1, 29.5, 29.1, 25.6, 25.0, 24.5, 23.4, 14.2, 11.3.

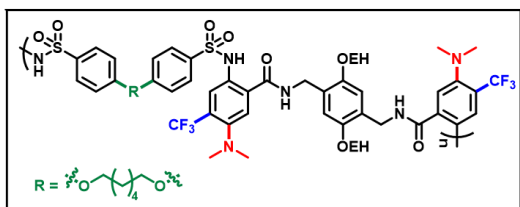
WP2



¹H NMR (400 MHz, CD₂Cl₂) δ 10.60 (s, 2H), 7.82–7.68 (m, 6H), 7.24 (s, 2H), 6.97–6.88 (m, 6H), 6.80 (s, 2H), 4.48 (d, $J = 5.0$ Hz, 4H), 3.89 (s, 4H), 2.62 (s,

12H), 1.78–1.62 (m, 2H), 1.48–1.13 (m, 16H), 0.85 (t, $J = 7.3$ Hz, 6H), 0.80 (t, $J = 6.7$ Hz, 6H). **¹³C NMR** (100 MHz, CD₂Cl₂) δ 167.2, 159.9, 151.5, 149.3, 135.2, 134.2, 130.1, 129.8, 129.5, 129.2, 129.0, 127.6, 126.0, 125.6, 124.9, 122.2, 121.6, 120.2, 119.5, 119.3, 114.0, 78.0, 71.7, 45.8, 40.7, 40.1, 31.0, 29.4, 24.5, 23.4, 14.2, 11.3.

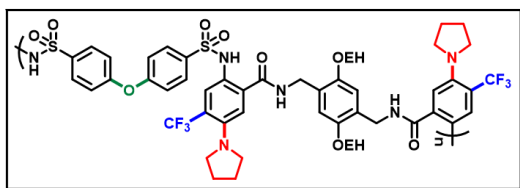
WP3



¹H NMR (400 MHz, CDCl₃) δ 10.32 (s, 2H), 7.77 (s, 2H), 7.66 (d, $J = 8.8$ Hz, 4H), 7.17 (s, 2H), 6.98 (s, 2H), 6.81–6.67 (m, 6H), 4.54 (d, $J = 4.9$ Hz, 4H), 4.00–3.85 (m, 8H), 2.61 (s, 12H), 1.83–

1.67 (m, 6H), 1.54–1.16 (m, 20H), 0.88 (t, $J = 7.5$ Hz, 6H), 0.83 (t, $J = 7.0$ Hz, 6H).

WP4



¹H NMR (400 MHz, CDCl₃) δ 9.69 (s, 2H), 7.66 (s, 2H), 7.63 (d, $J = 8.8$ Hz, 4H), 6.90 (s, 2H), 6.84 (br, 4H), 6.78 (d, $J = 8.8$ Hz, 4H), 4.42 (d, $J = 5.0$ Hz, 4H), 3.95–3.78 (m, 4H), 3.22 (br, 8H),

1.90 (br, 8H), 1.74–1.62 (m, 2H), 1.47–1.15 (m, 18H), 0.86 (t, $J = 7.4$ Hz, 6H), 0.80 (t, $J = 7.0$ Hz, 6H).

4.6. Supporting Information

4.6.1. Photophysical Properties and Thermodynamics of Model Compounds

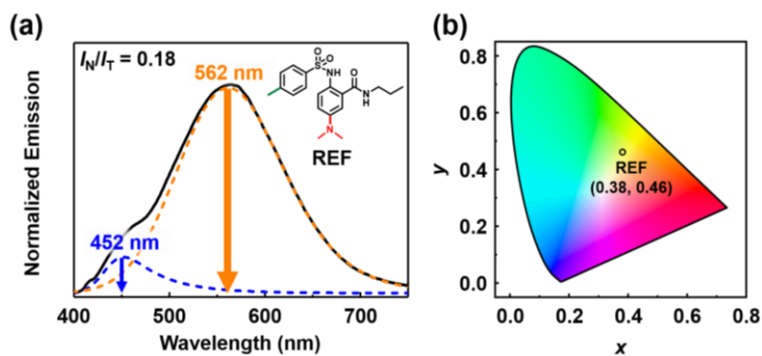


Figure S4.1. Photophysical properties of reference molecule (**REF**) in benzene solution (10 μ M) at 298 K. (a) Normalized emission (solid line) and deconvoluted emission (dashed lines assigned for normal (blue) and tautomer (orange), respectively) spectra and (b) the corresponding 1931 CIE chromaticity diagram.

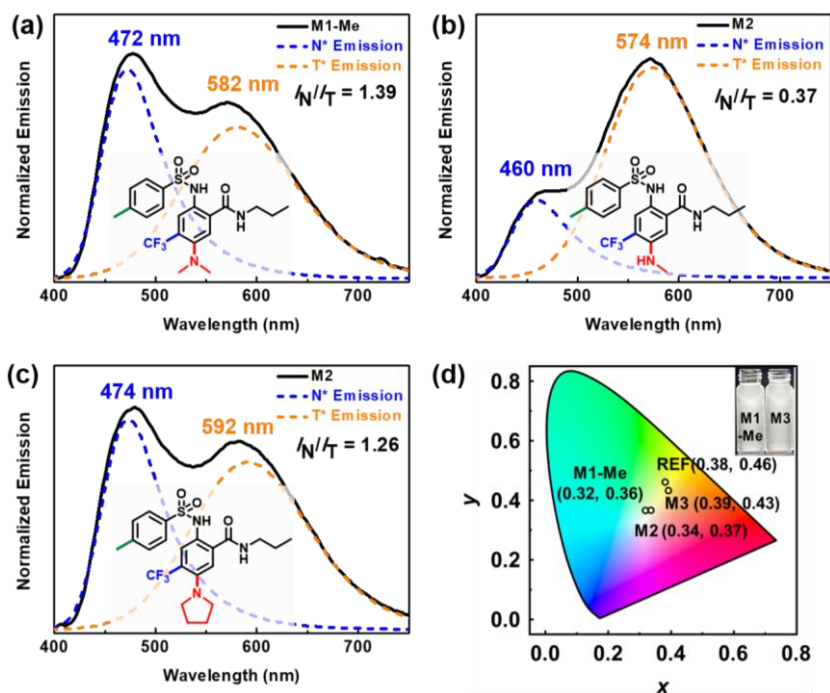


Figure S4.2. Normalized emission (solid lines) and deconvoluted emission (dashed lines assigned for normal (blue) and tautomer (orange), respectively) spectra of (a) **M1-Me**, (b) **M2**, and (c) **M3** in benzene solutions (10 μ M) at 298 K. (d) The corresponding 1931 CIE chromaticity diagram.

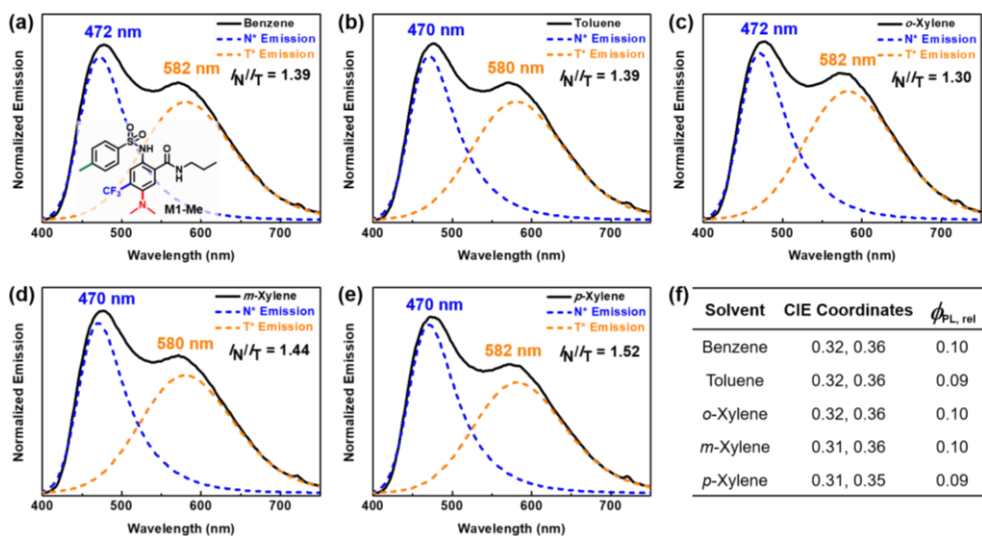


Figure S4.3. Normalized emission (solid lines) and deconvoluted emission (dashed lines assigned for normal (blue) and tautomer (orange), respectively) spectra of **M1-Me** in (a) benzene, (b) toluene, (c) *o*-xylene, (d) *m*-xylene, and (e) *p*-xylene solutions (10 μ M) at 298 K. (f) Table for 1931 CIE coordinates and relative quantum yields determined by quinine sulfate dihydrate in 0.5 M H₂SO₄ as a fluorescence standard.

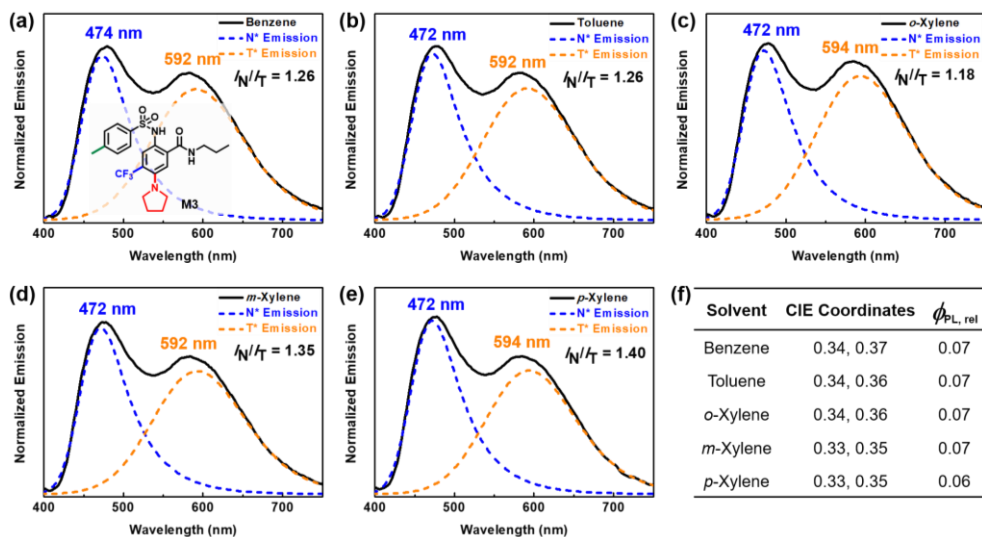


Figure S4.4. Normalized emission (solid lines) and deconvoluted emission (dashed lines assigned for normal (blue) and tautomer (orange), respectively) spectra of **M3** in (a) benzene, (b) toluene, (c) *o*-xylene, (d) *m*-xylene, and (e) *p*-xylene solutions (10 μ M) at 298 K. (f) Table for 1931 CIE coordinates and relative quantum yields determined by quinine sulfate dihydrate in 0.5 M H₂SO₄ as a fluorescence standard.

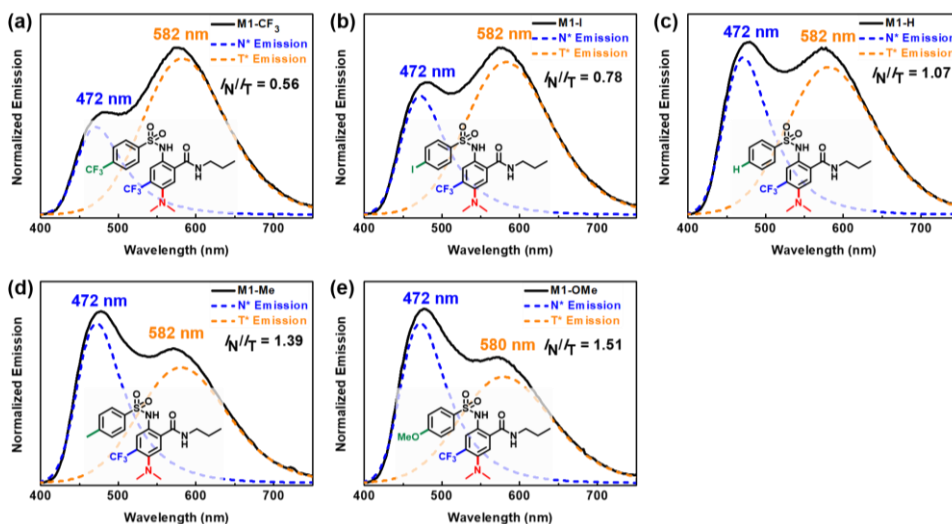


Figure S4.5. Normalized emission (solid lines) and deconvoluted emission (dashed lines) assigned for normal (blue) and tautomer (orange), respectively) spectra of (a) **M1-CF₃**, (b) **M1-I**, (c) **M1-H**, (d) **M1-Me**, and (e) **M1-OMe** in benzene solutions (10 μ M) at 298 K.

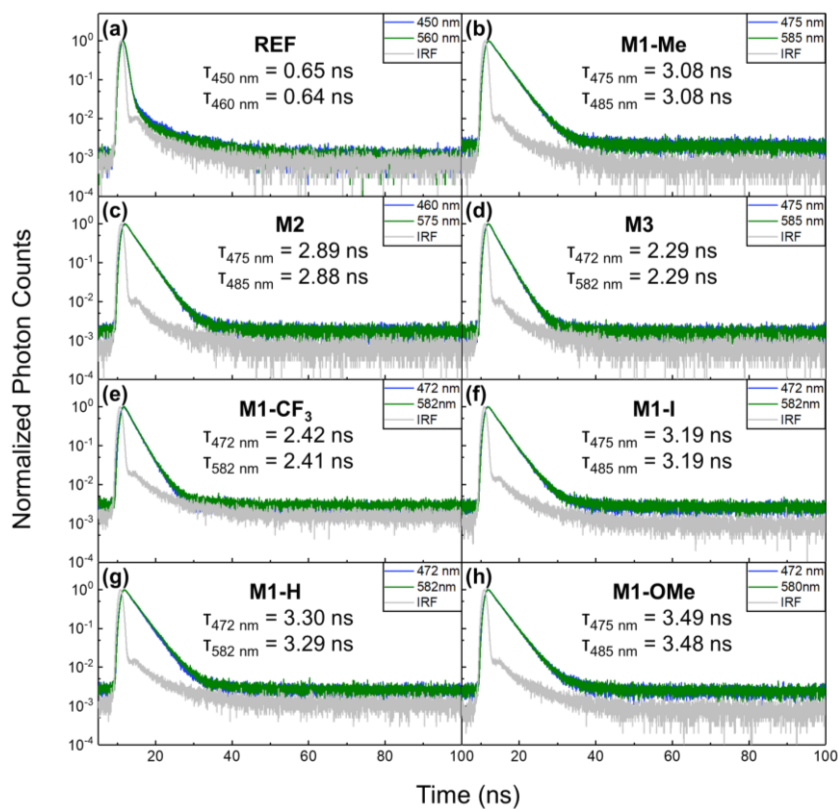


Figure S4.6. Transient photoluminescence spectra of (a) **REF**, (b) **M1-Me**, (c) **M2**, (d) **M3** (e) **M1-CF₃**, (f) **M1-I**, (g) **M1-H**, and (h) **M1-OMe**. Note that the decay curves of blue and yellow emissions are essentially superimposable for all model compounds.

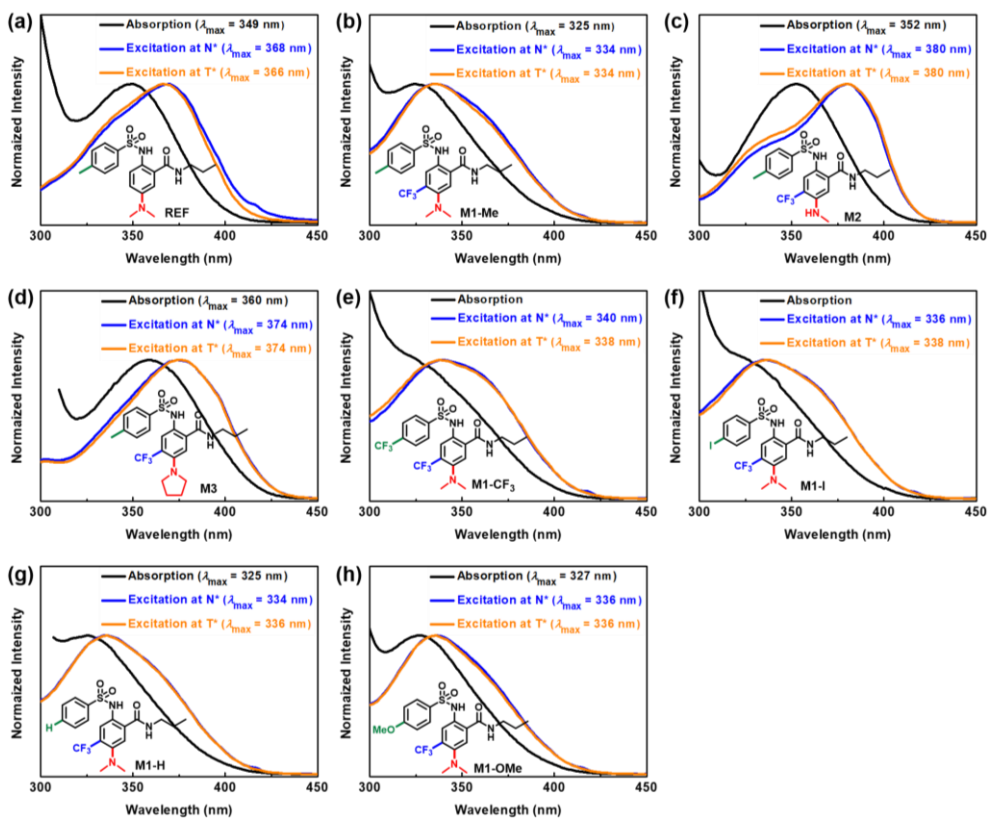


Figure S4.7. Normalized absorption (black lines) and excitation (blue and orange lines monitored at normal and tautomer emissions, respectively) spectra of (a) REF, (b) M1-Me, (c) M2, (d) M3, (e) M1-CF₃, (f) M1-I, (g) M1-H, and (h) M1-OMe in benzene solutions (10 μM) at 298 K.

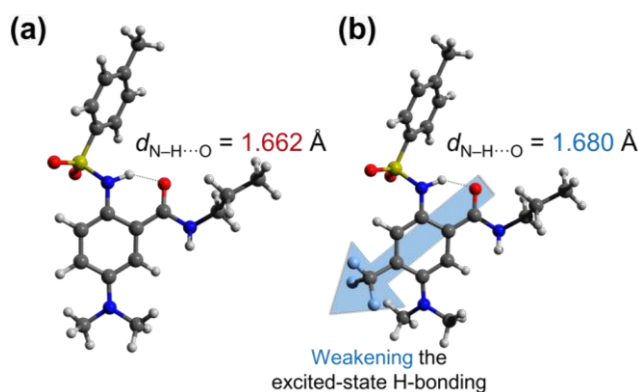


Figure S4.8. Calculated hydrogen bonds lengths in the first excited-state (N^*) of normal form (a) REF and (b) M1-Me (TD-DFT, M06/6-31++G(d,p) level of theory).

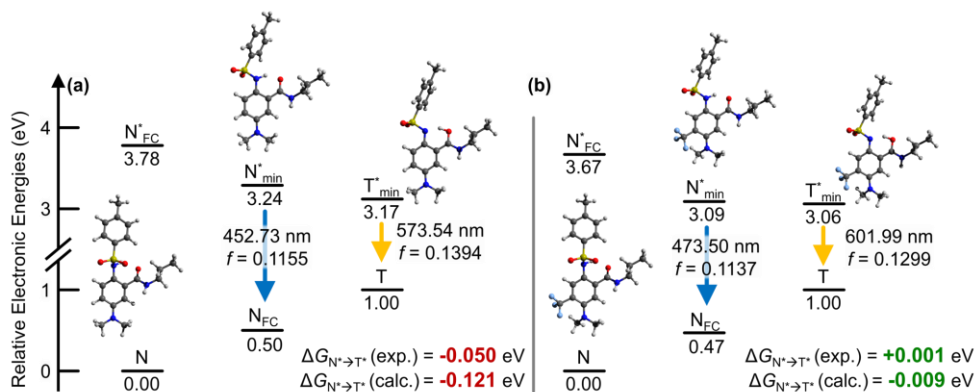


Figure S4.9. Schematic energy diagrams along with energy-minimized geometries related to emission processes and semi-experimental/theoretical $\Delta G_{N' \rightarrow T^*}$ values for (c) **REF** and (d) **M1-Me**. Semi-experimental $\Delta G_{N' \rightarrow T^*}$ values were derived as in the following references.^{39,41}

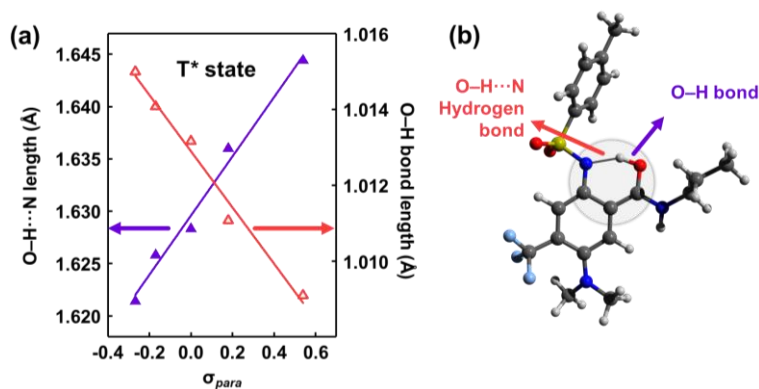


Figure S4.10. (a) Plots showing correlation between σ_{para} and calculated H-bond length (O-H...N) or O-H bond length in the first excited-state of tautomer form (T*). (b) Energy-minimized structure of **M1-Me** in T* state showing the positions of O-H...N hydrogen bond and O-H bond.

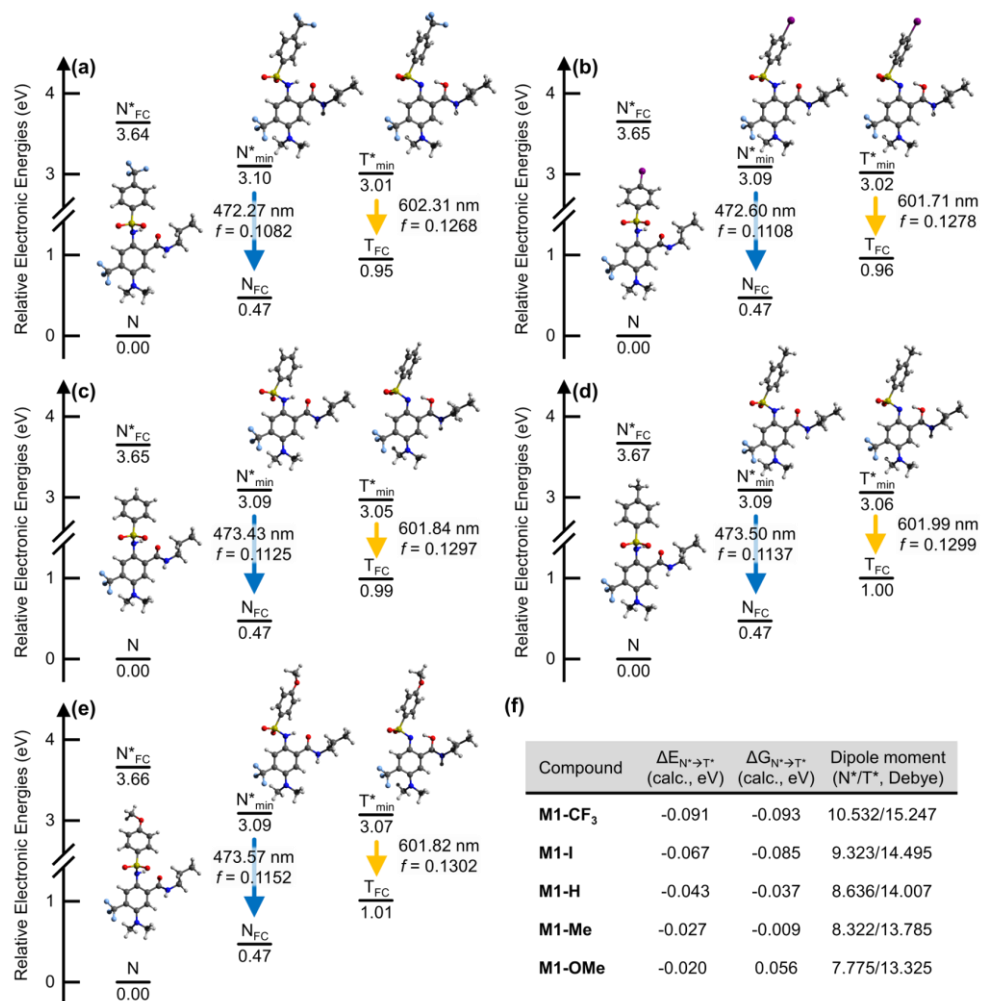


Figure S4.11. Schematic energy diagrams along with energy-minimized geometries related to emission processes for (a) **M1-CF₃**, (b) **M1-I**, (c) **M1-H**, (d) **M1-Me**, and (e) **M1-OMe**. (f) Table for theoretical $\Delta E_{N^* \rightarrow T^*}$, $\Delta G_{N^* \rightarrow T^*}$, and dipole moments of **M1** series.

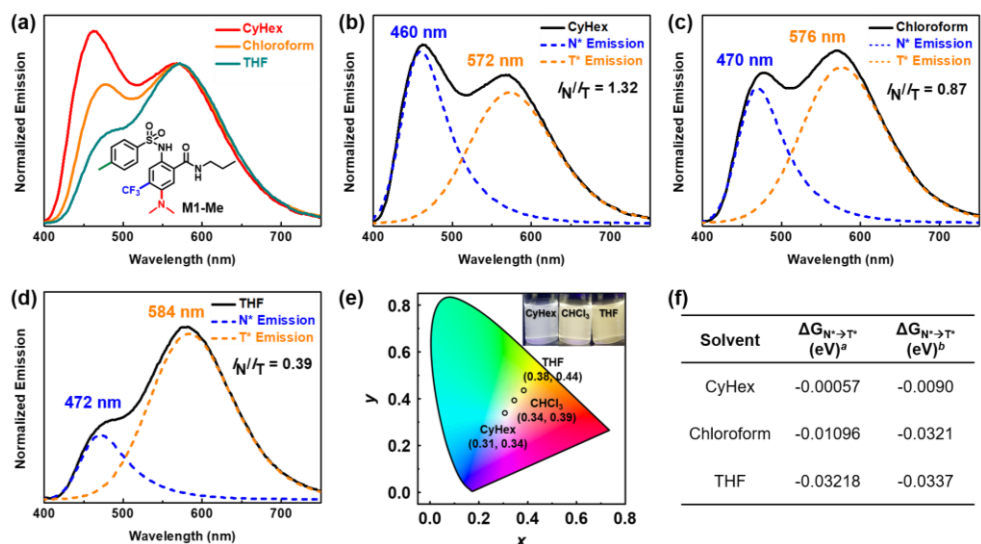


Figure S4.12. Photophysical properties of **M1-Me** in various solutions (10 μ M) at 298 K. (a) Normalized emission spectra of **M1-Me** in cyclohexane (red), chloroform (orange), and THF (green). Normalized emission (solid lines) and deconvoluted emission (dashed lines assigned for normal (blue) and tautomer (orange), respectively) spectra of **M1-Me** in (b) cyclohexane, (c) chloroform, and (d) THF. (e) 1931 CIE chromaticity diagram and photograph of **M1-Me** in cyclohexane, chloroform, and THF. (f) Table for $\Delta G_{N^* \rightarrow T^*}$ values of **M1-Me** in various solutions. ^asemi-experimental values derived as in the following references.^{39,41} ^bTheoretical values by DFT/TD-DFT calculations.

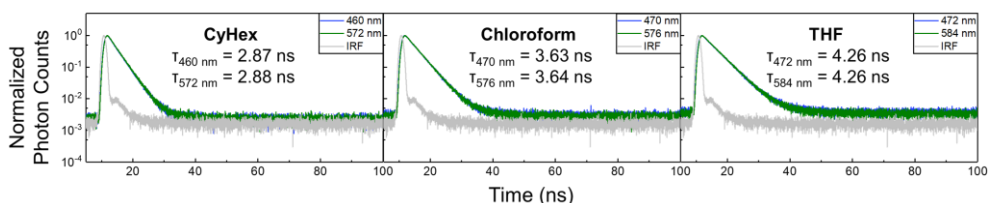


Figure S4.13. Transient photoluminescence spectra of **M1-Me** in cyclohexane (CyHex), chloroform, and THF solutions. Note that the decay curves of blue and yellow emissions are essentially superimposable for all cases.

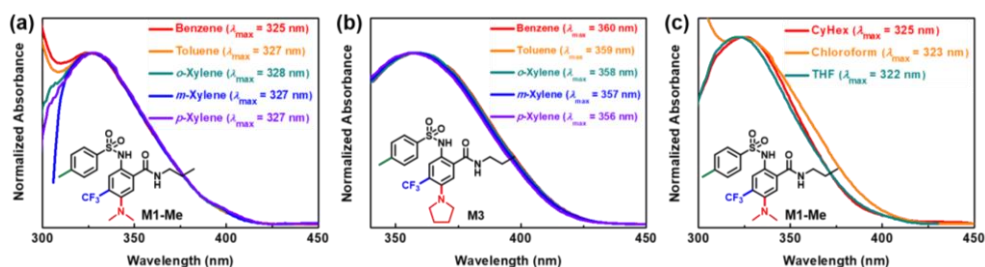
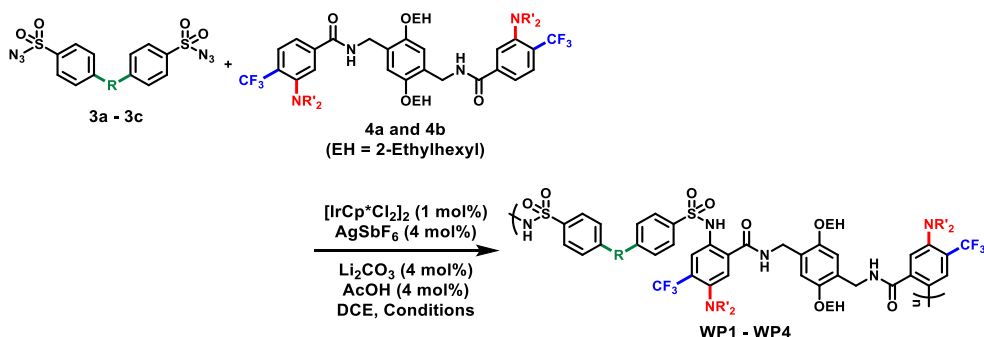


Figure S4.14. Absorption spectra of (a) **M1-Me**, (b) **M3** in non-polar solvents (10 μ M), and (c) **M1-Me** in cyclohexane (CyHex), chloroform, and THF solutions (10 μ M) at 298 K.

4.6.2. Optimization of Polymerization

Table S4.1. Optimization of Polymerization



Entry	Polymer	Benzamide	Sulfonamide	Temp.	Conc.	Time	Conv. ^a	M_n (\bar{D}) ^b	Yield ^c
1	WP1	3a	4a	60 °C	0.25 M	17 h	>99%	5.9 k (1.36)	99%
2	WP1	3a	4a	60 °C	0.4 M	15 h	99%	33.3 k (1.45)	84%
3	WP1	3a	4a	50 °C	0.5 M	16 h	>99%	46.9 k (1.49)	99%
4	WP2	3b	4a	60 °C	0.1 M	17 h	95%	6.3 k (1.42)	87%
5	WP2	3b	4a	60 °C	0.4 M	15 h	94%	10.5 k (1.41)	88%
6	WP2	3b	4a	50 °C	1.25 M	13 h	97%	10.9 k (1.44)	95%
7	WP2	3b	4a	50 °C	1.5 M	13 h	98%	12.6 k (1.57)	94%
8	WP3	3c	4a	25 °C	0.1 M	24 h	95%	8.2 k (1.19)	54%
9	WP3	3c	4a	60 °C	0.1 M	5 h	97%	11.4 k (1.39)	70%
10	WP3	3c	4a	60 °C	0.25 M	5 h	>99%	30.2 k (1.76)	81%
11	WP4	3b	4b	60 °C	0.25 M	6 h	96%	12.0 k (2.25)	81%
12	WP4	3b	4b	50 °C	0.5 M	3 h	94%	24.3 k (2.70)	92%

^aDetermined by ¹H NMR analysis of the crude reaction mixture. ^bAbsolute molecular weights determined by THF SEC using a multiangle laser light scattering (MALLS) detector. ^cIsolated yields after purification from methanol.

4.6.4. SEC Traces of Polymers

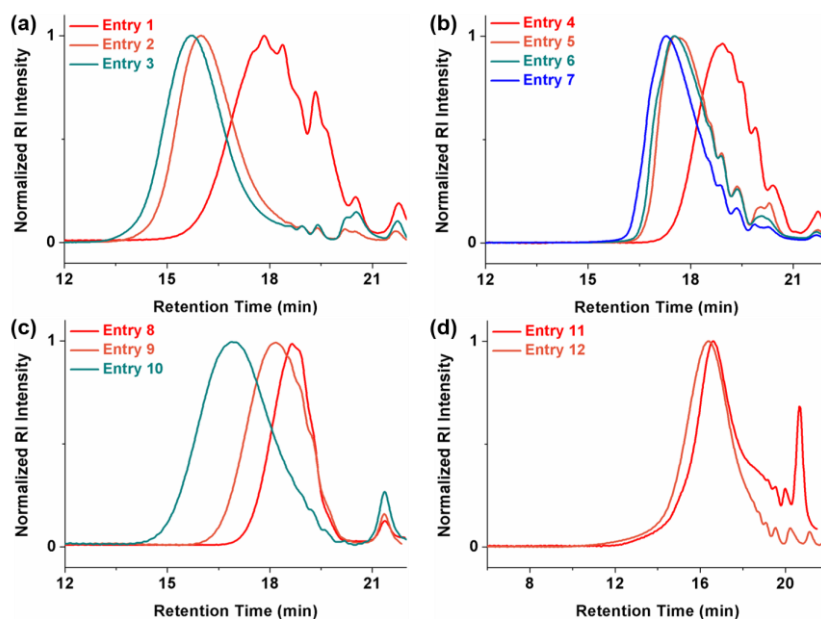


Figure S4.15. SEC traces for polymers in Table 4.1. (a) **WP1** (entries 1–3). (b) **WP2** (entries 4–7). (c) **WP3** (entries 8–10). (d) **WP4** (entries 11 and 12).

4.6.5. Photophysical Properties of Polymers

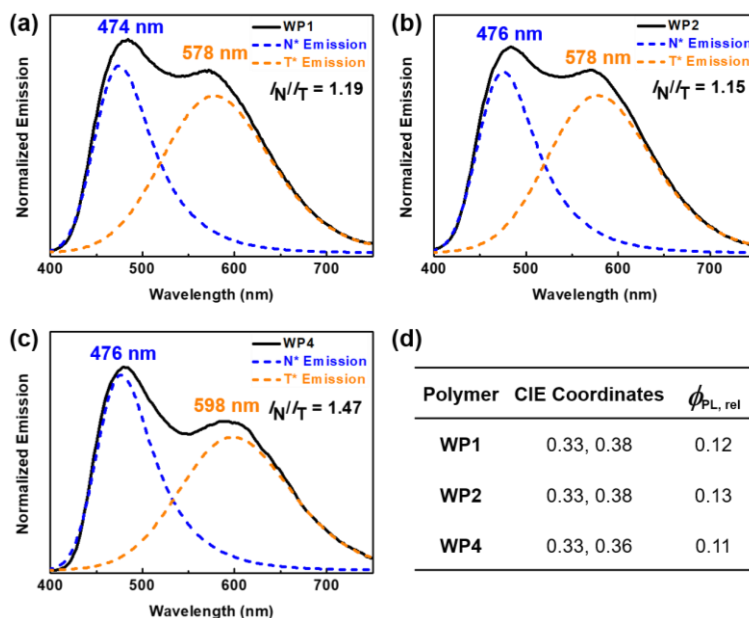


Figure S4.16. Normalized emission (solid lines) and deconvoluted emission (dashed lines assigned for normal (blue) and tautomer (orange), respectively) spectra of (a) **WP1**, (b) **WP2**, and (c) **WP4** in benzene solutions (10 μ M) at 298 K. (d) Table for 1931 CIE coordinates and relative quantum yields determined by quinine sulfate dihydrate in 0.5 M H_2SO_4 as a fluorescence standard.

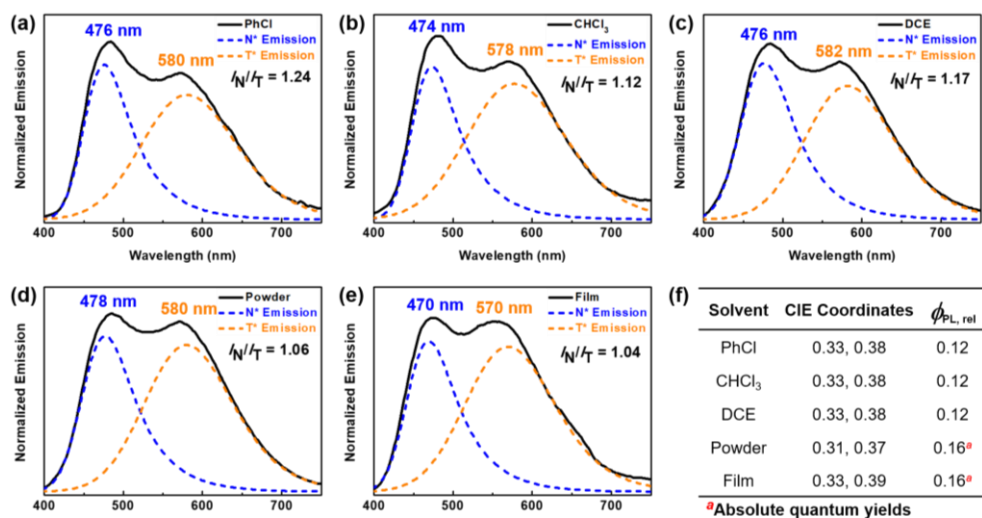


Figure S4.17. Normalized emission (solid lines) and deconvoluted emission (dashed lines assigned for normal (blue) and tautomer (orange), respectively) spectra of **WP3** in (a) chlorobenzene, (b) chloroform, (c) 1,2-dichloroethane, (d) powder, and (e) film state. (f) Table for 1931 CIE coordinates and relative quantum yields determined by quinine sulfate dihydrate in 0.5 M H₂SO₄ as a fluorescence standard.

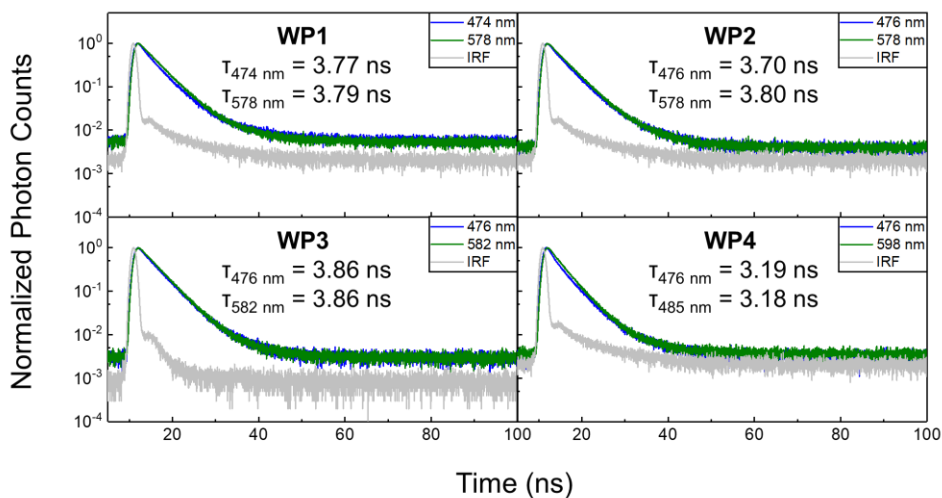


Figure S4.18. Transient photoluminescence spectra of **WP1–WP4**. Note that the decay curves of blue and yellow emissions are almost superimposable.

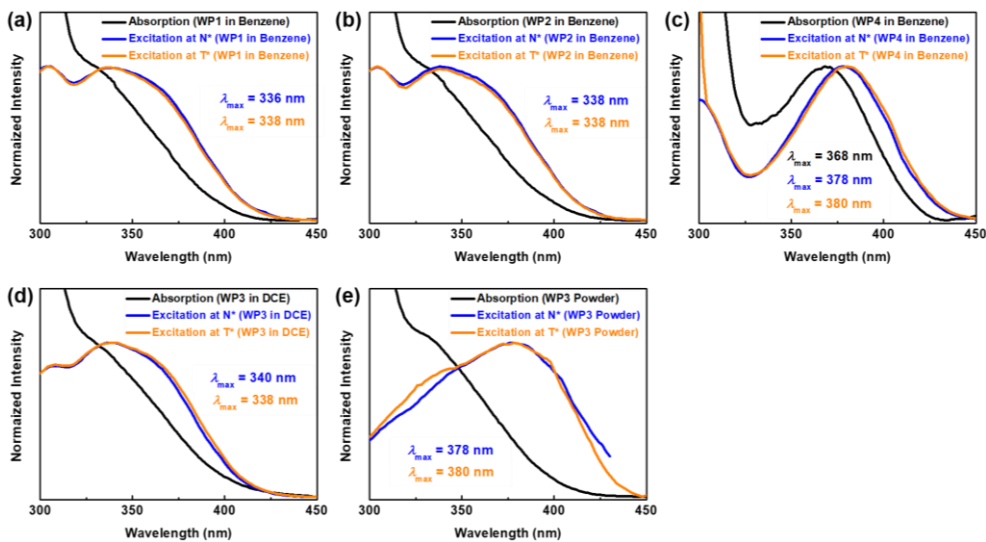


Figure S4.19. Normalized absorption (black lines) and excitation (blue and orange lines monitored at normal and tautomer emissions, respectively) spectra of (a) **WP1** in benzene, (b) **WP2** in benzene, (c) **WP4** in benzene, (d) **WP3** in 1,2-dichloroethane, and (e) **WP3** in powder state. (f) Normalized emission spectra of **WP3** with different molecular weights.

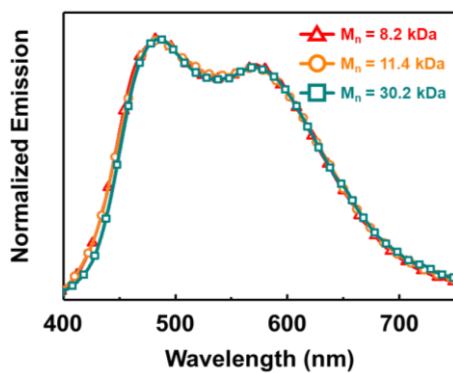


Figure S4.20. Normalized emission spectra of **WP3** with different molecular weights (8.2 kDa, 11.4 kDa, and 30.2 kDa) in DCE solutions ($10 \mu\text{M}$) at 298 K. Absolute quantum yields were determined by integrating sphere.

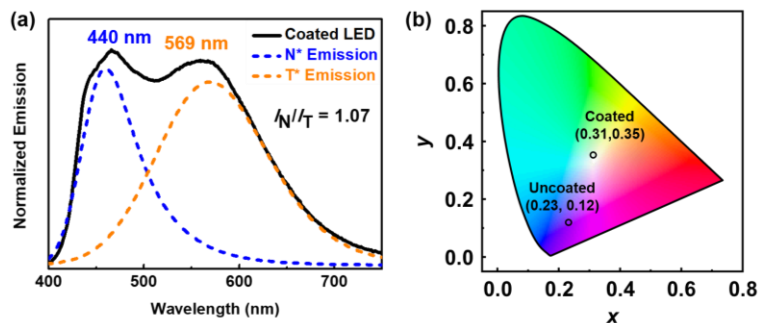


Figure S4.21. (a) Normalized absorption (black lines) and excitation (blue and orange lines monitored at normal and tautomer emissions, respectively) spectra of coated LED with **WP3**. (b) 1931 CIE chromaticity diagram of uncoated LED and **WP3**-coated LED.

4.6.6 TGA and DSC Profiles of Polymers

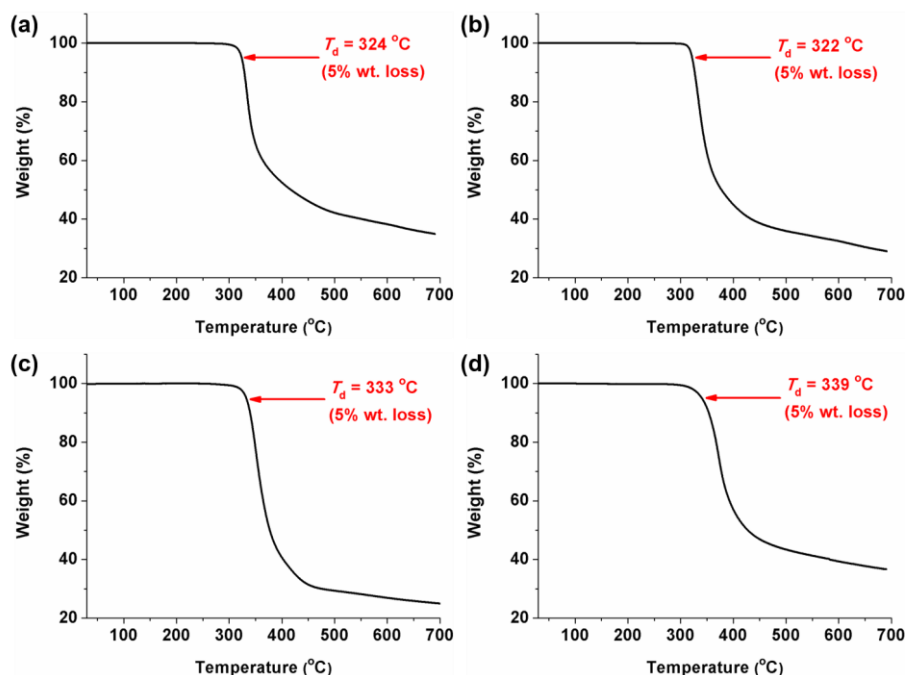


Figure S4.22. Thermogravimetric analysis (TGA) profiles of (a) **WP1**, (b) **WP2**, (c) **W3**, and (d) **WP4**.

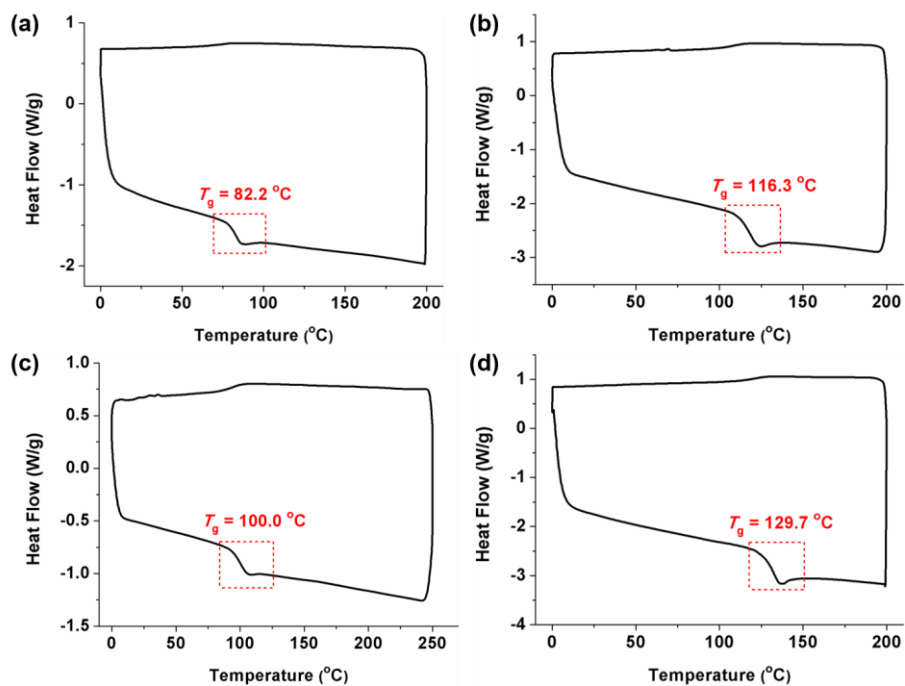
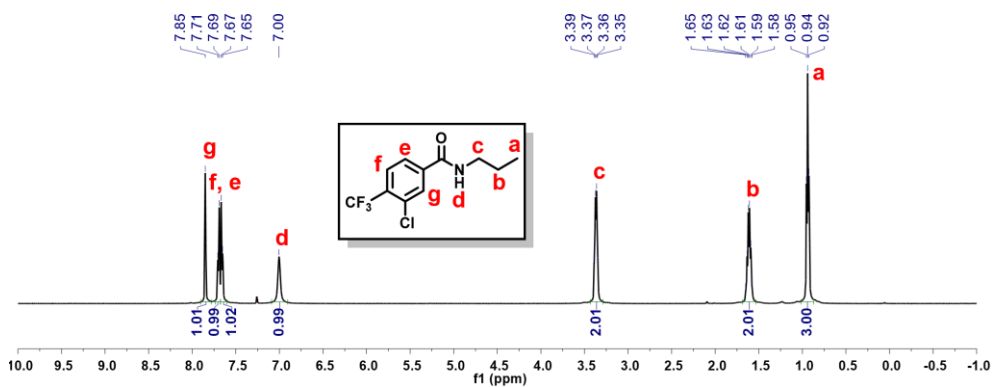


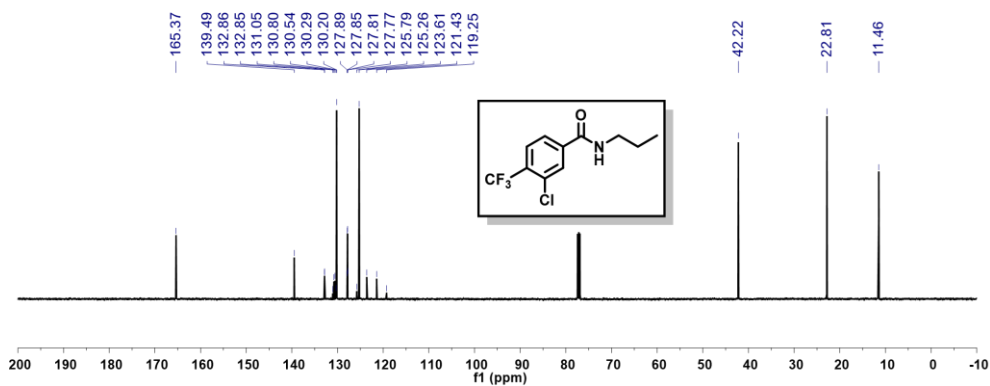
Figure S4.23. Differential scanning calorimetry (DSC) profiles of (a) **WP1**, (b) **WP2**, (c) **WP3**, and (d) **WP4**.

4.6.7. ^1H and ^{13}C NMR Spectra of Model Compounds, Monomers, and Polymers

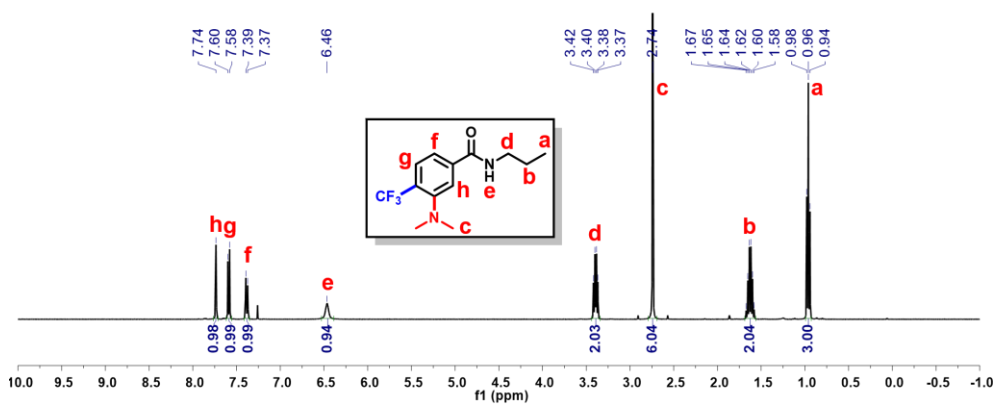
B ^1H NMR (500 MHz, CDCl_3)



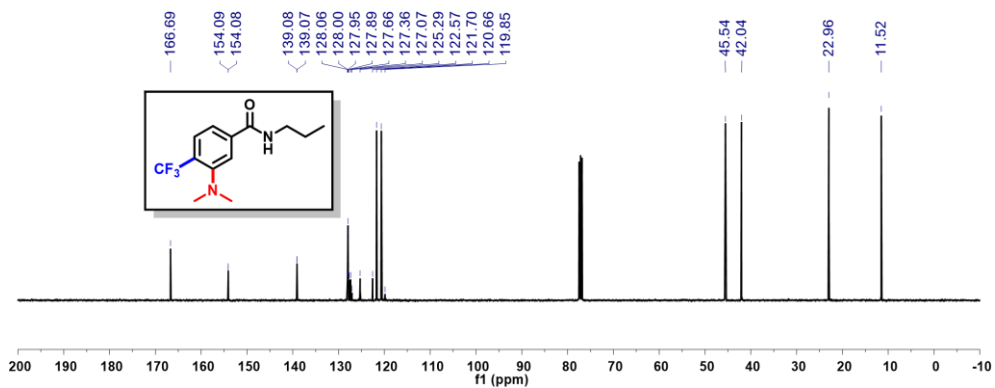
B ^{13}C NMR (125 MHz, CDCl_3)



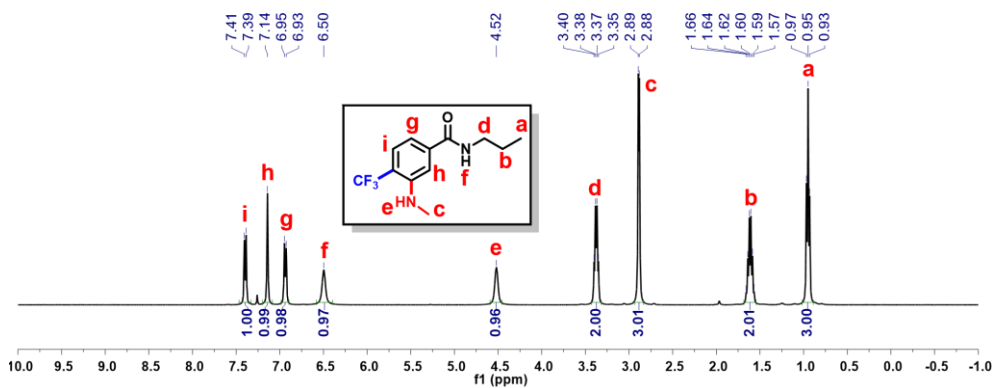
2a ^1H NMR (400 MHz, CDCl_3)



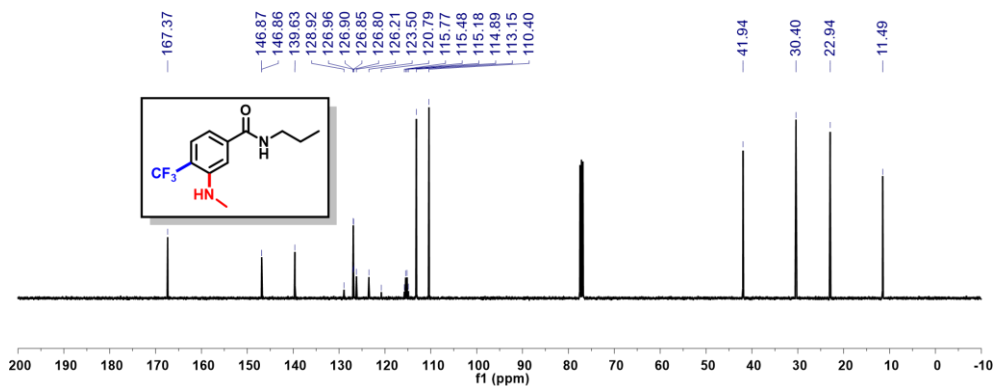
2a ^{13}C NMR (100 MHz, CDCl_3)



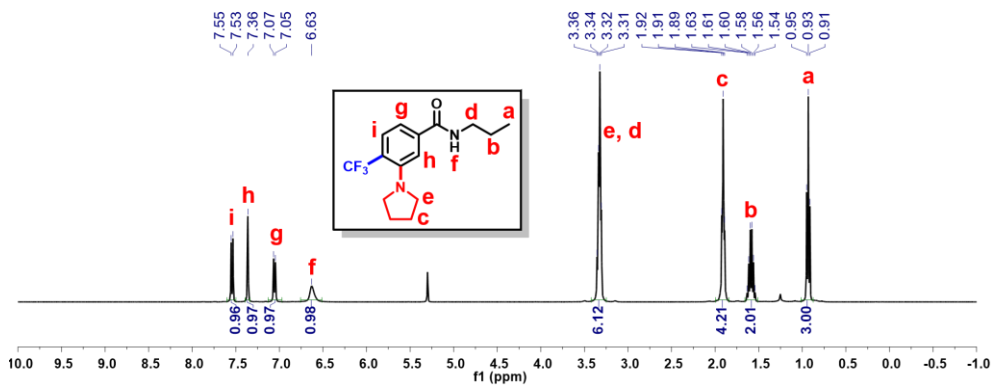
2b ^1H NMR (400 MHz, CDCl_3)



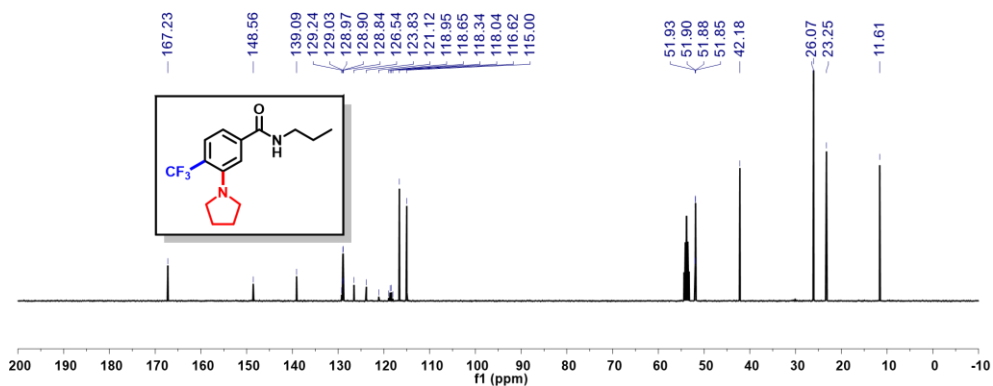
2b ^{13}C NMR (100 MHz, CDCl_3)



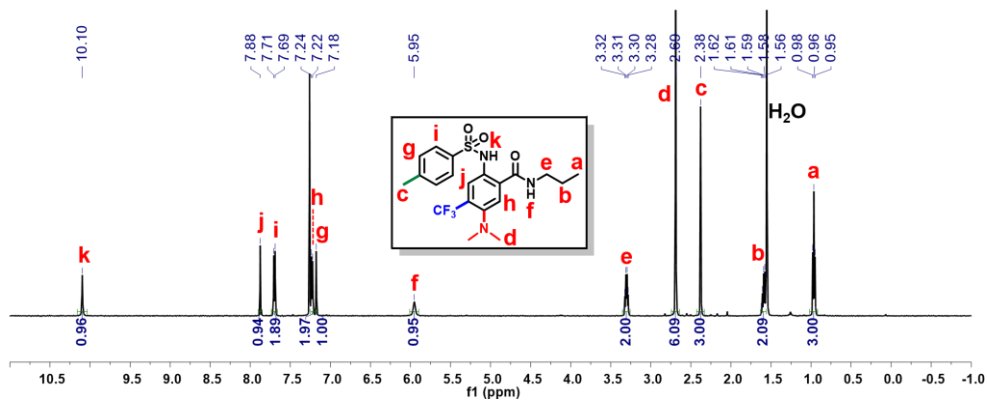
2c ^1H NMR (400 MHz, CD_2Cl_2)



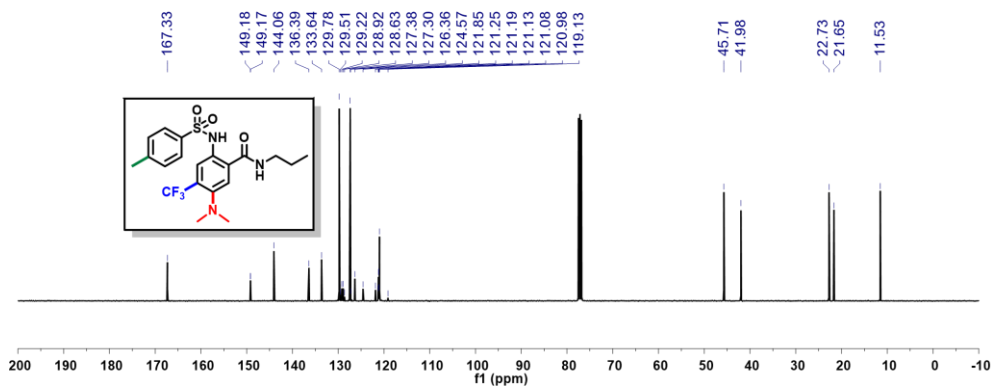
2c ^{13}C NMR (100 MHz, CD_2Cl_2)



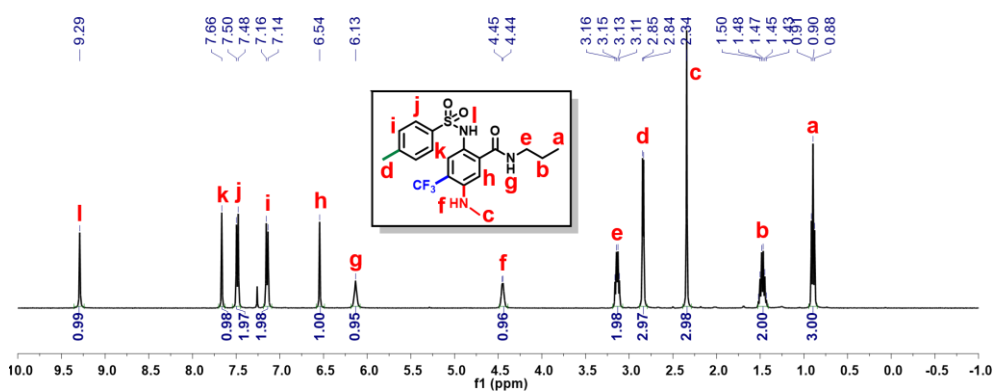
M1-Me ^1H NMR (500 MHz, CDCl_3)



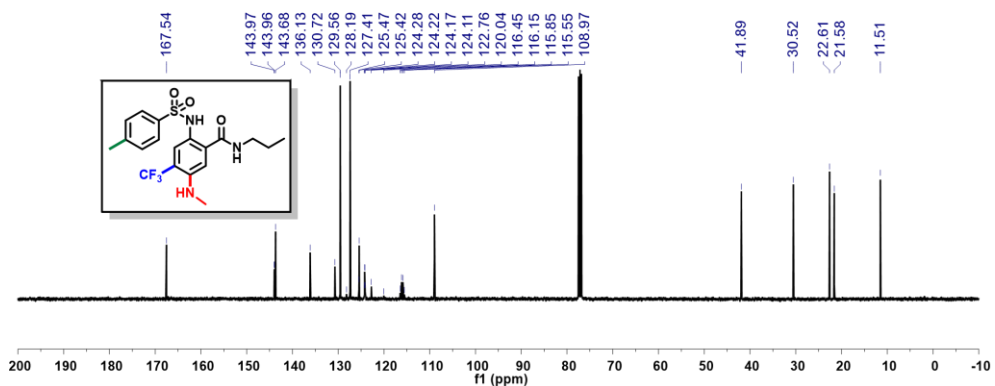
M1-Me ^{13}C NMR (100 MHz, CDCl_3)



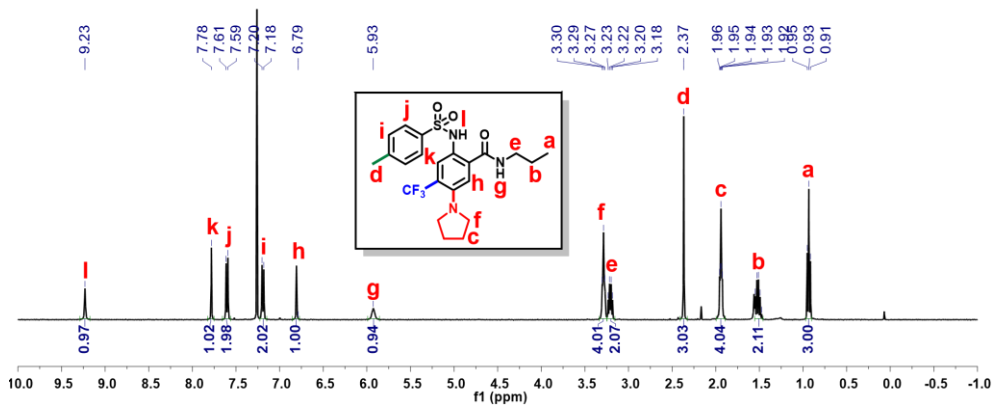
M2 ^1H NMR (400 MHz, CDCl_3)



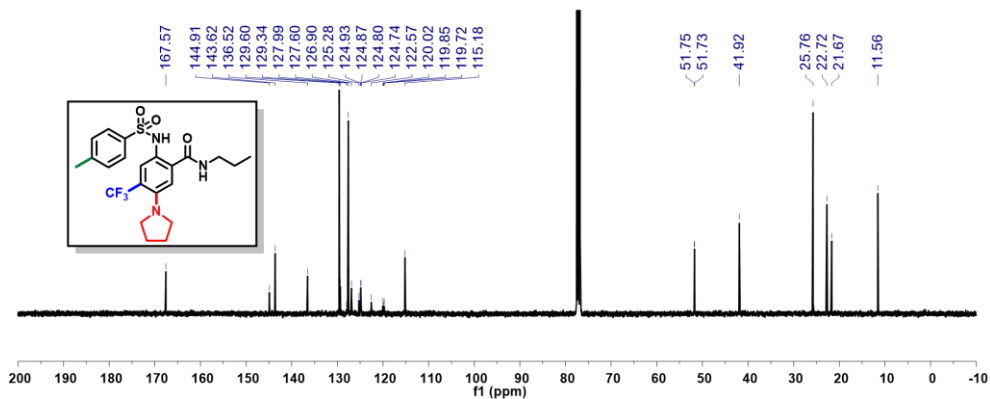
M2 ^{13}C NMR (100 MHz, CDCl_3)



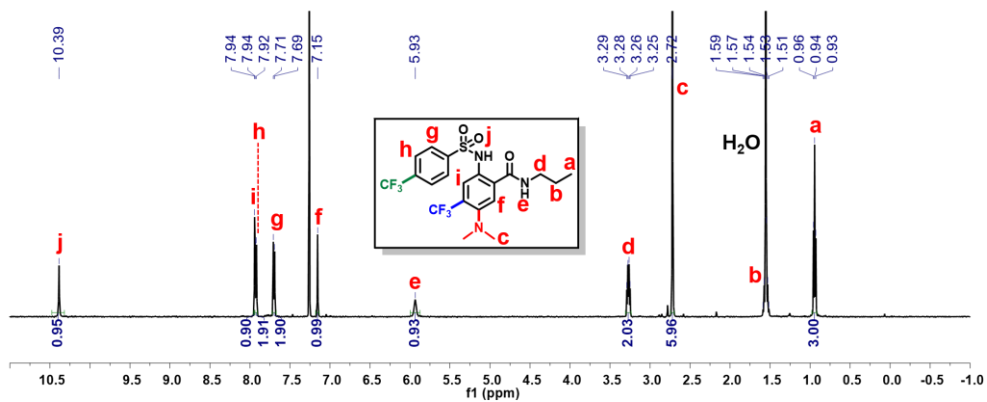
M3 ^1H NMR (400 MHz, CDCl_3)



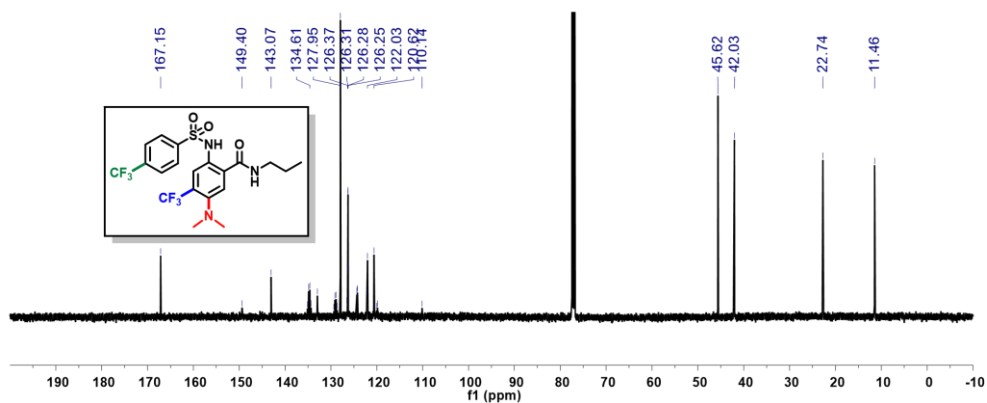
M3 ¹³C NMR (100 MHz, CDCl₃)



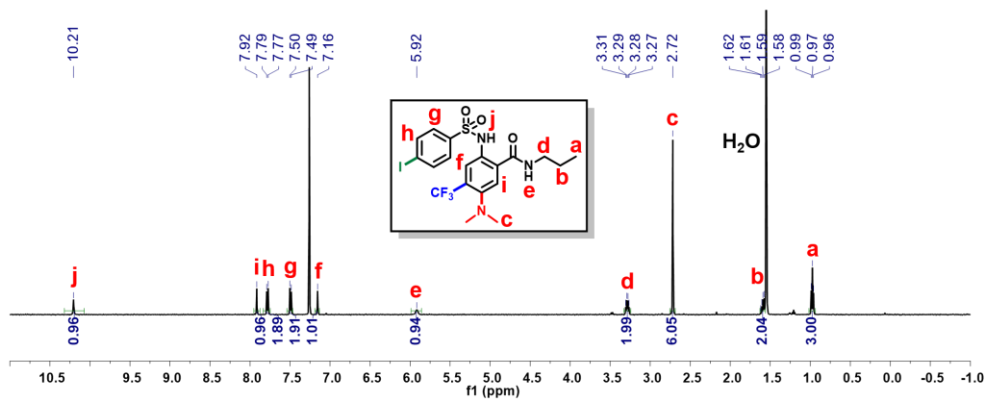
M1-CF₃ ¹H NMR (500 MHz, CDCl₃)



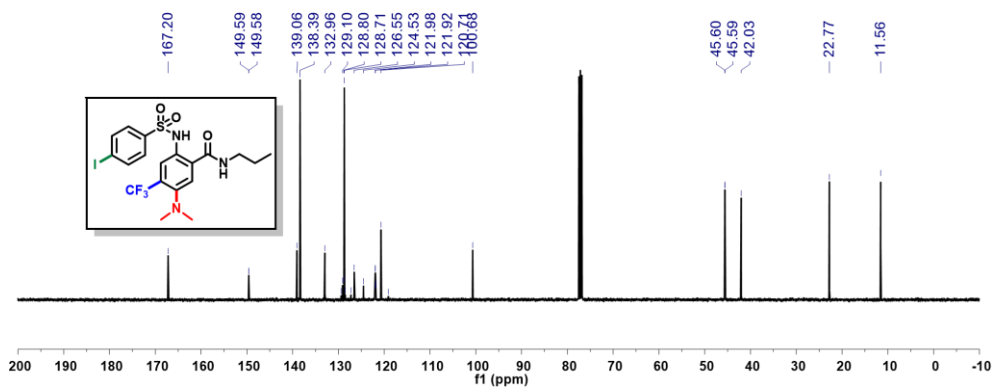
M1-CF₃ ¹³C NMR (125 MHz, CDCl₃)



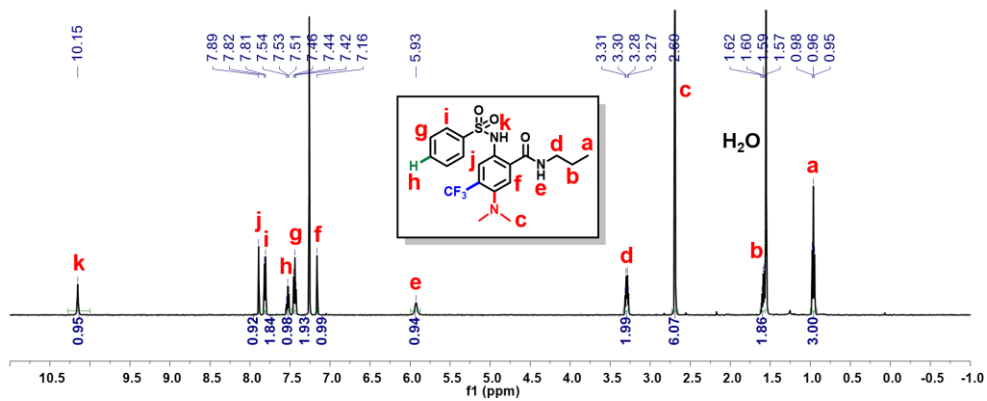
M1-I ^1H NMR (400 MHz, CDCl_3)



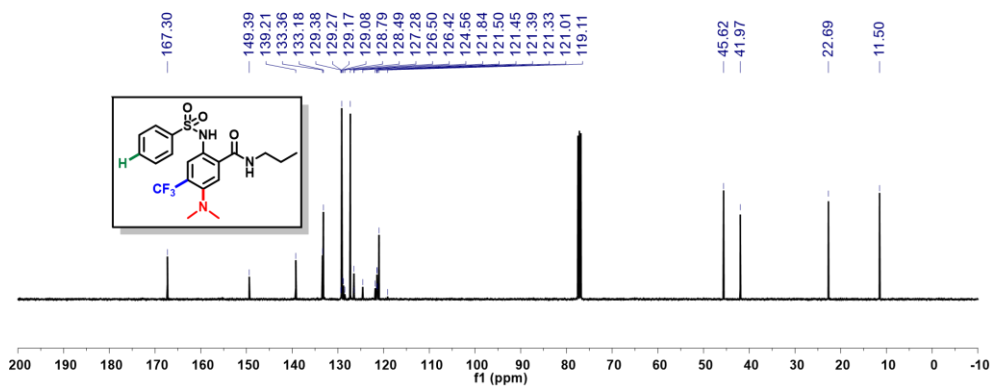
M1-I ^{13}C NMR (100 MHz, CDCl_3)



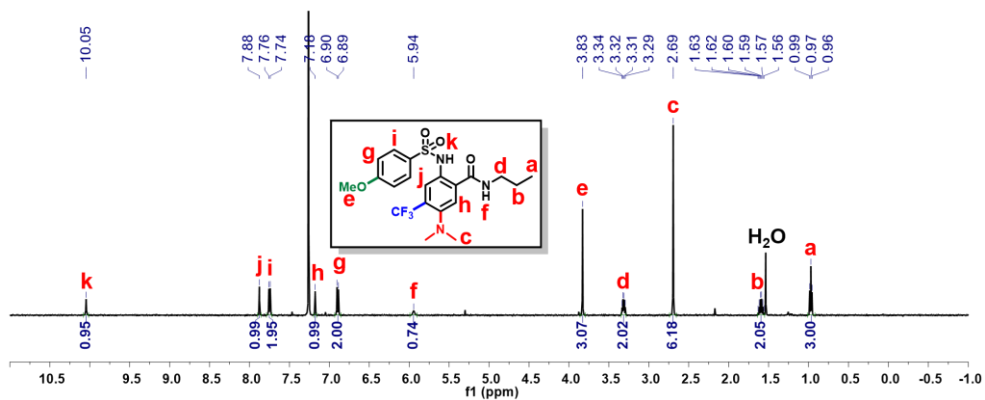
M1-H ^1H NMR (500 MHz, CDCl_3)



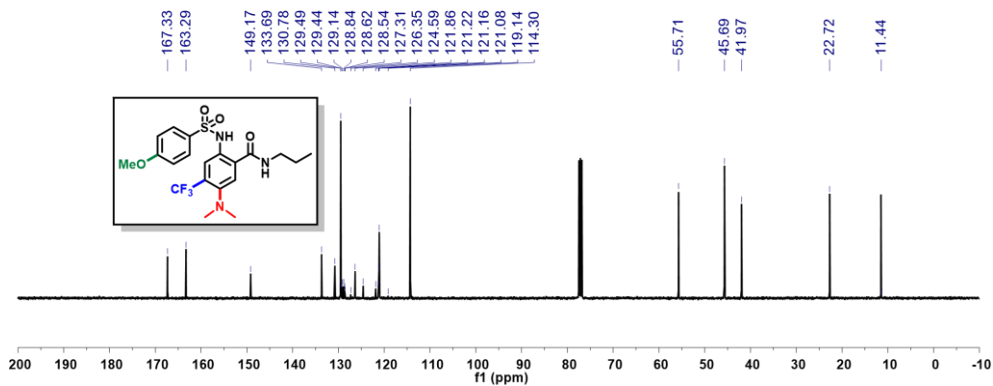
M1-H ^{13}C NMR (100 MHz, CDCl_3)



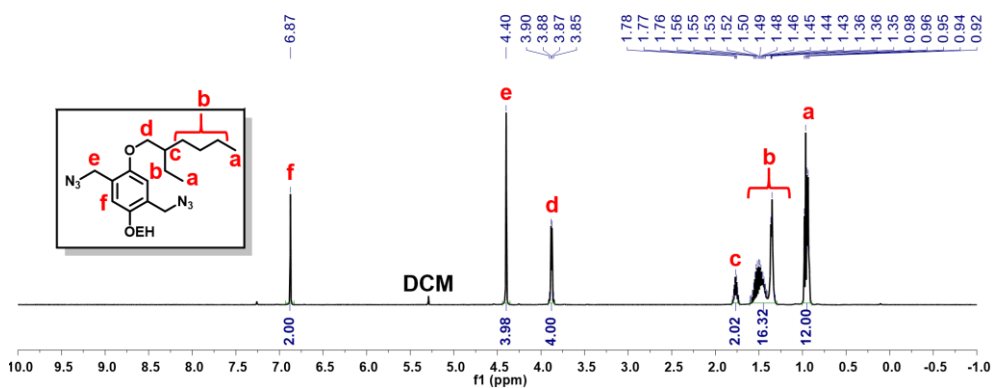
M1-OMe ^1H NMR (500 MHz, CDCl_3)



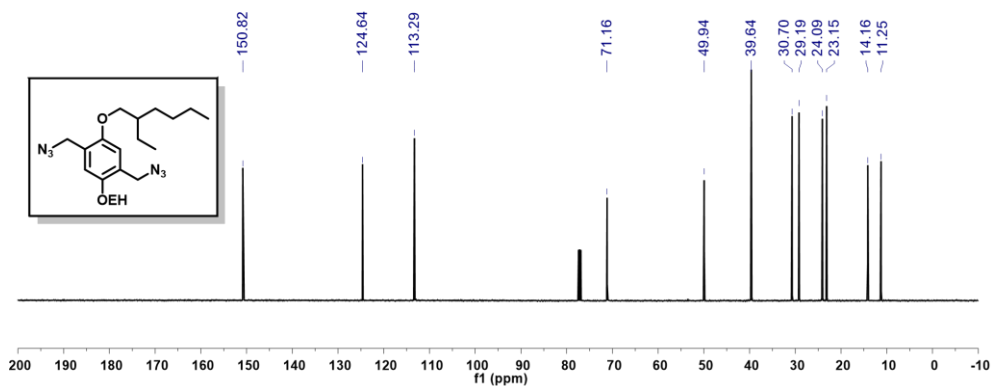
M1-OMe ^{13}C NMR (100 MHz, CDCl_3)



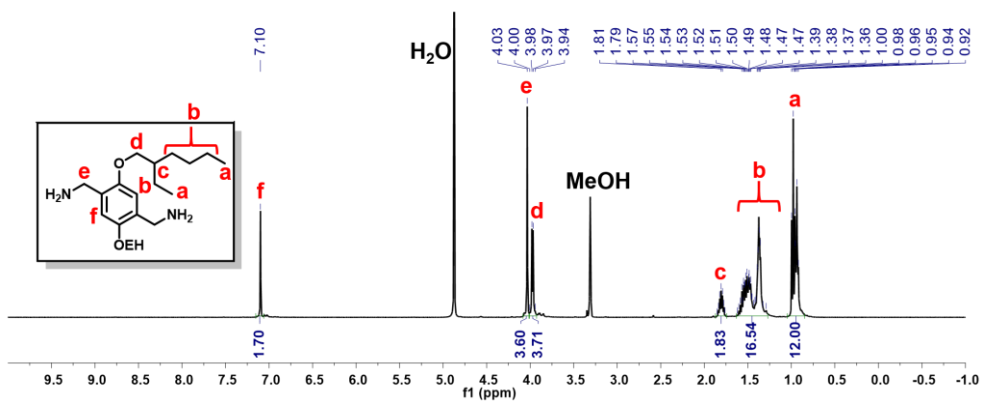
D ^1H NMR (500 MHz, CDCl_3)



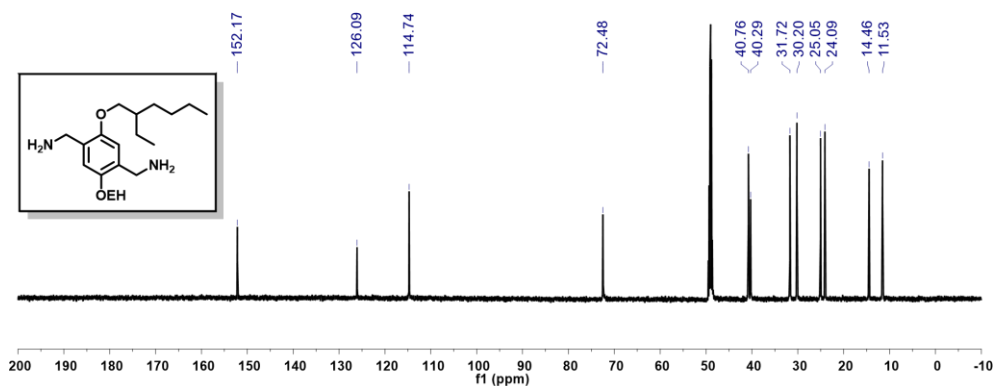
D ^{13}C NMR (125 MHz, CDCl_3)



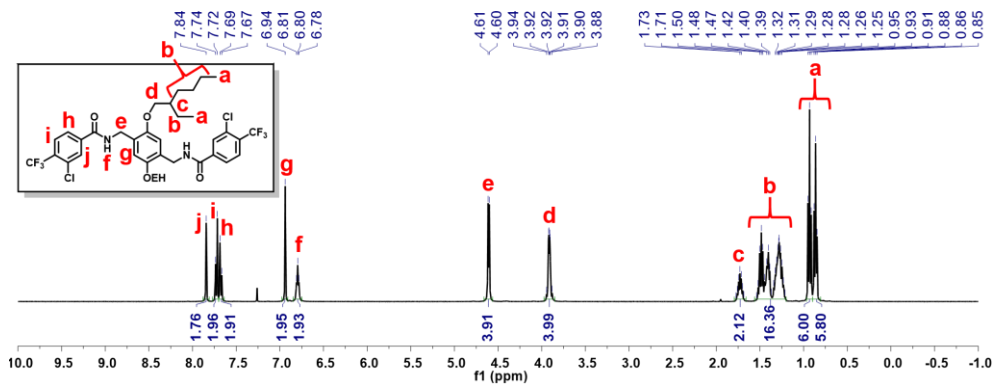
E ^1H NMR (500 MHz, CD_3OD)



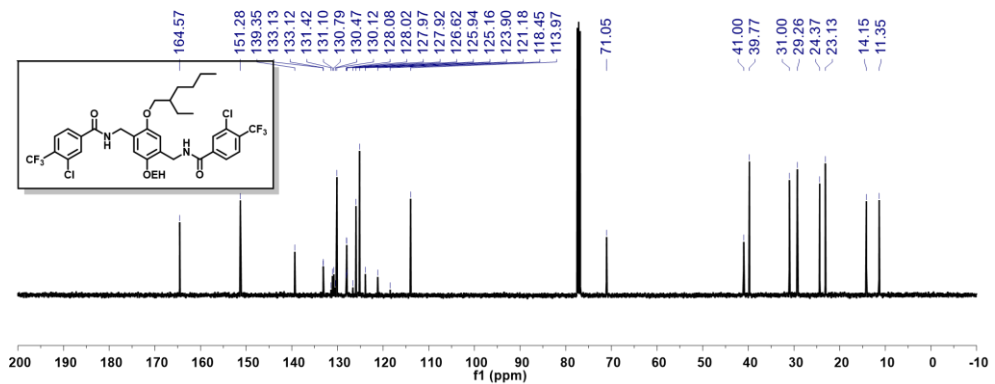
E ^{13}C NMR (125 MHz, CD_3OD)



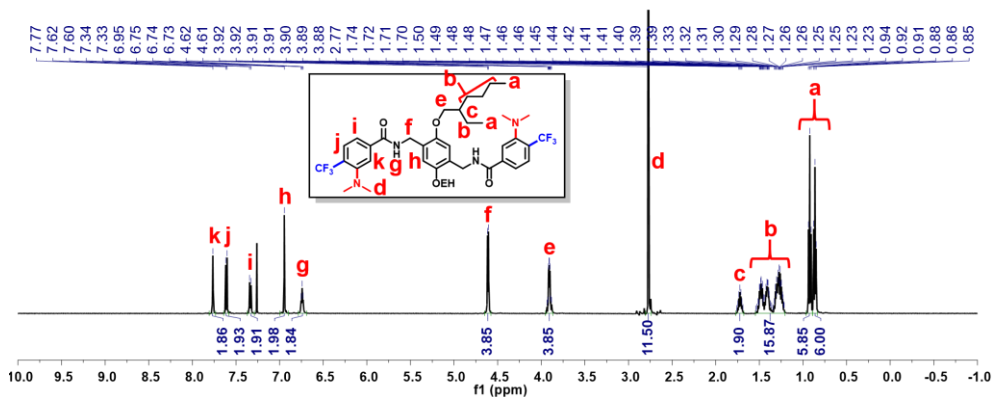
F ^1H NMR (400 MHz, CDCl_3)



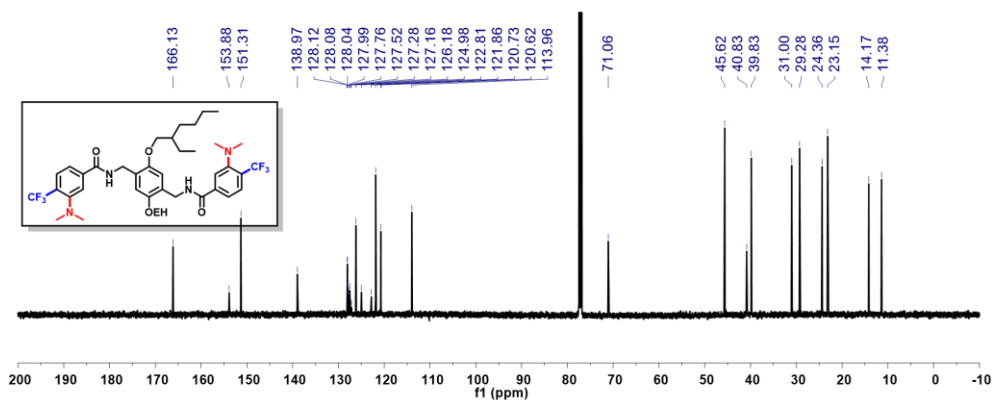
F ^{13}C NMR (100 MHz, CDCl_3)



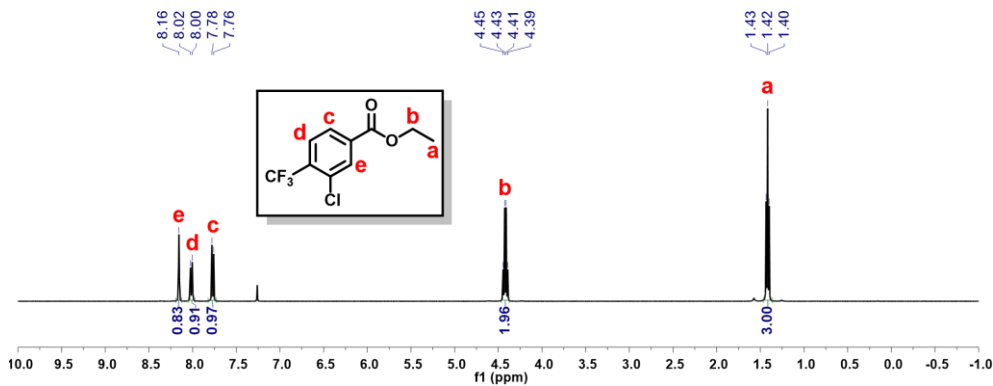
4a ^1H NMR (500 MHz, CDCl_3)



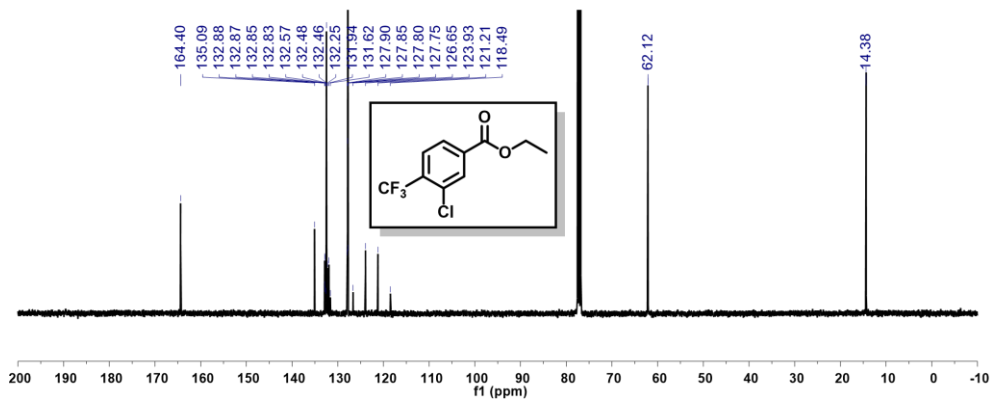
4a ^{13}C NMR (125 MHz, CDCl_3)



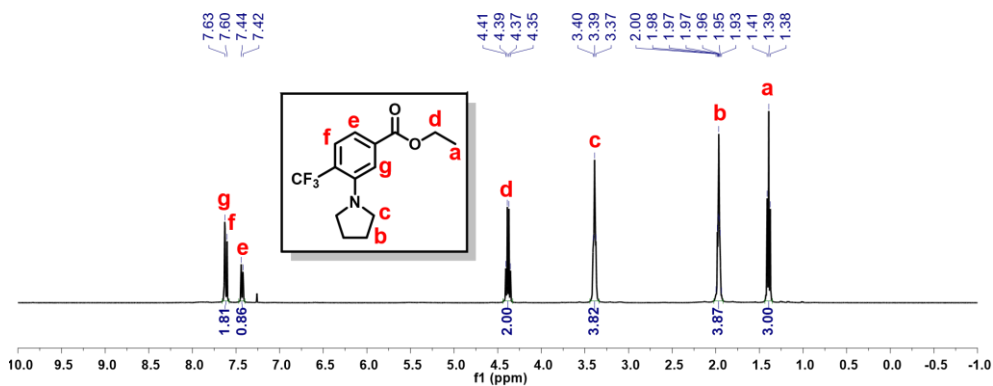
G ^1H NMR (400 MHz, CDCl_3)



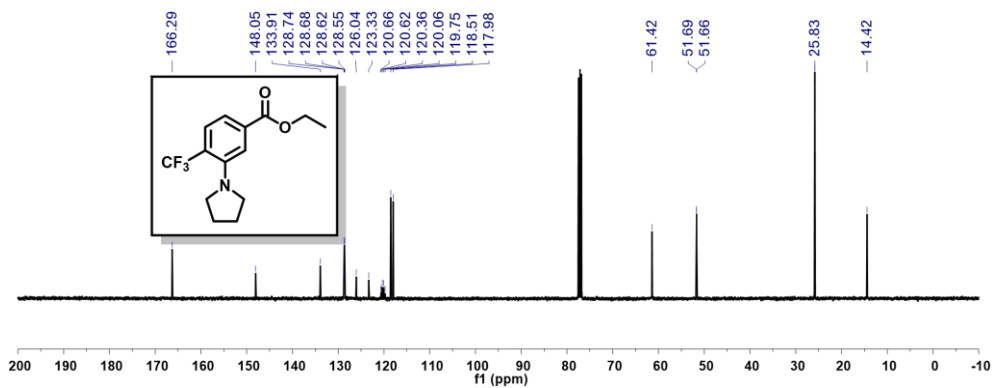
G ^{13}C NMR (100 MHz, CDCl_3)



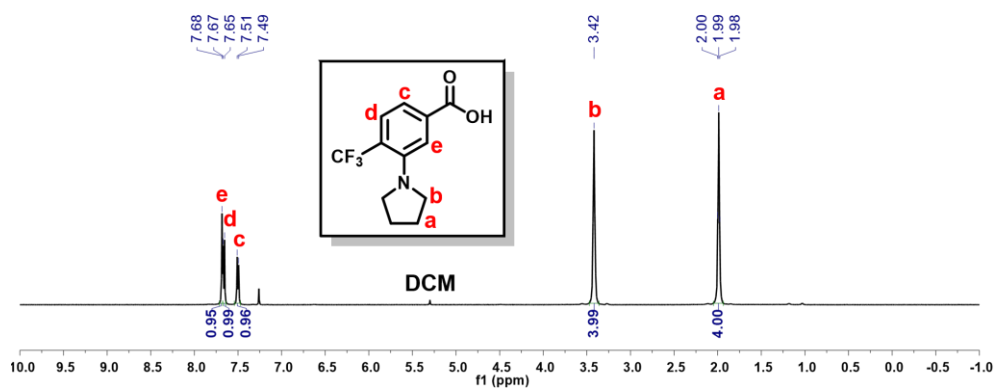
H ^1H NMR (400 MHz, CDCl_3)



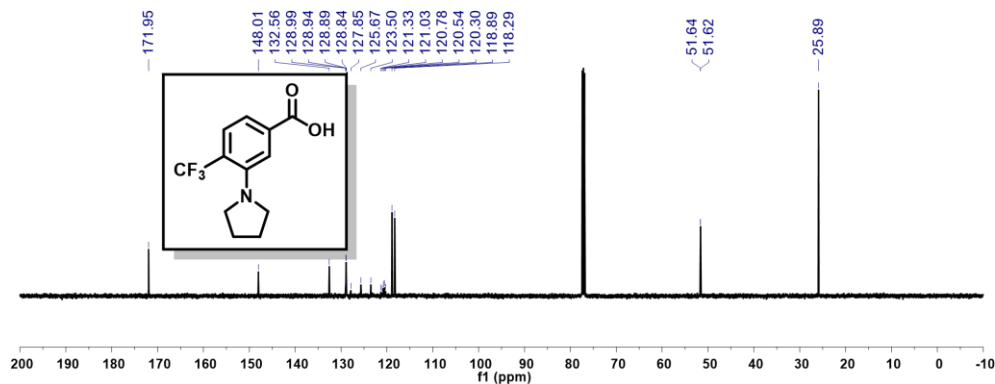
H ^{13}C NMR (100 MHz, CDCl_3)



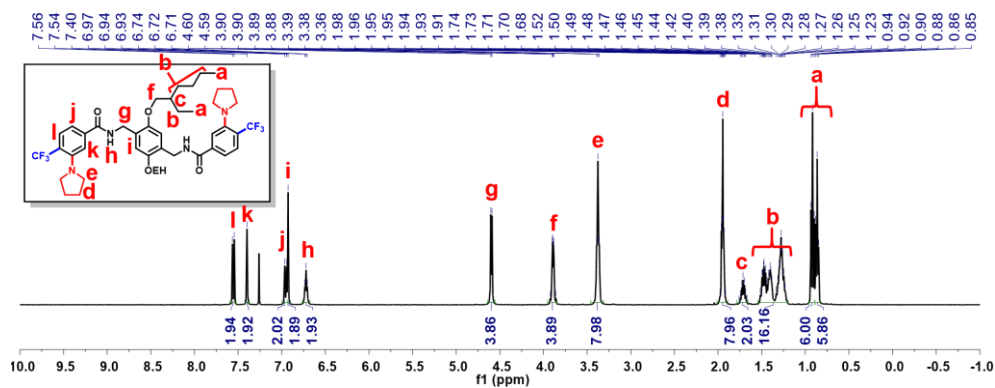
I ^1H NMR (500 MHz, CDCl_3)



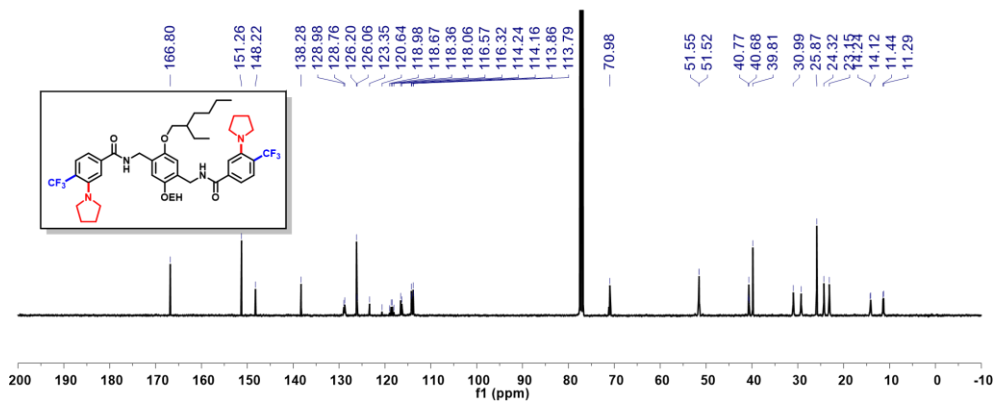
I ^{13}C NMR (125 MHz, CDCl_3)



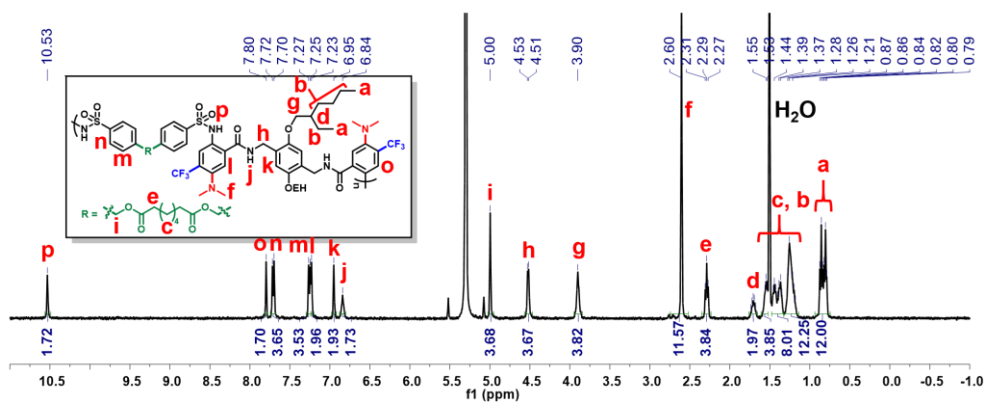
4b ^1H NMR (400 MHz, CDCl_3)



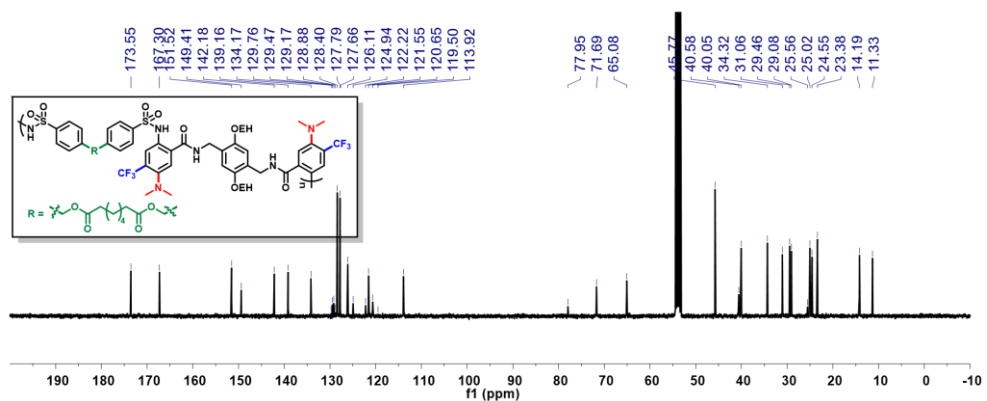
4b ^{13}C NMR (100 MHz, CDCl_3)



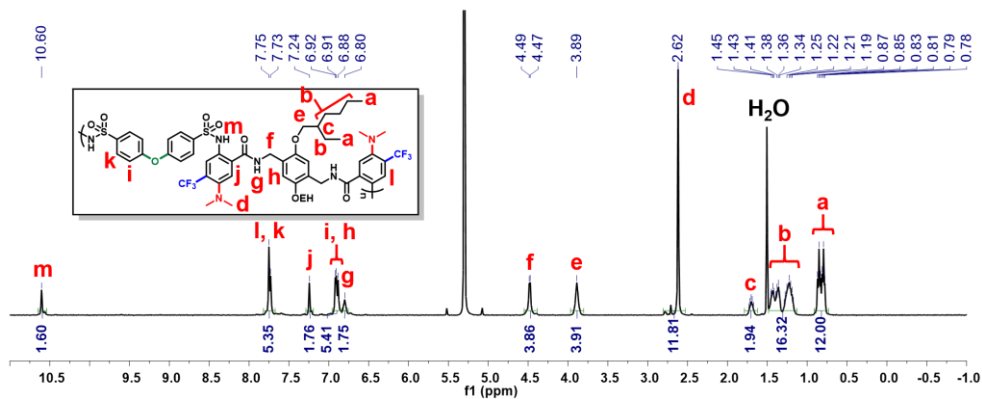
WP1 ^1H NMR (400 MHz, CD_2Cl_2)



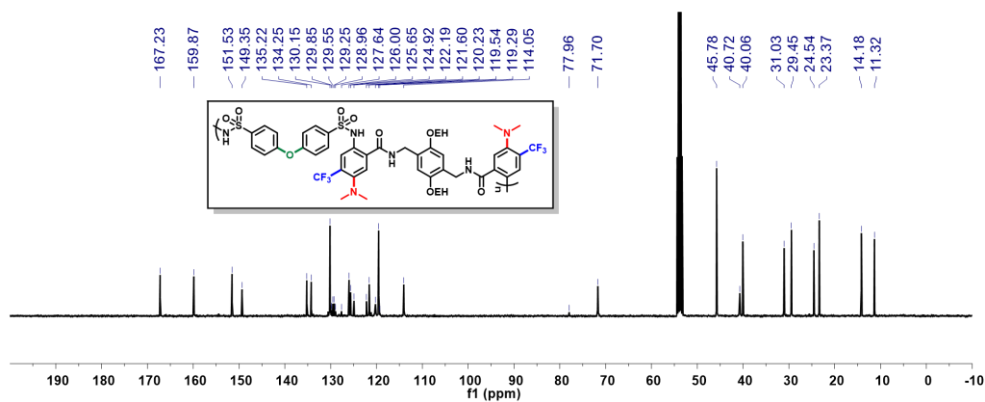
WP1 ^{13}C NMR (100 MHz, CD_2Cl_2)



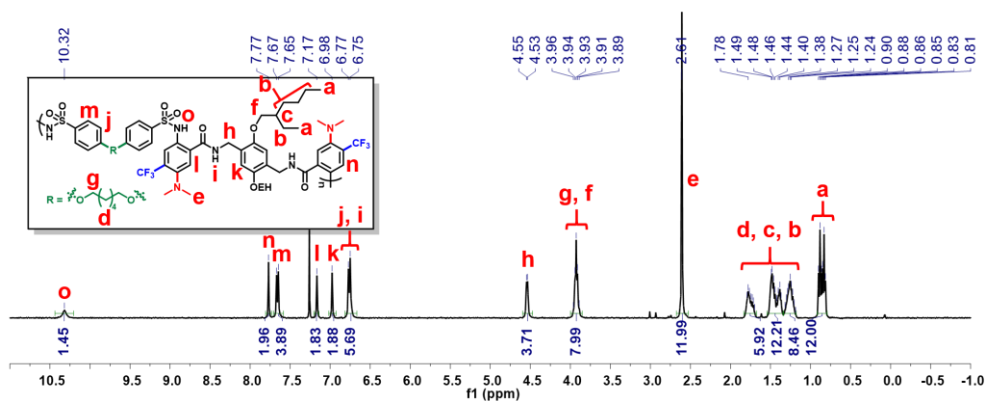
WP2 ¹H NMR (400 MHz, CD₂Cl₂)



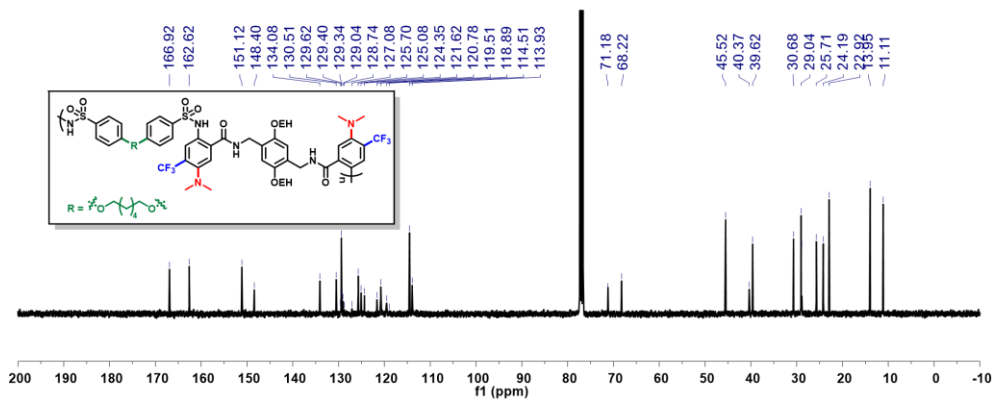
WP2 ¹³C NMR (100 MHz, CD₂Cl₂)



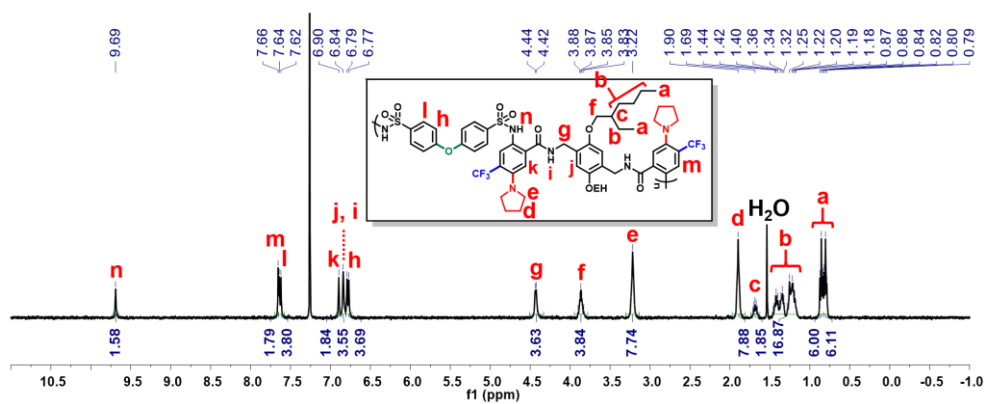
WP3 ¹H NMR (400 MHz, CDCl₃)



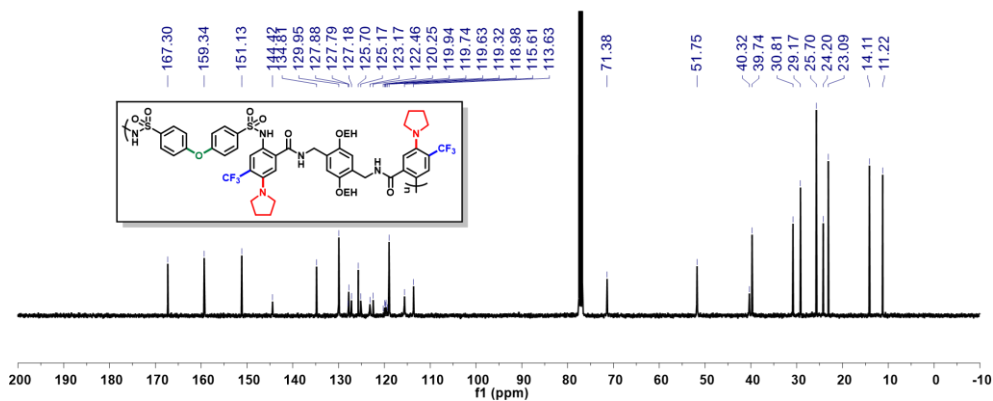
WP3 ¹³C NMR (100 MHz, CDCl₃)



WP4 ¹H NMR (400 MHz, CDCl₃)



WP4 ¹³C NMR (100 MHz, CDCl₃)



4.7. References

*Portions of this chapter have been previously reported, see: Hwang, S.-H.; Kim, H.; Ryu, H.; Serdiuk, I. E.; Lee, D.; Choi, T.-L. *J. Am. Chem. Soc.* **2022**, *144*, 1778–1785.

- (1) Wu, H.; Ying, L.; Yang, W.; Cao, Y. *Chem. Soc. Rev.* **2009**, *38*, 3391–3400.
- (2) Kamtekar, K. T.; Monkman, A. P.; Bryce, M. R. *Adv. Mater.* **2010**, *22*, 572–582.
- (3) Farinola, G. M.; Ragni, R. *Chem. Soc. Rev.* **2011**, *40*, 3467–3482.
- (4) Ying, L.; Ho, C.-L.; Wu, H.; Cao, Y.; Wong, W.-Y. *Adv. Mater.* **2014**, *26*, 2459–2473.
- (5) Tang, C.; Liu, X.-D.; Liu, F.; Wang, X.-L.; Xu, H.; Huang, W. *Macromol. Chem. Phys.* **2013**, *214*, 314–342.
- (6) Guo, T.; Zhong, W.; Zou, J.; Ying, L.; Yang, W.; Peng, J. *RSC Adv.* **2015**, *5*, 89888–89894.
- (7) Ravindran, E.; Varathan, E.; Subramanian, V.; Somana-than, N. *J. Mater. Chem. C* **2016**, *4*, 8027–8040.
- (8) Sahin, O.; Cinar, M. E.; Tekin, E.; Mucur, S. P.; Topal, S.; Suna, G.; Eroglu, M. S.; Ozturk, T. *ChemistrySelect* **2017**, *2*, 2889–2894.
- (9) Liang, J.; Zhong, Z.; Li, S.; Jiang, X.-F.; Ying, L.; Yang, W.; Peng, J.; Cao, Y. *J. Mater. Chem. C* **2017**, *5*, 2397–2403.
- (10) Ravindran, E.; Somanathan, N. *J. Mater. Chem. C* **2017**, *5*, 4763–4774.
- (11) Gioti, M.; Kokkinos, D.; Stavrou, K.; Simitzi, K.; An-dreopoulou, A.; Laskarakis, A.; Kallitsis, J.; Logothetidis, S. *Phys. Status Solidi RRL* **2019**, *13*, 1800419.
- (12) Nara, M.; Orita, R.; Ishige, R.; Ando, S. *ACS Omega* **2020**, *5*, 14831–14841.
- (13) Hwang, S.-H.; Choi, T.-L. *Org. Lett.* **2020**, *22*, 2935–2940.
- (14) Jang, Y.-J.; Hwang, S.-H.; Choi, T.-L. *Angew. Chem., Int. Ed.* **2017**, *56*, 14474–14478.
- (15) Jang, Y.-J.; Hwang, S.-H.; Noh, J.; Choi, T.-L. *Macromolecules* **2018**, *51*, 7476–7482.
- (16) Chang, D. W.; Kim, S.; Park, S. Y. *Macromolecules* **2000**, *33*, 7223–7225.
- (17) Kim, S.; Chang, D. W.; Park, S. Y. *Macromolecules* **2002**, *35*, 6064–6066.
- (18) Rodembusch, F. S.; Leusin, F. P.; Bordignon, L. B.; Gallas, M. R.; Stefani, V. *J. Photochem. Photobiol. A* **2005**, *173*, 81–92.
- (19) Rodembusch, F. S.; Campo, L. F.; Stefani, V.; Samios, D.; da Silveira, N. P. *Polymer* **2005**, *46*, 7185–7190.
- (20) Campo, L. F.; Rodembusch, F. S.; Stefani, V. *J. Appl. Polym. Sci.* **2006**, *99*, 2109–2116.
- (21) Kim, T. H.; Kim, H. J.; Kwak, C. G.; Park, W. H.; Lee, T. S. *J. Polym. Sci. A: Polym. Chem.* **2006**, *44*, 2059–2068.
- (22) Chu, Q.; Medvetz, D. A.; Pang, Y. *Chem. Mater.* **2007**, *19*, 6421–6429.

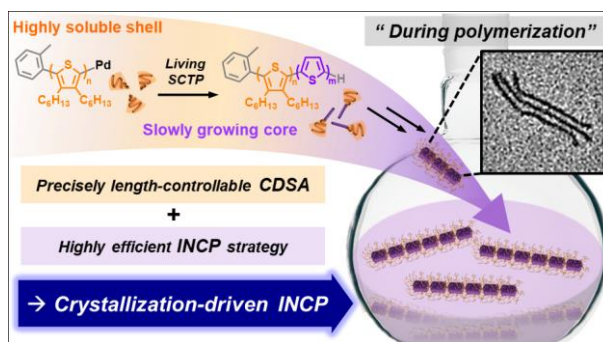
- (23) Kanosue, K.; Shimosaka, T.; Wakita, J.; Ando, S. *Macromolecules* **2015**, *48*, 1777–1785.
- (24) Kanosue, K.; Augulis, R.; Peckus, D.; Karpicz, R.; Tamulevicius, T.; Tamulevicius, S.; Gulbinas, V.; Ando, S. *Macromolecules* **2016**, *49*, 1848–1857.
- (25) Ngororabanga, J. M. V.; Tshentu, Z. R.; Mama, N. *New J. Chem.* **2019**, *43*, 12168–12177.
- (26) Wang, Q.; He, L.; Zeng, D.; Zou, W.; Gong, F.; Xia, J.; Cao, Z. *Spectrochim. Acta Part A* **2020**, *226*, 117654.
- (27) Fujiwara, E.; Orita, R.; Vyšniauskas, A.; Franckevičius, M.; Ishige, R.; Gulbinas, V.; Ando, S. *J. Phys. Chem. B* **2021**, *125*, 2425–2434.
- (28) Liang, N.; Fujiwara, E.; Nara, M.; Ishige, R.; Ando, S. *ACS Appl. Polym. Mater.* **2021**, *3*, 3911–3921.
- (29) Kim, S.; Seo, J.; Jung, H. K.; Kim, J.-J.; Park, S. Y. *Adv. Mater.* **2005**, *17*, 2077–2082.
- (30) Park, S.; Kwon, J. E.; Kim, S. H.; Seo, J.; Chung, K.; Park, S.-Y.; Jang, D.-J.; Medina, B. M.; Gierschner, J.; Park, S. Y. *J. Am. Chem. Soc.* **2009**, *131*, 14043–14049.
- (31) Kim, S. H.; Park, S.; Kwon, J. E.; Park, S. Y. *Adv. Funct. Mater.* **2011**, *21*, 644–651.
- (32) Tang, K.-C.; Chang, M.-J.; Lin, T.-Y.; Pan, H.-A.; Fang, T.-C.; Chen, K.-Y.; Hung, W.-Y.; Hsu, Y.-H.; Chou, P.-T. *J. Am. Chem. Soc.* **2011**, *133*, 17738–17745.
- (33) Sakai, K.-I.; Ishikawa, T.; Akutagawa, T. *J. Mater. Chem. C* **2013**, *1*, 7866–7871.
- (34) Ye, J.; Liu, C.; Ou, C.; Cai, M.; Chen, S.; Wei, Q.; Li, W.; Qian, Y.; Xie, L.; Mi, B.; Gao, Z.; Huang, W. *Adv. Opt. Mater.* **2014**, *2*, 938–944.
- (35) Zhang, Z.; Chen, Y.-A.; Hung, W.-Y.; Tang, W.-F.; Hsu, Y.-H.; Chen, C.-L.; Meng, F.-Y.; Chou, P.-T. *Chem. Mater.* **2016**, *28*, 8815–8824.
- (36) Padalkar, V. S.; Seki, S. *Chem. Soc. Rev.* **2016**, *45*, 169–202.
- (37) Sakai, K.-i, Tsuchiya, S.; Kikuchi, T.; Akutagawa, T. *J. Mater. Chem. C* **2016**, *4*, 2011–2016.
- (38) Serdiuk, I. E. *J. Phys. Chem. C* **2017**, *121*, 5277–5286.
- (39) Samanta, S.; Manna, U.; Das, G. *New J. Chem.* **2017**, *41*, 1064–1072.
- (40) Serdiuk, I. E. *J. Phys. Chem. C* **2018**, *122*, 18615–18620.
- (41) Moraes, E. S.; Teixeira Alves Duarte, L. G.; Germino, J. C.; Atvars, T. D. Z. *J. Phys. Chem. C* **2020**, *124*, 22406–22415.
- (42) Benelhadj, K.; Muzuzu, W.; Massue, J.; Retailleau, P.; Charaf-Eddin, A.; Laurent, A. D.; Jacquemin, D.; Ulrich, G.; Zies-sel, R. *Chem. Eur. J.* **2014**, *20*, 12843–12857.
- (43) Tseng, H.-W.; Liu, J.-Q.; Chen, Y.-A.; Chao, C.-M.; Liu, K.-M.; Chen, C.-L.; Lin, T.-C.; Hung, C.-H.; Chou, Y.-L.; Lin, T.-C.; Wang, T.-L.; Chou, P.-T. *J. Phys. Chem. Lett.* **2015**, *6*, 1477–1486.

- (44) Harmata, M.; Zheng, P.; Huang, C.; Gomes, M. G.; Ying, W.; Ranyanil, K.-O.; Balan, G.; Calkins, N. L. *J. Org. Chem.* **2007**, *72*, 683–685.
- (45) Parr, R.G.; Yang, W. *Density Functional Theory of Atoms and Molecules*. Oxford University Press: New York, 1989.
- (46) Frisch, M. J.; Trucks, G. W.; Schlegel, H. B.; Scuseria, G. E.; Robb, M. A.; Cheeseman, J. R.; Scalmani, G.; Barone, V.; Petersson, G. A.; Nakatsuji, H.; Li, X.; Caricato, M.; Marenich, A. V.; Bloino, J.; Janesko, B. G.; Gomperts, R.; Mennucci, B.; Hratchian, H. P.; Ortiz, J. V.; Izmaylov, A. F.; Sonnenberg, J. L.; Williams-Young, D.; Ding, F.; Lipparini, F.; Egidi, F.; Goings, J.; Peng, B.; Petrone, A.; Henderson, T.; Ranasinghe, D.; Zakrzewski, V. G.; Gao, J.; Rega, N.; Zheng, G.; Liang, W.; Hada, M.; Ehara, M.; Toyota, K.; Fukuda, R.; Hasegawa, J.; Ishida, M.; Nakajima, T.; Honda, Y.; Kitao, O.; Nakai, H.; Vreven, T.; Throssell, K.; Montgomery, J. A., Jr.; Peralta, J. E.; Ogliaro, F.; Bearpark, M. J.; Heyd, J. J.; Brothers, E. N.; Kudin, K. N.; Staroverov, V. N.; Keith, T. A.; Kobayashi, R.; Normand, J.; Raghavachari, K.; Rendell, A. P.; Burant, J. C.; Iyengar, S. S.; Tomasi, J.; Cossi, M.; Millam, J. M.; Klene, M.; Adamo, C.; Cammi, R.; Ochterski, J. W.; Martin, R. L.; Morokuma, K.; Farkas, O.; Foresman, J. B.; Fox, D. J. Gaussian 16, Revision C.01, Gaussian, Inc., Wallingford CT, 2016.
- (47) Zhao, Y.; Truhlar, D. G. *Theor. Chem. Acc.* **2006**, *120*, 215–241.
- (48) Petersson, G. A.; Bennett, A.; Tensfeldt, T. G.; Al-Laham, M. A.; Shirley, W. A.; Mantzaris, J. J. *Chem. Phys.* **1988**, *89*, 2193–2218.
- (49) Tomasi, J.; Mennucci, B.; Cammi, R. *Chem. Rev.* **2005**, *105*, 2999–3094.
- (50) Kim, H.; Choi, T.-L. *ACS Macro Lett.* **2014**, *3*, 791–794.
- (51) Waser, J.; Gaspar, B.; Nambu, H.; Carreira, E. M. *J. Am. Chem. Soc.* **2006**, *128*, 11693–11712.
- (52) Suh, S.-E.; Chen, S.-J.; Mandal, M.; Guzei, I. A.; Cramer, C. J.; Stahl, S. S. *J. Am. Chem. Soc.* **2020**, *142*, 11388–11393.
- (53) Xiong, H.; Gu, Y.; Zhang, S.; Lu, F.; Ji, Q.; Liu, L.; Ma, P.; Yang, G.; Hou, W.; Xu, H. *Chem. Commun.* **2020**, *56*, 4692–4695.
- (54) Maiti, D.; Fors, B. P.; Henderson, J. L.; Nakamura, Y.; Buchwald, S. L. *Chem. Sci.* **2011**, *2*, 57–68.
- (55) Iadevaia, G.; Stross, A. E.; Neumann, A.; Hunter, C. A. *Chem. Sci.* **2016**, *7*, 1760–1767.

Chapter 5. Synchronous Preparation of Length-Controllable 1D Nanoparticles via Crystallization-Driven *in Situ* Nanoparticlization of Conjugated Polymers

5.1. Abstract

Precise size control of semiconducting nanomaterials from polymers is crucial for optoelectronic applications, but the low solubility of conjugated polymers makes this challenging. In this chapter, we prepared length-controlled semiconducting one-dimensional (1D) nanoparticles by synchronous self-assembly during polymerization. First, we succeeded in unprecedented living polymerization of highly soluble conjugated poly(3,4-dihexylthiophene). Then, block copolymerization of poly(3,4-dihexylthiophene)-*block*-polythiophene spontaneously produced narrow-dispersed 1D nanoparticles with lengths from 15 to 282 nm according to the size of a crystalline polythiophene core. The key factors for high efficiency and length-control are a highly solubilizing shell and slow polymerization of the core, thereby favoring nucleation-elongation over isodesmic growth. Combining kinetics and high-resolution imaging analyses, we propose a unique mechanism called crystallization-driven *in situ* nanoparticlization of conjugated polymers (CD-INCP) where spontaneous nucleation creates seeds, followed by seeded-growth in units of micelles. Also, we achieved “living” CD-INCP through a chain-extension experiment. We further simplified CD-INCP by adding both monomers together in one-shot copolymerization but still producing length-controlled nanoparticles.



5.2. Introduction

Self-assembly of conjugated polymers (CPs) is an attractive method for preparing electronically useful semiconducting nanomaterials with various nanostructures.^{1,2} In particular, colloidally stable semiconducting one-dimensional (1D) nanostructures have been actively investigated for numerous optoelectronic applications^{3–14} because efficient exciton or charge transport along their nanostructures could affect the device performance.^{10,11,15} Therefore, precise control of the size and shape of nanostructures has become an important subject. However, this was challenging because of the high crystallinity and low solubility of the CPs, leading to irregular aggregation.

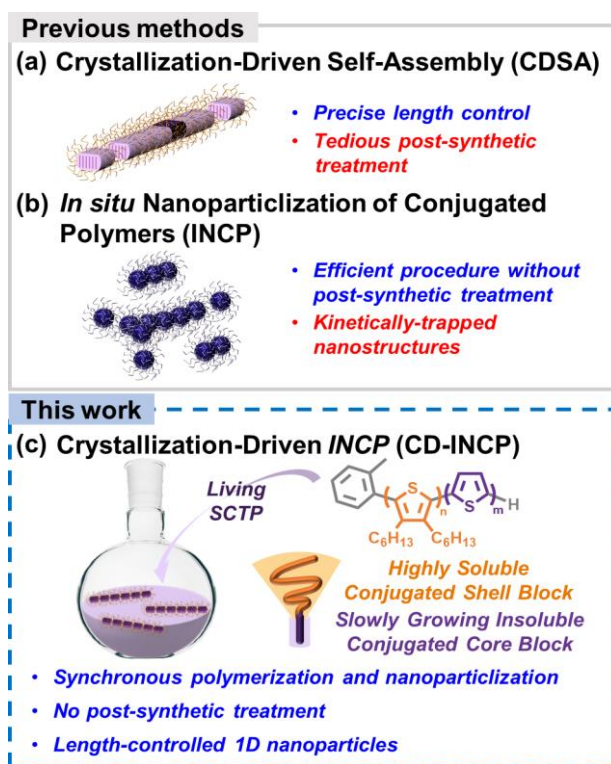


Figure 5.1. Strategies to prepare semiconducting 1D nanostructures. (a) Conventional living CDSA methods showing precision size control but requiring tedious post-synthetic treatment. (b) INCP without any post-synthetic treatment but sacrificing size and shape control. (c) CD-INCP method combining advantages of both living CDSA and INCP strategies to produce uniform conjugated 1D nanoparticles with precise length control.

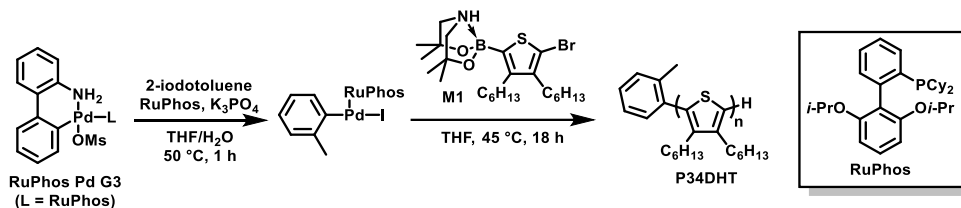
After pioneering reports from the Manners group, who first introduced the living crystallization-driven self-assembly (CDSA) strategy,^{16–19} several groups succeeded in controlling the length of semiconducting 1D nanowires using block copolymers (BCPs) containing CPs (Figure 5.1a).^{10,11,20–22,25,26} Successful length control was achieved by

modulating competing pathways. First, by attaching a solubilizing shell block or heating, the solubility of CPs should be sufficiently marginal to behave as unimers and seeds. Then, one should prepare uniform seed micelles where the unimers are attached selectively for controlled elongation without self-nucleation. Despite their achievements, optimization of the seed preparation and elongation processes is laborious and time-consuming. Therefore, eliminating these post-synthetic treatment processes would significantly simplify the production of nanostructures. To prepare semiconducting nanoparticles more efficiently, we developed a one-pot process called *in situ* nanoparticlization of conjugated polymers (INCP) even without any post-synthetic treatment (Figure 5.1b; see **Chapter 1.1.5** for details).^{27–34} Despite this efficiency, the INCP strategy lacked control of the size or shape of the resulting nanostructures because a rapid increase in the π – π interactions among the core blocks triggered fast micellization, leading to self-nucleation, and kinetically trapped nanostructures via an isodesmic or step-growth manner.

If combining the advantages of both INCP and CDSA methods is possible, we envisioned that this would lead to length-controlled π -conjugated 1D nanoparticles directly during polymerization. To achieve this goal, we proposed two criteria: first to develop a new CP shell with high solubility and second to slow down polymerization of the core block to control the rate of self-assembly. Therefore, we paid attention to the polymerization of 3,4-dialkylthiophenes (34DATs) bearing two side chains, which have been widely used to enhance the solubility of conjugated polymers and control the packing structure.^{35–39} However, due to severe steric repulsion between di-substituted monomers, living polymerization of 34DATs by the most popular KCTP method has not been successful.^{40,41} We envisioned that solving this synthetic challenge would successfully provide a solution for controlling the size of nanostructures via nucleation-elongation or the chain-growth mechanism. In this chapter, we demonstrate the first successful living Suzuki-Miyaura catalyst-transfer polymerization (SCTP) of 34DHT and its block copolymers, enabling a highly efficient self-assembly process called crystallization-driven *in situ* nanoparticlization of conjugated polymers (CD-INCP). This process can prepare uniform and length-controlled semiconducting 1D nanoparticles directly during polymerization (Figure 5.1c). This is the first example of forming semiconducting nanostructures whose lengths are synchronously controlled from 15 nm to 282 nm during polymerization. From kinetics and high-resolution imaging analyses, we identified the key factors for CD-INCP and proposed its mechanism. Moreover, we demonstrated the “living” CD-INCP process by further chain-extension from the pre-synthesized 1D nanoparticles as seeds and the most efficient one-shot (adding both monomers together) block copolymerization, which also directly produced length-controlled semiconducting 1D nanostructures.

5.3. Results and Discussion

Table 5.1. SCTP of **M1** Using the RuPhos Pd G3 Precatalyst.^a



Entry	M/I	RuPhos (equiv) ^b	THF/H ₂ O (v/v)	M _n (Đ) ^c	Yield (%) ^d
1	25	1.5	0.01 M (30/1)	6.8 kDa (1.14)	99
2	50	1.5	0.01 M (30/1)	13.5 kDa (1.07)	99
3	70	1.5	0.01 M (30/1)	17.2 kDa (1.17)	99
4	85	6	0.01 M (30/1)	20.3 kDa (1.26)	86
5	100	6	0.01 M (10/1)	22.2 kDa (1.17)	75
6	125	6	0.01 M (10/1)	28.0 kDa (1.32)	70
7	150	6	0.02 M (15/1)	35.0 kDa (1.32)	78
8	200	6	0.01 M (10/1)	39.4 kDa (1.41)	86

^aReaction conditions: **M1** (0.1 mmol), RuPhos Pd G3, RuPhos, 2-iodotoluene (1.0 equiv relative to the catalyst), K₃PO₄ (0.6 mmol), and THF/H₂O. ^bEquiv of the additional ligands relative to the catalyst. ^cAbsolute molecular weights determined by THF SEC using a multiangle laser light scattering (MALLS) detector. ^dIsolated yield after purification.

To achieve controlled polymerization of the challenging and bulky 34DHT monomer and prepare highly soluble CP, we attempted the powerful SCTP method, which has recently shown excellent control to give both N- and P-type conjugated polymers by optimizing the Pd precatalyst and masked boronates such as *N*-methyliminodiacetic acid (MIDA) and 4,4,8,8-tetramethyl-1,3,6,2-dioxazaborocane (Me₄DABO)⁴⁴ (Table 5.1). Gratifyingly, using a fast-initiating and highly active Buchwald precatalyst, RuPhos Pd G3, and **M1** bearing Me₄DABO boronate, which suppresses protodeboronation, P34DHT was successfully prepared in excellent yields (Table 5.1). Furthermore, with monomer/initiator (M/I) ratios ranging from 25 to 200, molecular weights of P34DHT were controlled linearly from 6.8 to 39.4 kDa with reasonable dispersity ($\bar{D} = 1.07\text{--}1.41$) (Table 5.1 and Figure S5.1). To obtain a higher M_n of P34DHT, adding more RuPhos ligand (6 equiv, entries 4–8) improved the control by effectively stabilizing the propagating chain-ends, thereby reducing the undesired chain transfer. In addition, increasing the water content or concentration (entries 5–8) to accelerate the propagation further improved the controlled SCTP. The matrix-

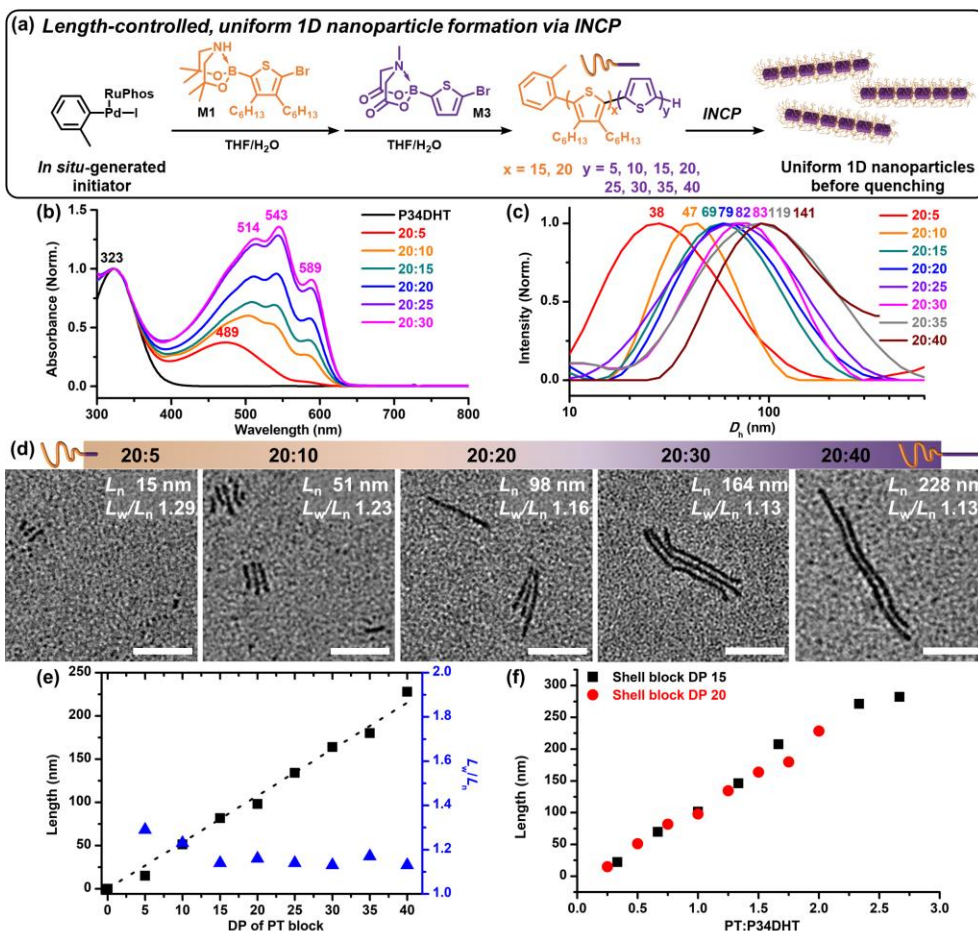


Figure 5.2. SCTP block copolymerization of P34DHT-*b*-PTs and synchronous self-assembly into length-controlled 1D nanoparticles. (a) Schematic representation how narrow disperse 1D nanoparticles were prepared from P34DHT-*b*-PTs. (b) UV-vis spectra (THF 0.05 g/L, RT), (c) DLS profiles (0.01 g/L or 0.05 g/L, THF solution at rt, spectra in full range is shown in Figure S5.6), and (d) TEM images of 1D nanoparticles taken from from the aliquots of P34DHT-*b*-PTs polymerization solutions. Numbers are the block ratios of P34DHT:PT. For other ratios, see Figure S5.6. Scale bars are 100 nm. (e) Plot illustrating increasing lengths of 1D nanoparticles from in situ solutions of P34DHT20-*b*-PTx, and their dispersity values. (f) Plot illustrating a linear relationship between lengths of 1D nanoparticles and their BCP's block ratio (PT:P34DHT).

assisted laser desorption/ionization time-of-flight mass spectrum of P34DHT ($M/I = 25$) revealed a peak series corresponding to the *o*-tol/H chain-end exclusively, supporting the chain-growth mechanism (Figure S5.2). The broad peak (d -spacing = 0.44–1.8 nm) in the film X-ray diffraction (film-XRD) of P34DHT and glass transition at -37 °C without any melting transition from the differential scanning calorimetry analysis revealed that P34DHT

is amorphous (Figure S5.3). Moreover, when 30 equiv of 3-hexylthiophene monomer containing MIDA boronate (**M2**) was added to the growing chain of P34DHT ($M_n = 4.2$ kDa and $\mathcal{D} = 1.17$), a diblock copolymer, P34DHT₁₅-*b*-P3HT₃₀ ($M_n = 13.6$ kDa and $\mathcal{D} = 1.27$), was obtained with the SEC trace clearly shifted from the first block to the higher molecular weight region (Figure S5.4). This demonstrates that a BCP with P34DHT can now be obtained via living SCTP.

Encouraged by our successful living polymerization results, we changed the second block to insoluble polythiophene (PT) without any side chain and prepared eight different P34DHT-*b*-PTs to examine INCP behavior. Specifically, we added 5 to 40 equiv of the thiophene monomer (**M3**) containing MIDA boronate to the growing chains of the P34DHT first block (**M1**/I = 20) (Figure 5.2a and Table S5.1; entries 1–8). Notably, all BCPs maintained a clear homogeneous solution without precipitation, even when the degree of polymerization (DP) of the PT core block was twice that of the P34DHT shell block, demonstrating its excellent stabilization. For all BCPs, ¹H NMR analyses showed identical spectra with the P34DHT homopolymer despite full consumption of **M3** after 18 h (Figure S5.5). This is a distinctive feature of INCP, where signals for the non-solvated core block disappear due to core-shell-type nanostructure formation.^{27–34} UV-vis spectroscopy of the *in situ* solution further helped in analyzing the features of the BCPs and nanostructures. First, there were two distinguishable absorptions, one corresponding to the P34DHT block ($\lambda_{\text{max,abs}} = 323$ nm) and the other for the PT block ($\lambda_{\text{max,abs}} = 489$ nm for P34DHT₂₀-*b*-PT₅). Notably, an increase in the DP of the PT block not only increased the relative absorption intensities of the core but also showed red-shifts in both $\lambda_{\text{max,abs}}$ and onset point (up to 514 nm and 631 nm, respectively) (Figure 5.2b). Furthermore, two distinct vibronic peaks at 589 nm and 543 nm (0–0 and 0–1, respectively) also became stronger, suggesting enhanced π - π interactions on the PT core leading to self-assembly.^{32,33} Finally, dynamic light scattering analysis provided further evidence of nanoparticlization, showing a gradual increase in hydrodynamic diameters (D_h) from 38 nm to 141 nm according to the elongation of the PT blocks (Figures 5.2c and S5.6b).

To further support the INCP process, an aliquot from each polymerization solution was taken before quenching and was imaged by transmission electron microscopy (TEM) (Figures 5.2d,e and S5.6c–e). Remarkably, all BCPs formed uniform 1D nanostructures with narrow length dispersity ($L_w/L_n = 1.13$ – 1.29), and their average lengths (L_n , from >50 samples) increased linearly from 15 to 228 nm, proportional to their DPs of the PT blocks from 5 to 40. To verify the stability of the nanoparticles, we quenched the polymerizations with HCl (aq), purified by precipitation, and checked their nanostructures in chloroform solution by TEM imaging (Figures S5.7 and S5.8). The lengths of the 1D

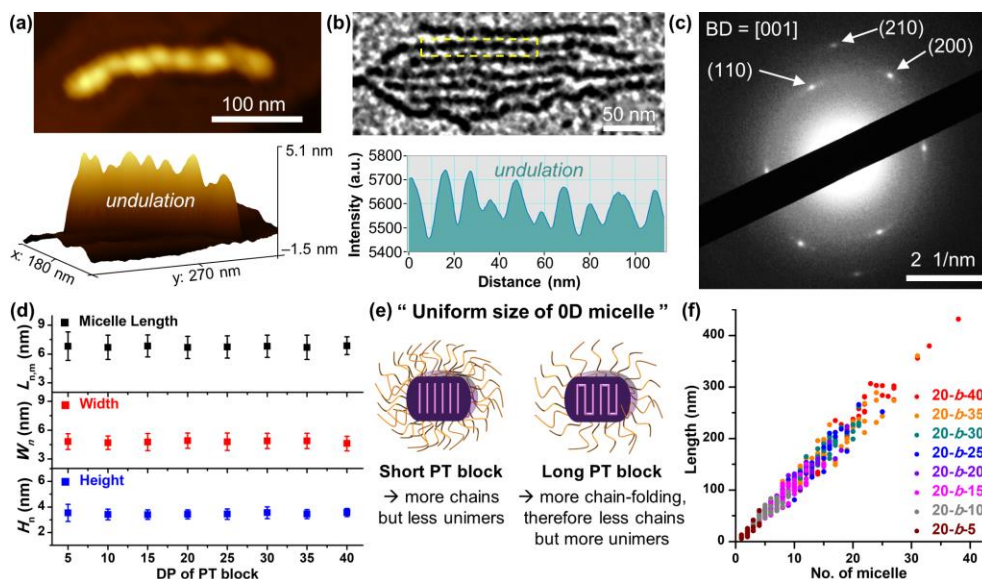


Figure 5.3. Structural analysis of 1D nanocaterpillars. (a) AFM top view and height profile images from P34DHT₂₀-*b*-PT₃₀ (b) TEM top view and line profile (intensity) images from P34DHT₂₀-*b*-PT₄₀. Both images reveal the undulating surface of the 1D nanostructure or nanocaterpillar. (c) SAED pattern corresponding to 1D nanocaterpillars from P34DHT₁₅-*b*-PT₄₀. (d) Average length ($L_{n,micelle}$), width (W_n), and height (H_n) values of individual 0D micellar building blocks composed of 1D nanostructures. Error bars are standard deviations of the measured values. (e) Scheme illustrating the uniform sizes of 0D micelles despite different DPs of the PT blocks for various BCPs. (f) Plot illustrating the linear dependence of lengths of nanocaterpillars on the number of 0D micelle units.

nanostructures still showed the same linear relationship up to DP = 35, and the initial structures were stable for 4 weeks (Figure S5.9). Notably, 1D nanostructures with uniform and tunable lengths were successfully prepared directly during the polymerization without any post-synthetic treatment processes, in contrast to typical CDSA, in which separate seed preparation by sonication and various conditions' screening for controlled elongation (e.g., temperature, concentration, and solvent) are required.

Next, to understand the effect of the shell block's DP on the length control, we prepared seven additional P34DHT-*b*-PTs by adding 5–40 equiv of **M3** into the growing P34DHT blocks with a lower DP ($M1/I = 15$, see Table S5.1; entries 9–15). Similarly, all BCPs generated uniform 1D nanostructures ($L_w/L_n = 1.13$ – 1.37), and their L_n increased linearly from 22 to 282 nm along with the core DPs (Figure S5.10). For the same DP of the core block, the smaller DP of the shell block led to longer nanostructures (e.g., 228 vs 282 nm for DP = 40 of the core block). Interestingly, when plotting L_n with respect to the block ratio (PT:P34DHT), it showed a good linear relationship irrespective of the shell DP

(Figure 5.2f). In short, we successfully controlled the lengths of 1D nanostructures to range from 15 to 282 nm by varying the block ratio from 0.25 to 2.67.

To understand the origin of this excellent length control, we conducted high-resolution atomic force microscopy (AFM) and TEM analyses and observed undulating surfaces of 1D nanoparticles or nanocaterpillars comprised of zero-dimensional (0D) micelles by height and line profiles (Figures 5.3a,b, S5.12, and S5.13). Similar to our previous INCP examples,^{27–30} if the driving force for the self-assembly was only the solvophobic interaction due to the low solubility of PT, kinetically trapped nanostructures without anisotropy would be generated from isotropic 0D micelles. However, the powder XRD (Figure S5.14a) suggested that the crystallization of the PT block drove the self-assembly. Moreover, spots in specific direction from selected area electron diffraction (SAED) (Figure 5.3c; $(hkl) = (110)$ d (d -spacing) = 0.45 nm; (200) d = 0.39 nm; (210) d = 0.32 nm) implied that interaction of the PT chains within and between the micelles had the same directionality, resulting in anisotropic growth. In addition, $(hk0)$ indexing of reflections suggested that the PT chain axis would be perpendicular to the substrate (Figure S5.14b).^{45,46} Based on these observations, a proper balance between the solubility and crystallinity of P34DHT-*b*-PTs might result in a unique self-assembly mechanism with characteristics of both INCP and CDSA.

To obtain detailed insights into the nanocaterpillars, we analyzed the sizes of each 0D micelle, a building block of nanocaterpillars, via AFM and TEM imaging (Figures 5.3d and S5.15). The average lengths ($L_{n,micelle} = 6.7–6.9$ nm), widths ($W_n = 4.6$ nm to 4.9 nm), and heights ($H_n = 3.4$ nm to 3.6 nm) of the 0D micelles were quite similar and independent of the DPs of PT blocks, in contrast to the total lengths, which were dependent on the DPs. This suggests that the longer the PT blocks, the more chain-folding would occur to form the consistent size, and the fewer BCP chains would occupy the same volume of a 0D micelle (Figure 5.3e). Therefore, BCPs with longer PT blocks would generate higher numbers of 0D micelles or unimers, leading to longer nanocaterpillars. Conversely, 0D micelles from the shorter PT blocks would require more BCP chains to form similar-sized 0D micelles, thereby decreasing the effective concentration of 0D micelles and resulting in shorter nanocaterpillars. This explains how the lengths of the nanocaterpillars showed a linear relationship with the number of 0D micelles in the nanocaterpillar (Figure 5.3f).

To obtain mechanistic insights into how increasing the number of micelles from longer PT chains leads to epitaxial growth of uniform nanocaterpillars during polymerization, we performed time-dependent monitoring of the self-assembly analyzed by UV-vis spectroscopy, AFM, and TEM (Figures S5.16–S5.19). Because the PT core block was undetectable by ¹H NMR and P3HT, the analogue of PT showed linear relationship

between molar extinction coefficients (ϵ) and molecular weights (Figure S5.16), we roughly estimated the DPs of PT blocks from their relative increment in absorption intensities in the UV-vis spectra (see Figure S5.17 for the calibration). After 30 min of polymerization (conversion = 8.3%), only 0D micelles were observed ($L_n = 10.9$ nm; Figure S5.18d). Subsequently, the lengths of the nanocaterpillars elongated linearly with the PT block conversion and followed the first-order kinetics (Figures 5.4a and S5.18c). Meanwhile, smaller objects with lower heights of 1.15 nm were observed, which we believe as the intermediate unimers for the seeded-growth mechanism resembling living polymerization (Figure S5.19c). To achieve length-controlled epitaxial growth, modulating the rates of seed formation and elongation processes is crucial.⁴⁷ In this regard, we reasoned that a highly stabilizing P34DHT shell and slow polymerization of the MIDA-based **M3** would provide good controllability because these would restrict successive seed formation and suppress the isodesmic step-growth mechanism. Furthermore, the slow growth of the core, which provides sufficient time for rearrangement and crystallization, helps in favoring the nucleation-elongation pathway and suppresses the formation of kinetically trapped micelles, which leads to irregular branching. To support this argument, we conducted two control experiments by synthesizing P3HT-*b*-PTs with a less soluble shell block (Table S5.2 and Figures S5.20–S5.22) and identical P34DHT-*b*-PTs but from a thiophene monomer (**M4**) containing more reactive pinacol boronate to accelerate polymerization (Table S5.3 and Figures S5.23–S5.25). In both cases, the length or morphology control was poor, emphasizing the importance of appropriate shell block and polymerization kinetics in achieving length control.

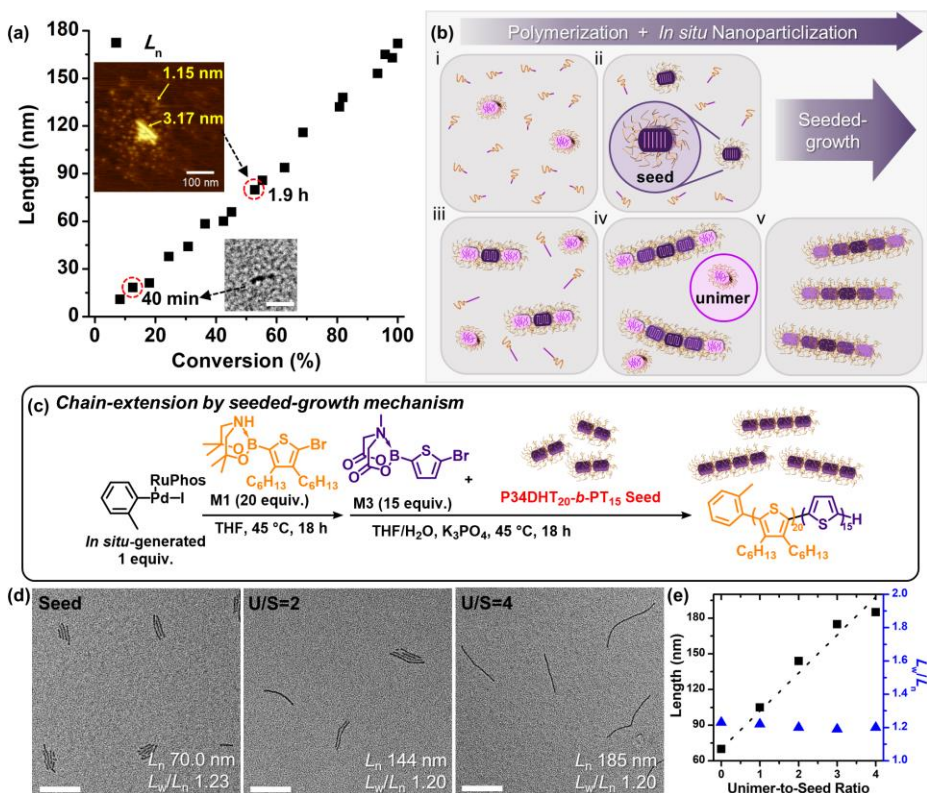


Figure 5.4. Time-dependent CD-INCP and its “livingness”. (a) Plot illustrating a linear relationship between the length of 1D nanostructures and the estimated conversion of **M3**. (b) Proposed mechanism of crystallization-driven *in situ* nanoparticlization of conjugated polymers (CD-INCP). (c) Schematic representation of living CD-INCP of newly synthesized P34DHT₂₀-b-PT₁₅ (unimer) on the pre-existing seed of P34DHT₂₀-b-PT₁₅. (d) TEM images of the aliquots from the living CD-INCP solution. Scale bars are 200 nm. (e) Plot illustrating the linear relationship between lengths and the unimer-to-seed ratio and their length dispersity values.

Based on these results, we proposed a mechanism for unprecedented length-controlled spontaneous self-assembly during polymerization, called crystallization-driven *in situ* nanoparticlization of conjugated polymers (CD-INCP) (Figure 5.4b). During the controlled growth of a core block,³² initial micelles are generated driven by solvophobic interaction in the early stage of block copolymerization. (Figure 5.4b-i). Among the metastable micelles stabilized by the P34DHT shell, some ripen into anisotropic crystalline seeds by chain rearrangement (Figure 5.4b-ii). Then, other metastable micelles produced later become unimer units and preferentially assemble on the crystalline surface of the seeds via a seeded-growth mechanism. These micellar unimers make undulating surfaces of 1D nanocaterpillars (Figure 5.4b-iii). With longer PT blocks, chain-folding produces more

unimeric micelles, which effectively increases the unimer-to-seed ratio, leading to longer nanocaterpillars (Figure 5.4b-iv,v). In short, CD-INCP, in which the advantages of both INCP and living CDSA processes are combined, efficiently produced nanocaterpillars with excellent precision.

Considering the seeded-growth mechanism, the chain-extension strategy of preparing unimer BCP from the pre-synthesized seeds would provide an additional length control via living CD-INCP. Therefore, we simply added different amounts of pre-synthesized P34DHT₂₀-*b*-PT₁₅ seeds ($L_n = 70$ nm) during the synthesis of P34DHT₂₀-*b*-PT₁₅ to vary the unimer-to-seed ratio (U/S) from 1:1 to 4:1 (Figure 5.4c and Table S5.4). TEM analysis revealed that the length of the resulting nanocaterpillars increased from 70 to 185 nm according to U/S while maintaining a narrow length dispersity of 1.2 (Figure 5.4d,e). This further supports the feasibility of the CD-INCP mechanism.

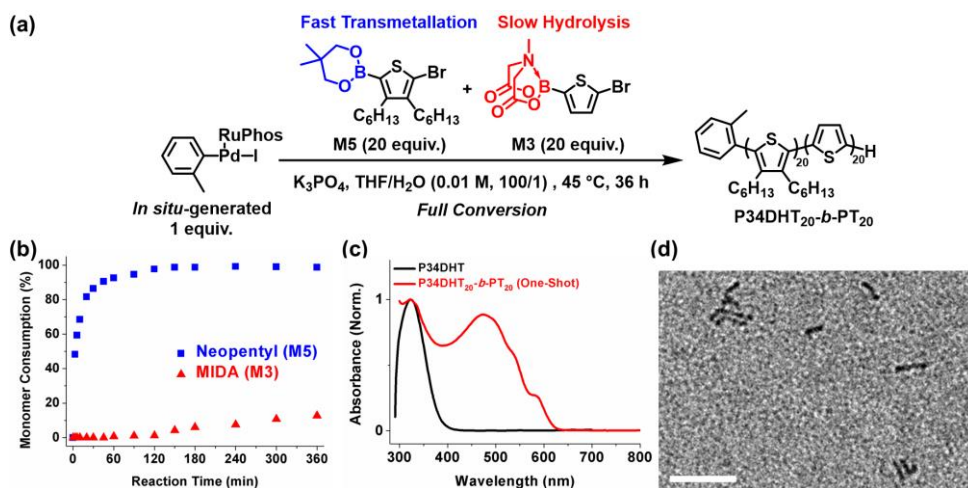


Figure 5.5. One-shot CD-INCP. (a) One-shot preparation of P34DHT₂₀-*b*-PT₂₀ by SCTP using **M5** and **M3**. (b) Kinetic plot showing consumption of **M5** and **M3** in one-shot copolymerization. (c) UV-vis spectra of P34DHT and P34DHT₂₀-*b*-PT₂₀ synthesized by one-shot SCTP (0.05 g/L, THF solution at rt). (d) TEM image of the aliquots from the one-shot copolymerization solution. Scale bar is 100 nm.

Recently, we achieved a unique one-shot SCTP block copolymerization of two alkylthiophenes by taking advantage of the vastly different reactivities of two monomers containing pinacol and MIDA-protected boronates.⁴²⁻⁴⁴ Likewise, a similar strategy of adding two monomers simultaneously would result in a more challenging but much simpler one-shot CD-INCP. Unfortunately, due to steric hindrance of the 3,4-dihexylthiophene unit, polymerization to form the solubilizing first block in copolymerization was much slower than the previous 3-hexylthiophene case (Figure S5.26). To secure a sufficient reactivity difference with **M3**, we synthesized a new 3,4-dihexylthiophene monomer (**M5**) containing

neopentyl glycol boronate, which showed 20-fold higher reactivity than pinacol boronate.⁴⁸ To perform one-shot CD-INCP, a monomer mixture of both **M5** (20 equiv) and MIDA-based **M3** (20 equiv) in THF was added together to a solution containing an *in situ*-generated initiator and was stirred at 45 °C for 36 h (Figure 5.5a). Time-dependent ¹H NMR monitoring of the crude copolymerization revealed that more reactive **M5** was fully converted to P34DHT within 2 h, followed by much slower polymerization of the core-forming **M3** (Figures 5.5b and S5.27). Kinetic analysis revealed that the propagation of **M5** was 198-fold faster than that of **M3** (0.0764 vs 0.000385; Figure S5.27c). The UV-vis absorption spectrum of the final polymer showed two characteristic absorption peaks corresponding to each block, supporting the successful synthesis of P34DHT-*b*-PT by the one-shot method (Figure 5.5c). Finally, TEM imaging also showed that P34DHT₂₀-*b*-PT₂₀ formed uniform nanocaterpillars with L_n of 43 nm ($L_w/L_n = 1.24$) (Figure 5.5d).

5.4. Conclusion

In conclusion of this chapter, we developed a new CD-INCP method to enhance both the preparation efficiency and length-control of semiconducting nanocaterpillars (15–282 nm) directly during polymerization without any post-synthetic treatment. This versatility, combining the advantages of both CDSA and INCP, was due to the successful polymerization of an unprecedented highly solubilizing conjugated P34DHT shell by a powerful SCTP. Second, slow polymerization of the PT core block leading to slow growth of the micelles suppressed the self-nucleation but facilitated the nucleation-elongation process via the chain-growth mechanism. Additionally, successful chain-extension from the preformed seeds demonstrated living CD-INCP. Lastly, by controlling the reactivity of the two monomers, we greatly simplified the CD-INCP by adding two monomers simultaneously (one-shot method), allowing for easier mass production of such semiconducting nanomaterials.

5.5. Experimental Section

Materials

All reagents and solvents which are commercially available were used without further purification, except for tetrahydrofuran (THF) which was distilled over sodium and benzophenone, and degassed by argon bubbling for 30 minutes before using on polymerization. Thin-layer chromatography (TLC) was carried out on MERCK TLC silica gel 60 F₂₅₄ and flash column chromatography was performed using MERCK silica gel 60 (0.040–0.063 mm).

Characterization of Substrates and Polymers

¹H NMR and ¹³C NMR spectroscopies were recorded by Varian/Oxford As-500 (500 MHz for ¹H NMR and 125 MHz for ¹³C NMR) and Agilent 400-MR (400 MHz for ¹H NMR and 100 MHz for ¹³C NMR) spectrometers. *High resolution mass spectroscopy (HRMS)* analyses were performed by the ultrahigh resolution ESI Q-TOF mass spectrometer (Bruker, Germany) in the Sogang Centre for Research Facilities. *Size exclusion chromatography (SEC)* analyses were carried out with Waters system (1515 pump and 2707 autosampler) and Shodex GPC LF-804 column eluted with HPLC-grade THF and filtered with a 0.2 μm PTFE filter (Whatman). The flow rate was 1.0 mL/min and temperature of column was maintained at 35 °C. For molecular weight characterization, Wyatt DAWN-HELEOS 8+ multi-angle light scatter (MALS) and Wyatt OptiLab T-rEx refractive index (RI) detectors (both maintained at 35 °C) were used. Molecular weights were determined from light scattering using dn/dc values calculated from batch mode measurements of polymer solutions at different concentrations. *Matrix-assisted laser desorption/ionization time-of-flight (MALDI-TOF)* mass spectrum was obtained by Bruker Daltonics autoflex II TOF/TOF using dithranol as a matrix. *Cyclic voltammetry (CV)* measurement was carried out on a CHI 660 Electrochemical Analyzer (CH Instruments, Inc., Texas, US) at rt using a degassed tetrahydrofuran (THF) solution of tetrabutylammonium perchlorate (Bu₄NClO₄, 0.1 M). The CV was recorded using a glassy carbon working electrode, a reference electrode of Ag/Ag⁺ (0.1 M AgNO₃ in acetonitrile) with a platinum wired counter electrode at a scan rate of 100 mV/s. *Thermogravimetric analysis (TGA)* and *differential scanning calorimetry (DSC)* were carried out under N₂ gas at a scan rate of 10 °C/min with Q10 and Q50 model devices (TA Instruments).

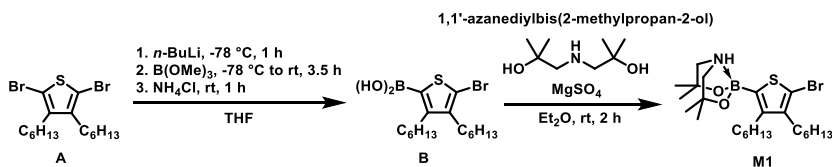
Characterization of Nanostructures

DLS data was obtained with polymer solution (0.01 g/L in general) in quartz glass cell (Hellma Analytics) by Malvern Zetasizer Nano-S. **UV-vis spectra** were obtained with polymer solution (0.05 g/L in general) in quartz glass cell by Jasco Inc (UV-vis spectrometer V-650). **AFM** analyses were performed using Bruker Multimode 8 and Nanoscope V controller (Veeco Instrument). Samples were prepared by spin coating (3000 rpm for 10 sec) one drop of polymer solution (ca. 10 μ L of 0.01 g/L solution) on HOPG or MICA substrates. **TEM** imaging was conducted using JEM-2100 (JEOL) at 120 kV. Polymer solutions were prepared in same manner with AFM and spin-coated to fomvar/carbon coated copper grids (TED PELLA, INC.). **Film-XRD** spectra was acquired from the National Instrumentation Center for Environmental Management at SNU using D8 Discover with GADDS (Bruker, Germany). Micelle widths, lengths, contour lengths, and heights of 1D nanoparticles were estimated from the TEM images manually using the ImageJ software package developed at the US National Institutes of Health. For statistical analysis, over 50 randomly picked nanoparticles were analyzed. Values of the number-average (X_n), weight-average (X_w), and standard deviation (σ) of nanocaterpillars were calculated as follows where N is the sample size.

$$X = L \text{ (length), } W \text{ (width), and } H \text{ (height); } X_n = \frac{\sum_{i=1}^n N_i L_i}{\sum_{i=1}^n N_i} \quad X_w = \frac{\sum_{i=1}^n N_i X_i^2}{\sum_{i=1}^n N_i L_i} \quad \sigma = \sqrt{\frac{1}{N} \sum_{i=1}^n (x_i - \mu)^2}$$

Preparation and Characterization of Monomers

2-(5-bromo-3,4-dihexylthiophen-2-yl)-6-methyl-1,3,6,2-dioxazaborocane-4,8-dione (M1)



A was prepared according to the previously reported synthetic method.⁴⁹ To a dried round-bottom flask equipped with a magnetic stir bar, A (2.05 g, 5.0 mmol) was added. The flask was evacuated and backfilled with argon three times, and then anhydrous THF (16.7 ml) was added. n -Buthyllithium (n -BuLi, 2.5 M solution in hexanes, 2.0 mL, 5.0 mmol) was added slowly at $-78\text{ }^\circ\text{C}$ and stirred for 1 h. $\text{B}(\text{OMe})_3$ (0.86 ml, 7.5 mmol) was then added to the flask. After stirring for 30 min at $-78\text{ }^\circ\text{C}$, the reaction was further left to stir for 3 h at room temperature and quenched with saturated ammonium chloride (NH_4Cl) aqueous solution for 1 h at room temperature. The reaction mixture was extracted with EtOAc three

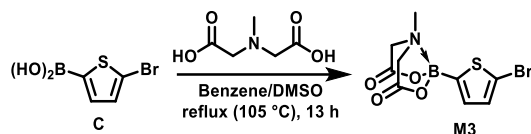
times, dried over MgSO₄, and evaporated under reduced pressure. The crude mixture of **B** was used for the next step without further purification.

To a dried round-bottom flask equipped with a magnetic stir bar, the crude mixture of **B**, 1,1'-azanediylbis(2-methylpropan-2-ol) (0.89 g, 5.5 mmol), which was prepared according to the previously reported synthetic method,⁴⁴ and MgSO₄ were added. The flask evacuated and backfilled with argon three times. After dissolving in Et₂O (16.7 mL) and stirring at rt for 2 h, the mixture was filtered and evaporated under reduced pressure to afford crude product, which was purified by column chromatography on neutral alumina gel (*n*-hexane/EtOAc = 1/1, R_f = 0.4) to afford **M1** as white solid (1.52 g, 3.04 mmol, 61%); ¹H NMR (500 MHz, CD₂Cl₂) δ 4.64 (s, 1H), 3.23 (dd, *J* = 12.1, 8.0 Hz, 2H), 2.87 (dd, *J* = 12.2, 4.2 Hz, 2H), 2.61–2.52 (m, 2H), 2.47–2.40 (m, 2H), 1.48–1.26 (m, 22H), 1.23 (s, 6H), 0.94–0.82 (m, 6H). ¹³C NMR (125 MHz, CD₂Cl₂) δ 144.7, 143.0, 110.0, 76.4, 62.9, 32.7, 32.4, 32.1, 31.0, 30.7, 30.5, 30.4, 30.1, 29.7, 28.9, 23.2, 23.1, 14.4. HRMS (ESI) *m/z*: [M + Na]⁺ Calcd for C₂₄H₄₃BBrNNaO₂S 522.2183; Found 522.2185.

2-(5-bromo-3-hexylthiophen-2-yl)-6-methyl-1,3,6,2-dioxazaborocane-4,8-dione (**M2**)

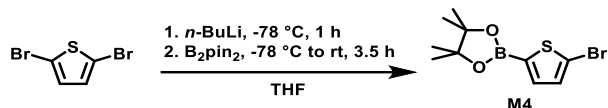
M2 was prepared according to the previously reported synthetic method.⁴²

2-(5-bromothiophen-2-yl)-6-methyl-1,3,6,2-dioxazaborocane-4,8-dione (**M3**)



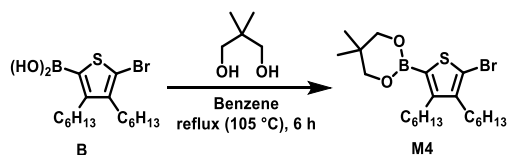
C was prepared according to the previously reported synthetic method.⁵⁰ To a dried round-bottom flask equipped with a Dean-Stark trap and a magnetic stir bar, **C** (1.03 g, 5.0 mmol) was added. The flask evacuated and backfilled with argon three times. *N*-Methyliminodiacetic acid (1.11 g, 7.5 mmol) was added and dissolved in anhydrous benzene (63 mL) and DMSO (7 mL). After being reflux at 105 °C for 13 h, the mixture was cooled to room temperature, extracted CH₂Cl₂ three times, washed with brine, dried over MgSO₄, and evaporated under reduced pressure to afford crude product, which was purified by column chromatography on silica gel (CH₂Cl₂/EtOAc = 1/1, R_f = 0.2) to afford **M3** as white solid (0.74 g, 2.3 mmol, 46%). The structure of **M3** was confirmed by comparison of its spectroscopic data with reported data.⁵¹

2-(5-bromothiophen-2-yl)-4,4,5,5-tetramethyl-1,3,2-dioxabrolane (**M4**)



To a dried round-bottom flask equipped with a magnetic stir bar, 2,5-dibromothiophene (1.17 ml, 10 mmol) was added. The flask was evacuated and backfilled with argon three times, and then anhydrous THF (33 ml) was added. *n*-Buthyllithium (*n*-BuLi, 2.5 M solution in hexanes, 4.0 mL, 10.0 mmol) was added slowly at -78 °C and stirred for 1 h. B₂pin₂ (3.73 mg, 15 mmol) was then added to the flask. After stirring for 30 min at -78 °C, the reaction was further left to stir for 3 h at room temperature. The reaction mixture was extracted with EtOAc three times, dried over MgSO₄, and evaporated under reduced pressure to afford crude product, which was purified by column chromatography on silica gel (*n*-hexane/EtOAc = 5/1, R_f = 0.6) to afford **M4** as brown liquid (1.71 g, 5.9 mmol, 59%). The structure of **M4** was confirmed by comparison of its spectroscopic data with reported data.⁵²

2-(5-bromo-3,4-dihexylthiophen-2-yl)-5,5-dimethyl-1,3,2-dioxazaborinane (**M5**)

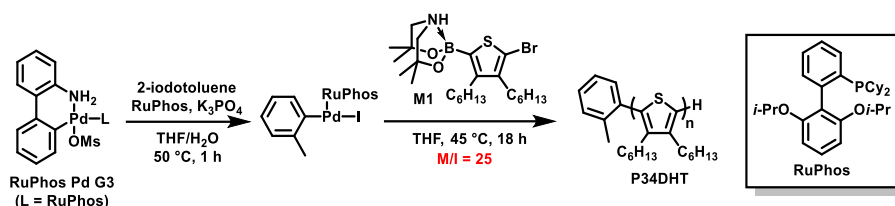


M5 was prepared by slightly modified procedure from the previous literature.⁴⁸ To a dried round-bottom flask equipped with a Dean-Stark trap and a magnetic stir bar, the crude mixture of **B**, which was prepared from **A** (5.0 mmol) was added. The flask evacuated and backfilled with argon three times. 2,2-Dimethyl-1,3-propanediol (0.58 g, 5.5 mmol) was added and dissolved in anhydrous benzene (50 mL). After being reflux at 105 °C for 6 h, the mixture was cooled to room temperature, extracted diethylether three times, washed with brine, dried over MgSO₄, and evaporated under reduced pressure to afford crude product, which was purified by column chromatography on silica gel (*n*-hexane/EtOAc = 20/1, R_f = 0.4) to afford **M5** as yellow liquid (0.78 g, 1.8 mmol, 35%); ¹H NMR (500 MHz, CD₂Cl₂) δ 3.70 (s, 4H), 2.78–2.72 (m, 2H), 2.52–2.47 (m, 2H), 1.49–1.39 (m, 4H), 1.39–1.23 (m, 12H), 0.98 (s, 6H), 0.87 (t, *J* = 6.9 Hz, 6H). ¹³C NMR (125 MHz, CD₂Cl₂) δ 152.5, 143.5, 115.2, 72.7, 32.5, 32.3, 32.0, 32.0, 30.1, 29.8, 29.8, 29.7, 28.6, 23.1, 23.0, 22.0, 14.3, 14.3. HRMS (ESI) *m/z*: [M + H]⁺ Calcd for C₂₁H₃₇BBro₂S 443.1785; Found 443.1041.

5.6. Supporting Information

5.6.1. Preparation and Characterization of Polymers

Synthesis of P34DHT by SCTP Using M1



To a round-bottom flask equipped with a magnetic stir bar, Buchwald Pd G3 precatalyst (0.004 mmol), 2-iodotoluene (0.004 mmol), RuPhos (0.006 mmol), and K_3PO_4 (0.6 mmol) were added. The flask was evacuated and backfilled with argon three times. Degassed THF (2 mL) and H_2O (0.33 mL) were then added. The mixture was heated and stirred at 50 °C for 1 h to prepare externally initiated catalyst. **M1** (0.1 mmol where $M/I = 25/1$) in degassed THF (8 mL) was then added to the flask, and the polymerization was left to stir at 45 °C for 18 h. The polymerization was quenched with 6*N* HCl solution (3 mL). The crude reaction mixture was diluted with CHCl_3 , washed with saturated NaHCO_3 (aq), dried over anhydrous MgSO_4 , and concentrated under reduced pressure. The polymer was purified by precipitation into methanol. The precipitate was collected by filtration, washed with methanol, and dried under vacuum.

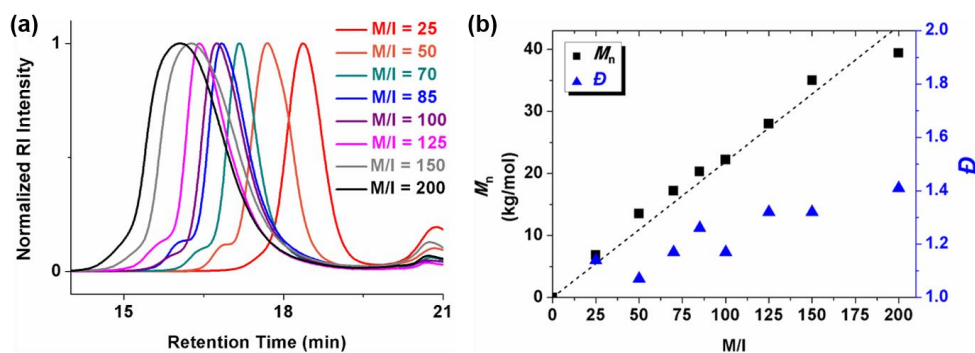


Figure S5.1. (a) THF SEC traces of P34DHT prepared using the RuPhos Pd G3 precatalyst and **M1** at M/I ratios ranging from 25 to 200. (b) Plots of M_n vs M/I ratios and their corresponding D .

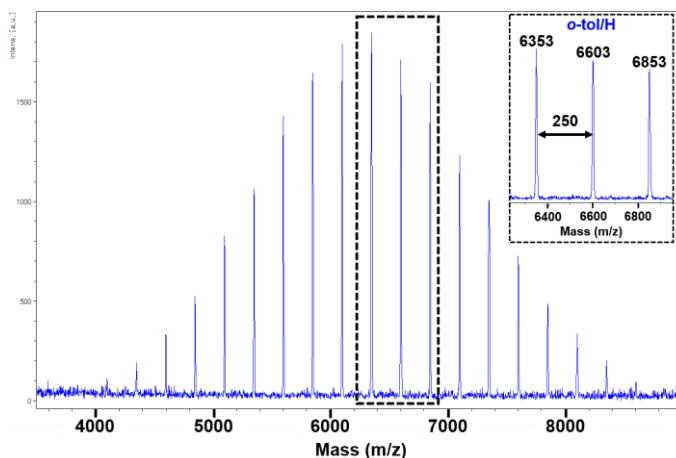


Figure S5.2. MALDI-TOF spectrum of P34DHT prepared by SCTP of **M1** (Table 5.1, entry 1).

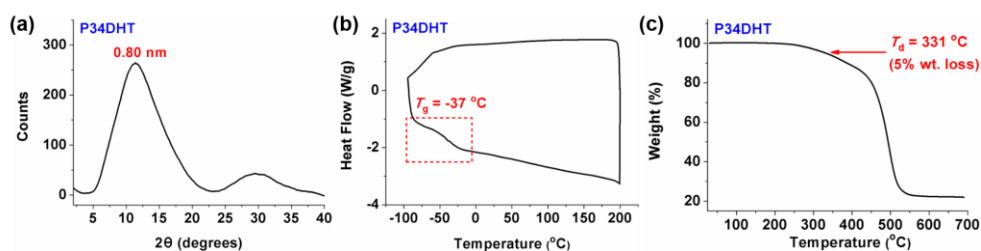


Figure S5.3. (a) Film XRD spectrum showing only broad peaks at d -spacing = 0.44–1.8 nm. (b) DSC thermograph showing T_g at -37 °C. (c) TGA thermograph showing $T_{d,95\%}$ at 331 °C.

Synthesis of P34DHT₁₅-*b*-PT₃₀ by SCTP Using **M1** and **M2**

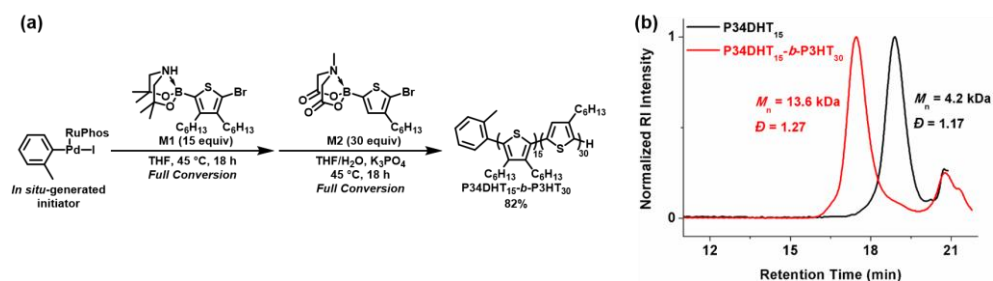
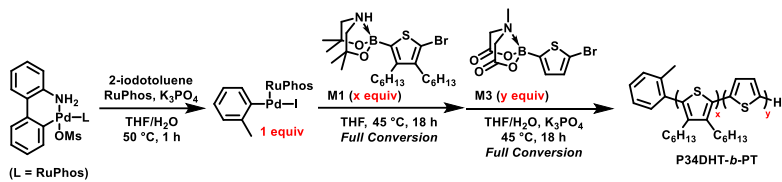


Figure S5.4. (a) Preparation of P34DHT₁₅-*b*-P3HT₃₀ by SCTP using **M1** and **M2** with RuPhos Pd G3 precatalyst. (b) THF SEC traces of macroinitiator and block copolymer corresponding to P34DHT₁₅ and P34DHT₁₅-*b*-P3HT₃₀, respectively. M_n and \bar{D} were determined by THF SEC calibrated using polystyrene standards.

To a round-bottom flask equipped with a magnetic stir bar, RuPhos G3 precatalyst (0.005 mmol), 4-iodobenzonitrile (0.005 mmol), RuPhos (0.03 mmol), and K_3PO_4 (0.45 mmol) were added. The flask was evacuated and backfilled with argon three times. Degassed THF (2 mL) and H_2O (0.25 mL) were then added. The mixture was heated and stirred at 50 °C 15 minutes to prepare externally initiated catalyst. **M1** (0.075 mmol where M/I = 15/1) in degassed THF (5.5 mL) was then added to the flask, and the polymerization was left to stir at 45 °C for 16 h. Subsequently, **M2** (0.15 mmol where M/I = 30/1) in degassed THF (7.5 mL) and K_3PO_4 (0.45 mmol) in degassed H_2O (0.25 mL) were added to the flask, and the polymerization was left to stir at 45 °C for 18 h. The polymerization was quenched with 6*N* HCl solution (5 mL). The crude reaction mixture was diluted with $CHCl_3$, washed with brine, dried over anhydrous $MgSO_4$, and concentrated under reduced pressure. The polymer was purified by precipitation into methanol. The precipitate was collected by filtration, washed with methanol, and dried under vacuum.

Synthesis of P34DHT-*b*-PTs by SCTP Using M1 and M3

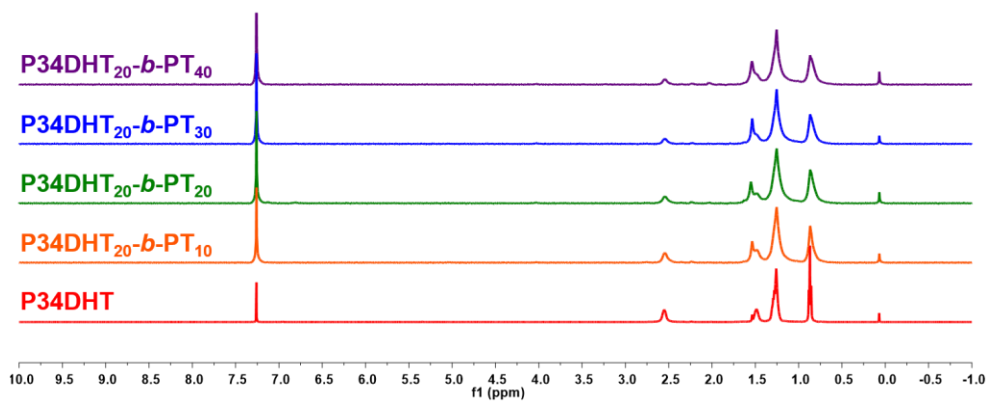


To a round-bottom flask equipped with a magnetic stir bar, RuPhos G3 precatalyst (0.0025 mmol), 2-iodotoluene (0.0025 mmol), RuPhos (0.015 mmol), and K_3PO_4 (0.3 mmol) were added. The flask was evacuated and backfilled with argon three times. Degassed THF (2 mL) and H_2O (0.17 mL) were then added. The mixture was heated and stirred at 50 °C for 1 h to prepare externally initiated catalyst. **M1** (0.05 mmol or 0.0375 mmol where M/I = 20/1 or 15/1) in degassed THF (3 mL) was then added to the flask, and the polymerization was left to stir at 45 °C for 18 h. Subsequently, **M3** (0.0125 mmol, 0.025 mmol, 0.0375 mmol, 0.05 mmol, 0.0625 mmol, 0.075 mmol, 0.0875 mmol, and 0.10 mmol where M/I = 5/1, 10/1, 15/1, 20/1, 25/1, 30/1, 35/1, and 40/1, respectively) in degassed THF (0.25 mL, 0.5 mL, 0.75 mL, 1.0 mL, 1.25 mL, 2.5 mL, 3.75 mL, and 5.0 mL, respectively) and K_3PO_4 (0.0 mmol, 0.0 mmol, 0.0 mmol, 0.0 mmol, 0.075 mmol, 0.15 mmol, 0.225 mmol, and 0.3 mmol, respectively) in degassed H_2O (0.0 mL, 0.0 mL, 0.0 mL, 0.0 mL, 0.04 mL, 0.08 mL, 0.13 mL, and 0.17 mL, respectively) were added to the flask, and the polymerization was left to stir at 45 °C for 18 h. The polymerization was quenched with 6*N* HCl solution (5 mL). The crude reaction mixture was diluted with $CHCl_3$, washed with brine, dried over anhydrous $MgSO_4$, and concentrated under reduced pressure. The polymer was purified by precipitation into methanol. The precipitate was collected by filtration, washed with methanol, and dried under vacuum.

Table S5.1. Synthesis of P34DHT-*b*-PTs by SCTP Using **M1** and **M3**.

Entry	M1 (equiv) ^a	M3 (equiv) ^a	<i>M_n</i> (<i>D</i>) of P34DHT ^b	Yield (%) ^c
1	20	5	5.9 kDa (1.14)	87
2	20	10	6.2 kDa (1.15)	94
3	20	15	6.3 kDa (1.14)	72
4	20	20	6.4 kDa (1.16)	90
5	20	25	5.8 kDa (1.15)	98
6	20	30	6.3 kDa (1.16)	99
7	20	35	6.1 kDa (1.14)	97
8	20	40	6.1 kDa (1.16)	93
9	15	5	4.7 kDa (1.15)	90
10	15	10	4.6 kDa (1.17)	89
11	15	15	4.9 kDa (1.18)	99
12	15	20	4.9 kDa (1.14)	99
13	15	25	4.8 kDa (1.16)	85
14	15	35	4.7 kDa (1.14)	83
15	15	40	4.6 kDa (1.15)	91

^aEquiv of additional ligand relative to catalyst. ^bDetermined by THF SEC calibrated using polystyrene standards. ^cIsolated yield after purification.

**Figure S5.5.** ¹H NMR spectra of P34DHT and P34DHT-*b*-PTs (500 MHz, CDCl₃).

5.6.2. TEM and AFM Images of 1D Nanoparticles

In Situ Nanostructure Analysis of P34DHT_{20-b}-PT_x

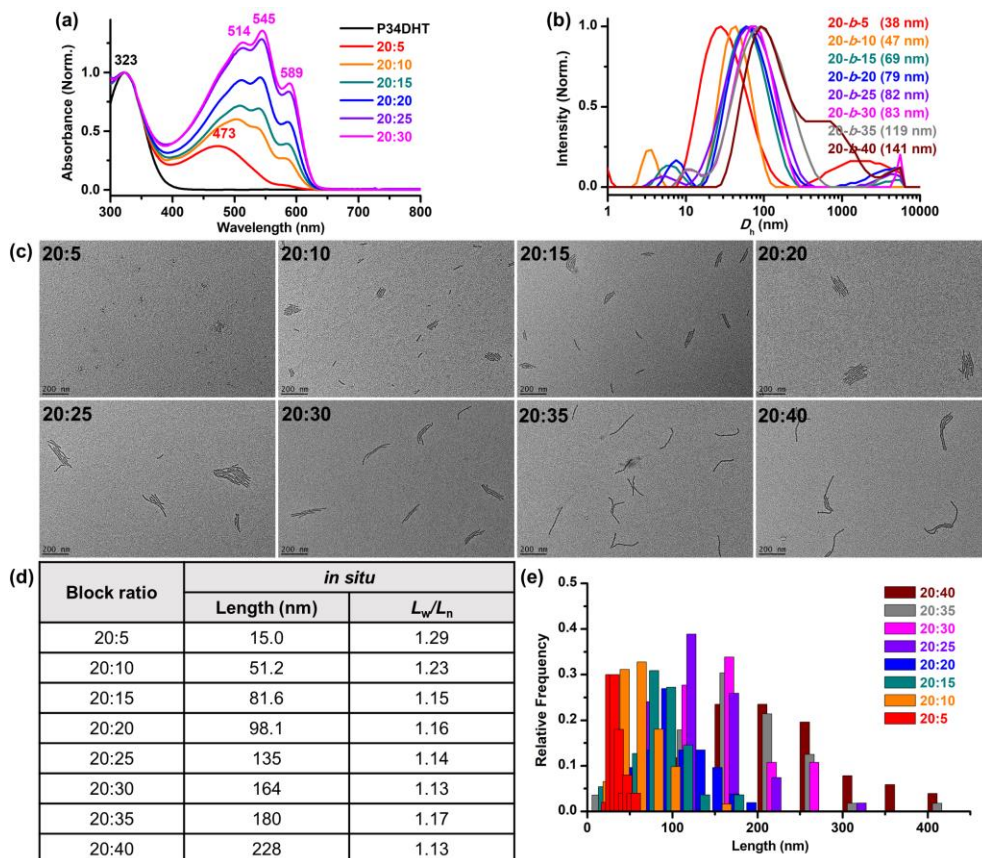


Figure S5.6. (a) UV-vis spectra (0.05 g/L, THF solution at rt) and (b) DLS profiles (0.01 g/L or 0.05 g/L, THF solution at rt) of nanoparticles from the aliquots of P34DHT-*b*-PT polymerization solutions. Absorbance intensities are normalized with intensity at 323 nm (P34DHT shell block absorbance). Intensities are normalized to [0,1] for DLS analysis. (c) TEM images of controlled 1D nanoparticles from *in situ* solution of eight P34DHT-*b*-PTs. BCPs with block ratio of P34DHT:PT=20:5, 20:10, 20:15, 20:20, 20:25, 20:30, 20:35 and 20:40. Scale bars are 200 nm. (d) Table of average length values of 1D nanoparticles and their length dispersity values. (e) Histogram of the contour length distribution of 1D nanoparticles.

After Precipitation, Nanostructure Analysis P34DHT_{20-b}-PT_x

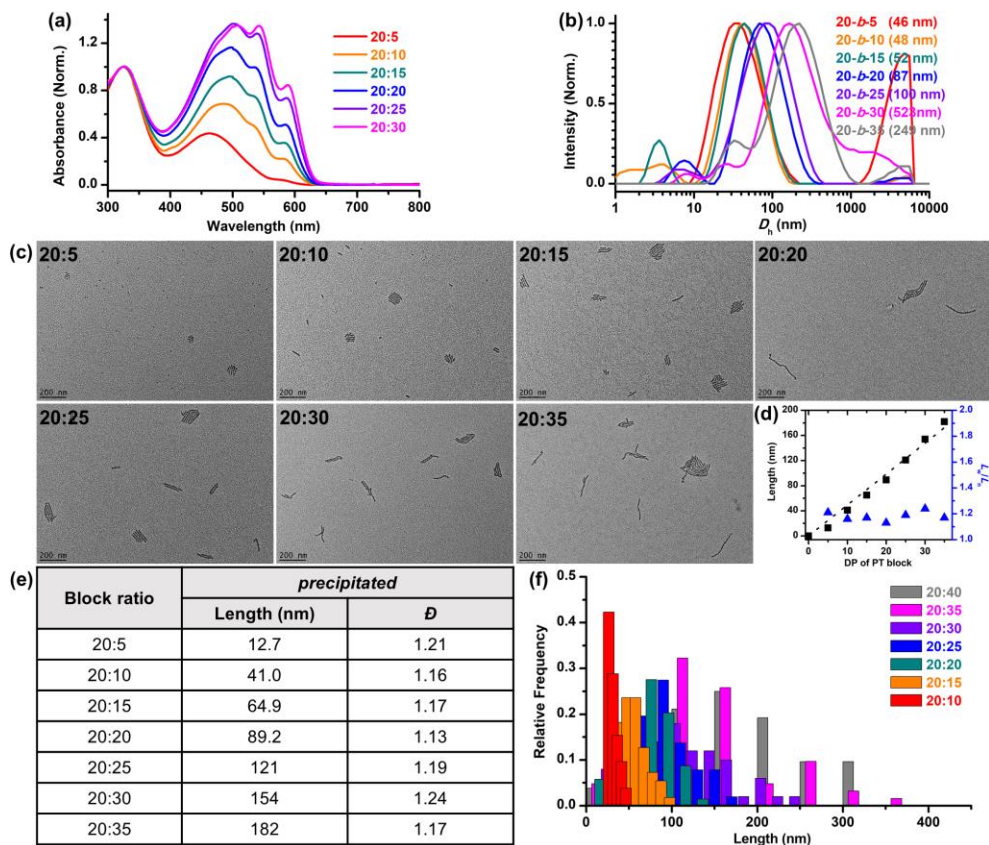


Figure S5.7. (a) UV-vis spectra (0.05 g/L, CHCl₃ solution at rt) and (b) DLS profiles (0.01 g/L or 0.05 g/L, CHCl₃ solution at rt) of nanoparticles from the aliquots of P34DHT-*b*-PT polymerization solutions. Absorbance intensities are normalized with intensity at 323 nm (P34DHT shell block absorbance). Intensities are normalized to [0,1] for DLS analysis. (c) TEM images of controlled 1D nanoparticles from *precipitated* seven P34DHT-*b*-PTs. BCPs with block ratio of P34DHT:PT = 20:5, 20:10, 20:15, 20:20, 20:25, 20:30 and 20:35. Scale bars are 200 nm. (d) Plot illustrating increasing lengths of 1D nanoparticles depending on DP of PT blocks, and their dispersity values. (e) Table of average length values of 1D nanoparticles and their length dispersity values. (f) Histogram of the contour length distribution of 1D nanoparticles.

AFM images of 1D nanostructures from P34DHT₂₀-b-PT_x

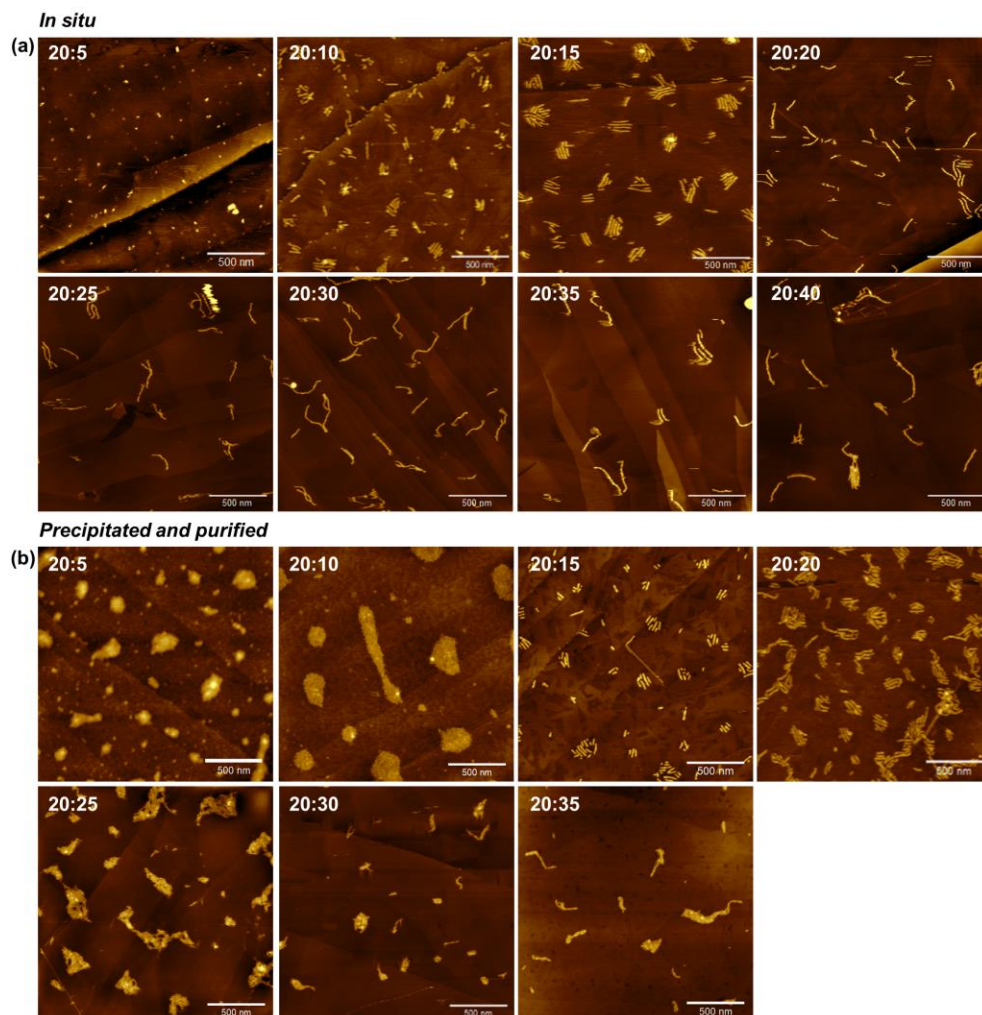
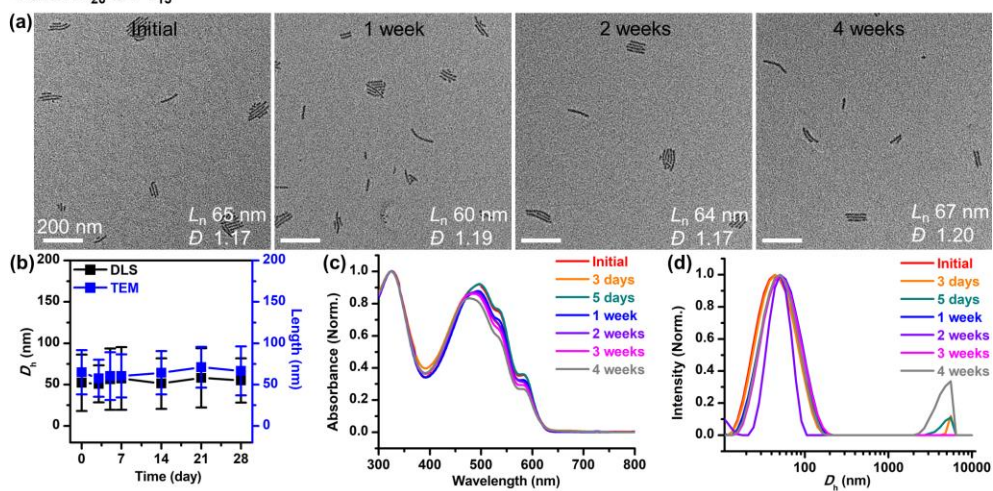


Figure S5.8. AFM height images (spin-coated on HOPG) of controlled 1D nanoparticles from (a) *in situ* and (b) *precipitated* P34DHT-*b*-PTs. BCPs with block ratio of P34DHT:PT = 20:5, 20:10, 20:15, 20:20, 20:25, 20:30, 20:35 and 20:40. Scale bars are 500 nm.

Long Term Stability

P34DHT₂₀-b-PT₁₅



P34DHT₂₀-b-PT₃₀

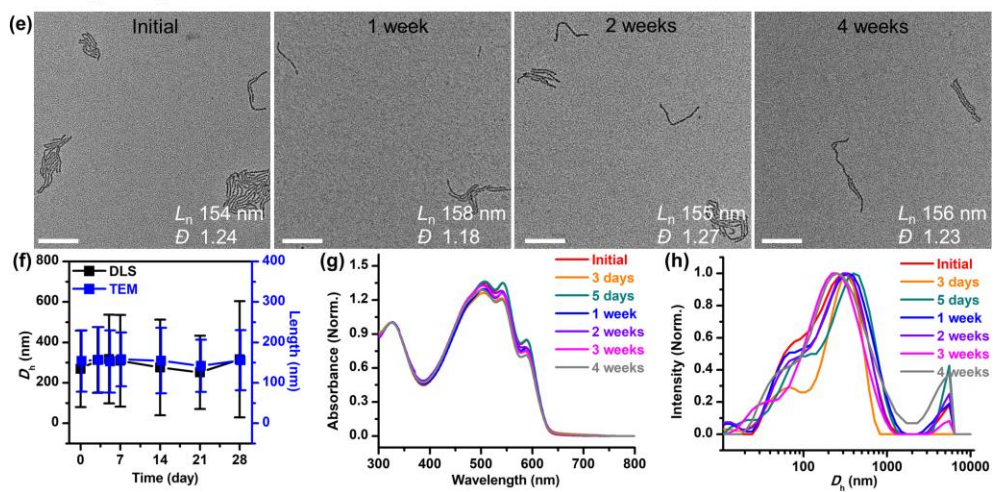


Figure S5.9. (a) TEM images, (b) constant hydrodynamic diameter and average lengths, (c) UV-vis spectra, and (d) DLS profiles (0.05 g/L, THF solution at rt) of 1D nanoparticles from precipitated P34DHT₂₀-b-PT₁₅ along the aging times. (e) TEM images, (f) constant hydrodynamic diameter and average lengths, (g) UV-vis spectra, and (h) DLS profiles (0.05 g/L, THF solution at rt) of 1D nanoparticles from precipitated P34DHT₂₀-b-PT₃₀ along the aging times. Scale bars are 200 nm. Absorbance intensities are normalized with intensity at 323 nm (P34DHT shell block absorbance). Intensities are normalized to [0,1] for DLS analysis.

In Situ Nanostructure Analysis of P34DHT₁₅-b-PT_x

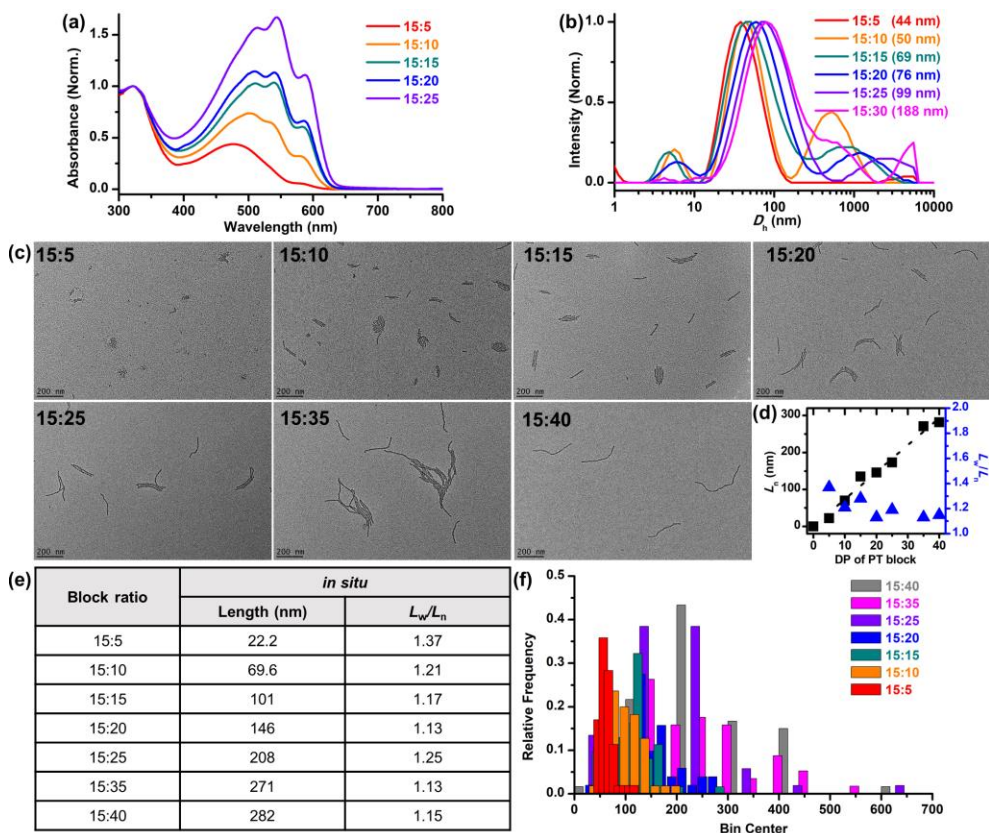


Figure S5.10. (a) UV-vis spectra (0.05 g/L, CHCl₃ solution at rt) and (b) DLS profiles (0.01 g/L or 0.05 g/L, CHCl₃ solution at rt) of nanoparticles from the aliquots of P34DHT-*b*-PT polymerization solutions. Absorbance intensities are normalized with intensity at 323 nm (P34DHT shell block absorbance). Intensities are normalized to [0,1] for DLS analysis. (c) TEM images of controlled 1D nanoparticles from precipitated seven P34DHT-*b*-PTs. BCPs with block ratio of P34DHT:PT = 15:5, 15:10, 15:15, 15:20, 15:25, 15:35 and 15:40. Scale bars are 200 nm. (d) Plot illustrating increasing lengths of 1D nanoparticles depending on DP of PT blocks, and their dispersity values. (e) Table of average length values of 1D nanoparticles and their length dispersity values. (f) Histogram of the contour length distribution of 1D nanoparticles.

After Precipitation, Nanostructure Analysis P34DHT₁₅-b-PT_x

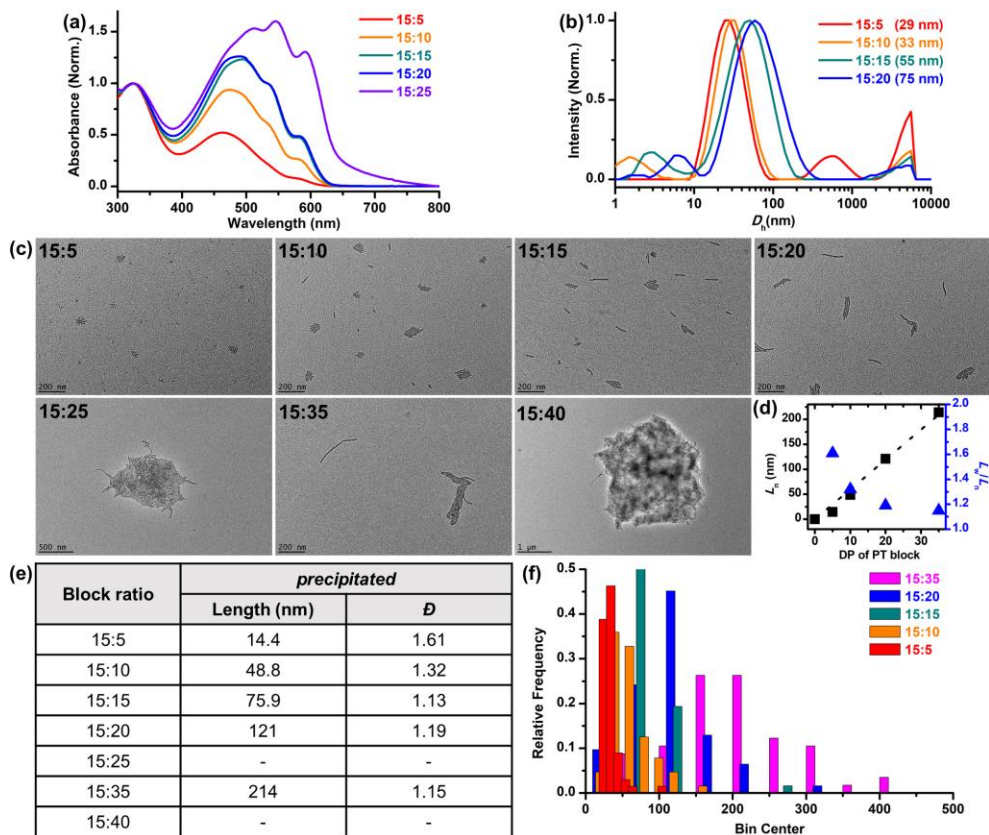


Figure S5.11. (a) UV-vis spectra (0.05 g/L, CHCl₃ solution at rt) and (b) DLS profiles (0.01 g/L or 0.05 g/L, CHCl₃ solution at rt) of nanoparticles from the aliquots of P34DHT-*b*-PT polymerization solutions. Absorbance intensities are normalized with intensity at 323 nm (P34DHT shell block absorbance). Intensities are normalized to [0,1] for DLS analysis. (c) TEM images of controlled 1D nanoparticles from *precipitated* seven P34DHT-*b*-PTs. BCPs with block ratio of P34DHT:PT = 15:5, 15:10, 15:15, 15:20, 15:25, 15:35 and 15:40. Scale bars are 200 nm. Scale bars are 500 nm for 15:25 BCP and 1000 nm for 15:40 BCP. (d) Plot illustrating increasing lengths of 1D nanoparticles depending on DP of PT blocks, and their dispersity values. (e) Table of average length values of 1D nanoparticles and their length dispersity values. (f) Histogram of the contour length distribution of 1D nanoparticles.

5.6.3. Structural analysis of 1D Nanoparticles

Undulation

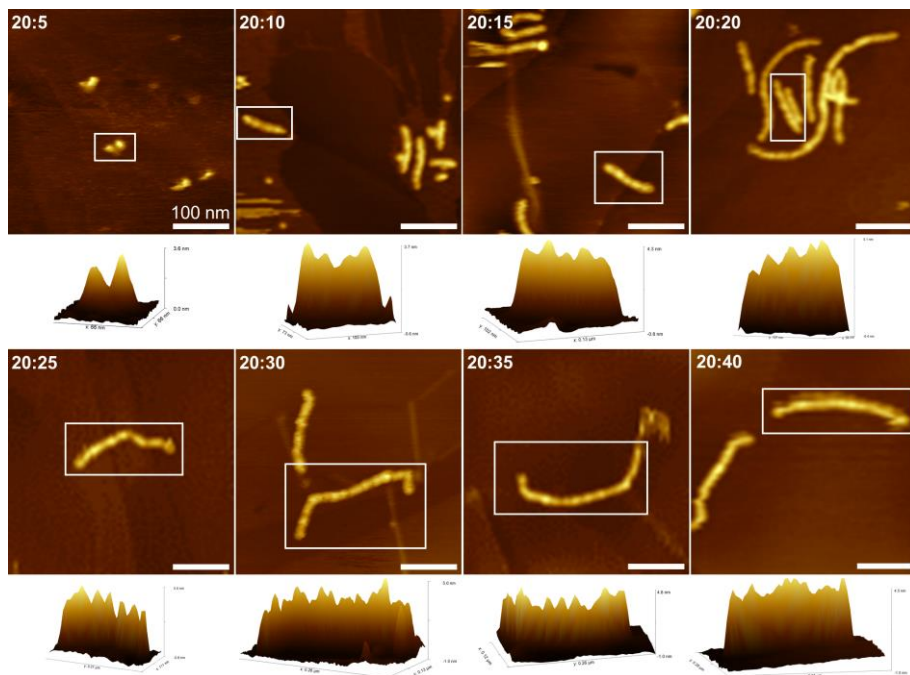


Figure S5.12. AFM Height Images and Height Profiles of P34DHT-*b*-PTs showing Undulating Surfaces. AFM height mode images of controlled 1D nanoparticles from *precipitated* seven P34DHT-*b*-PTs. BCPs with block ratio of P34DHT:PT = 20:5, 20:10, 20:15, 20:20, 20:25, 20:30, 20:35 and 20:40. Scale bars are 100 nm. Height profiles are from 1D nanostructures inside the white boxes.

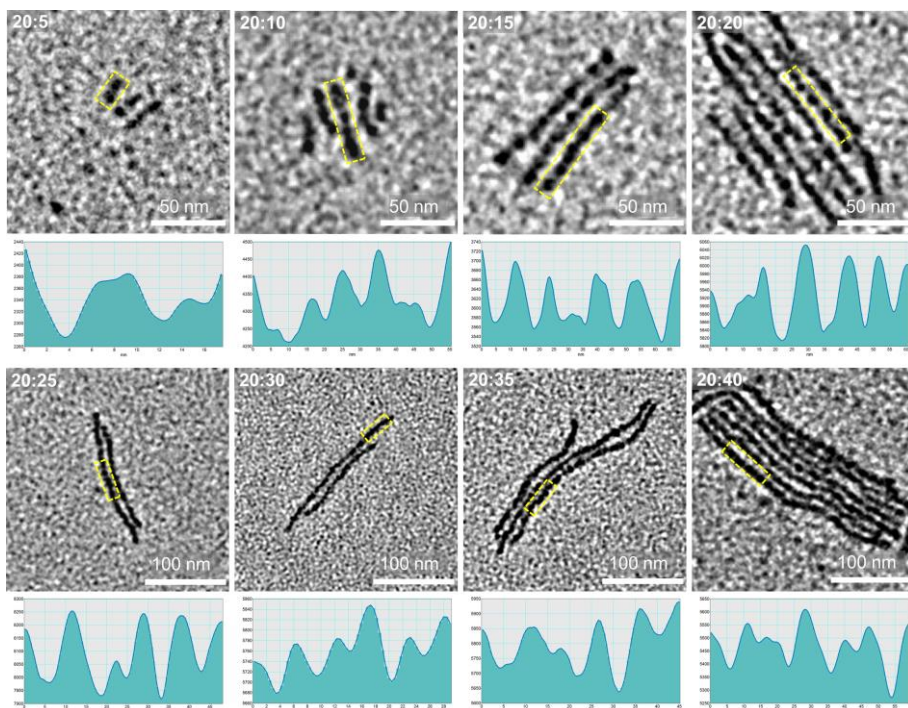


Figure S5.13. TEM Images and Line Profiles of P34DHT-*b*-PTs showing Undulating Surfaces. HR-TEM images of controlled 1D nanoparticles from *in situ* solution of seven P34DHT-*b*-PTs. BCPs with block ratio of P34DHT:PT = 20:5, 20:10, 20:15, 20:20, 20:25, 20:30, 20:35 and 20:40. Line profiles are from 1D nanostructures inside the white boxes.

Crystallinity

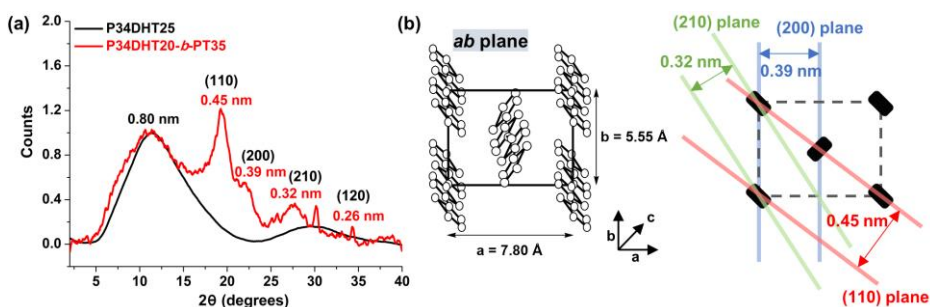


Figure S5.14. (a) Powder XRD spectra of P34DHT₂₀-*b*-PT₃₅ showing crystalline peaks with (*hk*0) reflections of PT core block ((110) *d* (*d*-spacing) = 0.45 nm; (200) *d* = 0.39 nm; and (210) *d* = 0.32 nm) and broad amorphous peak of P34DHT shell block at *d*-spacing = 0.44–1.8 nm. Counts are normalized with the counts at *d*=0.80 nm (peak from P34DHT shell block). (b) Schematic illustration of polythiophene crystal unit cell. *ab* plane is shown. *a* = 7.80 Å, *b* = 5.55 Å, *c* ≈ 7.70 Å (estimated from the thiophene monomer), monoclinic or orthorhombic unit cell. Unit cell and *d*-spacing values are reported in the following references.⁴⁶

0D Micelle Size

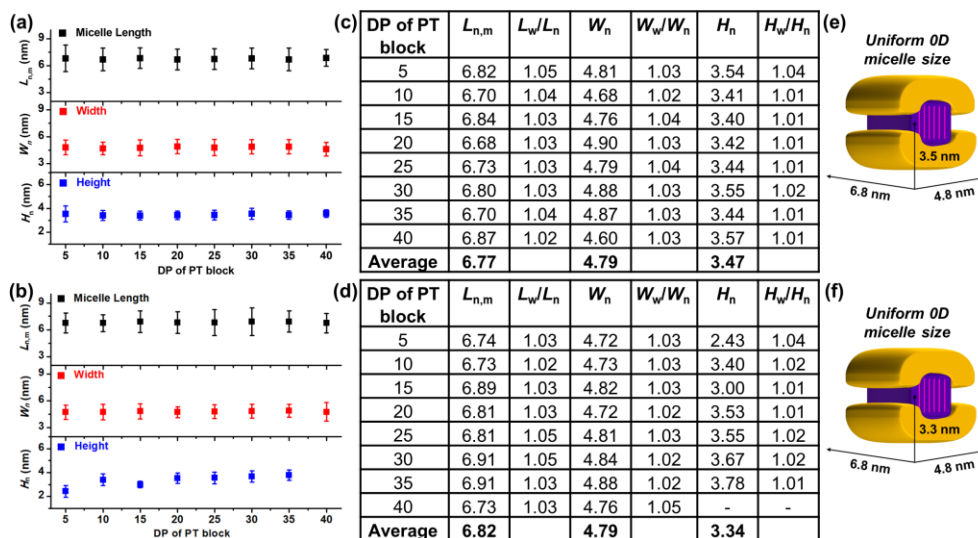


Figure S5.15. Structural information of 1D nanostructures of P34DHT₂₀-*b*-PT_x. Plots of lengths, widths and heights of 0D micelles depending on DP of PT block from (a) *in situ* and (b) *precipitated* samples. Table of length ($L_{n,micelle}$), width (W_n) and height (H_n) values of 0D micelles from (c) *in situ* and (d) *precipitated* samples. Scheme of uniform size having 0D micelle from (e) *in situ* and (f) *precipitated* samples.

5.6.4. Time-dependent Nanostructure Analysis

Calculation of DP and Conversion of PT Core Block in Time-dependent Experiment

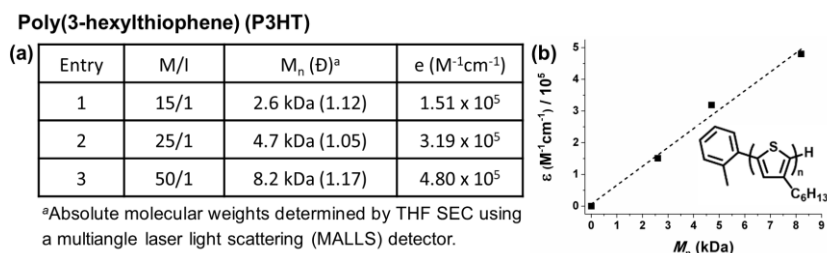


Figure S5.16. Linear relationship between molar extinction coefficient (ϵ) and molecular weight. Three P3HTs, the analogue of PT, having different molecular weights with the controlled SCTP method⁴² were analyzed by UV-vis spectroscopy. The molar extinction coefficients (ϵ) increased linearly along with molecular weights of P3HT as shown in the above table (a) and graph (b).

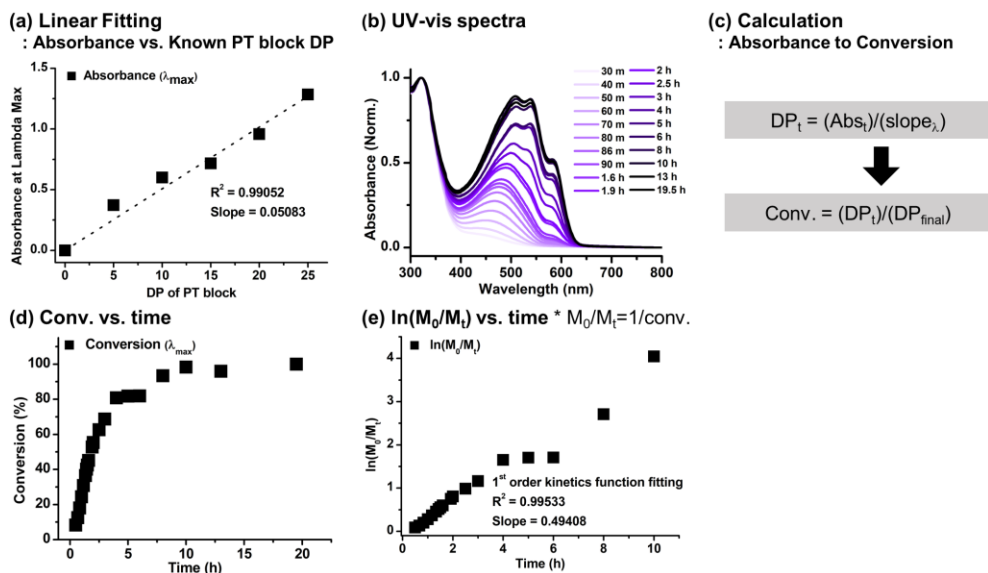


Figure S5.17. Procedure of calculating insoluble PT block's DP in *time-dependent (kinetic)* experiment from known PT block's DP of P34DHT-*b*-PTs by UV-vis absorbance analysis. (a) Linear fitting of 'Absorbance at λ_{max} vs. DP of PT block' plot. Slope represents increased absorbance per DP of PT block. Relative absorbances of PT core blocks in UV-vis analysis by setting the similar molecular weight having P34DHTs' absorption as a standard were measured. In other words, the absorbance of PT block depends on only the molar extinction coefficients (ϵ) of PT block without concentration effect. (b) UV-vis absorbance spectra along time after **M3** addition. The feed ratio of 20:20:1 (**[M1]**:**[M3]**:**[I]**) was used for the experiment. After some time, aliquots were taken from the reaction mixture and diluted with THF for UV-vis spectra. (c) DP at the time point (DP_t) is calculated by dividing absorbance at λ_{max} in time-dependent UV-vis spectra (Abs_t) by the slope calculated in (a). Then, conversion is calculated by dividing DP_t by the final estimated DP at the end of polymerization (DP_{final}). (d) Plot illustrating calculated conversion at each time point. (e) First-order kinetics plot of polymerization.

Structural Analysis by TEM in Time-dependent Experiment

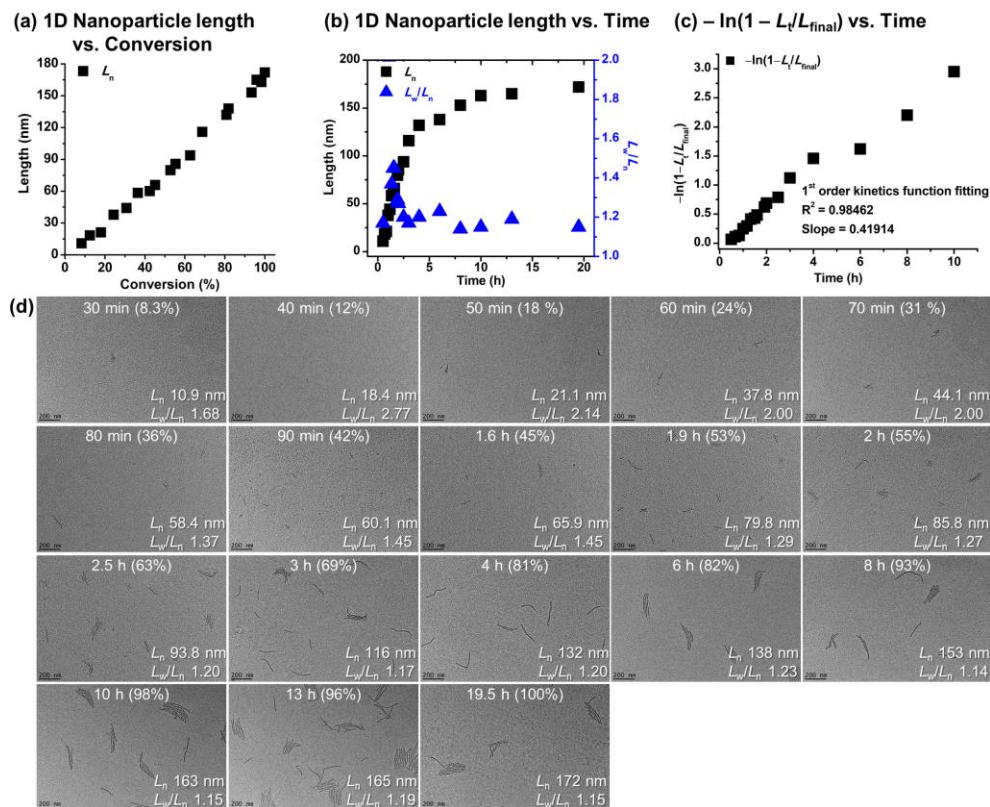


Figure S5.18. The feed ratio of 20:20:1 ([M1]:[M3]:[I]) was used for the experiment. After some time, aliquots were taken from the reaction mixture and diluted with THF for TEM analysis. (a) Plot illustrating a linear relationship between lengths of 1D nanostructures and estimated conversions of M3. (b) Plot illustrating 1D nanoparticles' lengths and dispersity values at each time point. (c) First-order kinetics plot of *in situ* nanoparticlization. (d) TEM images showing *in situ* nanoparticlization of P34DHT-*b*-PT. Numbers in parentheses are conversions at that time. Scale bars are 200 nm.

Structural Analysis by AFM in Time-dependent Experiment

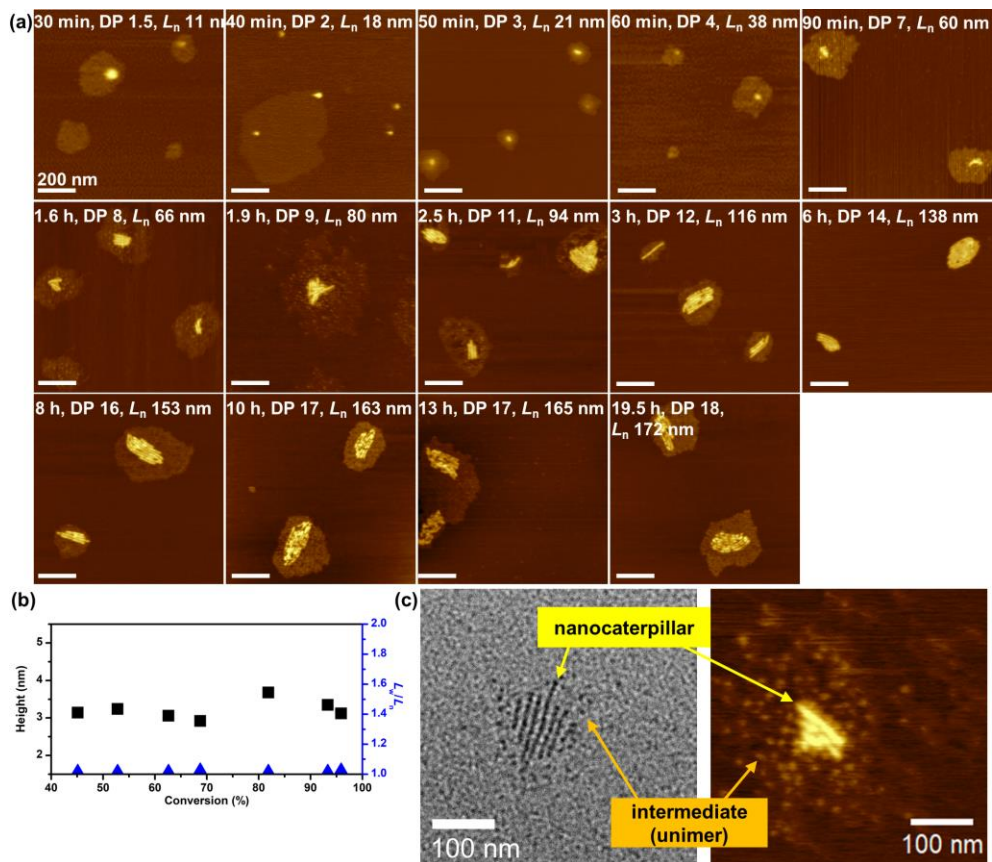
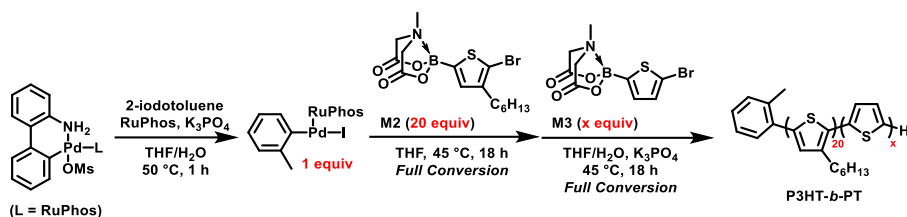


Figure S5.19. (a) AFM images showing *in situ* nanoparticlization of P34DHT-*b*-PT. The feed ratio of 20:20:1 ([M1]:[M3]:[I]) was used for the experiment. After some time, aliquots were taken from the reaction mixture and diluted with chloroform for AFM analysis. THF 0.01 g/L solutions were spin-coated on MICA surfaces. Scale bars are 500 nm. (b) Plot showing constant height values of 1D nanostructures along the conversion of PT block. (c) Highly magnified TEM and AFM image showing nanocaterpillars and intermediate structures. Aliquot was taken after 1.9 hour. Scale bars are 100 nm.

5.6.5. Control Experiments

Synthesis of P3HT-*b*-PTs by SCTP Using **M2** and **M3**



To a round-bottom flask equipped with a magnetic stir bar, RuPhos G3 precatalyst (0.0025 mmol), 2-iodotoluene (0.0025 mmol), RuPhos (0.015 mmol), and K_3PO_4 (0.3 mmol) were added. The flask was evacuated and backfilled with argon three times. Degassed THF (2 mL) and H_2O (0.17 mL) were then added. The mixture was heated and stirred at 50 °C for 1 h to prepare externally initiated catalyst. **M2** (0.05 mmol where $M/I = 20/1$) in degassed THF (3 mL) was then added to the flask, and the polymerization was left to stir at 45 °C for 18 h. Subsequently, **M3** (0.05 mmol, 0.075 mmol, and 0.10 mmol where $M/I = 20/1$, 30/1, and 40/1, respectively) in degassed THF (1.0 mL, 2.5 mL, and 5.0 mL, respectively) and K_3PO_4 (0.0 mmol, 0.15 mmol, and 0.3 mmol, respectively) in degassed H_2O (0.0 mL, 0.08 mL, and 0.17 mL, respectively) were added to the flask, and the polymerization was left to stir at 45 °C for 18 h. The polymerization was quenched with 6N HCl solution (5 mL).

Table S5.2. Synthesis of P3HT-*b*-PTs by SCTP Using **M2** and **M3**.

Entry	M3 (equiv) ^a	M_n (Đ) of P3HT ^b	Yield (%) ^c
1	20	5.1 kDa (1.16)	72
2	30	5.5 kDa (1.14)	70
3	40	5.1 kDa (1.17)	80

^aEquiv of additional ligand relative to catalyst. ^bDetermined by THF SEC calibrated using polystyrene standards. ^cIsolated yield after purification.

Nanostructure Analysis of P3HT-*b*-PTs with Different Block Ratios

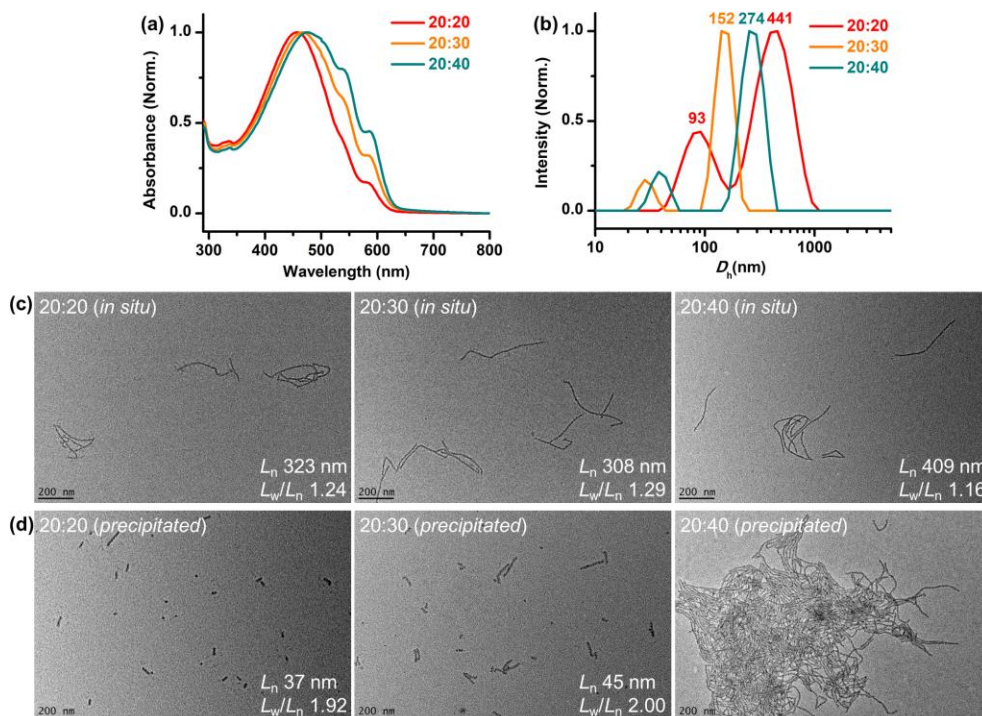


Figure S5.20. (a) UV-vis spectra and (b) DLS profiles from *in situ* solution of three P3HT-*b*-PTs (0.05 g/L, THF solution at rt). Absorbance intensities are normalized with intensity at 323 nm (P34DHT shell block absorbance). Intensities are normalized to [0,1] for DLS analysis. TEM images of uncontrolled 1D nanoparticles from (c) *in situ* aliquots (0.01 g/L, THF solution) and (d) precipitated samples (0.01 g/L, CHCl₃ solution) of three P3HT-*b*-PTs. BCPs with block ratio of P3HT:PT = 20:20, 20:30, 20:40. Scale bars are 200 nm.

Calculation of DP and Conversion of PT Core Block in Time-dependent Experiment

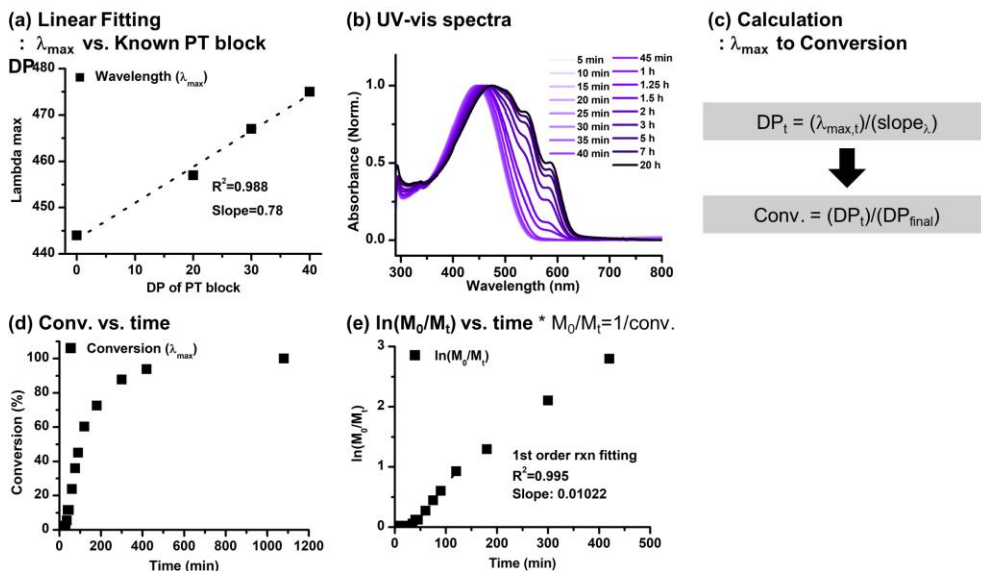


Figure S5.21. Procedure of calculating insoluble PT block's DP in *time-dependent (kinetic)* experiment from known PT block DP of P3HT-*b*-PTs by UV-vis absorbance analysis. (a) Linear fitting of ' λ_{\max} vs. DP of PT block' plot. Slope represents increased wavelength per DP of PT block. (b) UV-vis absorbance spectra along time after **M3** addition. The feed ratio of 20:30:1 (**[M2]**:**[M3]**:**[I]**) was used for the experiment. After some time, aliquots were taken from the reaction mixture and diluted with THF for UV-vis spectra. (c) DP at the time point (DP_t) is calculated by dividing λ_{\max} in time-dependent UV-vis spectra ($\lambda_{\max,t}$) by the slope calculated in (a). Then, conversion is calculated by dividing DP_t by the final estimated DP at the end of polymerization (DP_{final}). (d) Plot illustrating calculated conversion at each time point. (e) First-order kinetics plot of polymerization.

Structural Analysis by TEM in Time-dependent Experiment

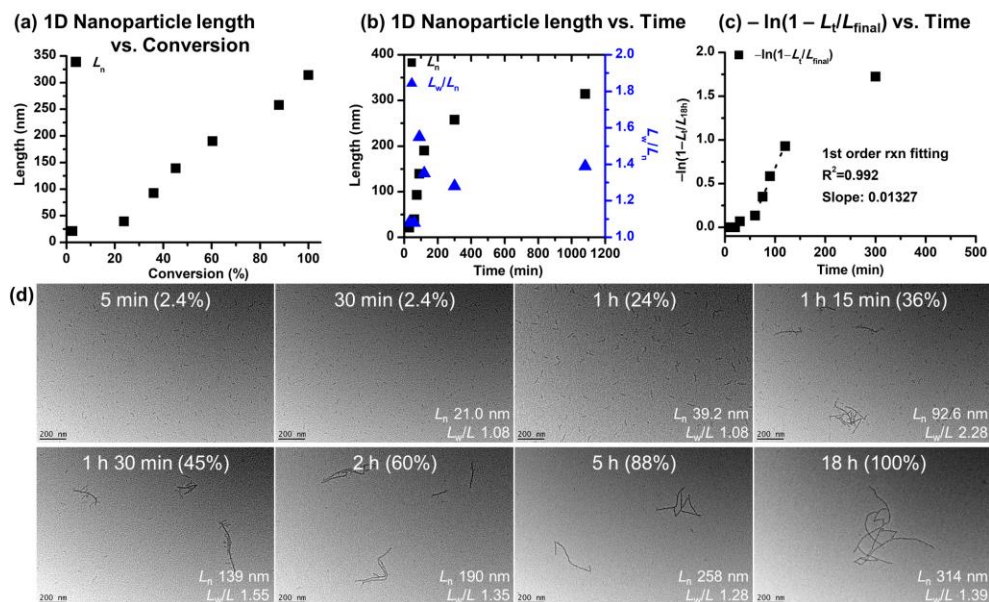
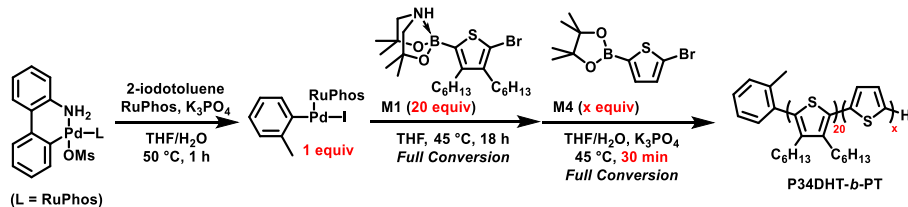


Figure S5.22. The feed ratio of 20:30:1 ([M2]:[M3]:[I]) was used for the experiment. After some time, aliquots were taken from the reaction mixture and diluted with THF for TEM analysis. (a) Plot illustrating a linear relationship between the length of 1D nanostructures and the estimated conversion of M3. (b) Plot illustrating 1D nanoparticles' lengths and dispersity values at each time point. (c) First-order kinetics plot of *in situ* nanoparticlization. (d) TEM images showing *in situ* nanoparticlization of P3HT-*b*-PT. Numbers in parentheses are conversions at that time. Scale bars are 200 nm.

Synthesis of P34DHT-*b*-PTs by SCTP Using M1 and M4



To a round-bottom flask equipped with a magnetic stir bar, RuPhos G3 precatalyst (0.0025 mmol), 2-iodotoluene (0.0025 mmol), RuPhos (0.015 mmol), and K_3PO_4 (0.3 mmol) were added. The flask was evacuated and backfilled with argon three times. Degassed THF (2 mL) and H₂O (0.17 mL) were then added. The mixture was heated and stirred at 50 °C for 1 h to prepare externally initiated catalyst. M1 (0.05 mmol where M/I = 20/1) in degassed THF (3 mL) was then added to the flask, and the polymerization was left to stir at 45 °C for 18 h. Subsequently, M4 (0.025 mmol, 0.05 mmol, and 0.075 mmol where M/I = 10/1, 20/1, and 30/1, respectively) in degassed THF (0.5 mL, 1.0 mL, and 2.5 mL, respectively) and

K₃PO₄ (0.0 mmol, 0.0 mmol, and 0.15 mmol, respectively) in degassed H₂O (0.0 mL, 0.0 mL, and 0.08 mL, respectively) were added to the flask, and the polymerization was left to stir at 45 °C for 30 min. The polymerization was quenched with 6N HCl solution (5 mL).

Table S5.3. Synthesis of P34DHT-*b*-PTs by SCTP Using **M1** and **M4**.

Entry	M4 (equiv) ^a	M _n (Đ) of P34HT ^b	Yield (%) ^c
1	10	6.0 kDa (1.16)	66
2	20	6.3 kDa (1.15)	53
3	30	6.2 kDa (1.15)	54

^aEquiv of additional ligand relative to catalyst. ^bDetermined by THF SEC calibrated using polystyrene standards. ^cIsolated yield after purification.

Nanostructure Analysis of P34DHT-*b*-PTs Synthesized with M4

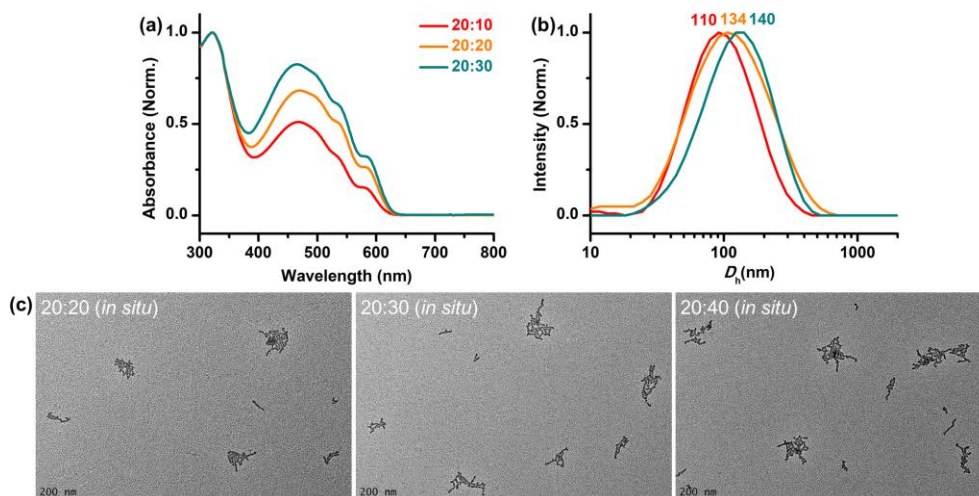


Figure S5.23. (a) UV-vis spectra and (b) DLS profiles from *in situ* solution of three P34DHT-*b*-PTs (0.05 g/L, THF solution at rt). Absorbance intensities are normalized with intensity at 323 nm (P34DHT shell block absorbance). Intensities are normalized to [0,1] for DLS analysis. (c) TEM images of uncontrolled 1D nanoparticles from *in situ* aliquots (0.01 g/L, THF solution) of three P34DHT-*b*-PTs. BCPs with block ratio of P3HT:PT = 20:20, 20:30, 20:40. Scale bars are 200 nm.

Calculation of DP and Conversion of PT Core Block in Time-dependent Experiment

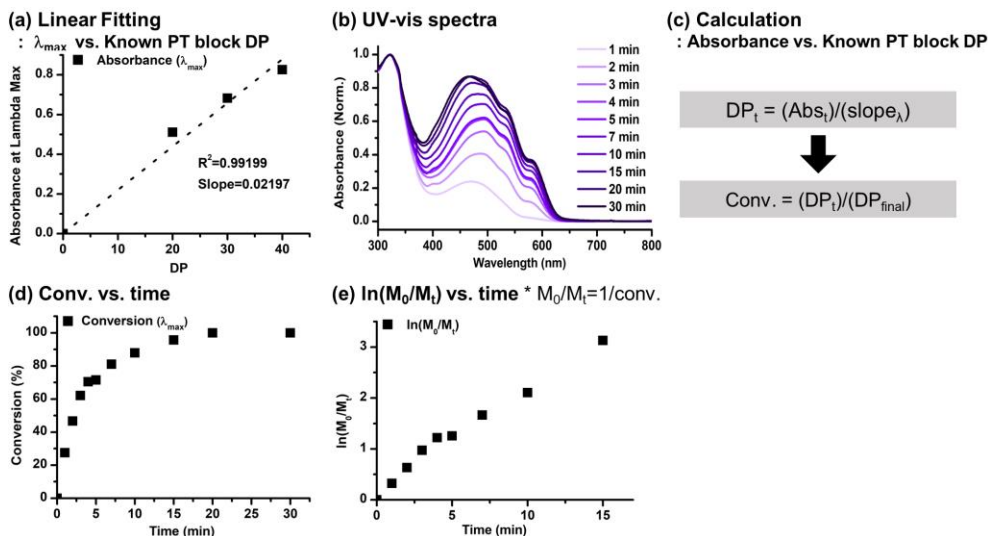


Figure S5.24. Procedure of calculating insoluble PT block's DP in *time-dependent (kinetic)* experiment from known PT block DP of P34DHT-*b*-PTs synthesized with **M4** by UV-vis absorbance analysis. (a) Linear fitting of 'Absorbance at λ_{\max} vs. DP of PT block' plot. Slope represents increased absorbance per DP of PT block. (b) UV-vis absorbance spectra along time after **M4** addition. The feed ratio of 20:30:1 (**[M1]**:**[M4]**:**[I]**) was used for the experiment. After some time, aliquots were taken from the reaction mixture and diluted with THF for UV-vis spectra. (c) DP at the time point (DP_t) is calculated by dividing absorbance at λ_{\max} in time-dependent UV-vis spectra (Abs_t) by the slope calculated in (a). Then, conversion is calculated by dividing DP_t by the final estimated DP at the end of polymerization (DP_{final}). (d) Plot illustrating calculated conversion at each time point. (e) First-order kinetics plot of polymerization.

Structural Analysis by TEM in Time-dependent Experiment

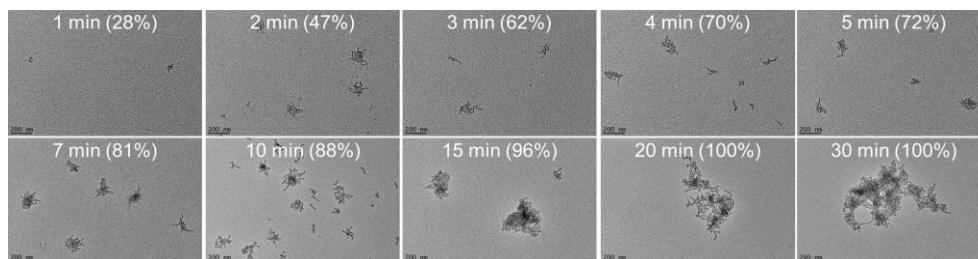
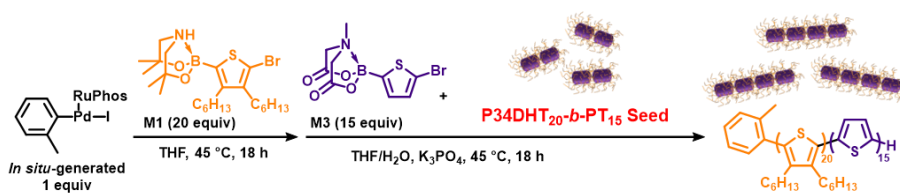


Figure S5.25. The feed ratio of 20:30:1 (**[M1]**:**[M4]**:**[I]**) was used for the experiment. After some time, aliquots were taken from the reaction mixture and diluted with THF for TEM analysis. TEM images showing *in situ* nanoparticulation of P34DHT-*b*-PT. Numbers in parentheses are conversions at that time. Scale bars are 200 nm.

5.6.6. “Living” CD-INCP



To a round-bottom flask equipped with a magnetic stir bar, RuPhos G3 precatalyst (0.0025 mmol), 2-iodotoluene (0.0025 mmol), RuPhos (0.015 mmol), and K_3PO_4 (0.3 mmol) were added. The flask was evacuated and backfilled with argon three times. Degassed THF (2 mL) and H_2O (0.17 mL) were then added. The mixture was heated and stirred at 50 °C for 1 h to prepare externally initiated catalyst. **M1** (0.05 mmol where M/I = 20/1) in degassed THF (3 mL) was then added to the flask, and the polymerization was left to stir at 45 °C for 18 h. Subsequently, **M3** (0.0375 mmol where M/I = 15/1) and pre-synthesized **P34DHT₂₀-b-PT₁₅** (15.60 mg, 7.80 mg, 5.20 mg, and 3.90 mg where U/S = 1, 2, 3, and 4, respectively) in degassed THF (3.8 mL, 1.9 mL, 1.25 mL, and 1.0 mL, respectively) were added to the flask, and the polymerization was left to stir at 45 °C for 18 h.

Table S5.4. Synthesis of P34DHT-*b*-PTs Using **M1**, **M3**, and pre-synthesized seed.

Entry	U/S	M_n (Đ) of P34HT ^a
1	1	5.5 kDa (1.18)
2	2	6.2 kDa (1.16)
3	3	5.5 kDa (1.17)
4	4	5.4 kDa (1.16)

^aDetermined by THF SEC calibrated using polystyrene standards.

5.6.6. One-Shot CD-INCP

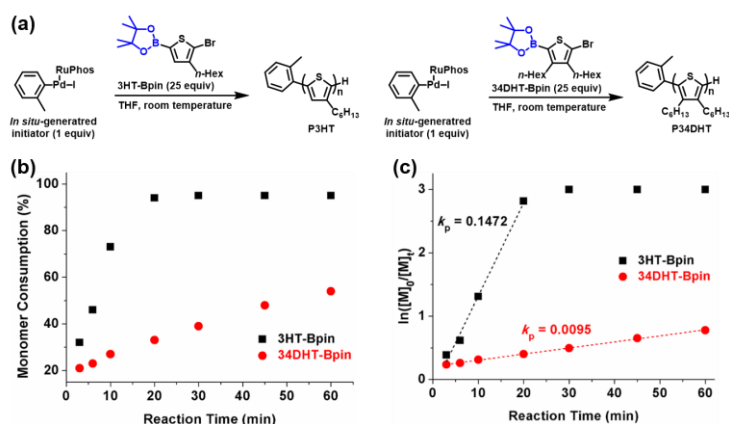


Figure S5.26. (a) Preparation of P3HT and P34DHT by SCTP using **3HT-Bpin** and **34DHT-Bpin**, respectively. (b) Consumption vs time and (c) Logarithmic consumption vs time plots for each polymerization. The propagation rate of **3HT-Bpin** was 15-fold faster than that of **34DHT-Bpin** (0.1472 vs 0.0095 for the rate constants).

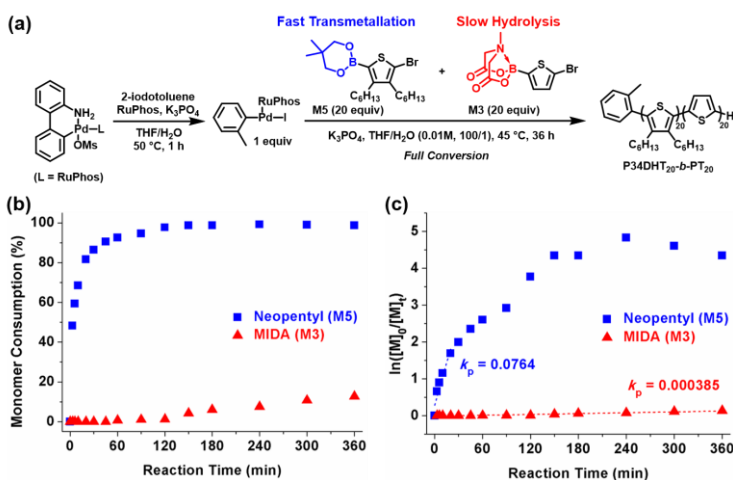


Figure S5.27. (a) One-shot preparation of P34DHT₂₀-b-PT₂₀ by SCTP using both **M5** and **M3**. To a round-bottom flask equipped with a magnetic stir bar, Buchwald Pd G3 precatalyst (0.0025 mmol), 2-iodotoluene (0.0025 mmol), RuPhos (0.015 mmol), and K₃PO₄ (0.6 mmol) were added. The flask was evacuated and backfilled with argon three times. Degassed THF (2 mL) and H₂O (0.1 mL) were then added. The mixture was heated and stirred at 50 °C for 1 h to prepare externally initiated catalyst. Both **M5** (0.05 mmol) and **M3** (0.05 mmol) in degassed THF (8 mL) was then added to the flask, and the polymerization was left to stir at 45 °C for 36 h. (b) Consumption vs time to compare reactivities of **M5** and **M3**. (c) Logarithmic consumption vs time plots for the one-shot polymerization. The propagation rate of **M5** was 198-fold faster than that of **M3** (0.0764 vs 0.000385 for the rate constants).

5.6.7. Cyclic Voltammogram of P34DHT

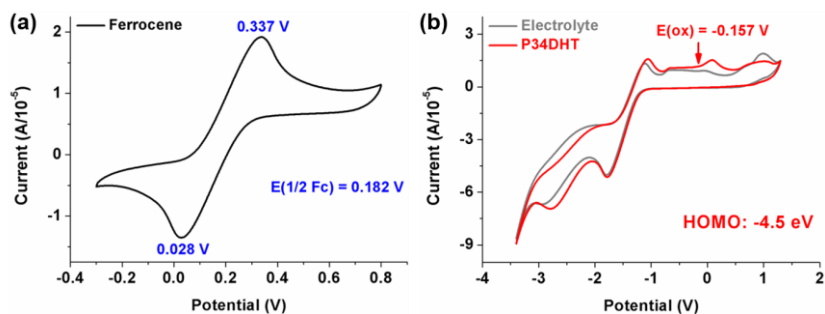


Figure S5.28. (a) $E_{1/2}$ (Ferrocene) = 0.182 V was obtained from a result of ferrocene/ferrocenium. (b) The HOMO energy level of P34DHT is -4.5 eV.

5.6.8. TGA and DSC Profiles of P34DHT-*b*-PTs

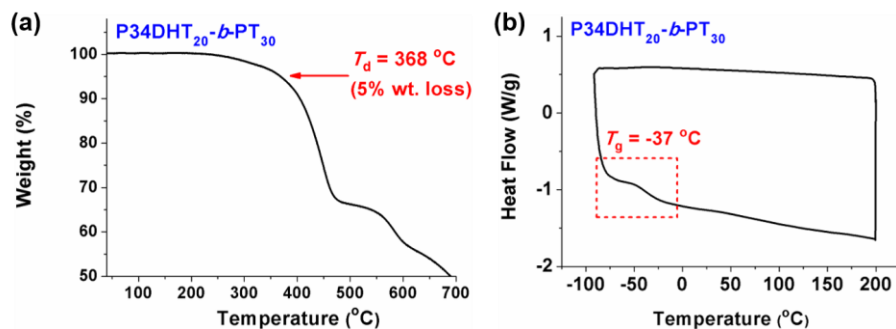
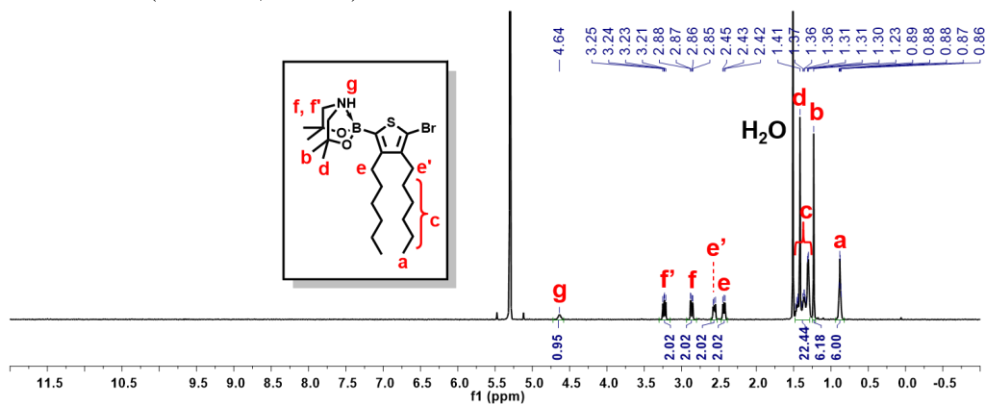


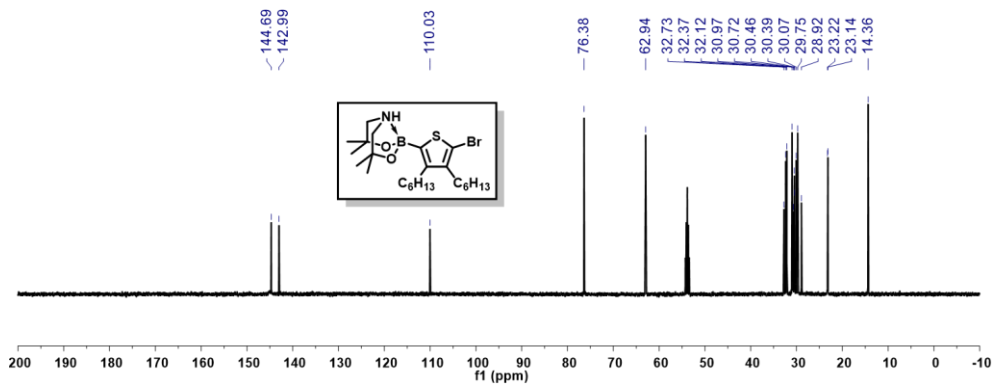
Figure S5.29. (a) TGA thermograph showing $T_{d,95\%}$ at 368 °C and (b) DSC thermograph showing T_g at -37 °C of P34DHT₂₀-*b*-PT₃₀.

5.6.9. ¹H and ¹³C NMR Spectra of Monomers and Polymers

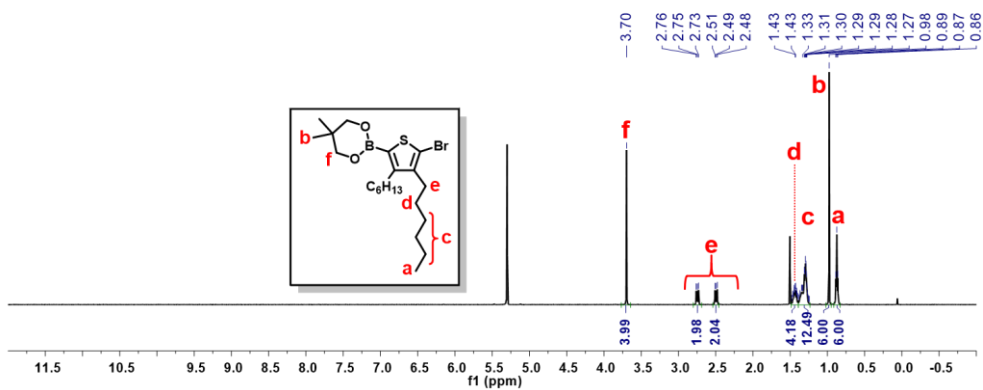
M1 ¹H NMR (500 MHz, CD₂Cl₂)



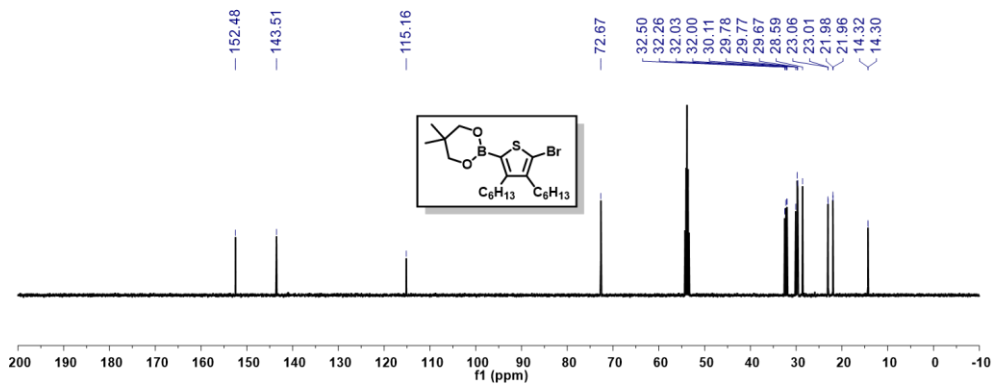
M1 ^{13}C NMR (125 MHz, CD_2Cl_2)



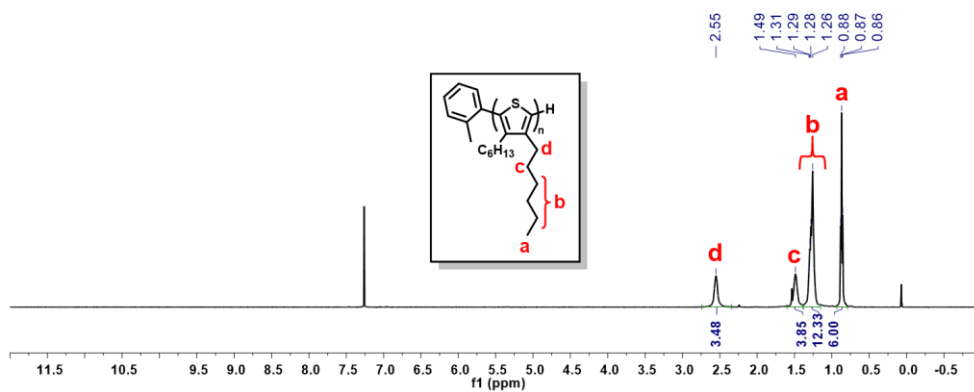
M5 ^1H NMR (500 MHz, CD_2Cl_2)



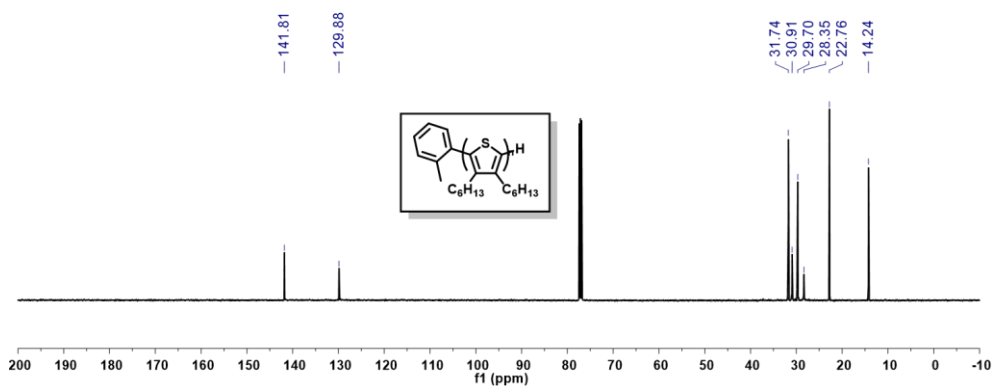
M5 ^{13}C NMR (125 MHz, CD_2Cl_2)



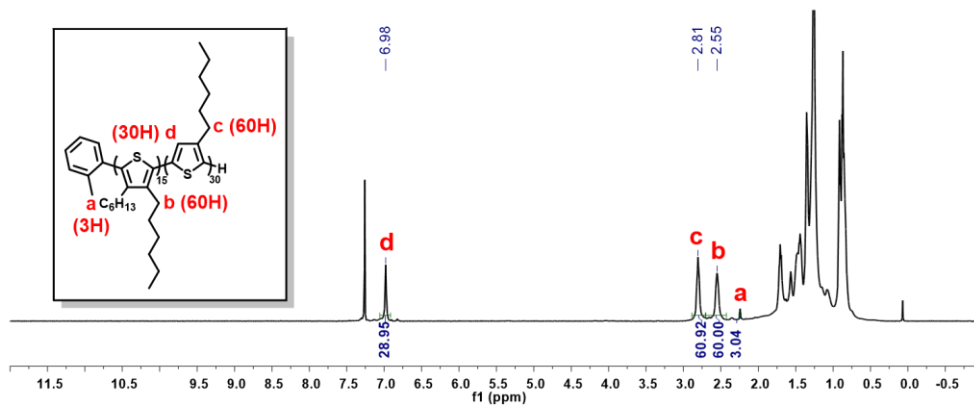
P34DHT ^1H NMR (500 MHz, CDCl_3)



P34DHT ^{13}C NMR (125 MHz, CDCl_3)



P34DHT_{15-b}-P3HT₃₀ ^1H NMR (500 MHz, CDCl_3)



5.7. References

*Portions of this chapter have been previously reported, see: Hwang, S.-H.; Kang, S.-Y.; Yang, S.; Lee, J.; Choi, T.-L. *J. Am. Chem. Soc.* **2022**, *144*, 5921–5929.

- (1) MacFarlane, L. R.; Shaikh, H.; Garcia-Hernandez, J. D.; Vespa, M.; Fukui, T.; Manners, I. *Nat. Rev. Mater.* **2021**, *6*, 7–26.
- (2) Feng, L.; Zhu, C.; Yuan, H.; Liu, L.; Lv, F.; Wang, S. *Chem. Soc. Rev.* **2013**, *42*, 6620–6633.
- (3) Chen, J. Y.; Su, C. Y.; Hsu, C. H.; Zhang, Y. H.; Zhang, Q. C.; Chang, C. L.; Hua, C. C.; Chen, W. C. *Polymers* **2019**, *11*, 1501–1516.
- (4) Wang, S.; Pisula, W.; Müllen, K. *J. Mater. Chem.* **2012**, *22*, 24827–24831.
- (5) Mele, E.; Lezzi, F.; Polini, A.; Altamura, D.; Giannini, C.; Pisignano, D. *J. Mater. Chem.* **2012**, *22*, 18051–18056.
- (6) Lin, H. W.; Lee, W. Y.; Chen, W. C. *J. Mater. Chem.* **2012**, *22*, 2120–2128.
- (7) Lin, C. J.; Hsu, J. C.; Tsai, J. H.; Kuo, C. C.; Lee, W. Y.; Chen, W. C. *Macromol. Chem. Phys.* **2011**, *212*, 2452–2458.
- (8) Camposo, A.; Pensack, R. D.; Moffa, M.; Fasano, V.; Altamura, D.; Giannini, C.; Pisignano, D.; Scholes, G. D. *J. Am. Chem. Soc.* **2016**, *138*, 15497–15505.
- (9) Merlo, J. A.; Frisbie, C. D. *J. Phys. Chem. B* **2004**, *108*, 19169–19179.
- (10) Li, X.; Wolanin, P. J.; MacFarlane, L. R.; Harniman, R. L.; Qian, J.; Gould, O. E.; Dane, T. G.; Rudin, J.; Cryan, M. J.; Schmaltz, T. *Nat. Commun.* **2017**, *8*, 15909.
- (11) Jin, X. H.; Price, M. B.; Finnegan, J. R.; Boott, C. E.; Richter, J. M.; Rao, A.; Menke, S. M.; Friend, R. H.; Whittell, G. R.; Manners, I. *Science* **2018**, *360*, 897–900.
- (12) Hu, Z.; Shao, B.; Geberth, G. T.; Vanden Bout, D. A. *Chem. Sci.* **2018**, *9*, 1101–1111.
- (13) Chang, M.; Choi, D.; Egap, E. *ACS Appl. Mater. Interfaces.* **2016**, *8*, 13484–13491.
- (14) Yin, K.; Zhang, L.; Lai, C.; Zhong, L.; Smith, S.; Fong, H.; Zhu, Z. *J. Mater. Chem. Commun.* **2011**, *21*, 444–448.
- (15) Zhang, R.; Li, B.; Iovu, M. C.; Jeffries-El, M.; Sauve, G.; Cooper, J.; Jia, S.; Tristram-Nagle, S.; Smilgies, D. M.; Lambeth, D. N.; McCullough, R. D.; Kowalewski, T. *J. Am. Chem. Soc.* **2006**, *128*, 3480–3481.
- (16) Gilroy, J. B.; Gadt, T.; Whittell, G. R.; Chabanne, L.; Mitchels, J. M.; Richardson, R. M.; Winnik, M. A.; Manners, I. *Nat. Chem.* **2010**, *2*, 566–570.
- (17) He, Y.; Eloi, J.; Harniman, R. L.; Richardson, R. M.; Whittell, G. R.; Mathers, R. T.; Dove, A. P.; O'Reilly, R. K.; Manners, I. *J. Am. Chem. Soc.* **2019**, *141*, 19088–19098.
- (18) Qiu, H.; Gao, Y.; Boott, C. E.; Gould, O. E. C.; Harniman, R. L.; Miles, M. J.; Webb, S. E. D.; Winnik, M. A.; Manners, I. *Science* **2016**, *352*, 697–701.

- (19) Petzetakis, N.; Dove, A. P.; O'Reilly, R. K. *Chem. Sci.* **2011**, *2*, 955–960.
- (20) Fukui, T.; Garcia-Hernandez, J. D.; MacFarlane, L. R.; Lei, S.; Whittell, G. R.; Manners, I. *J. Am. Chem. Soc.* **2020**, *142*, 15038–15048.
- (21) Kynaston, E. L.; Nazemi, A.; MacFarlane, L. R.; Whittell, G. R.; Faul, C. F. J.; Manners, I. *Macromolecules* **2018**, *51*, 1002–1010.
- (22) Tao, D. L.; Wang, Z. Q.; Huang, X. Y.; Tian, M. W.; Lu, G. L.; Manners, I.; Winnik, M. A.; Feng, C. *Angew. Chem., Int. Ed.* **2020**, *59*, 8232–8239.
- (23) Shin, S.; Menk, F.; Kim, Y.; Lim, J.; Char, K.; Zentel, R.; Choi, T.-L. *J. Am. Chem. Soc.* **2018**, *140*, 6088–6094.
- (24) Nie, J.; Wang, Z.; Huang, X.; Lu, G.; Feng, C. *Macromolecules* **2020**, *53*, 6299–6313.
- (25) Shin, S.; Gu, M.-L.; Yu, C.-Y.; Jeon, J.; Lee, E.; Choi, T.-L. *J. Am. Chem. Soc.* **2018**, *140*, 475–482.
- (26) Yang, S.; Choi, T.-L. *Chem. Sci.* **2020**, *11*, 8416–8424.
- (27) Yoon, K.-Y.; Lee, I.-H.; Kim, K. O.; Jang, J.; Lee, E.; Choi, T.-L. *J. Am. Chem. Soc.* **2012**, *134*, 14291–14294.
- (28) Yoon, K.-Y.; Lee, I.-H.; Choi, T.-L. *RSC Adv.* **2014**, *4*, 49180–49185.
- (29) Yoon, K.-Y.; Shin, S.; Kim, Y.-J.; Kim, I.; Lee, E.; Choi, T.-L. *Macromol. Rapid Commun.* **2015**, *36*, 1069–1074.
- (30) Shin, S.; Yoon, K.-Y.; Choi, T.-L. *Macromolecules* **2015**, *48*, 1390–1397.
- (31) Lee, I.-H.; Amaladass, P.; Yoon, K.-Y.; Shin, S.; Kim, Y.-J.; Kim, I.; Lee, E.; Choi, T.-L. *J. Am. Chem. Soc.* **2013**, *135*, 17695–17698.
- (32) Lee, I.-H.; Amaladass, P.; Choi, T.-L. *Chem. Commun.* **2014**, *50*, 7945–7948.
- (33) Lee, I.-H.; Amaladass, P.; Choi, I.; Bergmann, V. W.; Weber, S. A. L.; Choi, T.-L. *Polym. Chem.* **2016**, *7*, 1422–1428.
- (34) Lee, I.-H.; Choi, T.-L. *Polym. Chem.* **2016**, *7*, 7135–7141.
- (35) Andreani, F.; Salatelli, E.; Lanzi, M.; Bertinelli, F.; Fichera, A. M.; Gazzano, M. *Polymer* **2000**, *41*, 3147–3157.
- (36) Kokubo, H.; Sato, T.; Yamamoto, T. *Macromolecules* **2006**, *39*, 3959–3963.
- (37) Ko, S.; Verploegen, E.; Hong, S.; Mondal, R.; Hoke, E. T.; Toney, M. F.; McGehee, M. D.; Bao, Z. *J. Am. Chem. Soc.* **2011**, *133*, 16722–16725.
- (38) Higashihara, T.; Wu, H.-C.; Mizobe, T.; Lu, C.; Ueda, M.; Chen, W.-C. *Macromolecules* **2012**, *45*, 9046–9055.
- (39) Ko, S.; Kim, D. H.; Ayzner, A. L.; Mannsfeld, S. C. B.; Verploegen, E.; Nardes, A. M.; Kopidakis, N.; Toney, M. F.; Bao, Z. *Chem. Mater.* **2015**, *27*, 1223–1232.
- (40) Senkovskyy, V.; Sommer, M.; Tkachov, R.; Komber, H.; Huck, W. T. S.; Kiriy, A. *Macromolecules* **2010**, *43*, 10157–10161.

- (41) Tkachov, R.; Senkovskyy, V.; Komber, H.; Kiriy, A. *Macromolecules* **2011**, *44*, 2006–2015.
- (42) Seo, K. B.; Lee, I. H.; Lee, J.; Choi, I.; Choi, T. L. *J. Am. Chem. Soc.* **2018**, *140*, 4335–4343.
- (43) Lee, J.; Park, H.; Hwang, S.-H.; Lee, I.-H.; Choi, T.-L. *Macromolecules* **2020**, *53*, 3306–3314.
- (44) Lee, J.; Kim, H.; Park, H.; Kim, T.; Hwang, S.-H.; Seo, D.; Chung, T. D.; Choi, T.-L. *J. Am. Chem. Soc.* **2021**, *143*, 11180–11190.
- (45) Mo, Z.; Lee, K. B.; Moon, Y. B.; Kobayashi, M.; Heeger, A. J.; Wudl, F. *Macromolecules* **1985**, *18*, 1972–1977.
- (46) Kovacic, P.; Willis, S. M.; Matichak, J. D.; Assender, H. E.; Watt, A. A. *Org. Electron.* **2012**, *13*, 687–696.
- (47) Wehner, M.; Würthner, F. *Nat. Rev. Chem.* **2020**, *4*, 38–53.
- (48) Delaney, C. P.; Kassel, V. M.; Denmark, S. E. *ACS Catal.* **2020**, *10*, 73–80.
- (49) Siram, R. B. K.; Tandy, K.; Horecha, M.; Formanek, P.; Stamm, M.; Gevorgyan, S.; Krebs, F. C.; Kiriy, A.; Meredith, P.; Burn, P. L.; Namdas, E. B.; Patil, S. *J. Phys. Chem. C* **2011**, *115*, 14369–14376.
- (50) Tietz, J. I.; Seed, A. J.; Sampson, P. *Org. Lett.* **2012**, *14*, 5058–5061.
- (51) Bagutski, V.; Grosso, A. D.; Carrillo, J. A.; Cade, I. A.; Helm, M. D.; Lawson, J. R.; Singleton, P. J.; Solomon, S. A.; Marcelli, T.; Ingleson, M. J. *J. Am. Chem. Soc.* **2013**, *135*, 474–487.
- (52) Qiu, D.; Mo, F.; Zheng, Z.; Zhang, Y.; Wang, J. *Org. Lett.* **2010**, *12*, 5474–5477.

Abstract (Korean)

국문 초록

다기능성 고분자의 합성 방법론 및 다양한 응용: 화학종 검출, 다색발광 및 조절된 자가조립

황 순 혁
화학부
서울대학교 대학원

산업적 응용에 활용될 수 있는 새로운 기능성 물질에 대한 수요가 끊임없이 지속됨에 따라, 이를 충족시키기 위해 기능성 고분자에 대한 다양한 학술연구들이 활발히 진행되어 왔다. 고분자에 기능성을 부여하는 것은 특유의 중합법 활용, 작용기 도입의 조절, 혹은 외부자극 등 다양한 방법을 통해 가능해진다. 이러한 기능성 고분자의 성능은 고분자 사슬의 화학 구조뿐만 아니라, 나노구조체의 형태에도 큰 영향을 받기 때문에 추가적인 기능을 이끌어내는 것이 가능해진다. 새로운 기능성 고분자 개발을 촉진시키기 위한 노력의 일환으로, 새로운 중합법 개발에 대한 수많은 연구들이 활발히 지속되어 왔다. 그러나, 기능성 고분자 개발의 촉진을 저해하는 여러 요소들 중 복잡하고 긴 단량체 준비과정이 주된 요인으로 작용해왔다.

이러한 맥락에서, 본 논문은 기능성 고분자의 발전을 저해하는 한계점을 극복할 수 있는 새로운 중합법의 개발 사례를 보고한다. 또한, 자극-감응 고분자 재료, 발광 재료, 전도성 나노구조체 등 기능성 고분자에 대한 다양한 연구 방향을 기술한다.

[3,3]-시그마 결합 자리옮김 반응은 매우 유용한 반응임에도 불구하고, 결합의 형성과 끊어짐이 동시에 일어나는 특성 때문에 중합법으로써 활용되지 못했다. 이러한 맥락에서, 제2장에서는 매우 간단하고 효율적인 이민 형성을 거쳐 탄소-탄소 결합을 결합없이 입체선택적으로 형성함으로써 고분자를 합성하는 다이아자-코프 자리옮김 중합법 (DCRP) 개발에 대해 서술한다. 생성된 고분자는 입체적으로 순수한 살렌 구조를 포함하기 때문에 아연 양이온을 선택적 검출할 수 있는 고성능 발광 화학종 검출기로써의 응용까지도 가능하다.

하나의 합성 조건으로부터 혹은 더 나아가 단일 반응물로부터 다색발광 형광체를 자유자재로 만들 수 있는 효율적인 합성법을 개발하는 것은 합성적 측면에서 매우 요구되는 바이다. 이러한 측면에서, 제3장에서는 직접적인 탄소-수소 결합의 아마이드화 (DCA) 반응이 들뜬 상태 분자내 양성자 이동 (ESIPT)을 통한 발광 메커니즘을 통해 백색을 포함하여 다색발광 물질을 효율적으로 합성할 수 있는 합성법임을 입증한다. DCA 반응은 작용기의 위치와 전자적 특성에 관계없이 훌륭한 합성효율을 보이기 때문에 원하는 형광을 자유자재로 얻는 것을 가능하게 해준다.

백색발광 고분자를 얻기 위한 지금까지의 여러 연구들은 가시광 영역 전체를 효과적으로 포함하기 위한 전략으로써 다중발광체 기반의 랜덤 공중합체 합성에 집중해왔다. 그러나 이러한 전략은 저조한 색 재현성의 한계점을 지닌다. 3장에서 입증한 DCA의 합성적 장점을 적극 활용함으로써, 제4장에서는 훌륭한 색 재현성을 지닌 단일형광체 기반의 백색발광 동종 중합체를 합성할 수 있는 직접적인 탄소-수소 결합의 아마이드화 중합법 (DCAP) 전략에 대해 보고한다. 이 고분자는 추가적인 매트릭스의 도움 없이도 고체상에서 백색발광을 내놓기 때문에 코팅된 백색발광 다이오드를 용액 공정을 통해 손쉽게 제작하는 것이 가능하다.

전도성 고분자 기반의 나노구조체의 크기와 형태를 정교하게 조절하는 것은 광전자적 성능에 매우 중요한 부분이지만, 전도성 고분자의 낮은 용해도는 불규칙적인 응집을 유도하여 이들의 정교한 조절은 상대적으로 제한적이다. 마지막 제5장에서는 길이조절이 가능한 일차원 전도성 나노구조체를 스즈키-미야우라 축매-이동 중합 (SCTP) 과정동안 바로 만듦으로써 나노구조체 준비과정의 효율을 높여주는 전략인 전도성 고분자의 결정화유도를 통한 반응내 나노구조체화 (CD-INCP)를 보고한다.

핵심어: 기능성 고분자, 다이아자-코프 자리옮김 중합법, 발광 화학종 검출기, 직접적인 탄소-수소 결합의 아마이드화 중합법, 들뜬 상태 분자내 양성자 이동, 발광 재료, 전도성 고분자의 결정화유도를 통한 반응내 나노구조체화, 전도성 나노구조체

학번: 2017-23693